PHYSIK-DEPARTMENT

Electronic and Geometric Properties of Organic and Metal-Organic Layers

Doktorarbeit

von

Runyuan Han

TECHNISCHE UNIVERSITÄT MÜNCHEN

TECHNISCHE UNIVERSITÄT
MÜNCHEN

Physik Department E20

Molekulare Nanowissenschaften & Chemische Physik von
Grenzflächen

Electronic and Geometric Properties of Organic and Metal-Organic Layers

Runyuan Han

Vollstädiger Abdruck der von der Fakultät für Physik der Technischen Universität München zur Erlangung des akademischen Grades eines Doktors der Naturwissenschaften (Dr. rer. nat.) genehmigten Dissertation.

Vorsitzender:	Univ.-Prof. Dr. J. Leo van Hemmen (i.R.)
Prüfer der Dissertation:	1. Univ.-Prof. Dr. Johannes Barth
	2. Priv.-Doz. Dr. Christoph P. Hugenschmidt

Die Promotion wurde am 29.09.2015 bei der Technischen Universität München eingereicht und durch die Fakultät für Physik am 28.10.2015 angenommen.

Abstract

Self assembled monolayers (SAMs) of organic molecules may find diverse technological applications ranging from corrosion protection to sensors and molecular electronics. One important reason for this versatility is that the structure of SAMs can be designed flexibly both in terms of the choice of individual molecular building blocks and of the ordering at the nanoscale. In the main body of this thesis, three types of aromatic SAMs made of molecules with either identical headgroup or tailgroup are adsorbed onto Co(0001) surface under UHV conditions to study the relationship between the structure and properties of the SAMs from the perspectives of bonding character, molecular orientation, thermal stability and charge transfer dynamics. A toolbox including X-ray Photoelectron Spectroscopy, Ultraviolet Photoelectron Spectroscopy, Near Edge X-ray Absorption Fine Structure, Thermal Programmed Desorption and the so-called Core Hole Clock method on the basis of Resonant Auger Electron Spectroscopy is employed for the investigation. This study is stimulated by the potential role of aromatic SAMs grown on ferromagnetic substrates for the development of molecular electronics and spintronics. In the final part, the chemical reactivity of ruthenium tetraphenyl porphyrin (Ru-TPP) monolayers self-assembled on Ag(111) and Ag(110) surfaces is studied, focusing specifically on the interaction of the supported metal complexes with molecular oxygen, as motivated by the potential application of such systems in the field of site-selective heterogeneous catalysis.

Contents

1 Introduction **1**

2 Experimental Methods **4**

2.1 X-Ray Photoelectron Spectroscopy, Ultraviolet Photoelectron Spectroscopy and Auger Electron Spectroscopy 4

2.2 Near Edge X-ray Absorption Fine Structure 11

2.3 Thermal Programmed Deorption and Low Energy Electron Diffraction 16

2.4 The Core Hole Clock Method 19

3 Experimental Setup **25**

3.1 The UHV Chamber 25

3.1.1 The Hemispherical Electron Energy Analyzer and Partial Electron Yield Detector 29

3.2 Photon Sources: Undulators, X-Ray Tube and Helium Lamp 32

4 Self Assembled Monolayers on Metal Substrates **38**

4.1 Fundamentals of SAMs on Metal Substrates 39

4.2 4-Fluorobenzoic Acid SAMs on Co(0001) 48

4.2.1 Experimental Results and Discussion 51

4.2.1.1 Structure Characterization with XPS and NEXAFS 51

4.2.1.2 Thermal Stability of 4-FBA/Co(0001) Monolayer . 59

4.2.1.3 Charge Transfer Dynamics 62

4.2.2 Conclusions for the 4-FBA/Co(0001) Monolayer 75

4.3 4-Cyanobenzoic Acid SAMs on Co(0001) 75

4.3.1 Experimental Results and Discussion 77

4.3.1.1 Structural Characterization with XPS and NEXAFS 77

4.3.1.2 Charge Transfer Dynamics 84

4.3.2 4-CBA/Co(0001): Conclusions 88

4.4 4-Fluorothiophenol SAMs on Co(0001) 89

4.4.1 Introduction 89

4.4.2 Experimental Results and Discussion 90

4.4.2.1 4-FTP/Co(0001) Multilayer 91

4.4.2.2 4-FTP/Co(0001) Monolayer and Lower Coverage . 97

4.4.2.3 Charge Transfer Dynamics 102

4.4.3 Conslusions for the 4-FTP/Co(0001) SAM 106

5 Interaction with O_2 of Ru Tetraphenyl Porphyrin Monolayers Adsorbed on Ag Surfaces 108
5.1 Introduction 108
5.2 Experimental Results and Discussion 109
5.2.1 Preparation and Flattening of 2H-TPP on Ag(111) 110
5.2.2 Preparation and Flattening of Ru-TPP on Ag(111) 114
5.2.3 Interaction of Ru-TPP with Oxygen on Ag(111) 118
5.2.4 Interaction of Ru-TPP with Oxygen on Ag(110) 124
5.3 Conclusions 129

6 Summary, Conclusions and Outlook 132

A Determination of the Molecular Orientation in 4-FTP SAMs 136

B Dosing O_2 Through Sputter Gun onto Ru-TPP/Ag(111) Surface at 300 K 143

Bibliography 145

List of Figures 161

List of Acronyms 166

Acknowledgements 167

Chapter 1

Introduction

Self assembled monolayers (SAMs) are ordered molecular assemblies formed by organic molecules that spontaneously arrange themselves into ordered structures on solid or liquid surfaces. The applications of SAMs, including etching resists, corrosion protection, heterogeneous catalysis and molecular electronics *etc.*, have attracted significant attention in the past decade [1, 2]. Important reasons for the versatility of SAMs in those applications include: the possibility of assembling molecular building blocks into complex structures, the ease of preparation, and the vast choice of organic molecules and substrates *etc.* From a fundamental point of view, a detailed insight into self-assembly, structure-property relationships and interfacial phenomena is required for the broad and advanced exploitation of SAMs in technology. Nowadays, the research on SAMs represents an interdisciplinary field at the crossroad among chemistry, physics, biology, nanotechnology and engineering and allows fundamental studies of the electronic and geometric structure, the thermal stability and the interfacial charge transfer dynamics (or, from the perspective of static molecular conductance, "conductivity") of the SAMs.

Within this thesis, three types of aromatic SAMs grown on a ferromagnetic cobalt substrate are studied, focusing on their growth properties, bonding character, molecular orientation, thermal stability and charge transfer dynamics. The ferromagnetic substrates are more reactive and prone to oxidation than the traditional coinage metal substrates [3, 4], thus demanding UHV conditions for sample preparation and highly surface-sensitive analytical tools for characterization, which also explains the limited number of studies to date. However, proceeding from coinage metal substrates to reactive ferromagnetic substrates will contribute not only to

a better understanding of many mechanisms related to the properties of SAMs, but also to the investigation of the properties of molecules coupled to magnetic substrates which can be further exploited in the field of spin-dependent electronics [5]. On the other hand, as aromatic SAMs are promising for application in molecular electronics [6, 7], it is necessary to understand the relationship between the electron transfer dynamics and the molecular structure, the molecule-substrate coupling as well as the physical mechanism of electron transport. The spectroscopic approach called "Core Hole Clock" is a contact-free and atom (orbital)-selective approach for the investigation of interfacial electron transfer dynamics in the femtosecond domain [8–10], at variance with the conventional method of measuring current-voltage curves at the metal-molecule-metal junction [6]. To the best of our knowledge, the charge transfer dynamics at the cobalt/SAM interface under UHV conditions remains unexplored. The present study is devoted to test the structural quality of the aromatic SAMs in view of potential applications in molecular electronics *etc.*, as it has been demonstrated that ultrafast charge transfer occurs at the interface between the layer of chemically bonded molecules and the metal substrates [11, 12] and that the highly conductive aromatic molecules can be regarded as good candidates for "molecular wires" [7]. Specifically, the role of the headgroup and the influence of the tailgroup on the molecule-to-substrate interaction and the SAMs' ordering and stability are investigated. Moreover, the headgroup- and tailgroup-to-substrate charge transfer times are quantitatively determined and their dependence on the photon energy and radiation polarization is analyzed.

In a separate study presented in the final part of this thesis, monolayers of ruthenium tetraphenyl porphyrin (Ru-TPP) self-assembled on silver surfaces (Ag(111) and Ag(110)) are investigated focusing on the interaction with molecular oxygen. RuTPP molecules with four phenyl rings in the periphery and a Ru atom in the centre of the porphine macrocycle have received considerable attention due to the high catalytic activity for the oxidation of a variety of functional groups [13–15]. Within this thesis, a comparison of the reactivity of non-flattened and flattened species of such metal complexes supported on Ag(111) and Ag(110) surfaces is performed. The potential of Ru porphyrins in the field of site-selective heterogeneous catalysis is a strong motivation for this investigation.

The thesis is organized as follows: chapter 2 describes the experimental methods used for the investigation of the selected systems, including the fundamental

principles, the data acquisition and the analysis procedures. Chapter 3 gives a description of the experimental set-ups used in this work, including technical aspects and the equipment capabilities. Chapter 4 constitutes the main part of this thesis. Here, the fundamental aspects of SAMs are introduced and subsequently previous investigations of SAMs on coinage metal substrates are briefly reviewed. Prototypical SAMs of molecules with a fluorine or cyano tailgroup and anchored to a Co(0001) substrate by means of a thiolate or carboxylate headgroup are investigated under UHV conditions with polarized synchrotron radiation. The self-assembly of Ru-TPP molecules and their reactivity towards molecular oxygen on Ag(111) and Ag(110) surfaces are studied and compared in chapter 5. Finally, a summary and outlook conclude this thesis.

Chapter 2

Experimental Methods

This chapter briefly describes the experimental methods used for the system investigation, including fundamental principles, data acquisition and analysis procedures of the techniques. Some of the surface sensitive techniques such as XPS, UPS and NEXAFS can explore in detail the electronic and geometric properties of complex adsorbate-substrate systems. Moreover, Thermal Programmed Desorption (TPD) and Low Energy Electron Diffraction (LEED) provide very useful guidance in the preparation of the Self Assembled Monolayers (SAMs) and deposited ferromagnetic films that are included in this thesis. Finally, the primary technique in this work, Resonant Auger Electron Spectroscopy (RAES) enables to study the core level excitation and de-excitation processes initiated by X-ray photons, and the derived Core Hole Clock method is an effective contact-free approach to investigate the charge transfer dynamics between an adsorbate and the underlying metal substrate.

2.1 X-Ray Photoelectron Spectroscopy, Ultraviolet Photoelectron Spectroscopy and Auger Electron Spectroscopy

X-Ray Photoelectron Spectroscopy X-Ray Photoelectron Spectroscopy (XPS), also called Electron Spectroscopy for Chemical Analysis (ESCA), is a technique directly detecting core-level electrons excited upon absorption of photons. It is widely used in basic research and analysis of materials, particularly in surface

analysis. By means of XPS information on the elemental surface composition (except for H and He), the chemical environment and the oxidation state can be obtained.

In XPS experiments, the energy of the radiation is in the soft x-ray regime (0.1 - 2 KeV), and the excitation photons can either come from magnesium ($MgK\alpha_{1,2}$, $\hbar\omega = 1253.6eV$) or aluminum ($AlK\alpha_{1,2}$, $\hbar\omega = 1486.6eV$) anodes of standard laboratory sources or from high brilliance radiation generated in synchrotron facilities. Upon photon illumination, the excited electrons are ejected from the sample surface by photoelectric effect and separated according to their kinetic energy by an electron energy analyzer. Finally, the emitted electrons of given kinetic energy, which contribute to the intensity of a peak in the XPS spectrum are counted by, *e.g.*, a microchannel plate. If the kinetic energy of the emitted electron is denoted as E_k and the photoionized atom as M^+, the excitation process can be describe as:

$$M + ph(\hbar\omega) \rightarrow M^+ + e^-(E_k) \tag{2.1}$$

Whenever the electron final state reached upon excitation is above the vacuum level, electrons will overcome the energy barrier at the surface and be detected by energy analyzer. Figure 1(a) shows the schematic depiction of this process, and from the energy conservation it follows easily:

$$E_k = \hbar\omega - E_b - \phi_{spec} \tag{2.2}$$

This is the basic equation of Einstein's photoelectric effect used in spectroscopic applications. Here, the binding (E_b) and kinetic energy (E_k) are referenced to the Fermi level E_f and vacuum level, respectively, and since analyzer and sample are in most cases electrically connected, the work function which enters the equation is that of the analyzer (rather than that of the sample), denoted as ϕ_{spec}. Insulating or poorly conducting samples tend to be positively charged upon photoemission, and the binding energy scale must be calibrated against a reference peak with well-known binding energy (e.g., the C *1s* level at 285 eV of atomic carbon) [16]. Instead, for conducting samples the binding energy is simply calculated by using Eq.(2.2), if ϕ_{spec} is known or experimentally determined.

The XP spectrum is commonly analyzed by comparison with standard handbooks and available literature [17]. Upon excitation with X-rays, electrons in different

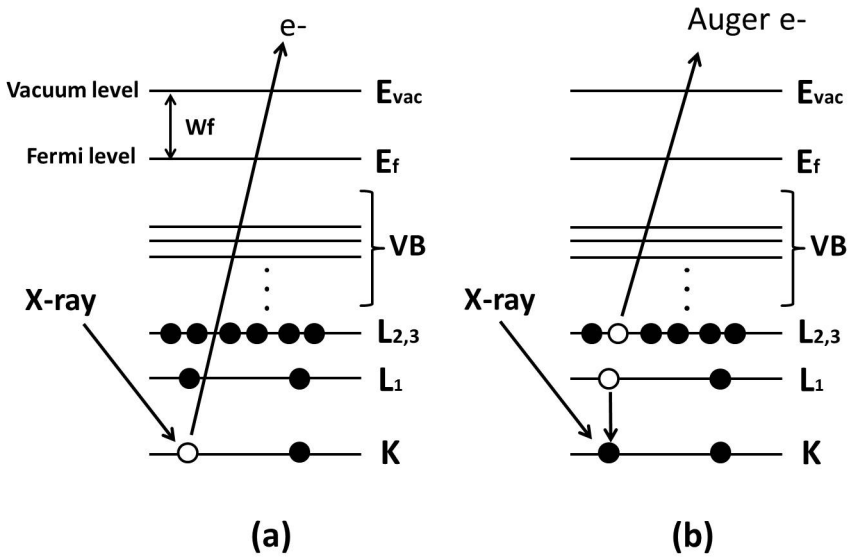

FIGURE 2.1: Schematic depiction of the X-ray photoemission and subsequent de-excitation process. Filled circles represent electrons, empty circles core holes (h).**(a)** X-ray induced photoemission, resulting in 1 hole final state. **(b)** Non-radiative Auger decay process of the excited core hole, resulting in 2h final state.

shells can be simultaneously excited and a series of lines will be displayed in the spectrum. Spin-orbit splitting can generate doublets with fixed binding energy spacing and intensity ratio, that is, the angular momentum ℓ of the unpaired electron left behind upon photo-ionization in the originally filled shell couples to the spin s, $\ell \pm s$, and generates splitting of the orbital (for p,d and f orbitals, but not for s orbitals). Multiplet splitting can also occur, when unpaired electrons are present in the outer shell of an atom, whose spin can couple to that of the core hole created by photoemission [18]. On the way to the surface, electrons may undergo multiple inelastic scattering and experience energy losses, thus contributing to a secondary electron background, which appears as a continuous tail on the low kinetic energy side of a photoelectron peak. Collective oscillations of valence electrons (plasma oscillations) also generate energy loss lines, and for a free electron gas their frequency and energy can be written as:

$$\omega_p = \sqrt{\frac{4\pi n e^2}{m_e}} \tag{2.3}$$

$$E_p = \hbar\omega_p \tag{2.4}$$

where n denotes the density of bulk conduction electrons, m_e the effective electron

mass, and E_p the quantized energy of the oscillation. The energy of a surface plasmon is roughly $\frac{1}{\sqrt{2}}$ of E_p (bulk) [19].

X-rays produced by the radiative decay of core holes in the K shell of Mg and Al ($K\alpha_{1,2}$) often contain to some extent higher energetic components like $K\alpha_{3,4}$ and K_β (satellites), and possibly the radiative decay of copper underneath the deposited Al and Mg film inside the X-ray tube together with the oxygen contamination in partly oxidized films may also contribute to the satellite lines. Fortunately, these satellite lines are at constant energy offset with respect to the main XPS line and therefore do not severely disturb the analysis of XP spectra. On the other hand, shake-up lines often show up several electron volts (eV) below in kinetic energy with respect to the main XPS line. These shake-up features are created when the energy of the absorbed photon also contributes to the excitation of a valence electron (besides the primary core electron) and shakes it up to a higher energy level; as a consequence the energy of the core electron is reduced, and a satellite structure appears a few eV (in the kinetic energy scale) below the core level line.

Furthermore, the binding energies of core-level electrons are very sensitive to the chemical environment of an atom, and the variation of binding energy results in shifts of the corresponding XPS peak called "chemical shifts". Chemical shifts arise, *e.g.*, in the initial state from the displacement of electronic charge from the atom to a ligand. The binding energy of the core electron of the ligated atom is dependent on the electronegativity of the ligands. For example, carbon atoms attached to fluorine and sulphur in a 4-fluorothiophenol molecule show different binding energies, higher than the carbon atoms in the phenyl ring.

While the chemical shift is often, predominantly, an initial state effect, the spin orbit splitting and multielectron excitations mentioned above are final state effects. Another very important final state effect, which needs to be considered, arises during relaxation of the ionized atom following creation of the core hole. Here, the remaining electrons of the emitted atom (intrinsic relaxation) and neighbouring atoms (extrinsic relaxation) rearrange themselves to partially screen the electron vacancy in the inner shell and minimize the total energy. As a consequence, the binding energy of the photoelectron is strongly reduced due to intra-atomic and interatomic screening [17]. Importantly, this binding energy reduction depends on the system in which the ionized atom is embedded. As a result, the binding energy of e.g., the same C *1s* species of 4-fluorobenzoic acid molecule (e.g., C *1s*

of C-F) in a monolayer and in multilayers deposited on a Ni(111) surface may be different in the measured spectra depending on the multilayer thickness. In particular, the C *1s* binding energy of the monolayer will be lower due to stronger screening of the core hole by the underlying metal substrate, as compared with that of multilayer [20], where the interaction between physisorbed molecules and the metal substrate is greatly suppressed, and the polarization screening from electrons of neighbouring molecules is relatively weak.

It should be noted that all XPS peaks have inevitably a finite linewidth due to the finite core-hole lifetime, resulting in a Lorentzian broadening. The total full width at half maximum (FWHM) ΔE of a peak is determined by the natural broadening due to the core-level lifetime $\Gamma_c = \hbar/\tau_c$, the X-ray line width ΔE_{xray} and the analyzer resolution $\Delta E_{analyzer}$ according to the following equation [21]:

$$\Delta E = (\Gamma_c^2 + \Delta E_{xray}^2 + \Delta E_{analyzer}^2)^{1/2} \tag{2.5}$$

A special advantage of using synchrotron radiation is given by the small band width of the radiation filtered by a suitable monochromator, which reduces the contribution of ΔE_{xray}. In additional to the instrumental effects, a number of decay channels, excitation of lattice vibrations and inhomogeneous broadening may also contribute to the linewidth of the peak, resulting in a Gaussian contribution to the line-shape. As a consequence, the measured spectra are often fitted using Voigt-type profiles. Additionally, the elemental stoichiometric ratios can be approximately obtained from XPS by the ratio of area of lines I_a/I_b after subtraction of a linear or a Shirley-type background:

$$\frac{a}{b} \propto \frac{\sigma_b \lambda_b I_a}{\sigma_a \lambda_a I_b} \tag{2.6}$$

where σ_a, σ_b denote the photoionization cross sections of level a and b, which are usually maximized at synchrotrons by employing an excitation energy about 100 eV above the ionization threshold. I is the integrated peak area, while λ is the inelastic mean free path (IMFP) of electrons in the solid and depends strongly on the kinetic energy of electrons. The as-chosen optimum photon energy will enable the photoelectrons to be ejected with a kinetic energy of about 100 eV, at which the IMFP is strongly reduced and therefore largely enhances the surface sensitivity of the measurements [22]. At any rate, due to the small IMFP of electrons, XPS

is a very surface sensitive technique even though X-rays can penetrate 1-10 μm in solids. The surface sensitivity can be further improved by increasing the angle of electron emission relative to the surface normal.

Auger Electron Spectroscopy The excitation of core-level electrons leads to a 1-hole state which is not stable. There are generally two pathways for the core-hole decay within the core-hole lifetime:

1. Radiative decay (i.e., emission of photons), also called X-ray fluorescence, which is more likely for deep core hole levels with high binding energy and for high Z elements.

2. Non-radiative decay or so-called Auger process, which is more likely for shallow core levels with low binding energy and low Z elements.

An Auger decay is a three-electron process and leaves the atom doubly-ionized. Here, the core hole with binding energy E_b is filled by a higher-lying electron with binding energy E_1, and the excess energy is transferred to another electron with binding energy E_2, which is then emitted as Auger electron. The Auger process is depicted in Figure 2.1 (b). The kinetic energy of the Auger electron is given by $E_{kin} = E_b - E_1 - E_2 - U(1,2)$, where $U(1,2)$ denotes the interaction energy of the two holes in the final state [17]. Auger Electron Spectroscopy (AES) is a surface-sensitive analytical tool that often utilizes a high energy electron beam (an electron gun is experimentally simpler and cheaper as compared to the production of X-rays) as an excitation source, due to the fact that kinetic energy of the Auger electron is independent of the excitation energy. A typical Auger spectrum contains closely-spaced groups of multiple peaks arising from final state effects. The interpretation and assignment of the spectral features in AES may be more difficult than in XPS, therefore AES is not used as much as XPS to gain information on the chemical environment. Herein, AES is mainly used in combination with RAES to explore the charge transfer dynamics, as will be further discussed in section 2.4.

Ultraviolet Photoelectron Spectroscopy Ultraviolet Photoelectron Spectroscopy (UPS) is a spectroscopic technique that employs vacuum UV (10-120 eV) radiation to excite electrons from weakly bound valence levels. A typical laboratory source is a Helium discharge lamp emitting at 21.2 eV (He I radiation) or

40.8 eV (He II radiation). A UPS spectrum provides information on the occupied density of states (DOS) of valence levels, revealing the electronic structure of the valence region in atoms, solids and molecules by analysing the kinetic energy and angular distribution of photoelectron intensity. Furthermore, by determining the position of the low kinetic energy cut-off and the high kinetic energy cut-off (Fermi level for metal) of a UPS spectrum at a precisely known photon energy, the work function of the material can be retrieved as:

$$\Phi = h\upsilon - W \tag{2.7}$$

thus giving insight into the interface charge distribution between adsorbate and substrate. Here, W is the width of the spectrum from the low kinetic energy cut-off to the high kinetic energy cut-off, and $h\upsilon$ the excitation energy of the discharge lamp. Note that in a UPS experiment, due to the low kinetic energy of the detected electrons, the external magnetic fields in the region between sample and detector have to be completely shielded to avoid distortion of the electron trajectory. In our set-up, Helmholtz coils are set around the chamber for magnetic field shielding (i.e., to compensate the earth's magnetic field.). Moreover, a negative bias (5-10 volts) is usually applied to the sample to increase the kinetic energy of the escaping photoelectrons and to obtain a steep low energy cut-off [23]. Additionally, by changing the polarization of the UV light and determining the resulting dichroism, the orientation of chemisorbed species on substrate can be obtained, providing a useful alternative to NEXAFS (see section 2.4) for structural information, without need for access to a synchrotron facility.

The polarization of the ultraviolet light from a UV discharge lamp can be changed by a continuously rotatable three-mirror linear polarizer [24]. Three directions of the polarization are employed in our measurement: A_z (polarization vector 7° off the surface normal), A_{xy} (polarization vector perpendicular to surface normal), and A_{xyz} (45° between polarization vector and surface normal). Depending on the symmetry of the oriented molecular orbitals (π^* or σ^* type, e.g., HOMO or partly occupied LUMO), the photoemitted intensity can be maximized when the polarization vector is along the axis of molecular orbital and minimized when it is perpendicular. Based on the spectrum measured with at least two extreme polarizations (A_{xy} *vs.* A_z), the geometry of the molecular orbital can be qualitatively analyzed and the molecular geometry can be inferred. Figure 2.2 shows

the UPS spectra measured at two different polarizations in normal emission for 4-fluorothiolphenol SAMs on Ni(111).

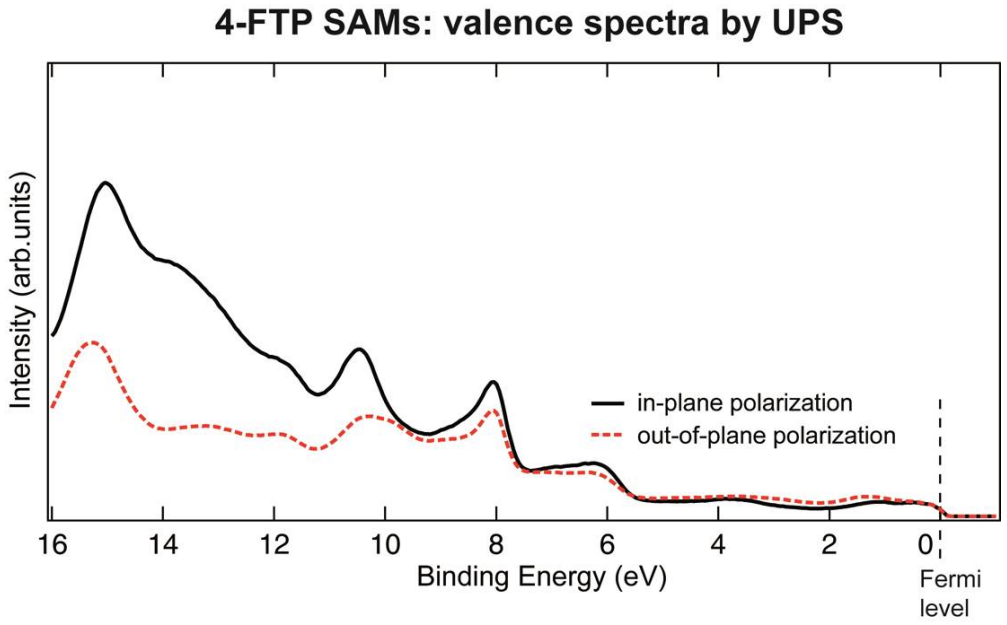

FIGURE 2.2: UPS spectra of the 4-FTP SAMs taken in normal emission at two different polarizations of the UV light, specifically with the electric vector oriented in-plane (A_{xy}, black line) or out-of-plane (A_z red dashed line) relative to the substrate surface.

2.2 Near Edge X-ray Absorption Fine Structure

Near Edge X-ray Absorption Fine Structure (NEXAFS)is a widely employed and powerful tool for the quantitative or semi-quantitative determination of molecular orientation, and its broad applicability ranges from relatively simple molecules adsorbed at surface to more complex biomolecules and bulk polymers. With high-brilliance synchrotron radiation, the adsorption structure of molecules, especially low-Z organic molecules consisting of light atoms like carbon, nitrogen, oxygen and fluorine, can be resolved. NEXAFS usually probes transitions from the K-edge of a low-Z atomic species into unoccupied unbound or quasi-bound molecular orbitals or continuum states. The X-ray absorption spectrum exhibits strong and distinctive features in the energy region below and up to about 50 eV above the absorption edge. NEXAFS explores the unoccupied DOS of molecules and solids, in contrast to XPS, which provides information on the occupied DOS. The acquisition of a NEXAFS spectrum can be accomplished in transmission mode, electron

yield detection mode or fluorescence mode. In the case of molecules adsorbed on a substrate surface, the electron yield detection mode is typically preferred because of the enhanced surface sensitivity. Therefore in the present work, the Auger electrons excited at a given photon energy at the absorption edge were detected by means of a partial yield detector. In this case, the number of detected decay electrons is assumed to be proportional to the absorption coefficient as the energy is continuously scanned through the absorption edge.

As an example, the origin of the NEXAFS features is schematically illustrated in Figure 2.3 (a). The effective potential landscape and the corresponding K-shell spectrum for a diatomic molecule such as CO or NO are shown. The absorption step arises from the excitation of core-level electrons into continuum or quasi-continuum states, and the transition into Rydberg states is often obscured. Close to the ionization threshold, resonant peaks are superimposed onto the step-like background: they occur when the energy of the incoming photons matches exactly the energy difference between the initial state and an unoccupied molecular orbital which is labelled as π^* or σ^* according to its symmetry.

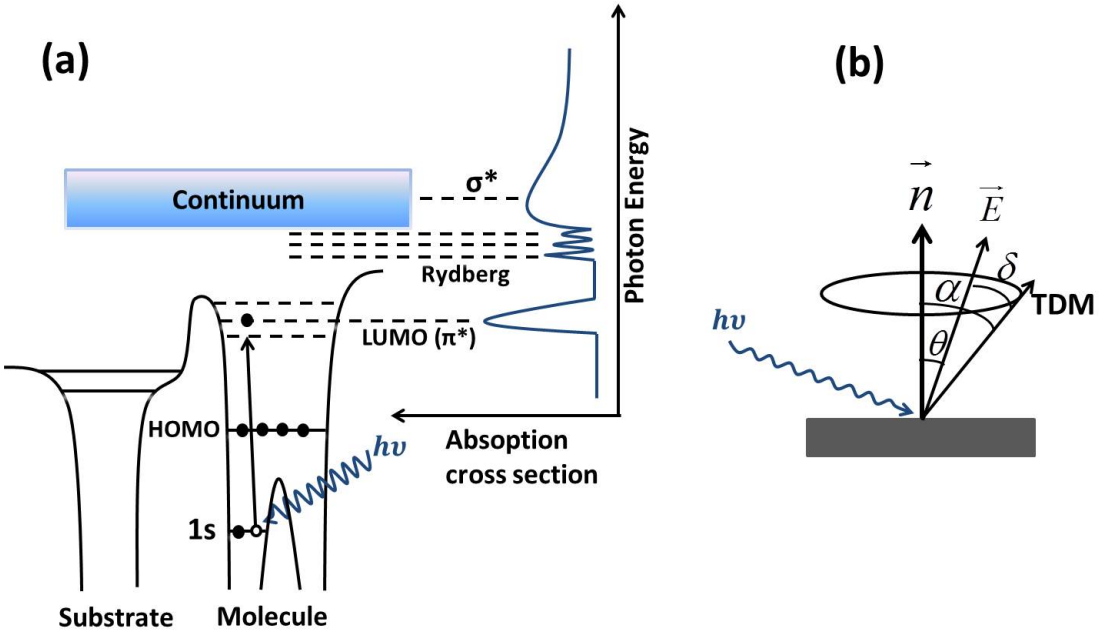

FIGURE 2.3: **(a)** Schematic depiction of the X-ray absorption process and resulting spectral features for a diatomic molecule like CO or NO in the NEXAFS region. **(b)** Depiction of the measurement geometry for a vector-type orbital, with $\vec{E}$ indicating the electric field vector, $\vec{n}$ the surface normal, and TDM the transition dipole moment vector.

The lowest unoccupied molecular orbital of an unsaturated organic molecule is usually a π^* orbital, giving rise to a sharp peak in the spectrum, while σ^* orbitals (often called *shape resonances*) appear at higher energies when the electron is excited just above the ionization potential (IP). Obviously, a 1s $\rightarrow \pi^*$ transition can only be observed for molecules with π bonding, *i.e.* with double and triple bonds or with an aromatic system.

The finite lifetime of the excited state and the vibrational motion of the molecule can lead to asymmetrical broadening of the observed NEXAFS features. The broadening of π^* type features due to the lifetime of the π^* resonance is generally small, the lifetime being determined by the de-excitation of the excited electron and decay of the core hole. Conversely, σ^* type resonances are often broadened due to the overlap of the final states with the continuum, which increases the possibility of decay into the continuum. In general, the higher the resonance lies in the continuumm the broader the linewidth. Taking also into account the molecular vibrations along the bond direction, this explains why most of the measured σ^*-type related features are very broad and asymmetric in shape.

The most important information NEXAFS provides in this thesis is the orientation of adsorbed molecules on surface, by exploiting the fact that the intensity of NEXAFS resonance is strongly polarization-dependent. The quantum mechanical description of the excitation process in the dipole approximation leads to the equation (Fermi's Golden Rule)[25]:

$$\sigma_X = \frac{4\pi^2 e^2}{m^2 \omega c} |\langle \psi_f | \overrightarrow{e} \cdot \overrightarrow{p} | \psi_i \rangle|^2 \rho_f(E) \propto |\overrightarrow{e} \cdot \langle \psi_f | \overrightarrow{p} | \psi_i \rangle|^2 \propto \cos^2(\delta) \tag{2.8}$$

where σ_X is the total absorption cross section, $|\psi_f\rangle$ is the final state orbital and $|\psi_i\rangle$ the initial state orbital, $\overrightarrow{e}$ denotes the unit vector in the direction of the electric field. Moreover, $\overrightarrow{p}$ is the sum momentum operator, and $\rho_f(E)$ is the density of final states; finally, the matrix element $\langle \psi_f | \overrightarrow{p} | \psi_i \rangle$ represents the so-called transition dipole moment (TDM).

Bonds and the associated molecular orbitals are highly directional, and given the spherical symmetry of the 1s initial state orbital the spatial orientation of the final state orbital determines the angular dependence of the K-shell spectra. As a consequence, the transition probability and the absorption cross-section depend on the direction of the electric field vector relative to the orientation of molecule

orbital. In general, π^* orbitals have the maximum amplitude normal to the bond axis, whereas σ^* orbitals have maximum amplitude along the bond axis.

For a 1s initial state and a directional final state orbital, the transition intensity is proportional to $cos^2(\delta)$ as shown in Eq. (2.8), with δ being the angle between the electric field vector and the final state orbital (see Fig. 2.3(b)). Therefore, the resonance intensity will reach its maximum when the electric vector is along the direction of the final state orbital and vanishes when electric field vector and orbital are exactly perpendicular. This in turn depends on the polarization direction of the radiation and the orientation of the molecule relative to the surface.

Molecules can be grouped into different classes depending on whether the π^* or σ^* orbital point into a specific direction (vector-type) or span a plane (plane-type). For example, single bonded molecules are characterized by a σ^* type orbital along the internuclear axis, double-bonded molecules by a σ^* and an orthogonal π^* orbital, and triple bonded molecules by a σ^* and two orthogonal π^* orbitals. In the last case, the two orthogonal π^* orbitals can be represented by a plane. Conversely, for an aromatic ring such as benzene, the atoms are arranged in a plane that contains the σ^* orbitals, while the π^* orbitals are described by a vector perpendicular to that plane [26]. Importantly, the direction of the maximum orbital amplitude determines the strength of absorption in the polarization dependent K-shell spectra. Therefore, a single orbital such as the σ^* bond of a diatomic molecule can be represented by a vector, while two orthogonal π^* orbitals or the σ^* orbitals of the aromatic ring can be represented by a plane.

If the substrate exhibits three-fold or higher symmetry (*e.g.* Ni(111) and Co(0001)), and the radiation is linearly polarized, the polarization dependence for the resonance intensity associated with vector type (I_ν) and plane-type orbitals (I_p) can be expressed as [25]:

$$I_v = \cos^2(\theta)cos^2(\alpha) + \frac{1}{2}\sin^2(\theta)sin^2(\alpha) \tag{2.9}$$

$$I_p = 1 - \cos^2(\theta)cos^2(\gamma) - \frac{1}{2}\sin^2(\theta)sin^2(\gamma) \tag{2.10}$$

where θ is the angle between electric vector and surface normal and α the angle between TDM and surface normal for the vector-type orbital. Similarly, γ is the angle between the vector normal to the plane and the surface normal (plane-type orbitals).

Often the molecular orientation can be accurately determined by measuring the resonance intensity for two extreme sample orientation relative to the incident X-ray beam and comparing the experimental intensity ratio to the theoretically predicted value. In our case, by rotating the sample with respect to the incoming synchrotron radiation beam, two extreme polarizations were obtained: A_{xy} ($\theta = 90°$) and A_z ($\theta = 7°$) polarization respectively. The measurement geometry is depicted in Figure 2.3 (b).

In general, the NEXAFS resonance intensity is most pronounced for molecular orbitals oriented parallel or perpendicular to the surface, in which case the adsorption configuration of molecules, parallel or perpendicular to the surface, can be determined precisely. For example, for a benzene ring lying flat on a surface, $\alpha = 0$ for a π^* resonance and the maximum intensity is reached for $\theta = 0$ (see Eq. (2.9)) when the electric field is perpendicular to the surface, while the intensity is completely quenched when the electric field vector is parallel to the surface. However, the situation becomes problematic when the molecular tilt angle (α or γ) is close to the so-called *magic angle* of about 55°: NEXAFS measurements cannot unambiguously distinguish such a case from that of random molecular orientation.

All NEXAFS spectra presented in chapter 4 were recorded with a home-made partial electron yield detector. The angle between sample and detector were fixed to achieve normal emission by always rotating sample and detector simultaneously relative to the incoming radiation, with the purpose of maintaining the same detection geometry under each polarization. For the SAMs deposited on epitaxial cobalt film, secondary electrons were suppressed by applying a retarding voltage, typically -150 V for C *1s*, -260 V for N *1s*, -400 V for O *1s* and -560 V for F *1s*. A standard normalization procedure was applied for all the measured spectra unless otherwise stated: $I_{nexafs} = (I_{adsorbate} - I_{clean})/I_{transmission}$, where the monochromator transmission intensity was measured with a GaAsP diode. Moreover, all spectra were normalized to have the height of the continuous step equal to 1.

2.3 Thermal Programmed Deorption and Low Energy Electron Diffraction

Thermal Programmed Desorption (TPD) is a important technique for the study of the kinetics and thermodynamics of desorption processes. During the measurements, the sample is usually heated at a constant rate, with the temperature T being a linear function of time t ($\beta(t) = dT/dt$), and the partial pressure of molecules evolving from the sample surface is measured with a Quadrupole Mass Spectrometer (QMS). A prerequisite for TPD measurements in a UHV chamber is that the signal monitored by the QMS must be proportional to the rate of desorption, so the pumping speed must be sufficiently high to avoid re-adsorption of desorbed particles onto the sample.

The QMS can filter the arriving ions according to their mass-to-charge ratio (m/e). It typically consists of four symmetrically-arranged cylindrical rods, and a DC bias U and a radiofrequency $V\cos(\omega t)$ (AC) are separately applied to the two pairs of opposite rods. The resolution of the spectrometer can be altered by changing the ratio of U/V. With an appropriate adjustment of the U/V ratio, ions of only one mass can pass through the electrode structure and reach the detector [27]. The filtered ions are counted by exploiting an electronic preamplifier with tunable amplification ratio, such that currents down to the pA range can be detected. Figure 2.4 sketches the schematic of a TPD measurement.

Since particles are separated according to their m/e ratio, doubly ionized ions appear in the spectrum at half their molecule mass, and triply ionized ions at one-third, *etc.* This implies that molecules with masses over 200 can be detected even by a mass spectrometer with a maximum range up to 75 amu (as in the case of the apparatus used in this thesis). To reduce the background signal, the mass spectrometer can be cooled with liquid nitrogen during the measurements.

In surface science adsorption can be divided into physisorption, which is essentially governed by weak van der Waals interaction, and chemisorption, which occurs when the adsorbed particles form chemical bonds with underlying substrate atoms, e.g., by hybridization of molecular orbitals with substrate states. Upon heating, the desorption of physisorbed and chemisorbed layers is also different. In a TPD

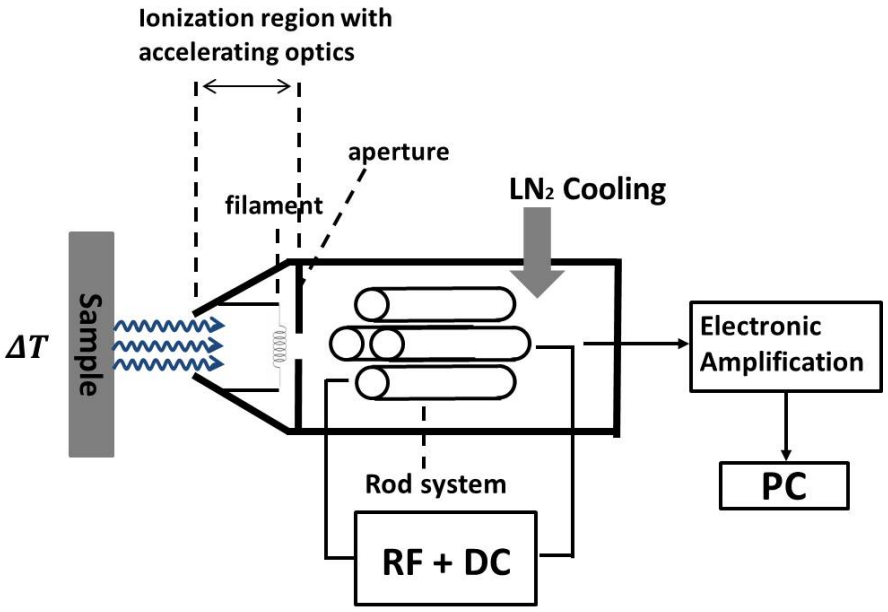

FIGURE 2.4: **(a)** Schematic depiction of the TPD measurement with a mass spectrometer.

spectrum, the rate of desorption is typically described by means of the Polanyi-Wigner equation [28]:

$$-\frac{d\theta_M}{dT} = \frac{\upsilon \cdot \theta_M^n}{\beta} \cdot \exp\left(\frac{-E_{des}}{R \cdot T}\right) \tag{2.11}$$

where υ is the frequency factor, θ_M the surface coverage, n the order of desorption, E_{des} the activation energy per mole for desorption, R the gas constant and β the linear heating rate. The factor θ_M affects the peak amplitude, and E_{des},υ, β, and θ_M all together determine the peak desorption temperature and peak shape. In practice, the zero-order desorption is often observed for multilayers, when the supply of molecules is approximately infinite: the desorption rate does not depend on the coverage ($n = 0$) and the temperature of the desorption peak (T_m) is shifted to higher values with increasing θ_M. In the 1st order desorption ($n = 1$), T_m is independent of the coverage, but dependent on the heating rate; a characteristic asymmetric peak profile is often shown and the peak amplitude is still proportional to the coverage. In the case of recombinative desorption, which arises from the slow recombination of atoms into a molecule that subsequently desorbs, *e.g.*, the H_2 desorption ($H+H \rightarrow H_2$) from atomic hydrogen adsorbed on a transition metal surface, desorption orders higher than 1 are observed. For instance, in $2nd$ order desorption at fixed β, T_m moves to lower T with increasing θ_M and the desorption

peak can be recognized by its characteristic nearly symmetric peak shape. Apart from these most commonly seen desorption peaks, defects, step-edges and even artifacts can cause additional features to appear in a TPD spectrum, which will not be detailed here.

In this thesis, TPD will be principally used to determine the 1st order desorption temperature necessary for the preparation of a monolayer from a thick multilayer, as well as to provide information on layer stability for the aromatic SAMs on transition metal substrate (Ni(111) and Co(0001)). For ruthenium-tetraphenylporphyrin (RuTPP) and free-base tetraphenylporphyrin (TPP) adsorbed on the Ag(111) surface, investigation of the 2nd order desorption peak of H_2 can provide information on the flattening [29] and ring-closing reactions thermally triggered on the original molecules [30]. Complex quantitative analysis will not be provided in this thesis.

Low Energy Electron Diffraction (LEED) The study of electron diffraction started with the famous experiment of Davisson and Germer in 1927. LEED is a surface sensitive technique for the determination of surface structures by bombardment with a collimated beam of low energy electrons (20-200 eV) and requires long-range order [31]. Within this technique, the diffracted electrons are accelerated to high energies to produce visible diffraction patterns on a fluorescent screen. In our work, LEED is employed to provide qualitative information on the symmetry and periodicity of the surface structure, thus offering a guidance for the deposition of metal films, e.g., deposition of cobalt film on a W(110) crystal. Quantitative analysis which applies the dynamical electron diffraction theory will not be included in this thesis.

LEED experiments are performed in an UHV environment (10^{-10} mbar). A typical LEED apparatus consists of an electron gun, a detector system that contains 3 or 4 hemispherical concentric grids (e.g., for grounding and retarding field) and a phosphor screen, as well as a camera pointed toward the screen for visualization of the diffraction pattern on the PC. During the acquisition of a LEED image on the fluorescent screen, normal incidence of the primary electron beam generates a pattern that reproduces the reciprocal lattice of the surface. The number of diffraction spots visible on the screen is controlled by the incident electron energy. The real space lattice can be constructed back from the LEED pattern, and the

surface can be characterized at least qualitatively in terms of surface periodicity and point group.

2.4 The Core Hole Clock Method

The ultrafast charge transfer (CT) across an interface, especially at a molecule-metal interface or a molecule-oxide interface whether or not induced by external photon excitations is a key issue in many research fields, such as organic semiconductor based photovoltaics [32, 33], dye-sensitized solar cells [34] and nanoscale molecular electronics [35]. Interfacial charge transfer also plays a fundamental role in the processes of adsorption, desorption and dissociation. In order to study the electron charge transfer dynamics from a molecule to a substrate or *vice versa*, it is very necessary to investigate these ultrafast processes in the real time domain.

Before the development of the core-hole clock approach, information on the CT time scales was usually provided either indirectly by analysis of the linewidth of the respective energy levels or directly by performing time-resolved pump-probe laser experiments [36]. The former method has been successfully applied to isolated atoms and molecules, but in the case of adsorbates on substrates, it becomes unreliable as other possible contributions to the adsorbate level profile need to be taken into consideration, *e.g.* inhomogeneous broadening *etc.* The pump-probe approach is an accurate and direct method to study the CT dynamics, whereby an electron is pumped to a higher energy state and the excited transient state is probed as a function of time following the initial excitation. The time resolution attainable with this technique depends largely on the temporal definition of the used laser pulses. Well-established laser pulses with length as short as tens of femtosecond enable the application of this technique in the time domain above 10 fs. The most recent developments improved the time duration of pulses to about 200 attoseconds, but attosecond pulses can only be realized in the extreme ultraviolet and low energy X-ray regime (90-150 eV) [37].

In addition to the pump-probe approach mentioned above, a synchrotron based soft X-ray spectroscopic method, exploiting the resonant excitation of a core level and the following core-hole decay, has been developed to probe the ultrafast interfacial CT dynamics in the low fs to several hundreds of attoseconds regime.

The availability of highly-monochromatized, high-flux 3rd generation synchrotron radiation tunable in energy contributed largely to the development of this method, where the bandwidth of the exciting radiation is chosen to be below the natural linewidth of the specific core level. Under this precondition and in combination with X-ray absorption measurements, tuning of the exciting photon energy through the core resonance of an atom enables clear separation of different decay channels, as described in detail below. The method relies on the intrinsic lifetime of the excited core level, which serves as an internal reference clock, and therefore is called Core Hole Clock (CHC) method. Compared with conventional techniques based on laser pulses, the CHC method has the following advantages:

(1) Core electrons are involved, conveying the elemental specificity unique to core-level spectroscopies.

(2) The use of the core hole as an internal clock opens up a route to study even faster CT processes, *e.g.* by use of Coster-Kronig channels in the attosecond regime.

(3) As CHC is a spectroscopic technique operating in the energy domain, tuning of the exciting photon energy allows to compare CT times of the same species in different coupling situations and to determine relative variations of the CT time across a resonance rather accurately [38], by promoting transition from a specific core level of a given element to close-lying unoccupied orbitals.

For example, the self-assembled monolayer of p-thiophenyl-nonafluorobiphenyl on Au(111) comprises four inequivalent carbon species [39], i.e. carbon atoms linked to F, H, S and aromatic carbons. These carbon species can be clearly resolved in the C 1s core level photoemission spectrum and X-ray absorption spectrum. By selecting the photon energy across the absorption threshold of e.g., C(H)1s to LUMO centered at 284.7 eV or C(F)1s to LUMO centred at 287.6 eV, a selective excitation of C 1s core level electrons to the LUMO levels can be achieved, thereby facilitating the investigation of CT dynamics related to different carbon species.

As mentioned above, this method is convenient for the investigation of electron transfer on the low-fs or sub-fs timescale by using the core hole lifetime as internal reference. The core hole lifetime (τ) can be determined by the full width at half maximum of the resonance according to the relationship $\tau \cong \hbar/\Gamma$, where Γ can be measured from the spectral width of photoelectron spectra. The core-hole lifetime is quite stable and depends weakly on the chemical environment. For example,

typical core-hole lifetimes are $\tau = 6.4$ fs for N *1s* and 6 fs for C *1s*, 3 fs for F *1s*, and 6 fs for O *1s*, *etc.* [40], which greatly facilitates the determination of interfacial CT times in the ultrafast time domain. In particular, A. Foehlisch *et al.* resolved an ultrafast CT as short as 320 as from an adsorbed sulphur atom to the underlying Ru(0001) substrate [37].

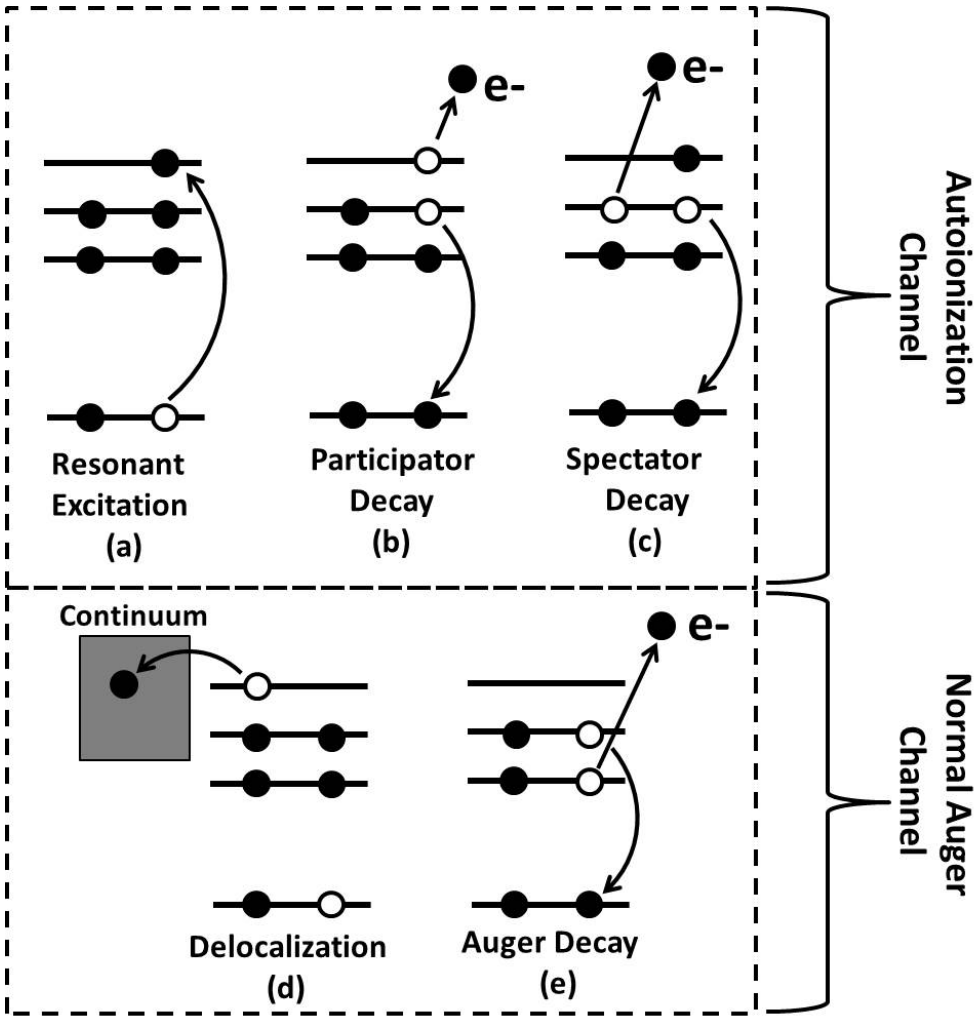

FIGURE 2.5: Schematic overview of the working principle of core hole clock spectroscopy. **(a)** A core-level electron is resonantly excited into the unoccupied molecular orbital (LUMO). The excited electron can decay via **(b)** participator decay channel leading to 1-hole final state, or **(c)** spectator decay channel leading to 2-hole-1-electron final state, or it delocalizes **(d)** to the coupled substrate before the core hole decays and the following **(e)** normal Auger decay leads to a 2-hole final state.

The working principle of the technique is summarized in Figure 2.5., which illustrates the excitation and deexcitation channels of interest here. Upon resonant

excitation as shown in panel (a) of the figure, a core-level electron can be resonantly excited to an unoccupied molecular orbital, typically the lowest unoccupied molecular orbital (LUMO). A transiently excited state and a core hole are created. If the resonantly excited electron is localized in the LUMO during the core hole lifetime (τ_c), the core hole can decay via either participator or spectator channels (altogether called "Autoionization", as shown in Figure 2.5 (b) and (c)). Conversely, if the populated molecular orbital couples strongly enough with the underlying substrate and lies in energy above the Fermi level E_f (i.e., $E_{res} > 0$), transfer of the excited electron to the continuum states is possible, which occurs on a characteristic time-scale called charge transfer time (τ_{CT}). The original neutral intermediate core-level state will then become ionized and decay via normal Auger channel, as shown in Figure 2.5 (e).

The participator decay channel is characterized by the participation of the excited electron in the "Auger decay" process (i.e., the resonantly excited electron takes up the excess energy and is ejected), leaving the system with a single valence vacancy and a charge of +1. This final state is equal to valence photoemission, but the core-hole assisted path has a larger cross-section for the core level of interest here [8]. In the spectator decay channel, the excited electron remains in the LUMO and acts as a spectator in the following Auger decay, where two valence vacancies exist in the final state, leaving the system in a 2-hole-1-electron final state. In the case of normal Auger decay, the decay channel following delocalization of the excited electron into the substrate corresponds to a quenching of the autoionization decay channels. Therefore, the autoionization decay that occurs within the time-scale of the core-hole lifetime represents the case in which there is no CT to the continuum states, while the normal Auger decay channel, characterized by a time-scale τ_{CT}, describes the case where CT to the continuum takes place. As a consequence, if τ_{CT} and τ_c are comparable the measured resonant decay spectrum will contain both autoionization and normal Auger components. A simple rate approach can relate the relative intensities of the autoionization and normal Auger channels, $I_{resonant}$ and I_{Auger}, to the core hole lifetime τ_c and the charge transfer time τ_{CT} according to [8]:

$$\tau_{CT} = \tau_c \left(\frac{I_{resonant}}{I_{Auger}} \right) \tag{2.12}$$

To determine the CT time from the above formula, the first step is to disentangle the respective components of autoionization and normal Auger decay in the measured decay spectrum. For an isolated atom or molecule (for which no CT to the continuum occurs), when the bandwidth of the exciting radiation is below the natural linewidth of the core-excited state, it is known that tuning of the photon energy across the core resonance energy leads to decay lines which disperse linearly with the photon energy (when the spectra are displayed in the kinetic energy scale), called "Auger Resonant Raman Effect" [10]. Making use of this effect, very different spectra are expected for the case that at the time of core-hole decay the excited electron is still localized on the adsorbate, or has already delocalized into the substrate. In the former case (spectator and participator decays) the behaviour of the decay spectra will be as for the isolated system, namely the kinetic energy of the decay electrons will disperse with the photon energy and the binding energy is constant (see Fig. 2.6). In the latter case (normal Auger decay), the delocalized electron has taken the information about the exact primary energy with it, and the kinetic energy of the decay electrons will stay constant with the photon energy. In detail, the participator decay channels can be easily recognized as the emitted electrons have the lowest binding energy (highest kinetic energy in the spectrum), but interference with the ordinary valence photoemission peaks may occur due to the identical final state (1-hole final state). Instead, the spectator decay and normal Auger decay channel can be distinguished because of the so called "spectator shift" (Fig. 2.6), where the kinetic energy of the electrons originating from the spectator decay is higher than the kinetic energy for normal Auger decay, due to the fact that the Coulomb repulsion between the two holes left after the spectator decay is partly screened by the resonantly excited electron, while in the normal Auger decay the repulsion of the two unscreened holes reduces the kinetic energy of the escaping electrons.

In practice, to decompose the measured decay spectrum into autoionization and normal Auger channels, pure autoionization have to be acquired on a similar system where no charge transfer takes place, *e.g.* resonant decay spectra of a multilayer [5] or resonant decay spectra of the same tailgroup but attached to a long enough alkyl chain to totally quench the normal Auger decay channel [9]. The pure Auger decay spectrum is typically obtained by exciting above threshold (off-resonance) consistently with the NEXAFS results (5-10 eV above the main resonant peak in our case). The experimentally obtained resonant decay spectra can

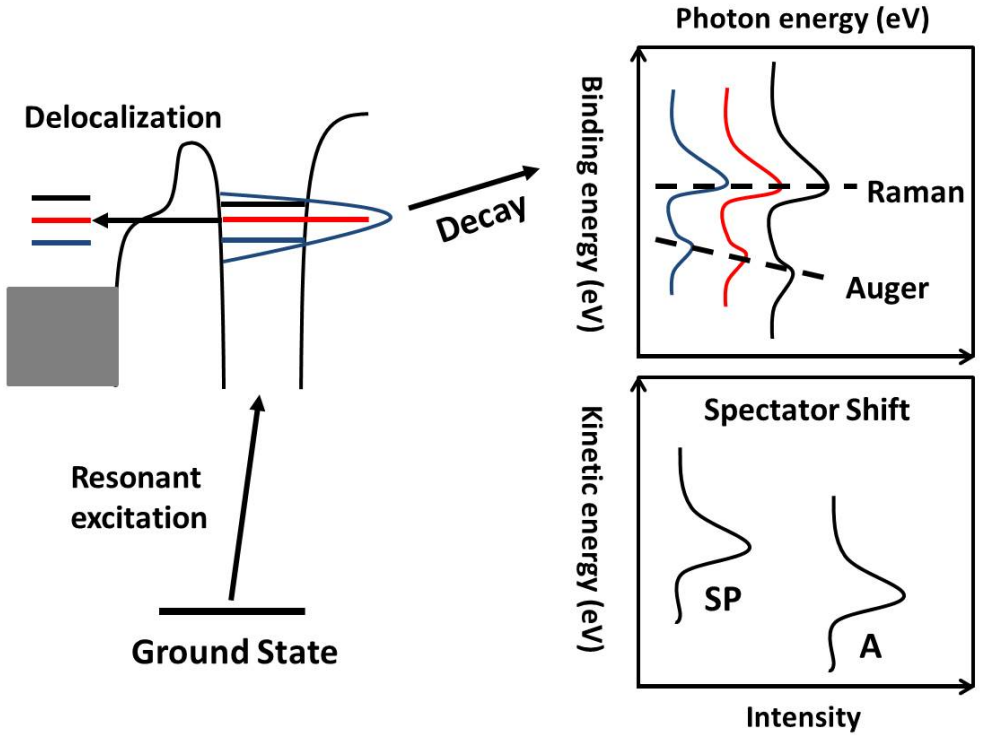

FIGURE 2.6: Schematic depiction of resonant excitation and core hole decay of an adsorbate on a substrate. Due to the Auger Resonant Raman Effect, the Raman channel (or autoionization) disperses with photon energy (fixed binding energy), while the Auger channel stays at constant KE (BE disperse with photon energy). The 'spectator shift' arises due to the screening by the resonance electron, and can be used to separate Auger and spectator decay channels in energy [10].

then be reproduced by a linear combination of the pure autoionization (coefficient: $I_{resonant}$) and pure Auger (coefficient: I_{Auger}) spectra. The ratio $I_{resonant}/I_{Auger}$ can be determined by minimizing the sum-squared residuals between the experimentally measured and the fitted spectra. In most cases, the value of the branching ratio inferred with reliable accuracy from the experimental spectra lies between 0.1 and 10. Therefore, within the framework outlined above, the range of charge transfer time accessible with the CHC method is approximately $0.1\tau_c \leq \tau_{CT} \leq 10\tau_c$.

Chapter 3

Experimental Setup

This chapter describes the experimental set-ups used in this work and is supposed to give insight into the technical aspects and equipment capabilities. The ultra-high-vacuum (UHV) chambers where the experiments were carried out and the attached electron detection systems are introduced. Besides, the available photon sources (*i.e.,* laboratory X-ray tube, ultraviolet light and undulator synchrotron beam) will also be briefly described.

3.1 The UHV Chamber

Pumping system and Pressure All the spectroscopic measurements introduced in chapter 4 and 5 are carried out in a home-made ultra-high vacuum (UHV) chamber with a base pressure better than 5×10^{-11} mbar. Electrons can be heavily scattered inelastically by gas molecules, and in addition residual gas molecules (especially H_2O and O_2) can easily adsorb onto the sample surface at cryogenic temperatures: both these factors can interference drastically with the execution of electron spectroscopy measurements. To ensure the base pressure mentioned above, the entire system is pumped by a turbo molecular pump (180 l/s) backed by another turbo molecular pumping station and a rotary pump, with the aid of a liquid nitrogen cooled titanium-sublimation pump (500 l/s). A small ion getter pump (20 l/s) serves as a back-up pump in case of the failure of turbo pumps for a short time. To reach the base pressure in the range of 10^{-11} mbar, the whole UHV

chamber needs to be baked to $200°C$ for at least 18 h, mainly to desorb water molecules sticking to the inner walls of the chamber. The pressure is measured by means of a Bayard-Alpert ionisation gauge, which consists of a glowing tungsten filament which emits electrons, a grid cage (anode) and the target electrode (cathode). The resulting ion current at the collector is a measure of the pressure, and the emission current of the tungsten filament can be adjusted according to the pressure of the chamber (the lower the pressure, the higher the emission current) to get a more accurate pressure reading and preserve the lifetime of the filament.

Chamber layout The UHV chamber consists of two communicating cylindrical chambers made of stainless steel, serving as preparation chamber and analyser chamber respectively, both of which can be rotated around their center axis. A second differential pumping stage is provided by a turbo molecular pump to maintain the ultra-high vacuum during the rotation. The sample manipulator is horizontally mounted and allows four degrees of freedom (three translation axes and a rotation around the manipulator axis), enabling to position the sample in every location of interest in the chamber for preparation and measurement. A fast entry load-lock system is mounted on top of the preparation chamber to allow fast insertion of sample without breaking the vacuum in the main chamber. The preparation chamber is equipped with a ribbon-type metal evaporator for preparing thin films of cobalt and iron supported on a W(110) crystal. During the evaporation, a thin metal sheet (0.05 mm * 10 mm * 25 mm in size) of high purity (99.99 %) is heated, and the metal sheet is carefully degassed before the first evaporation to ensure a clean film growth process. The film thickness is monitored by use of a quartz-mircobalance. A standard LEED optics is employed for checking the surface quality.

Dosing of gases and liquids into the chamber is achieved by using a leak valve. In UHV adsorption studies, the unit Langmuir (1 L = 10^{-6} torr*s) is used to quantify the exposure to a certain gas, i.e., 1 L is the gas dose that corresponds to a pressure increase to 10^{-6} torr for 1 s. In our chamber, the exposure can be precisely controlled to the level of 0.005 torr*s via a tailor made system, which greatly facilitate the preparation of different molecular layers in a reproducible way. All gases and vapours (including gases for sample sputtering such as Argon and Neon) are stored in a gas dosing system, which is pumped separately by a turbo molecular pump and connected to the main chamber via a capillary. Solid substances with

high vapour pressure were deposited by sublimation through a stainless steel tube directly leading to the sample, while substances with low vapour pressure can be heated above the sublimation point inside the crucible.

The analysis chamber is equipped with a Specs Phoibos 100 CCD electron analyzer, a standard partial electron yield (PEY) detector [41], a highly sensitive quadrupole mass spectrometer and an X-ray tube with a switchable twin anode producing non-monochromatic $MgK\alpha$ or $AlK\alpha$ radiation for laboratory-based XPS experiments. For these laboratory experiments, the chamber has also been equipped with an Omicron HIS-13 ultraviolet lamp with additional polarizer. For synchrotron experiments, the chamber was transported to the radiation source at Bessy II (Berlin) and the feed-through to the UV lamp attached directly to the beamline port. The whole UHV system is schematically depicted in Figure 3.1 [20, 42].

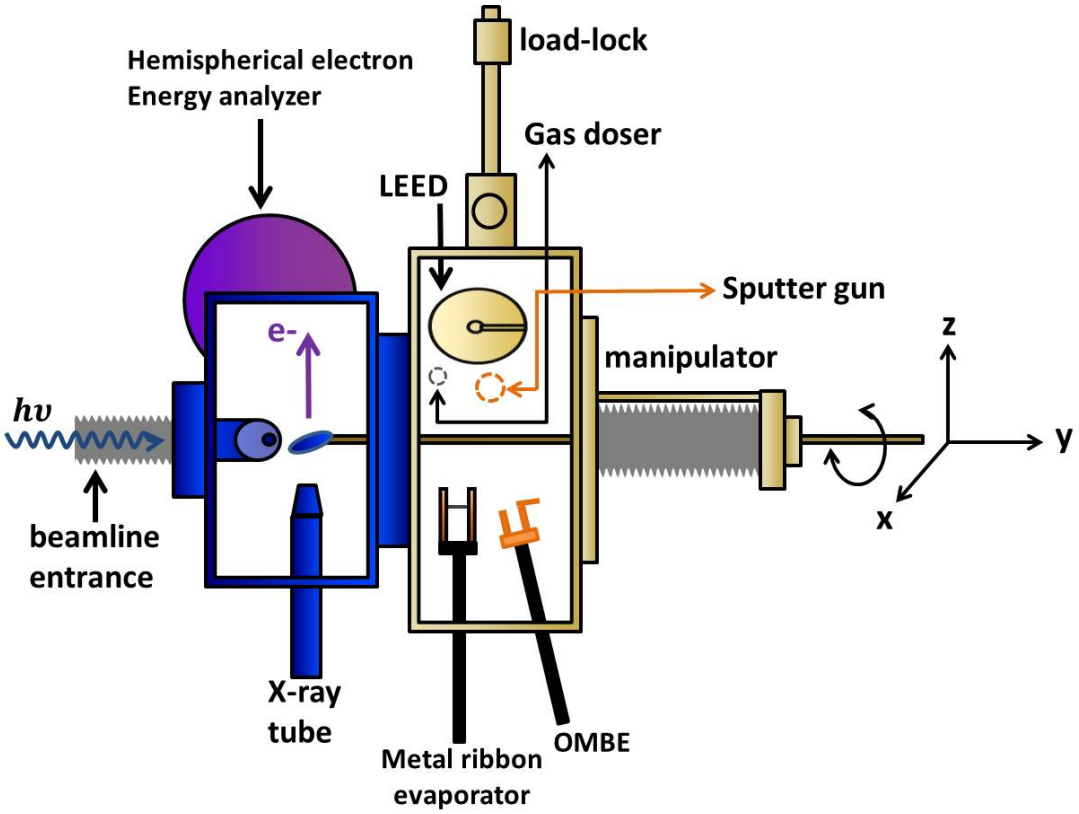

FIGURE 3.1: Schematic drawing of the UHV chamber used for our experiments within this work. Preparation chamber (yellow), analysis chamber (blue) and other parts of the chamber are depicted.

As noted above, the manipulator as well as the preparation and analysis chambers are connected by differentially pumped rotary feedthroughs, which allows independent rotation of all three parts around their longitudinal axis. With this design,

a fixed sample-PEY detector alignment can be achieved during X-ray absorption measurements. Rotation of the manipulator enables excitation of the sample with different polarizations, while rotating the analyzer (or PEY detector) in the same direction can keep other measurement parameters constant (e.g., detection geometry). Rotating the hemispherical electron energy analyzer alone allows to conduct angle dependent measurements of the emitted electron intensity. This design makes this chamber considerably more flexible than many other commercial ones.

Sample Treatment The sample surface is not only prone to be contaminated by interaction with residual gas particles, which can often be removed by gentle heating of the sample, but also by segregation of non-metallic contaminants in the crystal lattice, such as carbon, oxygen and sulphur. In the latter case, sputter-heat cycles are often used: the contaminated surface is first sputtered with ions (Ar^+ or Ne^+ are our common choices) accelerated to kinetic energy of about 1.0 keV, which leads to removal of the surface region layer by layer, and then the sample preparation can be completed by annealing to a pre-defined temperature in order to create a smooth and well-ordered clean surface. Repeated oxygen treatments can effectively remove atomic carbon from the surface; these essentially consist of cycles of oxygen exposures followed by heating to desorb chemisorbed carbon and oxygen. Electron bombardment heating of the sample enables annealing temperatures above 2000 K, high enough for cleaning tungsten crystals, while thermal radiative heating can reach maximum 700 K, high enough for cleaning e.g., an Ag(111) crystal. The sample can be cooled down to 25 K with a liquid helium flow-cryostat and to 80 K with a liquid nitrogen flow-cryostat integrated in the manipulator.

Sensitive adsorbate layers such as SAMs can be seriously damaged by prolonged X-ray exposure [43], especially on metal substrates that generate a large amount of secondary electrons upon excitation. During the synchrotron experiments, the area of the X-ray spot is about 1 mm^2 while our circular metal crystals are typically 10 mm in diameter. To reduce the effect of beam damage during the measurements, a chopper is installed on the path of the beamline and it can block the beam whenever the scan stops. Besides, the X-ray beam is scanned over the sample surface during the data acquisition by moving laterally the manipulator at low speed with a stepwise motor.

3.1.1 The Hemispherical Electron Energy Analyzer and Partial Electron Yield Detector

Hemispherical electron energy analyser (HSA) A commercial hemispherical electron energy analyzer (Specs Phoibos 100 CCD) is used for XPS, UPS and RAES measurements. A HSA consists of two metal hemispheres, which are arranged such that their centres of curvature are coincident. A voltage differences between the two hemispheres creates a radial electric field in the region between them. Electrons are injected into the gap between the hemispheres. If the electrons are travelling too fast, they will impinge on the outer hemisphere. If they are travelling too slowly, they will be attracted to the inner hemisphere. Hence only electrons in a narrow energy band centred at the pass energy (E_p) succeed in getting all the way round the hemispheres to the detector (see schematic diagram in Fig. 3.2). This dispersive set-up thus effectively allows separating the photoemitted electrons in kinetic energy.

A series of electron lenses is placed before the entrance slit of the hemispheres. This electron optics, which is a set of electrostatic lens units, collects a proportion of the emitted electrons which is then transferred through the apertures and focused onto the analyzer entrance slit. Electrons of given initial energy are detected by setting voltages in the lens system that focus the electrons of the required initial energy onto the entrance slit and retard their velocity so that their kinetic energy after passing through the transfer lens matches the pass energy of the hemispherical analyzer. Therefore, to record a spectrum over a range of kinetic energies it is necessary to scan the voltages applied to this lens system. The efficiency of the electrons detection depends drastically on these lens functions (prescription for these lens voltage).

All our measurements are performed operating the HSA in the Fixed Analyzer Transmission (FAT) mode. In this mode, the pass energy of the analyzer is held at a constant value, and it is entirely the task of the transfer lens system to retard the given kinetic energy to the range acceptable for the analyzer. For example, if the pass energy is 50 eV, then electrons of 1000 eV kinetic energy will have to be decelerated by 950 eV by the retarding voltage in order to be detected. After successfully travelling through the region between the hemispheres, the electrons will reach the exit slit where they are counted by a detection system consisting

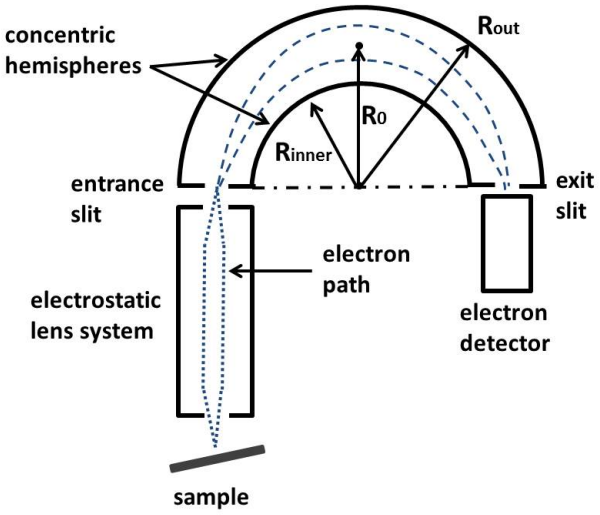

FIGURE 3.2: Schematic diagram of a hemispherical electron energy analyzer.

of a microchannel plate (which is essentially a 2D secondary electron multiplier), a phosphor screen and a CCD camera. The relationship between the pass energy and the voltage difference between the hemispheres is given by [44, 45]:

$$E_p = e\Delta V \left(\frac{R_{inner} R_{out}}{R_{out}^2 - R_{inner}^2} \right) \tag{3.1}$$

where e is the charge of the electron, R_{inner} and R_{out} are the radii of the inner and outer hemisphere, respectively, and R_0 is the mean radius of the hemispherical analyzer (in the specific case of the Specs Phoibos 100, $R_{out} = 1.25R_0$, $R_{inner} = 0.75R_0$, and $R_0 = (R_{inner} + R_{out})/2 = 100$ mm); ΔV is the potential difference between the inner and outer hemisphere. ΔV and E_p are fixed during a measurement and the retarding voltages of the lens system are scanned. After amplification by the channel plate, the electrons impinge on the phosphor screen and the emitted light is recorded by the CCD camera (640 x 480 pixels). The energy resolution of the spectrum is constant within a single spectrum but can be improved by choosing a small E_p at the price of reducing the measured signal intensity. The speed of the scan (or the rate of data acquisition) can be adjusted by changing the dwell time at each data point.

Partial electron yield detector In the soft X-ray regime, the acquisition of a NEXAFS spectrum can be accomplished in different ways. The most direct one is to monitor the attenuation of the photon beam after transmitting it through the sample, but this is usually only possible for largely transparent and relatively thin

samples, e.g., thin crystals or gas cells. Alternatively, the absorption spectra can be acquired in the electron yield or fluorescence yield modes [25]. In general, the electron yield mode ensures much higher surface sensitivity and is widely applied to thin films and adsorbates, whereas the fluorescence yield mode is typically used for more bulk-like systems and buried interfaces [46]. The probability for the core hole to decay by Auger electron emission is one or two orders of magnitude higher than that by fluorescent X-ray emission, and non-radiative Auger decay prevails for low-Z materials and shallow core holes. Therefore in this work on ultra-thin organic layers, NEXAFS spectra at the C, N, O, and F K-edges were always acquired in the electron yield mode.

Specifically, the partial electron yield (PEY) mode is more suited to obtain surface-sensitive information compared with the total electron yield (TEY) mode where the sample drain current is measured. A typical PEY detector is composed of two metal mesh grids for grounding and retarding voltages, a two-stage micro-channel plate (MCP) and a metal collector. A suitable retarding voltage excludes low-energy electrons emerging from deeper layers and bulk as well as extra signals from other lower-lying absorption edges. This procedure contributes to improve the surface sensitivity and to obtain a higher signal-to-background ratio. The PEY method provides high quality spectra and is widely used in the low-energy soft X-ray region. The Auger electron yield mode, a variant of the PEY method that collects only Auger electrons using an electron MCP detector, is even more surface sensitive but may suffers from lower signal-to-noise ratios [47]. Note, however, that soft X-ray absorption spectra recorded in the PEY mode with MCP may sometimes be distorted by a serious problem, due to the fact that MCP can detect not only electrons but also X-rays. In other terms, when a conventional MCP detector is used as electron detector in XAS experiments, the resulting spectra may be distorted by inclusion of unwanted fluorescent radiation. Thus, attention should be paid whether the PEY mode with an MCP detector provides reliable spectra or not. To overcome this problem, a novel PEY detector without MCP was used in our measurement performed using the UHV chamber described above.

The setup of this PEY detector is shown in Figure 3.3. It is based on the modification of a conventional LEED optics [41], which usually consists of 3 or 4 hemispherical grids in front of a hemispherical fluorescent screen. Grids and screen are arranged concentrically and cover a large solid acceptance angle of π sr. In our PEY detector, only 2 grids and the solid screen are retained. The first grid

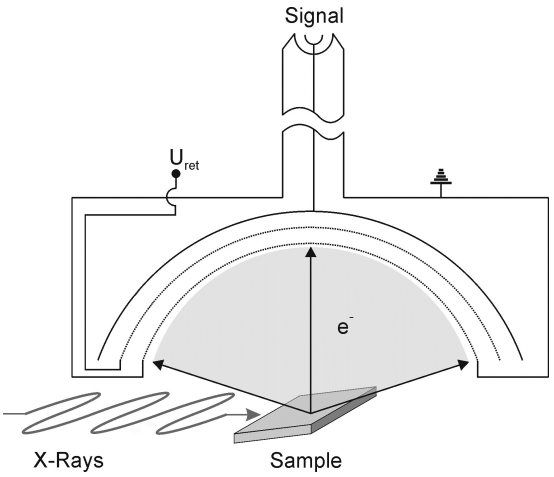

FIGURE 3.3: Schematic of the PEY detector assembled from standard replacement parts of a conventional LEED apparatus.

is grounded to avoid electric field from outside, and the second grid provides the negative retarding voltage as in conventional PEY detectors, to define the low energy cut-off. The screen serves as electron collector, and the electron current onto the collector is amplified outside the vacuum with a standard current amplifier. It is well-known that the emission of Auger decay electrons is strongly dependent on the polar angle, and angle-resolved Auger spectra can even be utilized for the determination of the orientation of adsorbed molecules [48]. Therefore, with the large acceptance angle used (π sr), the angular distribution of the Auger electrons can be integrated to eliminate spurious angular effects; moreover, a good signal-to-noise ratio is obtained despite the absence of a MCP. In our experimental setup, the synchrotron beam illuminates the sample with grazing incidence (7° with respect to the surface plane), and the polarization of the light is changed by rotating the sample and the detector simultaneously to avoid possible distorting effects in the measured spectra, e.g., effects from the different detection angles [20].

3.2 Photon Sources: Undulators, X-Ray Tube and Helium Lamp

Our experiments were performed at two 3rd-generation synchrotron radiation facilities, BESSY II in Berlin and Elettra in Trieste. Two beamlines were used for the measurement, namely U49-2 PGM1 at BESSY II and Aloisa at Elettra, respectively. In general, synchrotron radiation (SR) is emitted by charged particles

(electrons or positrons) accelerated to (nearly) the speed of light and forced to travel along a bent trajectory in applied magnetic fields. The emitted electromagnetic waves can cover the whole spectrum from the terahertz range through the visible light and UV regimes all the way to hard X-rays. A modern SR source normally consists of an electron gun for the regular supply of electrons, a linac and a booster synchrotron to gradually accelerate electrons to the energy at which they will be kept circulating, and a storage ring where the accelerated electrons are maintained on a closed path with constant energy by means of an array of magnets. Electrons in the storage ring have a fixed kinetic energy between 1 and 8 GeV, depending on the facility (1.7 GeV for BESSY II and 2-2.4 GeV for Elettra). Typical storage ring currents are in the range 100-500 mA, and electron injection is necessary every 8-24 hours unless the storage ring is operated in the "top-up" mode (as in both Bessy and Elettra). Importantly, electrons in the storage ring do not circulate around the trajectory in a continuous flow but in discrete bunches, and the synchrotron facility can work with three different modes: multi-bunch (which is the normal mode of operation we used), single bunch, and hybrid mode. As a consequence, synchrotron light can also be used for time-resolved experiments based on the time structure of the emitted radiation.

Straight sections of the storage ring are dedicated to insertion devices (undulators and wigglers etc.), which produces the most intense light with very high brilliance. The brilliance of a light source is defined as the photon flux per unit solid angle, unit source area and unit bandwidth, e.g., the brilliance at the U49-2 beamline of BESSY II is $5 \times 10^{18} ph/s/mrad^2/mm^2/0.1\%BW$. Generally speaking, the brilliance can be increased by either increasing the number of photons per second or decreasing source size and angular spread [49]. The section following the insertion device is the beamline, which comprises the front end, the beamline optics and the experimental hutch (measurement end station and chamber)

An undulator essentially consists of two periodic arrays of magnets with alternating polarity, which forces an electron passing in the gap onto a sinusoidal path. Radiation is emitted along the main axis and add up coherently because the magnitude of the oscillation is small. The brilliance of synchrotron radiation generated by an undulator is significantly higher than that of conventional X-ray tubes and dipole bending magnets. Due to the high kinetic energies of electrons, the electromagnetic radiation emitted is concentrated in a narrow cone around the main axis of motion as a consequence of relativistic effect [49]. When observed along

this axis (if not, another factor depending on θ_L should be taken into account, but $\theta_L = 0$ here), the wavelength of the emitted radiation can be expressed as:

$$\lambda_L(\theta_L = 0) \approx \frac{L}{2\gamma^2}\left(1 + \frac{K^2}{2}\right) \tag{3.2}$$

$$\gamma = \frac{1}{\sqrt{1 - \left(\frac{v}{c}\right)^2}} \tag{3.3}$$

$$K = \frac{eBL}{2\pi m_0 c} = 0.934 \times L[cm] \times B[Tesla] \tag{3.4}$$

where L is the period of the undulator (in the order of 3−5 cm) and γ is the Lorentz factor; e, m_0 in Eq. 3.4 are the charge and mass of the electron and c is the speed of light, and v in Eq. 3.3 is the electron velocity [49]. By changing the strength of the magnetic field B, one changes the magnitude of the electron oscillation and thus the fundamental wavelength. Variation of the magnetic field is achieved by changing the gap between the two rows of magnets. The undulator radiation also contains contributions of higher harmonic wavelengths that can be described as: $\lambda_n = \lambda_L/n$ $(n = 1, 2, 3...)$. Due to the symmetry of the electron displacement around the axis, even harmonics vanish on-axis and only odd harmonics can be detected [49]. In general, in a linear undulator (such as the planar-hybrid type undulator at U49-2), the emitted radiation is linearly polarized in the plane of the oscillation. However, in an APPLE (Advanced Planar Polarized Light Emitter) type undulator, the polarization of the radiation can be changed from horizontal or vertical to circular. An APPLE type undulator contains four rows of magnets, which can be shifted appropriately with respect to each other, in order to force the electrons on a spiral trajectory to produce radiation with circular polarization, or on a planar undulation parallel or perpendicular to the synchrotron plane to result in horizontally or vertically polarize light, respectively [49].

U49-2 PGM1 is an open-port beamline without a permanent experimental station [50]. Our chamber, described in section 3.1, can be connected to the beamline port. The beamline generates radiation with horizontal polarization, tunable in the 85-1600 eV energy range and with photon flux in the range $10^{12} - 10^{13}$ ph/s. The optical layout of the beam is shown in Figure 3.4. The radiation emitted

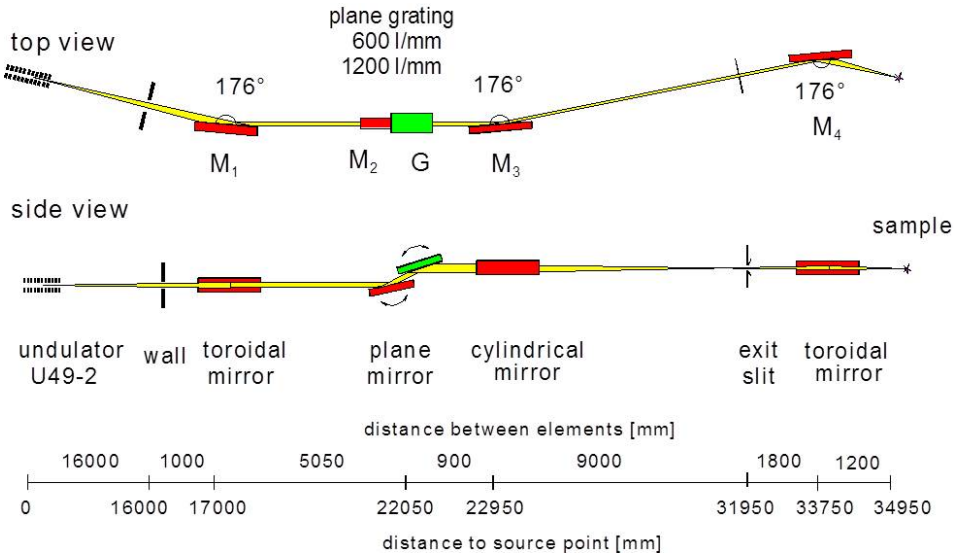

FIGURE 3.4: Optical layout of beamline U49-2 PGM1. [50]

from the undulator enters a plane grating monochromator (PGM) that only allows photons with a narrow energy band to pass through the exit slit (the energy resolution depending on the size of the exit slit). The beam is further collimated and directed onto the sample by a refocusing mirror (M4 in Figure 3.4).

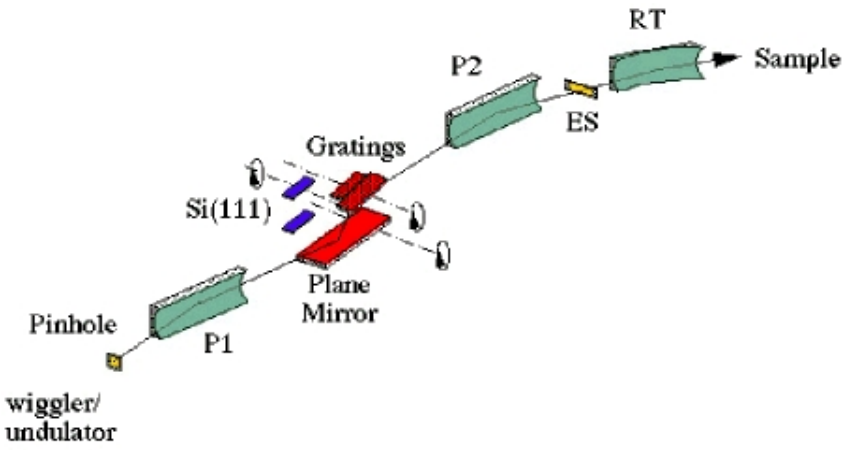

FIGURE 3.5: Optical layout of the beamline Aloisa in Elettra [51].

ALOISA in Elettra, as shown in Figure 3.5, is a beamline dedicated to surface science equipped with multitechnique end station. The light produced by the undulator is selected in angle by a pinhole and collimated by a paraboloidal mirror (P1). The light then impinges on the energy dispersing device which can be selected to be a plane grating for the low energy range (130-1500 eV) or silicon channel-cut monochromator for the high energy range (2800 to 8000 eV). The

light is focused onto the exit slits (ES) by a second paraboloidal mirror (P2) and refocused at the centre of the experimental chamber by a toroidal mirror (RT). The flux at the sample is above 10^{11} photon/s in the low energy range and around 5×10^{10} photon/s in the high energy range. The endstation is equipped with a combination of electron spectrometers and energy-resolved photodiodes for detecting both electrons and photons. More detailed information on the beamline and the end-station can be found in Ref. [51].

X-ray tube A standard X-ray tube purchased from *PSP Vacuum Technology* is used for laboratory- based XPS measurements. It consists of a cathode (made of thorium-oxide coated tungsten to reduce the work function and therefore increase the lifetime of the filament), a twin anode (Al and Mg films deposited onto a copper rod), a high voltage power supply (10 kV, to accelerate emitted electrons), an aluminium window (between source and sample) and a water cooling system to prevent the anode target from melting. All the parts are sealed in an evacuated tube which can be not only pumped directly through the mounting port but also differentially pumped with an ion pump [52]. The maximum emission current that can be applied through the cathode is 35 mA. Upon bombardment of the metal anode with accelerated electrons, discrete and narrow fluorescent lines (K_α and K_β, etc.) which superimpose on a weak continuous Bremsstrahlung background are generated. The energy of fluorescent radiation emitted by the X-ray tube is fixed (1486.6 or 1253.6 eV for Al and Mg $K\alpha$, respectively), and the brilliance of the light is several orders of magnitude lower than that of the synchrotron light.

VUV lamp A commercial VUV source (HIS 13) from *Omicron NanoTechnology* is used for laboratory- based UPS measurements [53]. It can be operated with various discharge gases such as helium, neon, and argon *etc*, and it is based on the principle of a cold cathode capillary discharge. The discharge current is electronically stabilised. The lamp is water cooled in order to allow for high discharged currents up to 300 mA. Continuous discharge can be reached if an increasing potential is applied between the ends of an insulating tube filled with gas. In our setup, two types of lines can be generated: lines of neutral atoms (e.g. HeI, NeI etc.) and lines of singly charged ions (e.g. HeII, NeII etc.). In the former case, the photon flux vs. discharge current shows a saturation characteristic (typically 80 mA for HeI around the onset of saturation), while in the latter case the maximum of photon flux is obtained shortly before attaining the pressure at which the lamp

Table 3.1: Positions and intensities of He discharge lines.

UV source	**Energy (eV)**	**rel.Intensity**	**Wavelength**	**Sat.shift(eV)**
$HeI\alpha$	21.22	100	58.43	0
$HeI\beta$	23.09	1.2-1.8	53.7	1.87
$HeI\gamma$	23.74	0.5	52.22	2.52
$HeII\alpha$	40.81	100	30.38	0
$HeII\beta$	48.37	less than 10	25.63	7.56
$HeI\gamma$	51.02	NA.	24.3	10.2

extinguishes (the photon yield strongly increases with decreasing pressure). In our measurements with HeI line (21.2 eV, 58.4 nm), a mixture of HeI, HeII and other satellite lines may be obtained since HeII is always emitted simultaneously with the strong HeI line. Table 3.1 shows the positions and relative intensities of the helium discharge lines.

The discharge gas is supplied via an all-metal leak valve, and gas with high purity, e.g., helium 6.0, is used. Two differential pumping stages are provided by turbo molecular pumps (each backed by a rotary pump), in order to limit the pressure increase in the experimental chamber to the 10^{-8} to 10^{-9} mbar range during the operation of the lamp. Furthermore, the UV lamp is equipped with a continuously rotatable three-mirror (gold coated) linear polarizer which is mounted directly on the second pumping stage. The rotation of the linear polarizer is ensured by a radial UHV rotary drive. The coating of gold ensures a polarization efficiency of 88% and a transmission of 8% at the HeI wavelength.

Chapter 4

Self Assembled Monolayers on Metal Substrates

In this chapter, the fundamentals of self assembled monolayers (SAMs) are first briefly introduced, including-among various aspects-the preparation, structure, bonding and the charge transfer dynamics of SAMs on metal substrates. Previous investigations on coinage metals (Au, Ag and Cu) are concisely reviewed, and the significance of investigating SAMs on ferromagnetic substrate is illustrated.

Afterwards, the measurements on SAMs at the core of this thesis are discussed. SAMs of 4-fluorothiolphenol (4-FTP), 4-fluorobenzoic acid (4-FBA) and 4-cyanobenzoic acid (4-CBA) adsorbed on deposited cobalt film under UHV conditions are studied from the perspectives of bonding character, molecular orientation, thermal stability and charge transfer dynamics. The choice of these three molecules with either identical headgroup or tailgroup favours the study of the influence of the headgroup- and tailgroup-substrate interactions on the properties of the SAMs. The performance of the 4-FBA SAM on Co(0001) is very similar to that on Ni(111). The tailgroup-to-substrate charge transfer (CT) time lies in the femtosecond range and decreases with increasing excitation energy. A similar trend was found for the headgroup-to-substrate CT, but a CT faster than 0.6 fs was determined from the RAES spectral analysis. Interestingly, the dynamic CT agrees well with the values predicted by the static molecular conductance. The 4-CBA/Co(0001) SAM was instead observed to exhibit larger disorder compared with the 4-FBA/Co(0001) SAM due to the stronger tailgroup-substrate interaction; as a result no tailgroup-to-substrate CT can be evidenced from the RAES spectra. However, the nitrile

tailgroup of 4-CBA SAM was employed as a spectroscopic marker to derive the twist angle of the molecule with NEXAFS due to the presence of two orthogonal π^* orbitals. Finally, as for the 4-FTP SAM on Co(0001), the presence of atomic sulfur, which is often observed in thiolate-bonded SAMs prepared by annealing of the multilayer, was avoided by a incremental vapour-phase deposition approach at 80 K; this resulted in a monolayer that was found to adopt a largely flat-lying orientation, in contrast to the upright orientation obtained by annealing of the multilayer. The tailgroup-to-substrate CT time of this 4-FTP SAM was found to depend not only on the excitation energy but also on the polarization of the radiation. In addition, CT in the 4-FTP submonolayer film appears to be faster than that in the monolayer.

4.1 Fundamentals of SAMs on Metal Substrates

Self-assembly can be generally defined as the spontaneous formation of complex hierarchical structures from pre-designed building blocks, involving multiple energy scales and multiple degrees of freedom [2, 54]. Specifically, self-assembled monolayers are ordered molecular assemblies that are formed by adsorption onto a surface of surfactant molecules with a specific affinity of their headgroup to the substrate. Fig. 4.1 shows the schematic of a SAM, including the constituents of a SAM-molecule (headgroup, backbone and tailgroup). Systematic research on systems related to SAMs was first performed by Zisman [55] in 1946, at which time the potential of self-assembly was not recognized and only limited interest was aroused. One main reason is that the underlying structural aspects and processes at the molecular level remained unexplored due to the lack of appropriate tools in those years. With the development of microscopic tools in the 1980s, Nuzzo and Allara showed that SAMs of alkanethiolates on gold could be prepared by adsorption of disulfides from dilute solutions [56], which can be regarded as a major milestone for recognizing the full potential of self-assembly. Since these early works, an almost unlimited number of self-assembled systems have been investigated until today.

From a fundamental point of view, SAMs offer unique opportunities to gain detailed insight into self-organization, structure-property relationships and interfacial phenomena. As both the head- and tailgroups of the constituent molecules

can be tailored, and a vast choice of substrate surface is available, a large variety of systems can be tailored. SAMs are prototypical systems for a fundamental understanding of the role of intermolecular, molecular-substrates and molecule-solvent interactions in phenomena such as ordering, growth, wetting, adhesion, lubrication, and corrosion [2]. From a technological point of view, SAMs find applications in a variety of fields, ranging from corrosion protection to sensors and molecular electronics. One important reason for SAMs being attractive in such diverse fields is probably that they can be designed flexibly both in terms of individual molecular building block, and at the material levels, which greatly favours the investigation of interactions at interfaces. Moreover, the properties of SAMs can be tuned by selectively modifying some functional groups while leaving the rest of the molecule unchanged, i.e., by the so called "Displacement of SAMs" [1]. Other reasons for the popularity of SAMs include: the ease of preparation, the possibility to assemble custom-designed building blocks in hierarchical structures of increasing complexity, the ability to achieve lateral structuring in the nanometer regime and various applications made possible by the features listed above. Nowadays, research on SAMs is increasing exponentially and represents an interdisciplinary field involving chemistry, physics, biology, nanotechnology and engineering. It also allows fundamental studies of the electronic, geometric and thermal-stable properties of SAMs on metal substrates as well as charge transfer dynamics from specific sites to the metal substrate, which will be the main content of this chapter. In the following, the preparation procedures, the substrate characteristics, and the bonding, structure as well as growth of SAMs will be discussed.

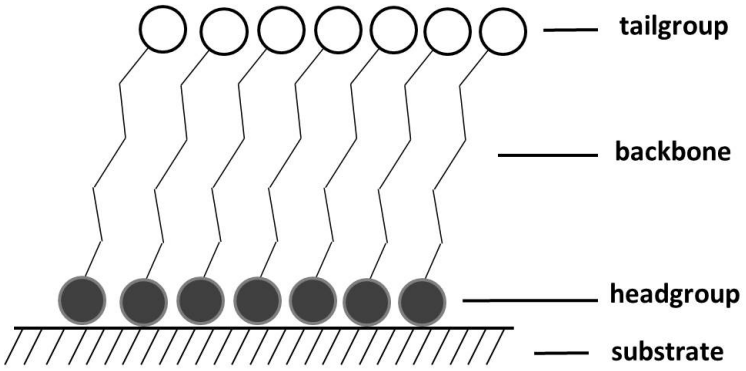

FIGURE 4.1: Schematic of SAM. Shaded circles indicate the chemisorbing headgroup and open circles the tailgroup, which can be selected from a variety of chemical functionalities [54].

Preparation methods Self-assembled monolayers presumably exploit the binding of a specific functional group of the molecule to the substrate; as such, the preparation of the films is possible both from solution and from gas phase (e.g., under UHV conditions). Assembly from solution following the Langmuir growth curve [54], i.e., by immersion of freshly-prepared gold, silver, palladium, and other substrate into a precursor solvent for ca. 12-18 h at room temperature, is convenient and sufficient for most applications of SAMs [9]. In this procedure, dense packing of adsorbates is achieved quickly while very long time is needed to maximize the density of molecules and minimize the defects in the SAM. The structure of the resulting SAMs are influenced by a number of factors: temperature, solvent, concentration of the precursor molecules, immersion time, concentration of oxygen in solution, cleanliness of substrate and chain length *etc.* Some of these factors are only known to a small degree and hard to control [1], e.g., the presence of contamination that is displaced progressively with the growth of SAM and can have some impact on the kinetics and limit the comparability of results from different works [54]. Conversely, adsorption from gas phase can be achieved by dosing the molecules with a controllable flux from a small container or glass bulb heated in a controlled way, and this method has been employed successfully in many works [57]. Adsorption from gas phase in UHV is very useful for studying the dynamics of assembly and preparing ordered structure at submonolayer coverage [58], so called "striped phase", and therefore the approach will be further discussed with respect to the 4-FTP/Ni(111) and 4-FTP/Co(0001) system in this thesis. Furthermore, deposition in UHV enables the use of atomically clean reactive substrates such as transitional metal substrates of ferromagnetic materials (Co, Ni, Fe), which can not be easily maintained free of contaminants during adsorption from solution. Moreover, by adsorbing SAMs under UHV conditions, single crystal surfaces can be used as substrates, facilitating model studies by means of a wide range of UHV-based techniques such as LEED, STM, and XPS *etc*, which offer insight down to the molecular scale. In contrast, typical substrates for SAMs deposited from solution are polycrystalline metal films on glass, silicon or mica composed of islands or grain sizes from 10 to 1000 nm with predominantly (111) texture [58, 59].

Substrates Previous literature studies mainly focused on thiolate-bonded SAMs on gold and silver surfaces [56, 60, 61]. Later works generally focus on expanding the type of molecules used to form the SAMs and the type of substrates used to support the SAMs. Among them, gold is the mostly used substrate due to

a number of reasons, notably, gold is easy to prepare and pattern in thin film, and it has good compatibility with living cells; most importantly, gold is inert, does not oxidize at temperature below its melting point and does not react with atomospheric O_2 and most chemicals, thus making it possible to handle samples under ambient conditions rather than UHV. Silver is the most studied substrates next to gold and it presents very similar properties, but it oxidizes in air; on the other hand, copper is more susceptible to oxidation than silver [59]. Research on palladium has also been reported [62]; this material has been much less studied but has many advantages like biocompatibility, inertness, and small grain size *etc*; all these properties make it a good alternative of gold.

The substrates used in this chapter, Co(0001) and Ni(111), are markedly more reactive and prone to oxidation as compared with the substrates mentioned above. The much more demanding preparation conditions typically call for UHV conditions and surface-sensitive analytical tools, explaining the limited number of studies to date. Proceeding from inert noble metal substrates to reactive ferromagnetic substrates will not only contribute to a better understanding of the mechanisms that are responsible for the electronic, geometric, thermal stability and charge transfer dynamics in SAMs, but also constitute an ideal playground for investigating the properties of molecules coupled to magnetic substrates that have potential applications in the field of spintronics [5]. Even though the easy formation of native oxide on nickel largely hinders the direct adsorption of SAMs from solution and sometimes requires the modification of the polycrystalline surface by electrochemical reduction methods [3], there has been some publications regarding the adsorption of thiols or carboxylates on Ni surfaces [63–72] either directly from solution or under UHV conditions. For instance, A.Vogt *et al* investigated the adsorption of 11-mercaptoundecanoic acid ($HOOC(CH_2)_{10}SH$) on Ni(111) under UHV condition and found that the molecule is adsorbed to Ni(111) via the sulfur atom with the carboxylic acid group directed away from the surface, which provides good clues for the better thermal stability of 4-FBA/Co(0001) as compared with 4-FTP/Co(0001), as will be discussed later in details. M. Neuber *et al.* studied the adsorption geometry of benzoic acid on Ni(110) under UHV conditions with XPS, TPD and NEXAFS. Comparatively, the number of studies of SAMs grown on cobalt surfaces is even more limited. P. Hoertz *et al.* reported a method for forming high surface coverage SAMs on electroreduced thin films of Ni, Co, and Fe using electroreduction approach or in the glove box, but non-negligible surface-oxide content was found [68]. However, the adsorption of SAMs on Co

surfaces under UHV conditions, to prevent interference of oxidation, has never been studied comprehensively studied. One possible explanation might be that clean nickel surfaces can be prepared more easily under UHV conditions in comparison to Fe and Co [73]; therefore most of the literature consider nickel as the prototypical ferromagnetic substrate despite the much lower Curie temperature [20].

Structure of SAMs Taking the extensively studied system of thiols on Au(111) as an example, the SAMs are anchored to the substrate by bonding through their headgroup. Upon adsorption, the thiol group undergoes deprotonation and forms a thiolate bond. The Au-S bond is relatively strong - a homolytic Au-S bond strength of the order of ca. 50 kcal/mol, while the homolytic bond strength of disulfide (S-S) can reach approximately 62 kcal/mol [1, 74]. Headgroups such as carboxylic acid [75] can also be used to couple the molecules to the surface. However, these bonds are much weaker as compared with the strong Au-S bond, the strength of Au-O bond being approximately 2 kcal/mol [76]. When a molecule with two coupling functional groups is adsorbed, the one with stronger strength will bond to the substrate and becomes the "headgroup", while the weaker one is often directed away from the surface and becomes the "tailgroup" [63]. There can even be some headgroup-headgroup interactions, e.g., dithiol molecules with both thiols coupled to the substrate and lying down on the surface in a full stretched mode may adopt a head-to-head configuration [54, 77]. The choice of a headgroup with suitable bond strength to the substrate is very important when a well-ordered structure is desired on the surface, e.g., dialkyl sulfides were reported to be poorly ordered and only physisorbed due to the lack of appropriate anchoring on gold surface [78].

The backbone of the SAMs is the part that separates the tailgroup and headgroup and acts as a physical barrier. The backbones are typically alkane chains or phenyl rings, corresponding to aliphatic or aromatic SAMs, respectively. The alkane chain length may influence the molecule configuration when the chain is in the corrugated (zig-zag-like) form, depending on whether chain-chain or headgroup-substrate interactions dominate; instead, the impact of the chain length for uncorrugated chains is generally negligible [54]. In an extreme case, the headgroup-substrate interaction will be less important when the alkane chain is extremely long ($n \to \infty$) ; while the chain-chain interaction cannot compete with the headgroup-substrate

interaction for short chains ($n \leq 8$) [79]. Phenyl rings are expected to introduce stronger molecule-substrate and molecule-molecule interactions and are more rigid than alkane chains. For example, the rigidity and orientation of the phenyl ring can prevent intermolecular hydrogen-bonding and the dimerization of the carboxylic groups that is commonly observed in the aliphatic monolayers [80]. Moreover, the length of the aromatic backbone has been shown to have an impact on the order of the SAM, e.g., A. Dhirani *et al.* investigated benzenethiols of different length (with 1, 2, and 3 phenyl rings) by STM and found that the degree of order of the SAM increased with the number of phenyl rings [81].

Finally, the tailgroup determines the surface properties of the SAM by defining the organic-ambient (or organic-vacuum) interface. The change of the tailgroup can have an influence on the molecular tilt angle and on possible superstructures due to endgroup-endgroup interactions and steric constraints [54]. H. Himmel *et al.* adsorbed alkanethiols with two different tailgroups (-OH and -COOH, respectively) on Au substrates and reported that alkylthiols with -COOH tailgroup are disordered and exhibit a high density of defects probably due to the interaction of the -COOH tailgroups via hydrogen bonds in the early stages of the growth. This prevents the formation of ordered SAM; on the contrary, the $-CH_3$ and $-OH$ terminated thiols can favour the formation of well-ordered SAMs [82, 83]. The impact of the tailgroup is also significant for adsorbed dithiols. Here, one thiol group couples to the substrate upon deprotonation and the second acts as a possible anchor to attach further building blocks in heterostructures at the SAM-ambient (or SAM-vacuum) interface. The molecules typically adsorb in a standing-up geometry [84]. Furthermore, the work function of the investigated systems can be tuned by changing the functional tailgroup, as indicated by the measured shift of the low-kinetic-energy photoemission cut-off in UPS [85]. Additionally, by tailoring the tailgroup or by using a mixture of different tailgroups, the wetting properties of SAM can be tuned, e.g., the contact angles of water was continously changed by the relative concentration of $-OH$ and $-CH_3$ terminated tailgroups in Ref. [2]. Finally, by selection of different tailgroups, one can change the starting site (-CN or -F in the present work) from which charge transfer to the metal substrate occurs, and the characteristic charge transfer times can be compared to each other. In this chapter, the influence of different tailgroups will be investigated by comparison of 4-FBA and 4-CBA SAMs on Co(0001) surface. The ability to engineer surface properties by an appropriate choice of the endgroup is one of the reasons for the popularity of SAMs.

As discussed above, the adsorption configuration of the SAMs molecules is determined by a number of factors: the arrangement of the headgroups on the substrate, the backbone-backbone interactions via van der Waals interactions and hydrogen bonding, the length and nature of the backbone, and the endgroup-endgroup interaction. However, some of the factors play a minor role in the aromatic (with only one phenyl ring) SAMs studied in this chapter. The full-coverage phase of the SAM corresponds to the highest possible packing of the molecules on the substrate, i.e., a saturated monolayer. For example, early studies of alkanethiols on Au(111) reported a $(\sqrt{3} \times \sqrt{3})R30°$ superstructure with respect to the underlying Au substrate, with the molecule tilted approximately by 34° away from the surface normal [86, 87]. Besides the "standing up" full-coverage phase, there exist also other structures and metastable configurations at low coverage, e.g., the so-called striped phase. At extremely low coverage, the molecules are expected to lie flat on the surface to maximize the interaction with the substrate. The existence of a lying down phase has been proved by previous works, e.g., R. Staub *et al.* prepared a SAM with low molecular surface density of decanethiol on Au(111) by annealing of the densely packed $(\sqrt{3} \times \sqrt{3})R30°$ structure [88]. The striped phase is also formed in the very initial stage of the adsorption process from gas phase; N. Camillone *et al.* for example reported that striped structures of alkanethiols $[CH_3 - (CH_2)_n - SH]$ on Au(111) surface can be prepared by thermal treatment of the closely-packed phase that is self-assembled from solution, or can be accessed directly by molecular beam deposition [89]. Upon further deposition, the striped phase gradually transforms into the full-coverage structure. The overall deposition follows approximately a two-stage process, with t_1 and t_2 being the characteristic time constant for the initial growth (formation of striped phase) and the later stage (reorientation and formation of standing-up phase) [90], and $t_1 \ll t_2$. Additional phases may exist at intermediate coverages between the striped and the full-coverage phase, but the structural evolution at intermediate coverage is very complex and there exists some controversy on whether the molecules are well-ordered or not [57, 91, 92]. For example, the striped phase for decanethiol on Au(111) corresponds to approximately 0.27 ML, whereas the final saturated phase corresponds to a coverage of $\sim$ 0.47 ML; the intermediate phases $(0.27ML \leq \theta \leq 0.47ML)$ might not lead to stable structures but only to transient metastable structures [91, 92]. Figure 4.2 shows the evolution of structures of decanethiol on Au(111) during growth from Ref. [92]. The molecules initially form a lattice gas phase (A) at extremely low coverage, and then adopt a striped phase

(B). After formation and decay of the striped phase, two intermediate phases (C and D) appeared before the saturation coverage phase (E) was finally achieved. At least five phases are observed during the approach to the saturated monolayer.

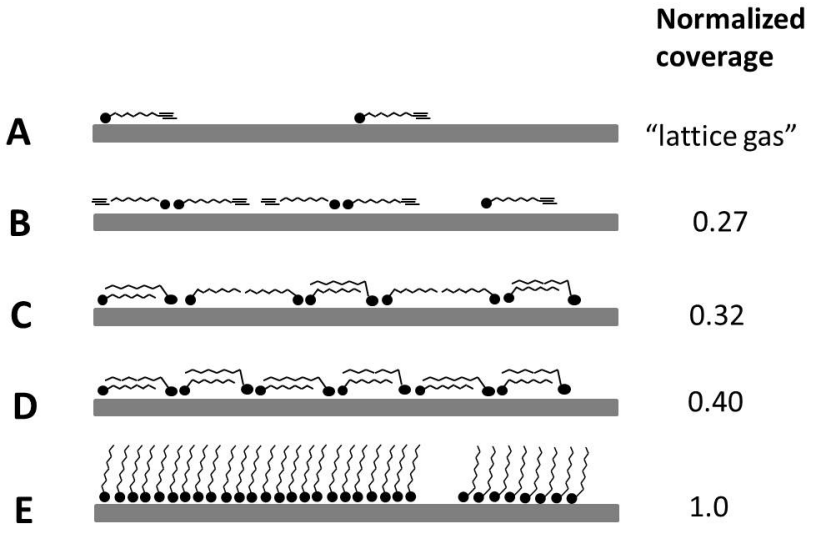

FIGURE 4.2: Sequence of (sub)monolayer phases with increasing coverage of decanethiol on Au(111). (A) Lattice gas at very low coverage. (B) Striped phase. (C) and (D) Intermediate phases. (E) Saturation phase. [92]. The indicated coverage is normalized to that of the saturated phase.

SAM growth When deposited under UHV conditions, the adsorption configuration depends sensitively on the growth parameters (deposition rate, temperature, partial pressure, density of defects on the substrate surface, etc.). The primary parameters that can be controlled are the substrate temperature and the partial pressure. An increase of the growth rate can be expected as the substrate temperature decreases, and the rate of transition from the chemisorption to physisorption will normally also increase with decreasing surface temperature; on the other hand, the increase of partial pressure will increase the deposition rate. Note that from the phase evolution described above, it may appear that the full-coverage phase can always be reached upon incremental deposition up to the final coverage. However, the intermediate phases are sometimes very stable and do not evolve further to the full coverage phase when increasing the coverage. For instance, alkanethiols deposited on Au(111) in gas phase only adopt intermediate coverage structures in the work of R. Gerlach *et al.* [93]. This can be presumably explained by the presence of strong van der Waals interactions between the backbone and the substrate, which hinders the transition from the intermediate to the final phase.

Charge transfer in SAMs Organic molecules have received considerable attention due to their potential application in molecular electronics, (e.g., Aviram *et al.* already in 1974 predicted rectifying behavior for a simple organic molecule with methylene bridge [94]), where they may provide notable advantages relative to the traditional semiconductor technology (e.g., low costs, ease of assembly, flexibility and small-size production). In this context, molecules with different behaviours, e.g., conducting, insulating, rectifying or amplifying characteristics *etc.*, need to be investigated. In particular, the relationship between the electron transfer dynamics and the molecular structure, the influence of the coupling to the substrate and the physical mechanism of electron transport have to be understood. In the past, the charge transport dynamics was generally studied by employing a metal-molecule-metal junction in order to measure current-voltage (I-V) curves, for example by contacting single molecules of SAMs with a STM tip or by bridging break junctions with individual molecules [6]. Herein, a different approach will be applied, consisting in the so called "Core Hole Clock" method. When a core-level electron of the tailgroup (or headgroup) is resonantly excited, it will delocalize into the substrate after a certain amount of time via tunnelling through the molecule (if energetically allowed). By recording the decay electrons emitted following the core-level excitation, the charge transfer time of the resonance electron can be extracted. More details have been given in section 2.4. This method has the advantage of being contact free. Indeed, it is generally recognized that the contact geometry might dramatically influence the measured I-V curves of the metal-molecule-metal junction. Therefore a contact-free approach can be of great value.

The electron transfer process at the molecule-substrate interface occurs as a transition from a metastable initial state in the molecule to a stable final state in the substrate, or *vice versa*. The interfacial electron transfer can be recognized as consecutive tunnelling processes from the transiently occupied molecular state (initial state), through discrete and localized bridge molecular states, to the substrate continuum (final state). Therefore, interface electron transfer strongly depends on the electronic interaction between the molecular state and the substrate continuum, as well as the coupling between consecutive localized molecular states. Direct electron transfer from molecule to substrate will be greatly favoured when the transiently occupied molecular state strongly couples to the substrate continuum and delocalizes through the whole molecule, which makes the molecule highly conductive and thus a good candidate for "molecular wires" [7]. Such effort has

been devoted to investigate chemically bonded molecule-substrate interfaces that favour ultrafast interfacial electron transfer, e.g., thiolate-metal (S-Au bond) interfaces [95]. Here, the strong electronic coupling between the molecular π states and the conducting states in the metal may greatly enhance the conductance through the molecule [96]. Furthermore, the molecular orientation and conformation affect the coupling between molecular orbitals and the metal continuum, as well as the delocalization of molecular orbitals, and hence the interface charge transfer. For instance, the 4-FTP/Au(111) with lying-down orientation of the molecules dramatically enhances the electronic coupling between the molecular π-electrons and metal d-bands as compared with the standing-up molecular phase, thereby resulting in ultrafast charge transfer in the low femtosecond regime [11, 12].

4.2 4-Fluorobenzoic Acid SAMs on Co(0001)

Thiolate-bonded SAMs have been extensively studied on inert metal surfaces, e.g., gold, silver and copper, as discussed in section 4.1. Some important properties of the SAMs, such as the thermal stability, are strongly dependent on the reactivity of the underlying metal substrate. The main reason is that the increased metal-S bond strength can make the molecules more susceptible to C-S bond cleavage [1, 97], resulting in an ill-defined SAM, which can greatly hinder the potential application of such SAMs in e.g., molecular electronics. The reactivity of the substrate can be increased moving from coinage metals to more active ferromagnetic metals, such as nickel, cobalt and iron surfaces. It is found for example, that benzenethiol adsorbed on Ni(111) undergoes C-S bond scission at temperatures above 200 K, leading to the presence of co-adsorbed atomic sulfur [98, 99]. In contrast, M. Neuber *et al.* have shown that benzoic acid ($C_6H_5 - COOH$) monolayers adsorbed on a Ni surface are stable even above room temperature [75]. The carboxylic group binds to the substrate in an upright geometry with the molecular plane perpendicular to the surface. Previous studies indicate that formic acid ($H - COOH$) molecules undergo O-H bond cleavage and adsorb as formate ($H - COO^-$) in a bidentate configuration, with the two oxygen atoms chemically equivalent [100, 101]. The same adsorption mechanism was observed for benzoic acid, resulting in a benzoate ($C_6H_5 - COO^-$) species with the molecular plane almost perpendicular to the surface [75, 102]. If a hydrogen atom in the para

position of the phenyl ring of benzoic acid is substituted with a fluorine atom, the surface properties of the SAM and the organic-vacuum interface can be changed, as discussed in section 4.1. The fluorine tailgroup can be used to obtain additional information on the molecular orientation by NEXAFS, and may serve as starting site for the transfer of resonantly excited electrons to the substrate within the CHC method.

In this section, 4-fluorobenzoic acid (4-FBA) SAMs on Co(0001) surface will be investigated with regards to bonding character, molecular orientation, thermal stability and charge transfer dynamics. The 4-FBA molecule has a single phenyl ring as a backbone, a carboxylic acid headgroup to anchor the molecule to the surface, and a fluorine substituent acting as tailgroup, which determines the properties of the SAM at the solid-vacuum interface. The sketch of a 4-FBA molecule is reported in Fig. 4.3 (a). 4-FBA was directly deposited onto the Co(0001) surface via a stainless steel dosing tube and the substrate was held at 80 K unless otherwise stated. The Co films were grown by evaporation from a resistively heated Co ribbon onto a freshly cleaned W(110) substrate kept at low temperature, and the cobalt film thickness (6-8 nm) was monitored by a home-made quartz microbalance which allows to control film growth to the picometer scale. The pressure during the Co deposition was in the 10^{-11} mbar range. The deposited cobalt overlayers were then annealed to 450 K for about 5 min to increase the mobility of the cobalt atoms on the W(110) surface, so as to achieve smooth (0001)-oriented films of high crystalline quality. The cleanliness of the film was then checked with XPS to assure the absence of contamination, while the good ordering of the film was established by LEED, which showed a sharp hexagonal pattern in reciprocal-space (Fig. 4.3 (b)), corresponding to the expected hexagonal unit cell in real-space. Prior to Co deposition, the W(110) single-crystal surface was cleaned by repeated cycles of Ar^+ or Ne^+ ion sputtering and annealing to 2500 K, and the cleanliness was also checked with XPS. Figure 4.3 (c) displays the XPS spectrum of the $W4f$ spin-orbit doublet from a freshly cleaned W(110) surface: the $W4f_{7/2}$ and $W4f_{5/2}$ both consist of two components, corresponding to photoelectrons emitted from atoms located on the surface and within the bulk, respectively, due to the so-called surface core level shift [17]. The latter arises due to uncoordinated surface atoms [103] and can only be observed when an excitation source with very narrow bandwidth, e.g., monochromatized synchrotron radiation, as well as a high-resolution electron energy analyzer are employed. The clear separation of the

surface and bulk components indicates an atomically smooth and clean W(110) surface prepared by the standard procedure described above.

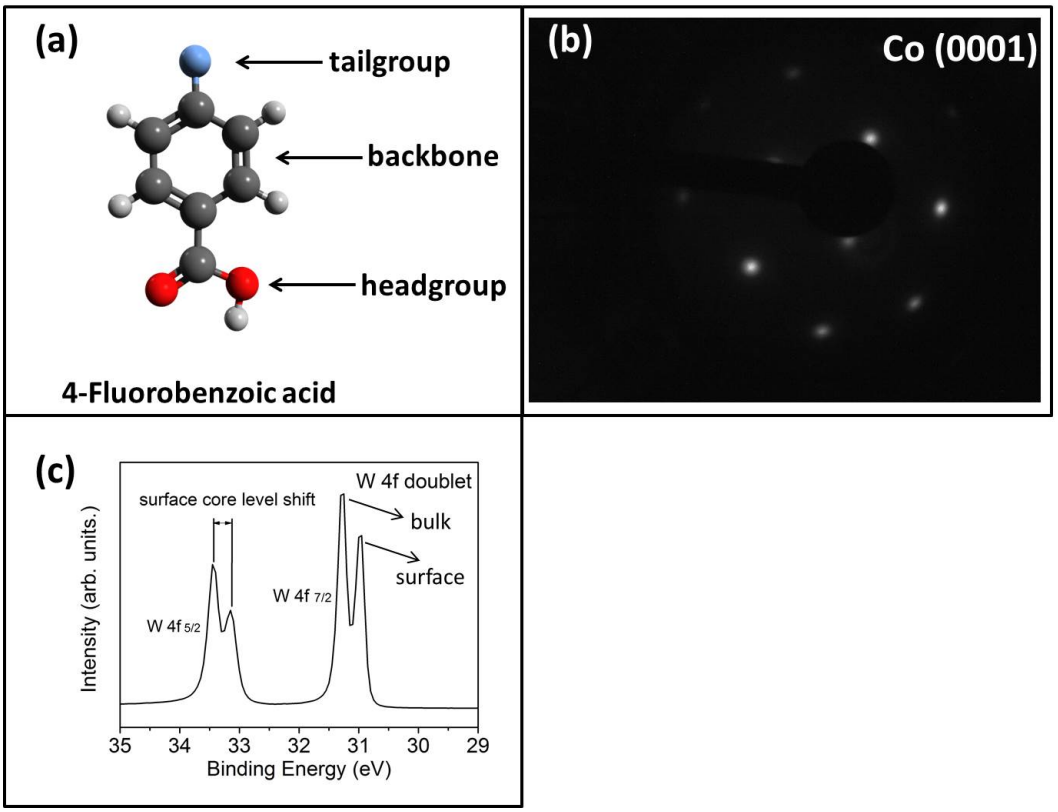

FIGURE 4.3: (a) Sketch of a 4-FBA molecule. (b) LEED pattern of a Co(0001) thin film of approximately 80 $\AA$ taken at an energy of 200 eV. (c) XP spectrum of the W 4f doublet from a pristine W(110) surface. The surface core level shift is indicated.

The experiments were carried out in a custom-designed UHV chamber operating at a base pressure below $5 * 10^{-11}$ mbar (details in chapter 3), using synchrotron radiation provided by the beamline U49/2 of the storage ring BESSY II in Berlin. XPS data were recorded with a Phoibos 100 CCD hemispherical electron analyzer in a grazing incidence / normal emission geometry. The Fermi edge measured under the same excitation and detection conditions as the respective core-level spectrum was used to calibrate the binding energy scale. To quantify the analysis of the photoelectron spectra, a Shirley-type background was subtracted, and a peak fitting routine based on Voigt functions was employed. NEXAFS spectra were acquired using our home-made PEY detector. Rotating the sample and the PEY analyzer simultaneously around the photon beam (incident at 7° with respect to the sample surface) resulted in a change of the direction of the E vector of the linearly polarized light relative to the sample surface without changing the detection geometry. The NEXAFS spectra were further processed by correction

for the clean surface contribution to the absorption and for the incident photon flux, and by subsequent normalization of the edge jump to one. The same chamber was also used off-line in Munich, when equipped with a conventional dual anode X-ray source for non monochromatized MgK_α and AlK_α radiation. TPD, XPS and UPS were used in these off-line experiments to further characterize the system. More details of the experimental methods and setup can be found in chapter 2 and 3.

4.2.1 Experimental Results and Discussion

4.2.1.1 Structure Characterization with XPS and NEXAFS

Multilayer First of all, a multilayer of 4-FBA was deposited by dosing vapors of the molecule through a gate valve onto the cold Co(0001) substrate (80K) for 5 min. The spectroscopic fingerprint of thin multilayer allows us to check readily the integrity of the molecules and provides a reference for interpreting the spectral features in the XPS and NEXAFS of the monolayer. The upper part of figure 4.4 shows the XP spectra of C 1s, O 1s and F 1s acquired for the 4-FBA multilayer. The C 1s spectrum of the multilayer shows three emission peaks at 285 eV, 287.1 eV and 289.5 eV, respectively, which can be assigned to carbon atoms of the phenyl ring (the most prominent peak), the carbon atom of the phenyl ring bonded to the fluorine substituent, and the carbon of the carboxyl group [104]. Carbon bonded to fluorine shows a large chemical shift of 2.1 eV to higher binding energy with respect to carbon in the phenyl ring due to the high electronegativity of fluorine. A similar effect occurs for the carbon bonded to two electronegative oxygen atoms in the carboxyl group, which is shifted to even higher binding energy by 4.5 eV. It should be noted that the peak areas in the C 1s spectrum (86%, 12% and 2% for C-H, C-F and C-O carbon atoms, respectively) deviate from the expected proportion of 5:1:1, presumably due to attenuation effects. The O 1s level of the multilayer consists of four components. The weak feature (proportion of 8%) at the lowest binding energy of 531.2 eV belongs to the carboxylate oxygen from the chemisorbed layer by comparison with the O 1s level of a monolayer as shown in Fig. 4.4 (e) [105]. The two components with identical intensity (both 36%) at 532.5 eV and 533.4 eV correspond to the two inequivalent oxygen species of the carboxyl group (carbonyl and hydroxyl oxygen, respectively). The feature at the

highest binding energy (of 534.7 eV) might instead, stem from oxygen-containing contamination adsorbed at the solid-vacuum interface of the multilayer, and it disappears after desorption of the physisorbed layer (see Fig.4.4(e)). Finally, the F 1s spectrum is relatively simple and shows only a single emission peak at 687.4 eV, as expected for the intact molecule.

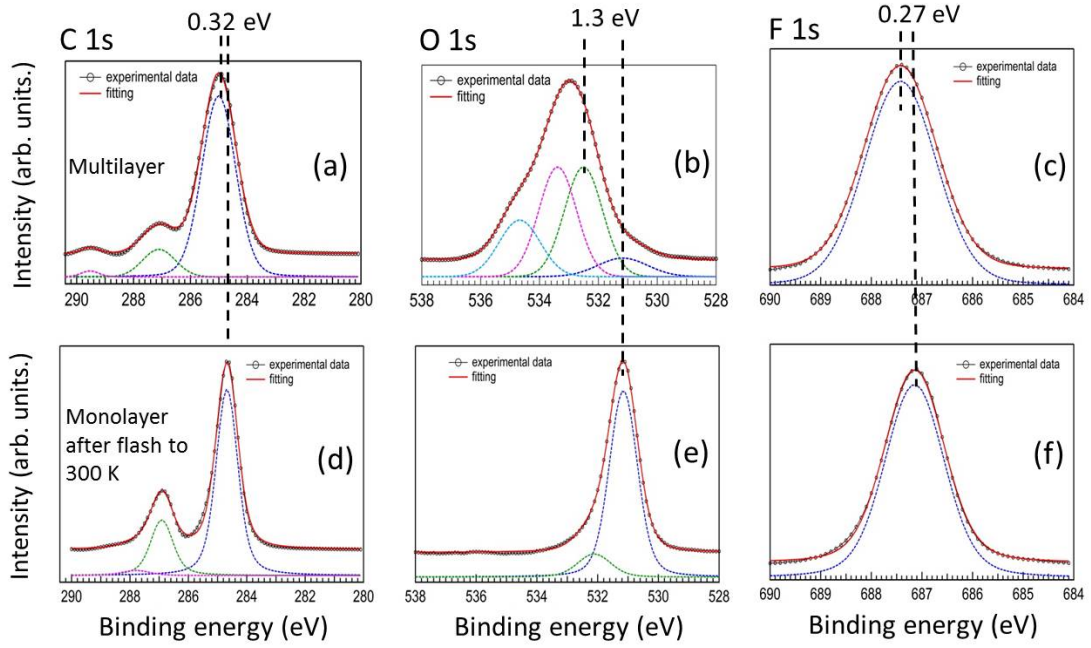

FIGURE 4.4: XP spectra (dots) and respective fittings (red continuous lines) of a 4-FBA multilayer (top) and monolayer (bottom) adsorbed on Co(0001): (a) C 1s; (b) O 1s; (c) F 1s core levels of multilayer and (d) C 1s; (e) O 1s; (f) F 1s core levels of monolayer. The fitted curves are superimposed on the experimental data, with different colours corresponding to different components. The black vertical lines highlight the binding energy shifts between multilayer and monolayer. The C 1s, O 1s and F 1s spectra were recorded at photon energy of 400 eV, 800 eV and 650 eV, respectively.

The corresponding NEXAFS spectra of the multilayer taken with two almost orthogonal light polarizations (A_{xy} vs. A_z) are shown in Figure 4.5. As for the carbon K edge, excitations of various non-equivalent C 1s sites to the energetically lowest unoccupied π^* orbitals are observed in the low energy region ($h\nu \leq 290$ eV). This low energy region is dominated by four peaks at 285.1 eV, 287.1 eV, 288.2 eV and 289.4 eV, respectively, which are slightly more intense for A_z polarization. The small dip below 285.0 eV is due to contamination on the beamline optics and could not be removed by the normalization procedure. According to previous investigations [106], the most intense resonance at 285.1 eV can be associated with an excitation from the C 1s level of the phenyl ring into the $1\pi^*$ molecular orbital.

Frederick et al. suggested that the energy level of $2\pi^*$ lies only 270 meV above the $1\pi^*$ molecular orbital [107], therefore it is likely that the electron excitation into $2\pi^*$ also contributes to the peak at 285.1 eV. Considering the observed chemical shift of about 2.1 eV in the XPS data of the carbon atom bonded to fluorine, the peak at 287.1 eV can be assigned to a transition from the C 1s level of this atom into the $1\pi^*$ molecular orbital. Similarly, we assign the weak shoulder at 289.4 eV to a transition from the C 1s level of the carboxyl group to the $1\pi^*$ level. As for the peak at 288.2 eV, it can be assigned to a transition from C 1s of the carboxylate group of the chemisorbed layer to the $1\pi^*$ level by reference of the XPS data in Fig. 4.4 (b) and comparison with the C K-edge spectra of monolayer shown in Fig. 4.7 (a). In addition, its energy separation relative to the $1\pi^*$ resonance at 285.1 eV of 3.1 eV equals almost exactly the energy difference of 3.07 eV between the lowest $1\pi^*$ and $1\sigma^*$ molecular orbitals as calculated by Frederick et al. [107], and therefore the phenyl ring C 1s to the $1\sigma^*$ transition might also contributes to the intensity of this peak. Above 290 eV, broad σ^* resonances dominate the spectrum and will not be further discussed here.

The C K-edge shows only a limited degree of linear dichroism. The intensity ratio of 0.77 between A_{xy} and A_z polarisations of the most intense resonance at 285.1 eV corresponds to an average tilt angle of approximately 52° between the transition dipole moment (TDM) of the π^* resonance and the surface normal. However, the NEXAFS data do not allow to distinguish between the situation of uniformly oriented molecules tilted by 52° with respect to the surface from that of random molecular orientation, due to the spatial averaging of the technique. On the other hand, based on the broadened XPS features of the multilayer compared to those of the monolayer (see Fig. 4.4 and discussion below), the latter situation seems more likely than the former.

The F K-edge spectra of the multilayer, shown in Fig. 4.5 (b), comprises several overlapping π^* and σ^* resonances, as it has been previously reported for adsorbed fluorinated aromatic molecules on gold [108]. The qualitative analysis of the molecular orientation through F K-edge data is therefore hampered, as it is difficult to determine whether a resonance stems entirely from a π^* or σ^*-type orbital due to the small energy shift of these orbitals [108].

In Fig. 4.5 (c), three pronounced features appear in the O K-edge spectrum of the multilayer, located at 531.7 eV, 533.9 eV, and 535.2 eV, respectively. These all

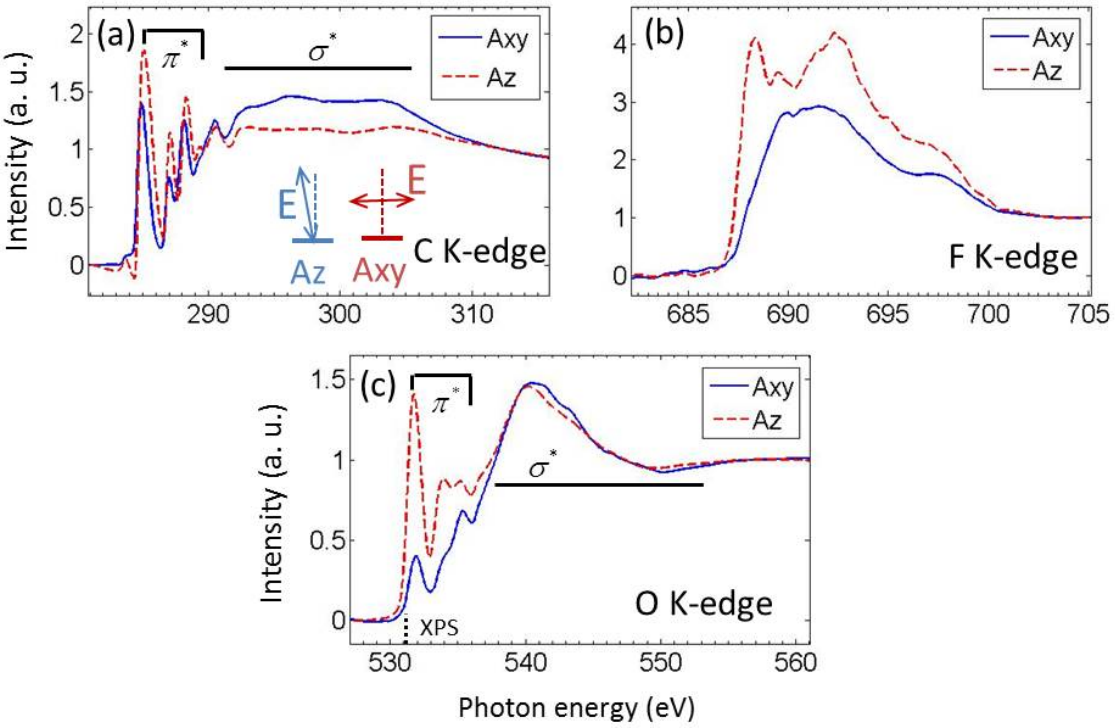

FIGURE 4.5: NEXAFS spectra of 4-FBA multilayer on Co(0001) at the (a) carbon, (b) fluorine and (c) oxygen K-edge for two different geometries, corresponding to electric field of the radiation almost parallel (A_z) or perpendicular (A_{xy}) to the surface normal as shown in the inset of (a). The dotted line in (c) denotes the binding energies of O 1s level determined from the XPS data of multilayer, corresponding to the excitation threshold.

belong to the π^* final-state resonances according to previous literature [100, 107, 109, 110]. Under the hypothesis that transitions to the unoccupied states in the underlying Co(0001) may be possible for the molecules in the chemisorbed layer, we have indicated the lowest O 1s binding energy (see Fig. 4.4 (b)) determined by the XPS data of the multilayer. This binding energy coincides well with the onset of the first K-edge feature. This first feature at 531.7 eV stems from the [O 1s]π^* resonance of the carboxylate-bonded layer by comparison with the XPS data, and the strong linear dichroism indicates a flat-lying molecular orientation in the first (chemisorbed) layer, considering that the transition dipole moment (TDM) of the [O 1s]π^* resonance is oriented perpendicular to the O-C-O plane. The other π^* type resonances above 531.7 eV originate from the physisorbed layer, and can be assigned to promotion of O 1s electrons of the carbonyl, the hydroxyl and the other oxygen-containing species, respectively, into the unoccupied π^* orbitals. The quenched dichroism relative to the feature at 531.7 eV might indicate a lack of order in the physisorbed layer. The energy region above 537 eV is dominated

by σ^* type resonances and shows almost no linear dichroism, suggesting that the molecules presumably do not have a preferential ordering in the multilayer.

TPD To determine the conditions for obtaining a 4-FBA/Co(0001) monolayer from the condensed multilayer, temperature programmed desorption (TPD) was employed. The corresponding TPD spectrum in Fig. 4.6 shows the signal of the QMS at a mass/charge ratio of 70, which corresponds to doubly ionized 4-FBA molecules ($F - C_6H_5 - COO^{2+}$). Due to the limited mass range of the apparatus used in this work (up to 75 amu), it was not possible to detect the intact (singly ionized) molecule; however, this limitation does not influence the accurate determination of the 1st order desorption temperature as discussed in chapter 2. In Fig. 4.6, the desorption peak at 240 K represents the most intense feature in the spectrum and corresponds to the desorption of the physisorbed multilayer. No other apparent features are observed up to 400 K, which is in agreement with the work of Neuber et al. [75]. According to this analysis, a monolayer can be prepared by flashing the multilayer to 300 K with a constant heating rate of 1 K/s as adopted during the TPD measurement.

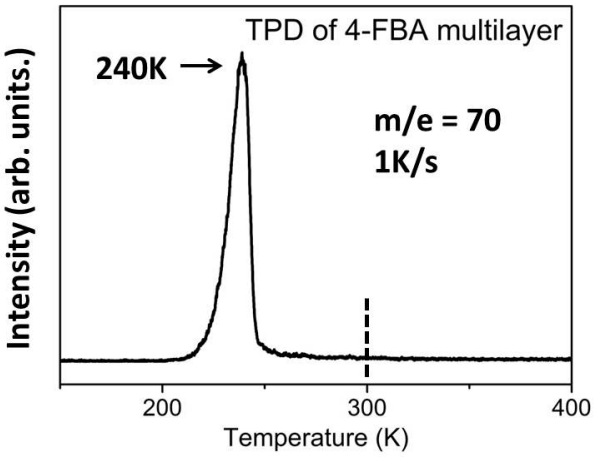

FIGURE 4.6: TPD spectrum of a 4-FBA/Co(0001) multilayer measured with a QMS, while ramping the temperature with a constant heating rate of 1 K/s. The condensed multilayer was deposited at 80 K after prolonged exposures. The peak value for multilayer desorption is indicated. The measured QMS signal corresponds to the mass/charge ratio of the intact 4-FBA molecule upon double ionization.

Monolayer The bottom of Fig. 4.4 illustrates the XP spectra of a 4-FBA monolayer prepared on Co(0001) by desorbing the multilayer as described above.

In the C 1s spectrum the main peak at 284.7 eV, which is 0.32 eV lower than its counterpart in the multilayer, belongs to the phenyl ring carbon and is typical for carbon of an aromatic ring not directly in contact with the surface. The C 1s binding energy of the fluorinated carbon is now shifted by -0.2 eV to 286.9 eV, indicating no drastic change of the chemical environment. Finally, the weak component at 287.8 eV is due to emission from carbon of the $COO-$ group and is strongly shifted by -1.7 eV compared to the corresponding peak in the multilayer [105]. The slightly reduced C 1s binding energies of the first two carbon species as compared to the multilayer is presumably due to the relaxation effect, a well-known final-state effect resulting from the screening of the core hole by the metal substrate. The much larger shift of the carboxylic carbon, instead, can be attributed to a true chemical shift, arising from deprotonation of the carboxylic headgroup and the formation of a chemisorptive bond with the cobalt substrate [75, 100]. Moreover, the closer distance of this functional group to metal surface is likely to induce a stronger screening of the core hole in the final state. The very low intensity of the carboxylate C 1s emission can be ascribed to the pronounced attenuation of the photoelectron signal from the carbon of the headgroup through the organic layer, since the inelastic mean free path at the chosen kinetic energy of 100 eV of the photoelectrons is of the order of 5 Å[111].

Similar to the C 1s of the $COO-$ group, the most pronounced feature of the O 1s level appearing at a binding energy of 531.2 eV (the same feature is visible in the XPS data of multilayer) is shifted by -1.3 eV compared to the multilayer data upon formation of the monolayer. Since a single sharp O 1s peak is observed, this confirms that the 4-FBA molecule undergoes O-H bond cleavage resulting in two equivalent carboxylate oxygen atoms, i.e., a bidentate bonding [106]. The weak O 1s shoulder at 532.1 eV can be presumably attributed to a small fraction of 4-FBA molecules adsorbed with non-equivalent oxygen atoms or in a different configuration relative to the majority of the molecules [75], however it only contributes less than 10% to the total oxygen signal and can be therefore regarded as a minority species.

Photoemission from the fluorine atom at the tailgroup provides further information on the integrity of the SAMs' molecule and on their interaction with the cobalt surface. The F 1s level of the monolayer again shows a single component at a binding energy of 687.1 eV, which is only 0.3 eV lower than that of the 4-FBA multilayer. This indicates that the fluorine atom does not experience a distinct

change of chemical environment in the final phase formed upon desorption of the multilayer. The implication is that the fluorine atom is not in the close vicinity of the metal surface, and the molecule in the monolayer are in a close-to-upright geometry.

NEXAFS spectra have been acquired to elucidate in more details and in a direct way the adsorption geometry of the 4-FBA SAM. Three geometries were considered with A_{xyz} corresponding to an angle of approximately 45° between the electric field of the radiation and the surface normal. As shown in Fig. 4.7, the C K-edge resembles that of the multilayer, except that now a much more distinct dichroism is visible in passing from A_{xy} to A_z polarization. The C K-edge spectrum is dominated by three sharp peaks at 285.0 eV, 287.1 eV and 288 eV, which are most intense for A_{xy} polarization. Considering the binding energy shifts in the C 1s XPS, they can be mainly attributed to π^* resonances originating from excitations of 1s electrons of the aromatic carbons, the fluorinated carbon and the carboxylate carbon, respectively, into the $1\pi^*$ orbital. In compliance with the analysis of the multilayer NEXAFS spectrum, a tentative energy diagram of the energy states involved in the transition from C 1s to π^* molecular orbitals is shown in Fig. 4.7 (b), based on the electronic energy levels of benzoate following Ref. [106, 107]. Due to the similarity of the NEXAFS and XPS spectra of mono- and multilayer, no drastic change in the electronic structure of the carbon has occurred except for a probable change of the molecular tilting angle. Analyzing the angular dependence of the most intense phenyl ring C 1s to $1\pi^*$ resonance at 285 eV according to equation 2.9 yields an angle of approximately 70° between the TDM and the surface normal, i.e., the molecules largely stand up on the Co(0001) surface.

In Fig. 4.7 (c), the main structure in the O K-edge spectrum acquired at A_{xy} polarization is dominated by two sharp resonances at 532.4 eV and 535.1 eV, both of which are above the excitation threshold (531.2 eV determined with XPS). The largest resonance at 532.4 eV comes from the excitation of the symmetrically bonded carboxylate oxygens into the lowest unoccupied π^* orbital, while transitions from O 1s of the minority species (see XPS) to the analogous π^* orbital probably gives rise to the second resonance at 535.1 eV [109]. Note that the intensity proportion of the second resonance to the largest resonance is clearly larger than its counterpart in the XPS data. This can be probably attributed to the overlap of the second resonance with the O 1s-to-3s resonance according to previous literature [109, 112]. Similar to the multilayer NEXAFS, broad σ^* resonances

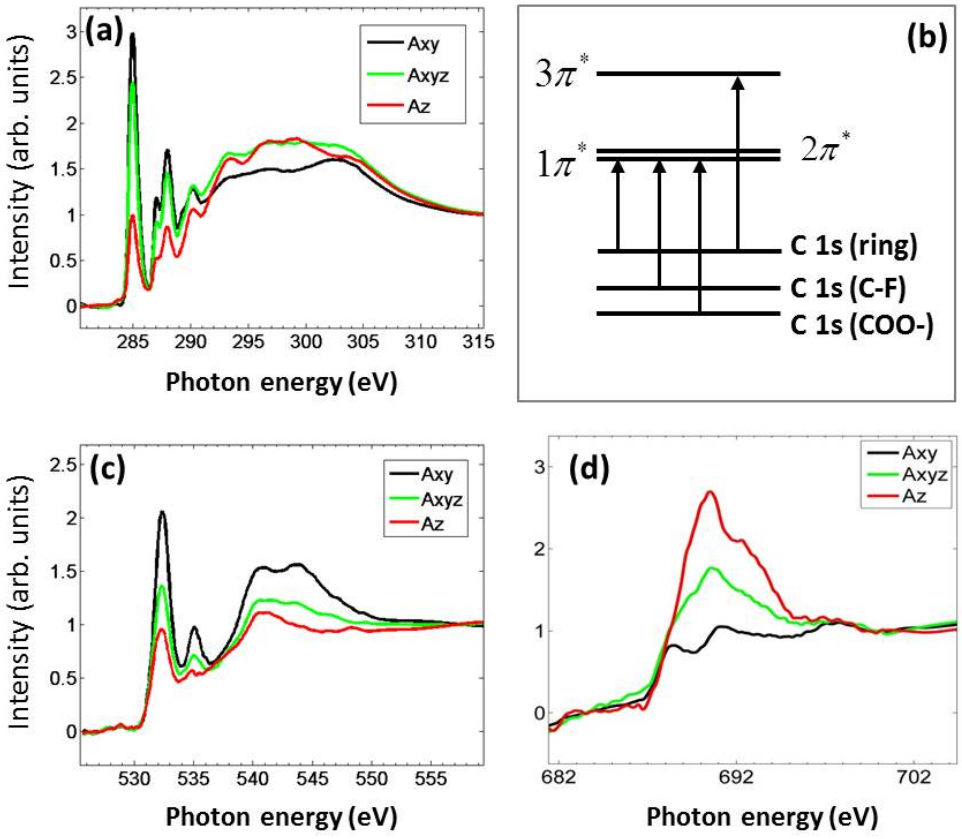

FIGURE 4.7: NEXAFS spectra of the 4-FBA monolayer on Co(0001) at the (a) carbon, (c) oxygen and (d) fluorine K-edge for three different geometries, corresponding to electric field of the radiation almost parallel (A_z), at an angle of 45° (A_{xyz}) or perpendicular (A_{xy}) to the surface normal. (b) Schematic representation of the molecular orbitals and possible transitions for the carbon K-edge [106, 107].

dominate the spectrum at photon energies above 537 eV. The NEXAFS spectrum recorded for A_{xy} polarization shows the strongest intensity of the two π^* resonances, indicating a standing-up carboxyl group. A quantitative analysis yields a tilt angle of 68° between the TDM and the surface normal, which is in excellent agreement with the analysis from the C K-edge data within the error bars (±10°).

Finally, the fluorine NEXAFS spectrum of the 4-FBA monolayer shows a much more pronounced polarization dependence than the multilayer, a more clear separation of different resonances and an overall larger intensity for the A_z polarization. The reversed sign of the dichroism compared with the carbon and oxygen K-edge spectra points towards a dominant role of σ^* resonances in the A_z curve and is in agreement with previous work [108]. The most prominent σ^* resonance at 690.5 eV with A_z polarisation again indicates the standing-up geometry of the molecule.

TABLE 4.1: XPS binding energies of the C 1s and O 1s core levels for multilayer and monolayer of 4-FBA on Co(0001)

multilayer	BE (eV)	assignment	**monolayer**	BE (eV)	assignment
C 1s 1	285.0	C-H	C 1s 1	284.7	C-H
C 1s 2	287.1	C-F	C 1s 2	286.9	C-F
C 1s 3	289.5	-COOH	C 1s 3	287.8	-COOH
O 1s 1	531.2	C-OO	O 1s 1	531.2	C-OO
O 1s 2	532.5	C=O	O 1s 2	532.1	C-OH
O 1s 3	533.4	C-OH			
O 1s 4	534.7	other			

TABLE 4.2: Energetic position and assignment of the observed C 1s and O 1s resonances for multilayer and monolayer of 4-FBA on Co(0001). PE denotes the photon energy.

multi.	PE (eV)	assignment	**mono.**	PE (eV)	assignment
C 1s 1	285.1	$1\pi^*$ C-H	C 1s 1	285.0	$1\pi^*$ C-H
C 1s 2	287.1	$1\pi^*$ C-F	C 1s 2	287.1	$1\pi^*$ C-F
C 1s 3	288.2	$1\pi^*$C-OO/$1\sigma^*$C-H	C 1s 3	288.0	$1\pi^*$ C-OO
C 1s 4	289.4	$1\pi^*$ C-OH	C 1s 4	289.4	$1\pi^*$ C-OH
O 1s 1	531.7	π^* C-OO	O 1s 1	532.4	π^* C-OO
O 1s 2	533.9	π^* C=O	O 1s 2	535.1	π^* C-OH
O 1s 3	535.2	π^* C-OH			
		1s-3s(σ^*)			

However, the strong overlapping of π^* and σ^* resonances hinders the quantitative analysis of the F 1s NEXAFS spectrum [108], e.g. the intensity of σ^* resonance at 690.5 eV might have contribution from the π^* resonance locating at only 500 meV higher photon energy [113, 114].

The binding energies of the C 1s and O 1s core levels measured with XPS as well as the corresponding positions of the resonances measured with NEXAFS for 4-FBA/Co(0001) multilayer and monolayer are summarized in Table 4.1 and 4.2.

4.2.1.2 Thermal Stability of 4-FBA/Co(0001) Monolayer

The above XPS and NEXAFS data demonstrate that a well-defined carboxylate-bonded 4-FBA monolayer can be prepared upon annealing the multilayer to 300 K. In view of technological applications, the thermal stability of the SAM is extremely important. In this section, this aspect will be investigated, using fast-XPS to follow

the monolayer evolution during annealing. The experiments were carried out off-line in our TUM laboratory employing non-monochromatized AlK_α radiation. The emission current of the X-ray source (30 mA), the pass energy of the analyzer (40 eV) as well as the energy step (0.1 eV) and dwell time (0.15 s) during data acquisition were properly set to ensure good statistics in the spectra. In fast-XPS, the temperature of the sample is linearly increased (0.5 K/s in this case), while XP spectra are acquired simultaneously. This allows direct monitoring of the temperature dependent evolution of core-level XP spectra, without the necessity of carefully selecting the temperature steps before acquiring the corresponding spectra. For each presented temperature-dependent core-level spectrum, a new preparation cycle was performed.

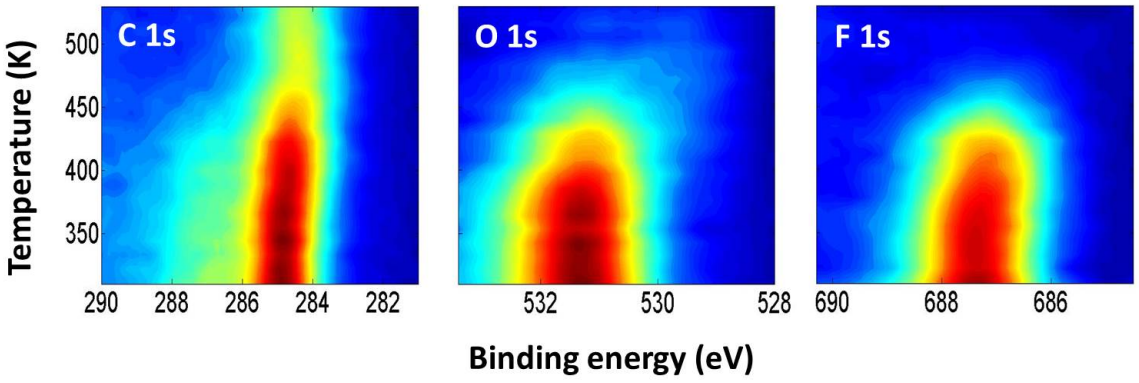

FIGURE 4.8: Fast-XPS spectra of 4-FBA monolayers adsorbed on Co(0001) for the C 1s (left), O 1s (middle) and F 1s (right) core levels. The contour plots show the intensity of the XPS signals as a function of binding energy and sample temperature. The intensity ranges from dark blue (lowest intensity) to dark red (highest intensity) and is normalized for each spectrum.

Figure 4.8 shows the fast-XPS spectra for the 4-FBA monolayer on Co(0001) in the temperature range of 300 to 550 K using a 2D contour plot representation. All three (C 1s, O 1s and F 1s) core levels do not show apparent changes below 390 K, both in intensity as well as binding energy position of the peak profiles, implying that the layer is thermally stable even at relatively elevated temperatures, similar to a 4-FBA monolayer adsorbed on a Ni(111) surface, which is thermally stable below 400 K [20]. Above 400 K, clear changes appear in all spectra, especially in the F 1s and O 1s core levels. First of all, in the C 1s contour plot the intensity of the phenyl ring emission peak at 284.7 eV as well as the C-F and C-OO C 1s signal at higher binding energies start to decrease in intensity and slightly shift to lower binding energy above 390 K, indicating C-F and C-OO bond breaking

and decomposition of the phenyl ring. For comparison, Barnes *et al.* studied the adsorption of benzene on Co($10\bar{1}0$) and found that a stepwise dehydrogenation of the ring occurs with the dehydrogenation step at about 380 K corresponding to formation of hydrocarbon fragments resulting from ring opening; in that case complete dehydrogenation occurred for temperatures above 550 K, leaving a carbonaceous residue [115]. In the work of Neuber *et al.*, benzoic acid on Ni(110) was found not to desorb intact (indeed, no desorption signal of the benzoate moiety was observed), but instead it undergoes decomposition with a desorption maximum for phenyl ring fragments at 545 K [75]. In our case, the decrease of the C-H carbon intensity slows down at 470 K, corresponding to the completion of the first decomposition process, leaving mainly hydrocarbon fragments on the surface since the XPS signal of oxygen and fluorine core levels have almost completely vanished at this temperature. In another C 1s contour plot with larger temperature range from 300 to 700 K (data not shown here), the fragments do not completely vanish even at 700 K, in contrast to the O 1s and F 1s counterparts.

As to the F 1s photoemission, the overall intensity decreases dramatically, resulting in a complete disappearance of fluorine at around 480 K. During the decrease of the F 1s signal, the shift of the binding energy is within 0.3 eV (which might be due to slight change of the molecular tilt angle upon annealing), and the lineshape of the signal is almost constant, indicating no intermediate product and a direct dissociation of the C-F bond with subsequent desorption of fluorine. Inspecting the O 1s plot, a very similar behaviour is observed as for F 1s. The main photoemission peak at 531.2 eV starts to decrease dramatically at 430 K and vanishes completely at approximately 480 K. This suggests that the oxygen is split off from the phenyl ring at elevated temperatures and readily desorbs, representing the dominant desorption channel. As the desorption of CO and CO_2 from benzoic acid does not occur below 500 K [75], the oxygen from 4-FBA might possibly desorb in the form of O_2. Furthermore, a weak signal at 529.5 eV gradually shows up at about 450 K, and vanishes above 500 K. According to its low binding energy, it might originate from oxygen that is chemisorbed on the cobalt surface. Above 500 K, it is likely to diffuse into the bulk or desorb alternatively.

Summarizing the results, the 4-FBA monolayer on Co(0001) is stable up to 390 K. At elevated temperatures, the C-F and C-OO bonds start to break and the phenyl ring decomposes gradually, leading to complete desorption of oxygen and fluorine at 500 K as well as to the adsorption of hydrocarbon fragments on the surface

up to 700 K. These results are in good agreement with the thermal stability of benzoic acid on Ni(110) [75] and 4-FBA on Ni(111) [20].

4.2.1.3 Charge Transfer Dynamics

Analysis of F 1s decay spectra As aromatic SAMs are promising for applications in molecular electronics [7, 11], it is very necessary to investigate the charge transfer dynamics between the SAMs' molecules and the underlying metal substrate. In this section, the dynamics of the tailgroup-to-substrate and headgroup-to-substrate electron transfer will be investigated. For the tailgroup (F 1s)-to-substrate charge transfer, an electron from the F 1s core level is resonantly excited into selected unoccupied orbitals, and decay electrons are analyzed with the Core Hole Clock method, as introduced in chapter 2. It turns out that the intermediate core-excited state can be dissociative when the F 1s core-level electron is excited into an antibonding σ^* orbital [116–118], thus resulting in the coexistence of both molecular and atomic features in the decay spectra, as will be discussed in detail in the following analysis.

First of all, the decay spectra of multilayer and monolayer will be evaluated. Figure 4.9 shows a 2D contour plot representation of the electron decay spectra following resonant F 1s excitation with photon energy covering the range of resonances observed by NEXAFS for the multilayer and monolayer. The electron emission intensity is described by the color scale as a function of the photon energy and the Auger kinetic energy. A_z polarization, with the electric vector of radiation almost parallel to the surface normal, was employed to measure the decay spectra. The F K-edge NEXAFS spectrum of the multilayer is shown in Fig. 4.9 (b). Consistent with the NEXAFS spectrum, the multilayer data of Fig. 4.9 (a) display a broad resonance ranging from 688 eV to 695 eV, which originates from resonant spectator and normal Auger decays. The dark red region of the contour plot, which corresponds to the highest intensity for the detected decay electrons, is in good agreement with the peaks of the multilayer NEXAFS spectra, as marked with arrows in Figure 4.9 (a, b). The contour plot of the monolayer shows a pronounced feature centered around an excitation energy of 690.5 eV, which is consistent with the sharper spectral profile of the monolayer NEXAFS (Fig. 4.7 (d)) compared with multilayer. Below photon energy of 693 eV, a dispersive feature originating from the resonant spectator decay can be clearly seen, but shifting

towards lower kinetic energy with increasing photon energy, which is probably due to the admixture of different Auger lines and the effect of vibration. The various decay channels converge into the Auger decay channel at a fixed kinetic energy of 654.8 eV, labelled "A", when the photon energy is above 693 eV. A variety of bands with higher kinetic energy and linear dispersion are attributed to the participator decay channels (labelled "P", it can be seen more clearly with the log scale in Figure 4.9 (d) and (e)). The intensity of the participator lines is relatively weak, as the decay spectrum of an atom with higher electronegativity like fluorine is dominated by the spectator channel [109]. Compared with the main Auger line at 654.8 eV, two more relatively weaker features (labelled "A2") with fixed kinetic energies appear at 660 eV and 662.7 eV, and they are considerably stronger in the decay spectra of the monolayer. As hinted above, C-F bond dissociation can occur after excitation of the F 1s electron into an antibonding σ^* orbital, which results in the presence of Auger decay channels originating from atomic fluorine determined according to their specific kinetic energy and the non-dispersive behaviour [116, 117]. This is indeed the origin of the lines denoted as "A2" in Fig. 4.9 (c).

Horizontal cuts at six different excitation energies of the decay spectra of monolayer are shown and compared in Figure 4.10 (b). It can be seen that the two features labelled "A2" ascribed to Auger decay channel of atomic fluorine increase gradually when increasing the photon energy above 688.3 eV and reach a maximum at the photon energy of 689.5 eV, instead of 690.5 eV, which is the absorption maximum of F K-edge as shown in Figure 4.10 (a). The two-peak structure of the Auger decay of atomic fluorine is assigned to different final-state configurations according to the previous observation in the dissociation of HF in gas phase [116, 117]. At elevated photon energies, the two Auger features are strongly suppressed and become negligible for decay spectra excited with photon energies higher than 691.5 eV, where the Auger decay channels of intact molecules start to dominate. Due to the largely upright geometry of the monolayer and the A_z polarization used for the acquisition of the decay spectra, the absorption at 689.5 eV along the C-F bond (populating the σ^* resonance) has the maximum probability to end up in a dissociated state and hence exhibits the strongest signal of Auger decay electrons from atomic fluorine, while the probability of obtaining an intact final state is enhanced with increasing photon energy. When the excitation energy increases, a faster depopulation of the excited σ^* resonance is normally expected due to the

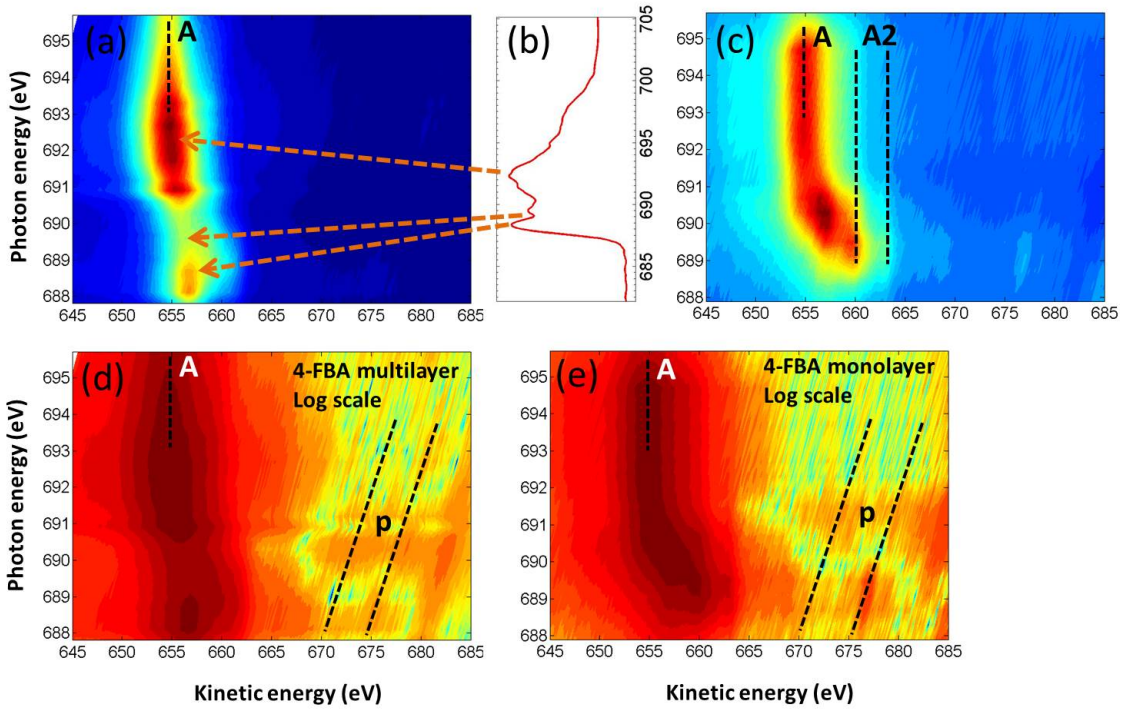

FIGURE 4.9: 2D contour plot representation of electron decay spectra for a 4-FBA (a) multilayer and (c) a monolayer on Co(0001) after resonant F 1s excitation as a function of the photon energy. The data in (a) and (c) are plotted on a linear scale, while (d) and (e) represent the same data on a logarithmic scale to facilitate the observation of the low intensity features. The fluorine K-edge NEXAFS spectrum of the multilayer is shown in (b) to aid the identification of spectral features in the contour plot. All the labelled decay channels are discussed in the text.

reduced barrier height for charge transfer from the resonantly excited orbital to the metal substrate [12]. However, exceptions exist, and a larger charge transfer time, or in other words slower depopulation of the resonance, was observed with increasing photon energy for Argon adsorbed on metal surfaces [38, 119, 120]. The evolution of the charge transfer time with photon energy in our case will be investigated in detail in the following section with respect to the 4-FBA/Co(0001) system.

PSD of 4-FTP/Ni(111) Our previous investigation of 4-fluorothiolphenol on the Ni(111) surface using photon stimulated desorption (PSD) effectively identified the ejection of atomic fluorine from the surface [20]. In the experiment, the F^+ fragments desorbing from the surface upon absorption of polarized radiation were monitored with a quadrupole mass spectrometer and the photon energy was scanned over the resonance to yield the intensity of the F^+ signal versus photon energy. The detection of F^+ ions showed that ultrafast dissociation of the C-F

bond occurs before the core hole created by resonant absorption decays. The case of 4-FBA on Co(0001) should be similar due to the very similar adsorption geometry of the molecules (largely upright) and the very close properties of the two ferromagnetic substrates. The experimental results indicate that the maximum intensity of the atomic F occurs at a photon energy of approximately 1 eV below the absorption maximum of the F K-edge NEXAFS spectrum of the 4-FTP/Ni(111) monolayer, similar to the case of 4-FBA/Co(0001). The distinct resonances from the PSD spectrum were correlated with the spectroscopic features of the NEXAFS spectra. Moreover, the PSD signal was shown to be polarization dependent, the F^+ signal being stronger for polarization along the C-F bond axis. This excludes the possibility of other hydrocarbon fragments with m/e=19 contributing to the PSD yield. These results indirectly support the conclusions drawn from the evaluation of the decay spectra concerning the atomic F component.

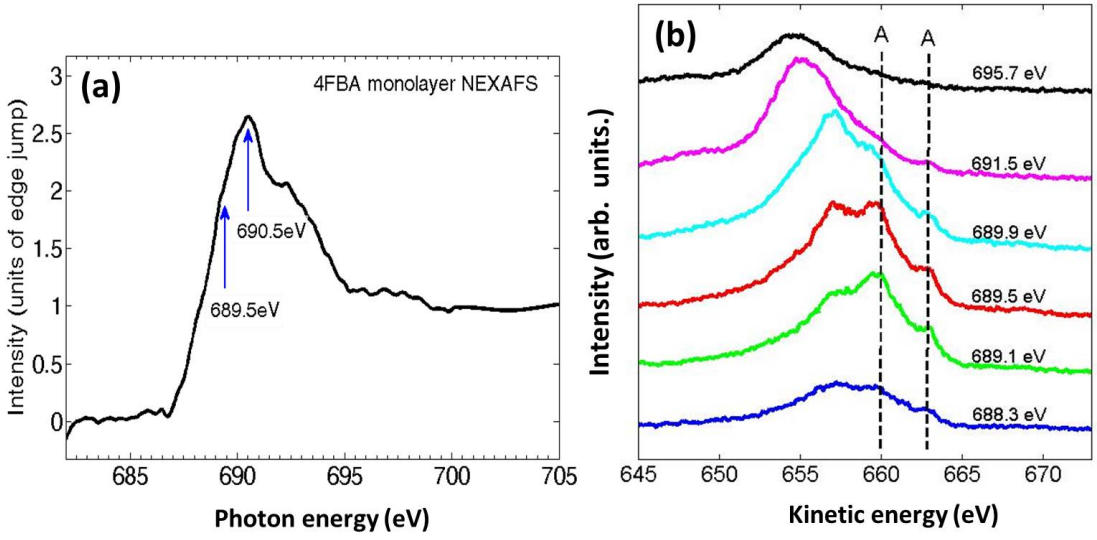

FIGURE 4.10: (a) Fluorine K-edge NEXAFS spectrum of the 4-FBA monolayer measured with A_z polarization, two involved σ^* type resonances are marked with arrows. (b) Horizontal cuts at several different excitation energies of the 2D contour plot of the monolayer of Figure 4.9.

Tailgroup to substrate charge transfer with the CHC method As discussed above, the resonant excitation populates a highly repulsive intermediate state, and the dissociation process must take place before the resonance depopulates [117]. This explains why the signature of atomic F is observed in the decay spectra. Since the time required to depopulate the resonance is given by the

electron charge transfer time to the substrate, the study of charge transfer dynamics of the 4-FBA/Co(0001) system will help to determine the timescale of the dissociation process.

In order to extract the charge transfer time of electron excited from the F 1s core level into the C-F σ^* resonance to the metal continuum, the decay spectra of the monolayer can be reconstructed as a linear combination of a pure resonant (or pure autoionization) and a normal Auger line with different intensity ratios. The multilayer decay spectra can be used to determine the spectral shape of the pure resonant decay channel, as the resonant decay is the only effective de-excitation mechanism in a condensed multilayer with negligible coupling to the metal substrate. Instead, the above-resonance excitation of the monolayer with 700 eV photon energy (approximately 10 eV above the resonant absorption maximum) contains only the normal Auger contribution. In addition, spectra measured about 10 eV below the onset of the F 1s resonance (680 eV in this case) need to be subtracted from all decay spectra to remove the non-resonant background. A linear combination of the pure resonant ($I_{resonant}$) and pure Auger (I_{Auger}) spectra can thus reproduce the measured decay spectra of the monolayer, and the charge transfer time can be determined by means of equation 2.12, where 3 fs is used as the core hole lifetime of F 1s.

Examples of reconstruction of the decay spectra are shown in Fig. 4.11 a-f. It can be noted that decay features of atomic F can hardly be observed from the decay spectra of multilayer shown in Figure 4.9 and the normal Auger spectrum measured at photon energy of 700 eV (as suggested by the high photon energy spectra of Fig. 4.10 (b)). Therefore it can be expected that the reconstruction of the monolayer decay spectra is less satisfactory at low excitation energies, where the atomic decay channels play a non-negligible role (Fig. 4.10 (b)). With higher excitation energies, the increased weight of the normal Auger contribution from the intact molecule will enable a better agreement between measured and reconstructed spectra. The weight of pure Auger and pure resonant contributions were determined by optimizing the Sum of Squared Residuals (RSS) between measured and reconstructed spectra.

As expected, in Fig. 4.11 (a) and (b) the atomic decay features of fluorine at 660 eV and 662.7 eV play a major role, and the reconstruction is not excellent. In (a) and (b), the pure resonant fraction is clearly larger than the pure Auger part, and the charge transfer time increases from 10.64 fs to 22 fs with decreasing Auger fraction

from 0.22 to 0.12. When the photon energy gradually increases in Figure 4.11 from (c) to (f), the Auger fraction also increases and much faster charge transfer times of 1.69 fs at 691.5 eV and 2.88 fs at 691.9 eV are achieved. Furthermore, the agreement between measured and reconstructed spectra improves with increasing photon energy as anticipated, even at the location of the atomic decay features. Figure 4.12 shows the overall trend of the charge transfer time as a function of the photon energy (panel (b)), together with the estimated Auger fractions (panel (a)). The error bars result from uncertainties of the reconstruction procedure. It can be seen that the charge transfer time is extremely large for four photon energies (marked with red crosses) around 689.5 eV, corresponding to energies at which the highest signal of atomic F is obtained. Here, the Auger fraction is too low to provide a reliable estimate of the charge transfer time [1], therefore we will not comment on these data in the following discussion.

In Figure 4.12, it can be observed that the charge transfer time decreases from 15.75 fs at the leading edge of the resonance to approximately 1 fs at 692.3 eV, which can be tentatively explained in terms of a decrease of the effective barrier height with increasing photon energy [38, 120, 121]. Previous studies have shown that the charge transfer time in adsorbate/substrate systems depends mainly on three parameters: the energetic position of the resonance relative to the Fermi level, the coupling of populated states with the unoccupied states of the substrate, and the available density of states acting as electron acceptors [8, 10, 12]. Taking into account the overlap of σ^* and π^* resonances at the F K-edge, the charge transfer dynamics shown herein can only be qualitatively analysed. The charge transfer time is longer at photon energies around 689.5 eV, where the maximum of F^+ signal is observed in the PSD spectrum. This indicates that a slow depopulation of the resonance is correlated with an increased dissociation of the C-F bond.

In conclusion, the above results show that the charge transfer from the core-excited tailgroup of 4-FBA molecule (fluorine) to the Co(0001) surface takes place on the femtosecond timescale and that the charge transfer time generally decreases with increasing photon energy, in good agreement with the charge transfer dynamics

[1] In the case of F 1s core level, these times correspond to long charge transfer time out of the range $0.3fs \leq \tau_{ct} \leq 30fs$ [10]), in which the CHC approach is reliable.

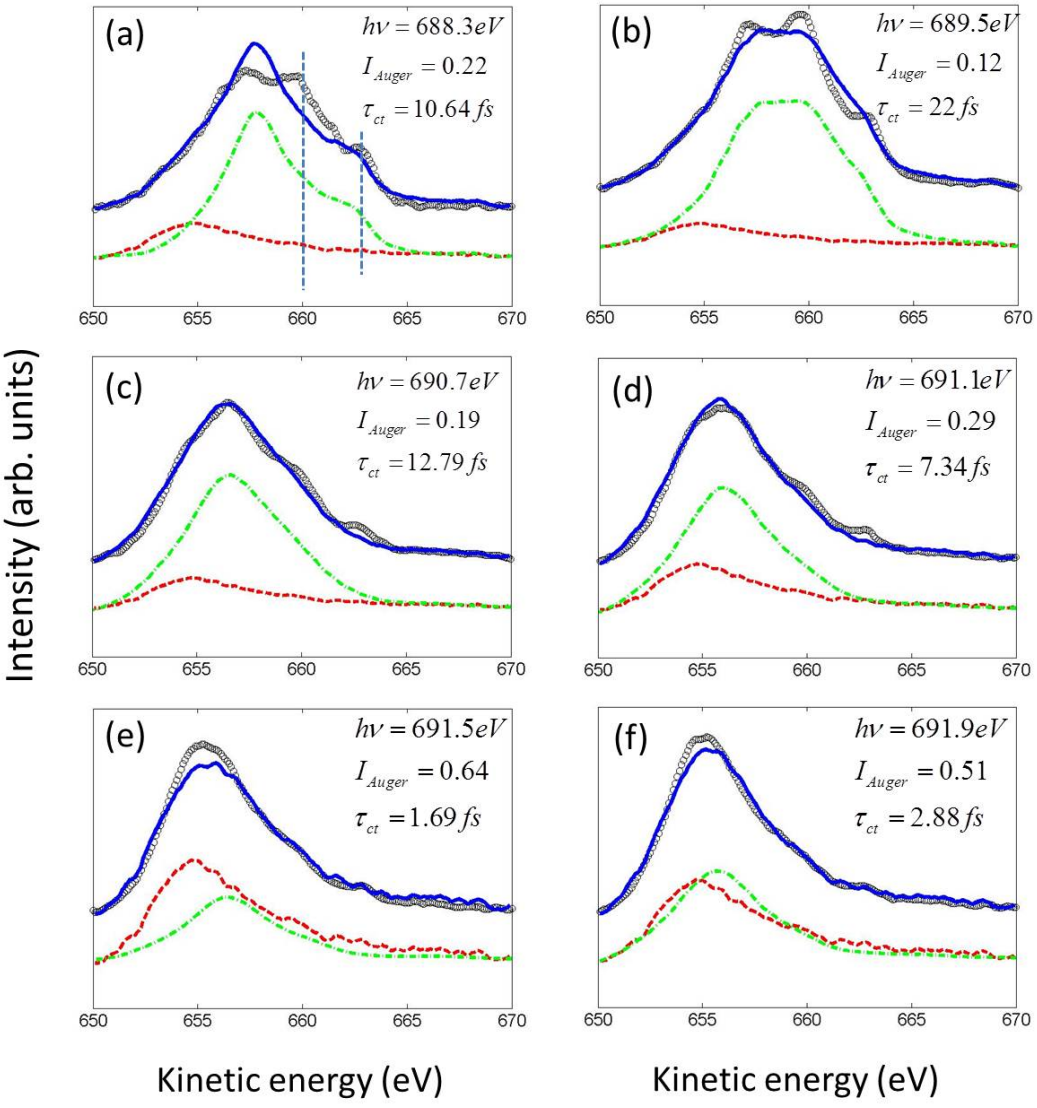

FIGURE 4.11: Reconstruction (blue lines) of the measured monolayer decay spectra (black circles) with the linear combination of the pure resonant (green dash-dotted lines) and pure Auger (red dash-dotted lines) lineshapes as mentioned in the text. The reconstruction at photon energies of (a) 688.3 eV, (b) 689.5 eV, (c) 690.7 eV, (d) 691.1 eV, (e) 691.5 eV and (f) 691.9 eV is shown. The corresponding results for the estimated charge transfer time and the Auger ratio are also reported in each plot. The vertical lines in panel (a) denote the location of the Auger decay features originating from atomic F.

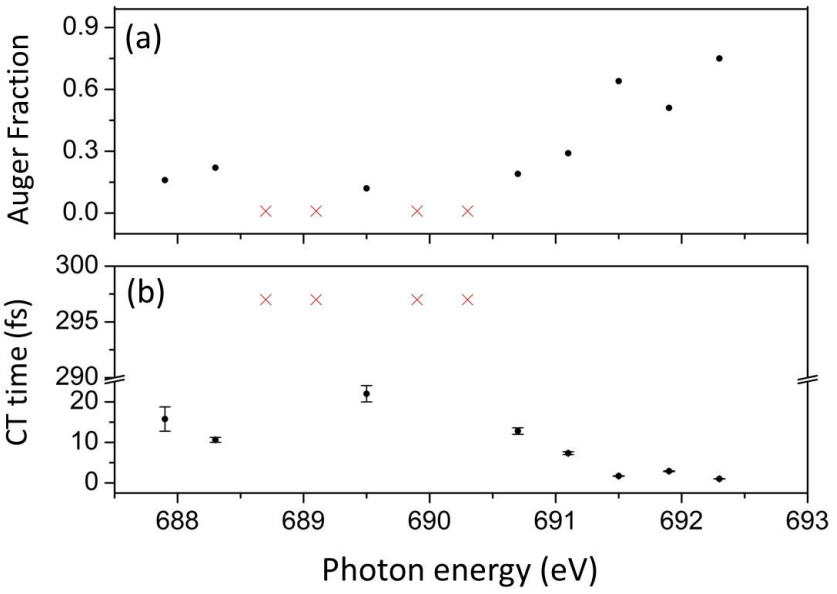

FIGURE 4.12: Auger fraction (a) and corresponding charge transfer time (b) following resonant absorption at the F K-edge as a function of the excitation energy. The red crosses represent data points out of the accessible range where the CHC approach provides reliable estimation of the charge transfer time.

of 4-FBA on Ni(111) [20] and other previous studies [9, 122]. Therefore, the good conductivity and high thermal stability of the 4-FBA/Co(0001) SAM make it a promising candidate for model studies in molecular electronics.

Analysis of O 1s decay spectra The resonant Auger decay spectra of oxygen were measured by collecting a set of band spectra with photon energies varying across the region of the $2\pi^*$ resonance at the O K-edge. For the monolayer of 4-FBA on cobalt, the main π^* type resonances measured with NEXAFS correspond to electrons excited from the O 1s core levels of symmetrically bonded carboxylate oxygens (O-C-O) to $2\pi^*$ orbital at 532.4 eV (see the sharpest feature in the O K-edge NEXAFS spectra shown in Fig. 4.7 (c)).

The resulting resonant Auger decay spectra are represented in a 2D contour plot in Fig. 4.13 (a). Only the resonantly enhanced features are included, while the direct photoemission contribution measured several eV before the absorption maximum (525 eV in this case) has been subtracted. Three dominant features with constant kinetic energy regardless of the excitation energy appear below 520 eV. These features correspond to two hole final states created by normal Auger decay processes where the excited $2\pi^*$ electrons delocalize into the substrate before

the 1s core hole is filled. Keller *et al.* studied the O KLL decay spectra for a saturated CO monolayer on Ru(0001) and observed not only the three above mentioned normal Auger features but also two small resonantly enhanced peaks with constant binding energies above 520 eV, resulting from decay channels where the resonantly excited $2\pi^*$ electron takes part in the autoionization (participator channel) [121, 123]. By plotting the same data in the intensity log scale and as a function of the binding energy to emphasize the autoionization decay channels (spectator and participator), the mentioned participator decay channels can be also observed in Fig. 4.13 (b). Furthermore, a number of additional features with fixed binding energy appear between 20 and 50 eV. They can be tentatively attributed to spectator decay channels with 2h1e final states according to the previous resonant Auger spectra of formid acid investigated by Hergenhahn *et al.*, who assigned states in the range from ca. 17 eV to 58 eV to 2h1e final states [109]. In that work, formic acid was studied in the gas phase and hence no normal Auger decay channels were observed. In our case, the three normal Auger features are largely dominant in intensity, whereas the participator and spectator decay channels display much weaker intensity and only become visible in the log scale plot.

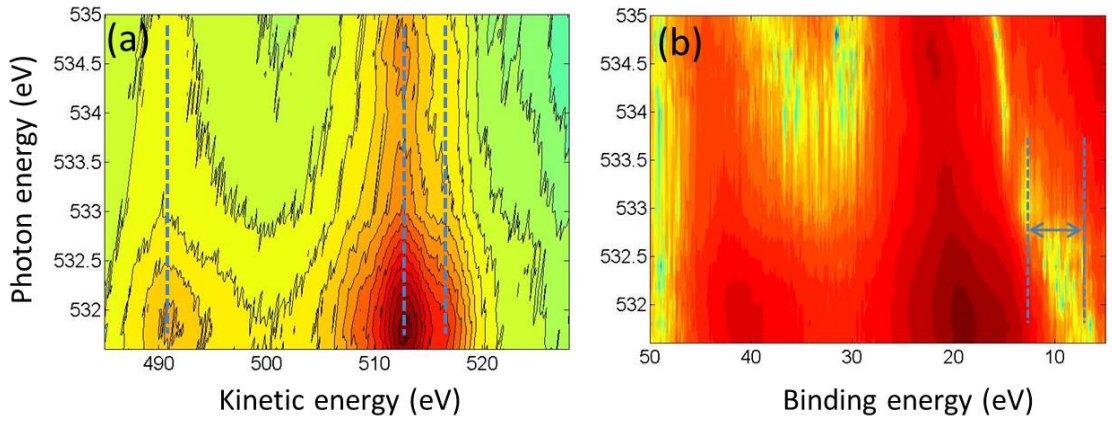

FIGURE 4.13: 2D contour plot representation of O KLL resonant Auger spectra (after subtraction of the photoemission background) at the O 1s to $2\pi^*$ resonance, as a function of the excitation energy. The excitation energy is finely detuned across the resonance width. (a) The plot as a function of the kinetic energy emphasizes the normal Auger decay channels. (b) The plot as a function of the binding energy with the intensity plotted in the log scale emphasizes the autoionization decay channels.

Similar to the CHC analysis for fluorine, the measured decay spectra of the monolayer can be reproduced by a linear combination of the pure autoionization and pure Auger contributions, which are provided by the resonant decay spectrum of multilayer at the respective excitation energy and by the decay spectra of the monolayer measured approximately 10 eV above the resonance (550 eV in this case), respectively. The non-resonant background recorded at photon energy 5 eV below the onset of the resonance as well as a Shirley-type background are subtracted from all decay spectra prior to the reproduction procedure. Note that the resonantly excited electrons can delocalize very quickly into the substrate because of the direct carboxylate bonding with the substrate, which leads to strong hybridization of the $2\pi^*$ orbital [121, 123]. Consequently, the participator and spectator decay channels are strongly suppressed and they overlap with the dominant normal Auger decay channels, reducing the accuracy of the CHC approach as compared with the less extreme branching ratios of normal Auger and autoionization channels of Fig. 4.11. However, the charge transfer time can still be estimated by taking the relative ratio of participator channels above the kinetic energy of 520 eV to the normal Auger channels between 510 and 520 eV from our measurements. Figure 4.14 shows the reconstruction procedures at the $2\pi^*$ resonance maximum (532.4 eV) and on its low energy side (531.8 eV). At 532.4 eV, we find an extreme fraction of 92% for the pure Auger channel as noted above. With the O 1s core-hole lifetime being of the order of 6 fs [123], the charge transfer can be estimated to be faster than 0.6 fs. A less extreme ratio of 81% was found on the low energy side of the $2\pi^*$ resonance maximum (Fig. 4.14 (a)), resulting in a charge transfer time of 1.41 fs.

Figure 4.15 shows the dependence of pure Auger fraction on the photon energy. Note that some data points are missing as the photon energy was not increased with a fixed energy step during the measurement. The error bars only indicate the uncertainty from the viewpoint of statistical analysis, and the accuracy at extreme ratios can be even lower due to the strong suppression of the pure autoionization decay channels. The pure Auger fraction increases strongly with the excitation energy above the $2\pi^*$ resonance maximum. Therefore, the charge transfer time decreases with photon energy, which again can be rationalized in terms of lowering of the effective tunnelling barrier. Keller *et al.* found an opposite tendency for the charge transfer time for chemisorbed CO on Ru(0001), that is the charge transfer time increased with increasing photon energy, and they attributed this dependence

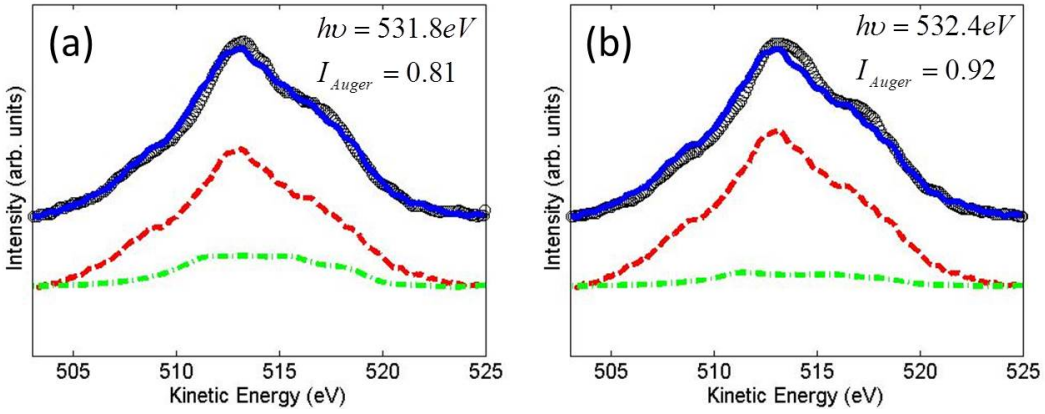

FIGURE 4.14: Reconstruction (blue lines) of the measured electron decay spectra (black circles) at the O K-edge by linear combination of pure resonant (green dash-dotted lines) and pure Auger (red dashed lines) lineshapes as discussed in the text. Reconstruction at photon energies of (a) 531.8 eV (low energy side of $2\pi^*$ resonance) and (b) 532.4 eV ($2\pi^*$ resonance maximum) are shown. The corresponding Auger ratios are also indicated in each plot.

to the decrease of the density of unoccupied d states of Ru(0001), which are available for the delocalization of the resonant electrons into the substrate [123]. In our case, the different degree of hybridization of the $2\pi^*$ resonance with cobalt as well as the different unoccupied density of Co d states might be at the root of the different energy dependence of the charge transfer time.

The dominant charge transfer (CT) pathway can be assumed to involve conductivity through the backbone and the tunnelling through carboxylate-Co anchor, based on our conclusion that more than 90% the molecules bond to the substrate via the carboxylate anchor, and that all the fluorine atoms are located at the SAM-vacuum interface and have no direct contact with the substrate. Within the framework of the CHC approach, it takes 1 to 22 fs for a resonantly excited F 1s electrons to tunnel to the substrate and a considerable fraction of the time is likely to be related to the CT through the aromatic backbone since CT through the Co-carboxylate anchor have been estimated to take only approximately 0.6 fs. Similar to previous CT study of aliphatic and aromatic SAMs [122, 124], the CT time in our case can be tentatively described by the formula $\tau = \tau_{carboxylate} \exp(\beta_{ph}\ell_{ph})$, where $\tau_{carboxylate}$ is the CT time across the carboxylate anchor (0.6 fs), β_{ph} is the attenuation factor of the aromatic backbone, and ℓ_{ph} is the backbone length [122]. Assuming $\ell_{ph} = 4.3$ $\mathring{A}$ [125], we obtain an β_{ph} values ranging from 0.75 $\mathring{A}^{-1}$ to 0.14 $\mathring{A}^{-1}$ with increasing excitation energy based on the CHC analysis. The results are

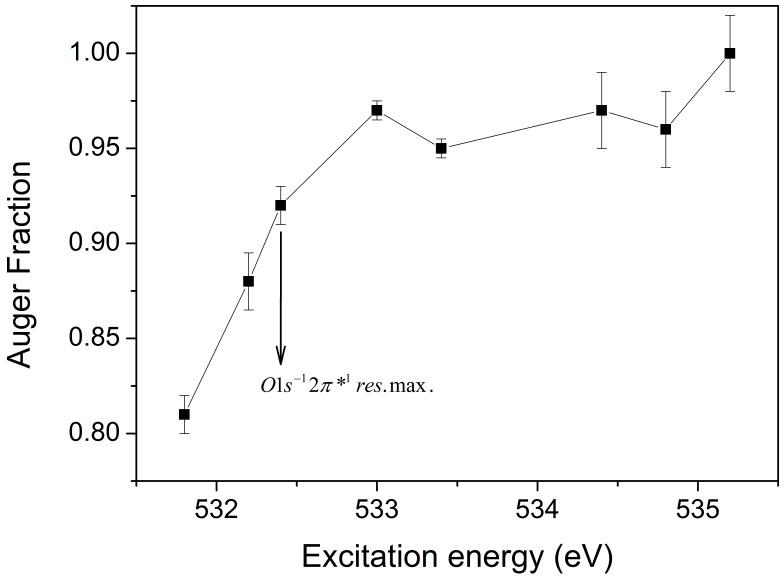

FIGURE 4.15: Variation of the normal Auger ratio as a function of the excitation energy. The arrow indicates the position of the maximum intensity of the O 1s to $2\pi^*$ resonance.

TABLE 4.3: Calculated attenuation factor β_{ph} of the aromatic chain when detuning the excitation energy across the resonance. The respective CT times τ (obtained with CHC approach) that are used for the calculation are also shown.

Energy (eV)	τ (fs)	β_{ph} ($\mathring{A}^{-1}$)	Energy (eV)	τ (fs)	β_{ph} ($\mathring{A}^{-1}$)
687.9	15.75	0.75	688.3	10.64	0.66
689.5	22	0.83	690.7	12.79	0.71
691.1	7.34	0.58	691.5	1.69	0.24
691.9	2.88	0.36	692.3	1.1	0.14

summarized in Table 4.3. As the variation of excitation energy can be regarded as a variation of the surface potential difference V ($V = E_{res} = E_{excitation} - BE$) for static molecular conductance, the change of β_{ph} with the photon energy is consistent with observations in static conductance that the attenuation factor can increase or decrease with applied bias [125, 126]. The reported static attenuation factor of aromatic chains for molecular conductance lies generally in the range between 0.27 $\mathring{A}^{-1}$ and 0.77 $\mathring{A}^{-1}$ [122, 126], which agrees well with our results obtained from the dynamic CT time.

Furthermore, according to the theoretical expression for static molecular conductance [124], the CT time can be expressed by $\tau = h/(2e \cdot \exp(-\beta_{ph}\ell_{ph}) \cdot E_{res})$, which provides the dependence on the surface potential difference E_{res} and the attenuation factor β_{ph}. With taken β_{ph} from Table 4.3, e the electron charge and

h the Planck constant, the CT time can be estimated from the point of view of static molecular conductance. The resulting static CT times are plotted together with the dynamic CT (CHC) times in Figure 4.16. The agreement is very good on the high excitation energy side, whereas the static CT time at low excitation energy is considerably higher. However, the identical trend and the good agreement above the resonance maxima (E_{exc} = 690.5 eV, according to NEXAFS data) may be regarded as a supporting evidence for the tunnelling CT mechanism.

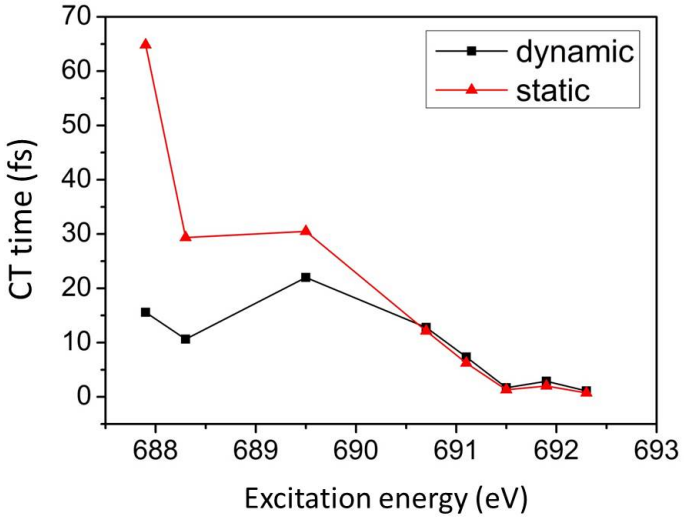

FIGURE 4.16: Comparison of the CT time of resonantly excited F 1s electrons determined with CHC approach (black) to the values calculated using the theory of static conductance (red). See text for details.

Summarizing the above results, after site-selective resonant core excitation of carboxylate bonded 4-FBA/Co(0001) SAMs with photon energy tuned across the O 1s to $2\pi^*$ resonance, the strong suppression of the autoionization decay channels was observed, corresponding to very fast charge transfer at the molecule-metal interface. It is possible to estimate an upper limit for the charge transfer time on the sub-femtosecond time scale using the CHC approach. Since the normal Auger decay channel has a relative weight of more than 90% at photon energy above the $2\pi^*$ resonance maximum, the charge transfer time must be lower than approximately 0.6 fs. Given the estimated charge transfer time through the carboxylate anchor, the attenuation factor through the backbone can be calculated and is found to decrease with increasing excitation energy, agreeing to some extent with the static conductance process.

4.2.2 Conclusions for the 4-FBA/Co(0001) Monolayer

A well defined monolayer of 4-FBA can be prepared on evaporated Co(0001) films under UHV conditions. It is thermally stable up to 390 K. The molecules in the as-prepared multilayer are largely flat-lying, while annealing the multilayer to 300 K leads to deprotonation of the carboxyl group, and a bidentate bonding of the molecules with cobalt is formed. NEXAFS data indicates an upright geometry for the adsorbed molecules in the monolayer, with an angle of approximately 70° between the phenyl ring and the underlying cobalt surface.

Using the Core Hole Clock approach we have measured the resonant Auger decay spectra of fluorine and oxygen, and determined the characteristic electron transfer time from the headgroup and the tailgroup, respectively, to cobalt. The charge transfer from the core-excited tailgroup to the Co(0001) surface takes place on the femtosecond time scale, and τ_{CT} generally decreases with increasing photon energy. The dissociation of the C-F bond and the resulting atomic fluorine decay channel have a distinct influence on the the decay spectra. As to the charge transfer from the headgroup to the substrate, the contribution of the autoionization decay channels was estimated to be less than 10% in the oxygen decay spectra excited with photon energies above the $2\pi^*$ resonance maximum, corresponding to a charge transfer time smaller than 0.6 fs. Moreover, the charge transfer time of the excited $2\pi^*$ electrons decreases with increasing photon energy across the resonance width. Finally, the dynamic charge transfer phenomenon can be associated with the static molecular conductance and a good agreement can be reached. The 4-FBA monolayer can thus represent an excellent model system in terms of thermal stability and conductivity for fundamental studies in the field of molecular electronics and spintronics.

4.3 4-Cyanobenzoic Acid SAMs on Co(0001)

As discussed in section 4.1, the tailgroup determines the surface properties of SAMs, and the change of tailgroup can influence the molecular configuration as well as the starting site for the electron transfer to the metal substrate. The cyano or nitrile (-CN) group is a perspective tailgroup within the general concept of SAM design for many reasons, e.g., its large dipole moment can be used

for the control of surface potentials and work functions, and the attachment of the CN group to the aromatic backbone enables direct probing of the molecular adsorption geometry with NEXAFS [127]. In addition, CN-terminated SAMs have proven to be a favourite choice for CHC investigations thanks to the large "spectator shift" between the decay spectra of the pure autoionization and normal Auger channels, thus facilitating the decomposition of the measured decay spectra [9, 122]. Another advantage for investigating charge transfer from the nitrogen atom of nitrile is that the excited electrons come exclusively from the π^* orbitals of the nitrile group, in contrast to decay spectra of carbon, where the initial site of the excitation is not unambiguously assigned due to charge delocalization in the phenyl ring [11]. The degeneracy of the two π^* orbitals of the CN group can be lifted upon interaction with the neighbouring aromatic ring, yielding in-plane and out-of-plane π^* orbitals differing in energy by approximately 1 eV [122]. Lifting of the degeneracy can be also induced by the interaction with an aliphatic backbone or a metals substrate, yielding much smaller energy separation in aliphatic CN-terminated SAMs (approximately 100 meV) [9] and larger splitting for the direct interaction with a metal substrate, e.g., a splitting of 3.5 eV was reported for acetonitrile adsorbed on Pt(111) surface [128]. Interestingly, the charge transfer from nitrile N 1s through an aromatic or aliphatic backbone into the substrate were found to depend strongly on the initially populated π^* molecular orbitals; specifically, different charge transfer efficiencies have been found for the in-plane and out-of-plane orbitals by selective excitation [9, 122]. In this section, SAMs of 4-cyanobenzoic acid (4-CBA) SAMs, a molecule that has just the different tail-group (CN) compared with 4-FBA, will be investigated focusing on the electronic structure, adsorption geometry and the charge transfer dynamics. We prepared 4-CBA SAMs on Co(0001) and characterized them by synchrotron based spectroscopies: XPS, NEXAFS and RAES. The shape of the RAES spectra and their dependence on the excited molecular orbital (the split π^* orbital at the CN group) will be discussed in detail.

The experimental procedure is very similar to that employed for 4-FBA on Co(0001), and the experiments were carried out in the same UHV chamber using soft X-ray radiation from the beamline U49/2 at BESSY II in Berlin. The cobalt film was prepared as described previously, while 4-CBA (solid) was sublimated by heating a glass crucible loaded with molecular powders to $110°C$, and brings the crucible directly in front of the freshly-evaporated Co(0001) films. Unless otherwise stated,

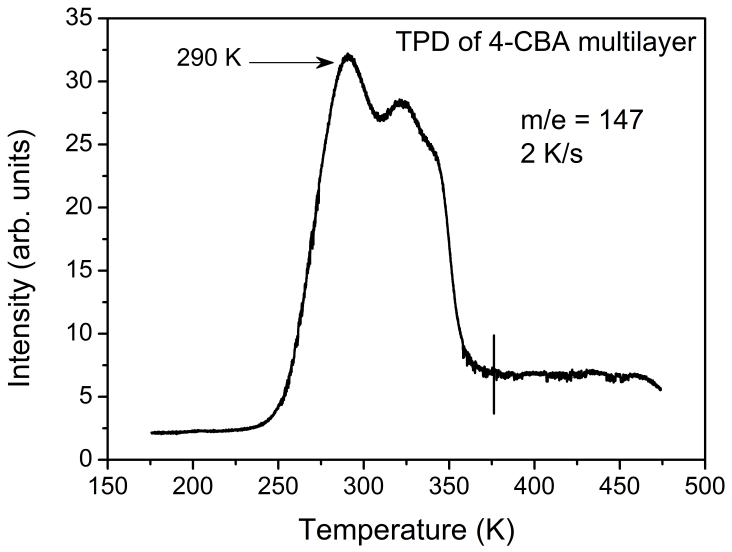

FIGURE 4.17: TPD spectrum of a 4-CBA multilayer measured with a QMS, while ramping the temperature with a constant heating rate of 2 K/s. The temperature chosen for the preparation of a saturated monolayer is indicated by the vertical line. The measured QMS signals correspond to the mass/charge ratio of the intact 4-CBA molecule upon double ionization.

the substrate was held at 300 K (RT) when exposed to the molecular vapours. TPD measurements on the 4-CBA multilayer on Ni(111) at a heating rate of 2 K/s yielded a broad desorption structure extending from 290 K to 350 K for the doubly ionized 4-CBA molecule, as shown in Fig. 4.17. The desorption peak of the condensed layer is not expected to depend strongly on the substrate. Therefore, a saturated monolayer of 4-CBA on Co(0001) could be prepared by annealing of the multilayer to 370 K at 2 K/s for a few seconds. Based on the TPD measurement, a similar thermal stability could be expected for 4-CBA/Co(0001) and 4-FBA/Co(0001) SAMs.

4.3.1 Experimental Results and Discussion

4.3.1.1 Structural Characterization with XPS and NEXAFS

XPS Characterization The C 1s, N 1s and O 1s XP spectra of the 4-CBA/Co(0001) SAM are presented in Fig. 4.18 a, b and c, respectively. In view of the chemical structure of 4-CBA, the C 1s spectrum can de mainly decomposed into four peaks at 284.2 eV, 285.5 eV, 286.5 eV and 288.3 eV, assigned

to aromatic carbon atoms in the phenyl ring, the aromatic carbon atom adjacent to the nitrile group, the nitrile carbon, and the carboxylic carbon, respectively. This is consistent with reported studies of aromatic or aliphatic SAMs with cyano tailgroup [124, 129]. Similar to the 4-FBA/Co(0001) SAM, the relative intensity of the carboxylic carbon is only 7% for 4-CBA, which can be explained by attenuation of the photoelectrons through the upright backbone of the molecules, such an orientation being indicated by NEXAFS (see below). The assignment of the photoemission peaks of the C 1s core level is summarized in Table 4.4.

The N 1s core level spectrum (Fig. 4.18 (b)) exhibits a major peak at a binding energy of 398.7 eV, which is assigned to the nitrile nitrogen atom and amounts to 82% of the overall signal. Note that the binding energy of this majority specie is close to that reported in Ref. [130], where SAMs with CN tailgroup contain molecules inclined by approximately 40° with respect to the surface normal. This shall reflect to some extent the adsorption geometry of 4-CBA on Co(0001), as the N 1s binding energy of the CN tailgroup has been shown to depend on the distance between the excitation site and the substrate, and is lower for the shorter molecules and molecule more tilted toward the surface due to stronger screening of the core hole by the conduction electrons in the metal substrate [124]. In Fig. 4.18(b), a minority specie appears at about 397.4 eV binding energy, with relative population of 17%. The binding energy of 397.4 eV falls exactly inside the range of values reported for atomic N species adsorbed on transition metal surfaces [131]. This would indicate breaking of the strong CN triple bond, and correspondingly atomic carbon shall be observed. However, no such a carbon specie characterized by a binding energy below 284 eV is obtained in the curve-fitting analysis of Fig. 4.18 (a), thus excluding the existence of atomic constituents and instead suggesting that the CN bond is still intact. Indeed, the RAES spectra of N shown later also rules out the presence of atomic N. Nakayama *et al.* studied the adsorption geometry of benzonitrile on nickel and palladium surfaces and concluded that the N 1s binding energy can be as low as 397.4 eV - 397.6 eV when the CN group coordinates to the metal surface via rehybridization of the triple CN bond, the N 1s binding energy being correlated with the degree of rehybridization [132]. Therefore, in the present work the rehybridization of the nitrile group with cobalt might give rise to the component at 397.4 eV. Another possible explanation for the low binding energy of this N species is the cleavage of the C-CN bond resulting CN fragments adsorbed on the surface. But again this would give rise to another peak on the low binding energy side of the aromatic C 1s peak (284.2 eV) according to our study of

TABLE 4.4: Photoemission at the C, O and N core levels and assignments.

Core level	**BE (eV)**	**assignment**
N 1s 1	397.4	rehybridized CN
N 1s 2	398.7	CN tilted away from the surface
C 1s 1	284.2	aromatic C
C 1s 2	285.5	aromatic C adjacent to -CN
C 1s 3	286.5	nitrile C
C 1s 4	288.3	carboxylate C
O 1s 1	531.1	symmetric bonding (bidentate)
O 1s 2	533.3	asymmetric bonding (canted)

4-cyanothiophenol on Ni(111) [133], and this is not the case. Therefore, based on the above discussion, the species at 397.4 eV (17%) will be tentatively assigned to a minority of molecules that interact more strongly through their tailgroup with the cobalt surface.

Finally, the O 1s core-level spectrum is shown in Fig. 4.18 (c), and can be decomposed into two peaks at 531.1 eV (70%) and 533.3 eV (30%). In analogue with the 4-FBA SAM on Co(0001) (section 4.2), we can assign the dominant component to a majority species, with the two oxygen of the carboxyl group coordinating symmetrically to the surface (bidentate adsorption). The binding energy of the second component is very close to that of the carbonyl O 1s of 4-FBA multilayer at 533 eV. However, the peak cannot be due to residual physisorbed molecules since it does not disappear with increasing annealing temperatures and the hydroxyl oxygen peak is missing. According to previous investigation of carboxylic acid SAMs on metal surfaces [134], the carboxyl group can also bond in a canted configuration with the carbonyl oxygen tilted away from the surface, thus resulting in two chemically distinct oxygen species. We therefore infer that the carbonyl oxygen can be tilted away from the surface giving rise to the peak at 533.3 eV, since the intact hydroxyl oxygen would instead show a peak at even higher binding energy (534.8 eV) according to our XPS data of 4-FBA/Co(0001). The canted adsorption (monodentate) is presumably related to the change of the tailgroup, since the 4-FBA/Co(0001) SAM is predominantly bonded in the bidentate form. We speculate that the stronger interaction of the CN group with the substrate is the reason for the monodendate bonding, as will be pointed out in the following discussion on the NEXAFS data.

NEXAFS Characterization The C, O and N K-edge spectra of the 4-CBA

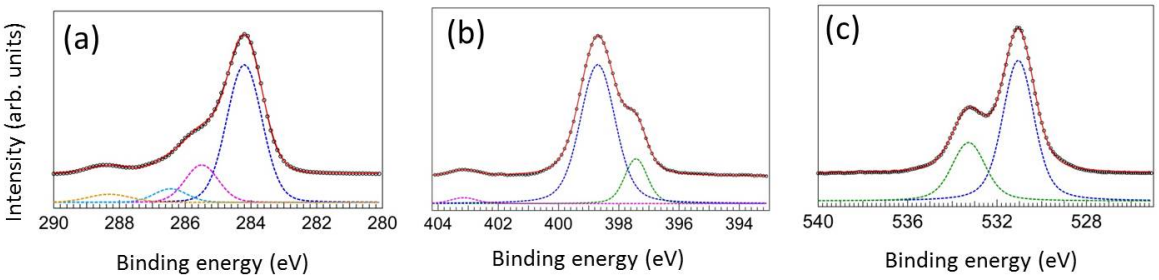

FIGURE 4.18: XP spectra (dots) and respective fitting (red continuous lines) of (a) C 1s, (b) N 1s, and (c) O 1s core levels of a 4-CBA monolayer on Co(0001). The fitted curves are superimposed onto the experimental data, with different colours corresponding to different components. The C 1s, N 1s and O 1s spectra were recorded at a photon energy of 400 eV, 500 eV and 650 eV, respectively.

TABLE 4.5: Resonances at the N K-edge and respective assignments.

resonance	**photon energy (eV)**	**assignment**
1	398.6	CN π^* out of plane
2	399.7	CN π^* in plane
3	401.2	CN π^* out of plane

SAM are presented in Fig. 4.19. The C K-edge spectrum in Fig. 4.19 (a) displays several absorption resonances at 284.8 eV, 286.7 eV and 288.1 eV. The peak at 284.8 eV is assigned to the $1\pi^*$ resonance of the phenyl ring, and the corresponding $2\pi^*$ resonance, lying only 270 meV above the $1\pi^*$ orbital, appears as a shoulder on the high energy side of the $1\pi^*$ absorption peak [107]. The resonances at 286.7 eV and 288.1 eV can be associated to the nitrile and carboxyl groups, respectively [130]. The most pronounced features of the O K-edge spectrum (Fig. 4.19 (b)) are at 531.9 eV and 534.4 eV, corresponding to transitions from the chemically distinct oxygen species bonded bidentately and in the canted form to the unoccupied $2\pi^*$ orbitals.

Finally, the N K-edge spectrum (Fig. 4.19 (c)) shows three distinct features centered at 398.6 eV, 399.7 eV and 401.2 eV, respectively. Their positions and assignments are summarized in Table 4.5. All these features can be associated with π^* excitations of the cyano group; they appear only when the cyano group is electrically coupled to the π^* system of the phenyl ring, which can be regarded as a characteristic fingerprint of the intact molecule in good agreement with previous work [9, 122, 124, 130, 135]. The double resonance ($\pi_1{}^*$ and $\pi_3{}^*$) is related to the conjugation between the π^* orbitals of the nitrile group and the adjacent phenyl

ring, resulting in two orthogonal π^* orbitals with different energies oriented either perpendicular ($\pi_1{}^*$) or parallel ($\pi_3{}^*$) to the ring plane. Therefore, the feature at 398.6 eV and 399.7 eV can be respectively assigned to the transition from N 1s into the out-of-plane $\pi_1{}^*$ and in-plane $\pi_3{}^*$ orbitals, while the resonance at 401.2 eV can be associated to the out-of-plane $\pi_4{}^*$ orbital of the cyano group [130]. The inset of Fig. 4.19 (c) shows the difference spectrum acquired at A_{xy} and A_z polarizations ($A_{xy} - A_z$), and the positive sign of the $\pi_1{}^*$ and $\pi_3{}^*$ dichroism suggests that the respective orbitals are both oriented largely parallel to the substrate. This points to molecules standing up on the surface in the monolayer. Fig. 4.19 (d) shows the NEXAFS spectrum of 4-CBA multilayer. The appearance of the three most pronounced π^* resonances demonstrates the integrity of the molecule. Interestingly, the suppression of the out-of-plane $\pi_1{}^*$ and $\pi_4{}^*$ resonances of the nitrile group under A_{xy} polarization indicates that the respective orbitals orient perpendicular to the substrate, i.e., in the multilayer the molecules tend to align flat.

The C and O K-edge spectra of the monolayer exhibit similar linear dichroism. The slightly weaker intensity of the π^* resonances under A_z polarizations indicates that the majority of the molecules lie with the phenyl ring and the C-OO plane tilted away from the surface, considering that the TDMs of the π^* resonances are all oriented perpendicular to the molecular axis. Quantitative analysis yields an average tilt angle of 36° relative to the surface normal, but XPS data have shown that not all the molecules are bonded in the bidentate form and this might result in a larger degree of disorder compared to the 4-FBA/Co(0001) SAMs.

The exact molecular orientation is described by two angles, the tilt angle of the molecular axis (β) and the twist angle (γ) of the aromatic backbone with respect to the plane spanned by the surface normal and the molecular axis, as drawn in Fig 4.20 (a) following the notation of Ref. [127]. With the known orientation of TDM (angle α) based on equation 2.9, the molecular tilt angle (β) can be generally estimated with the relationship $\cos(\alpha) = sin(\beta)cos(\gamma)$, where an empirical assumption of the twist angle is made [127]. For SAMs with cyano endgroup, it was proven that the twist angle can be accurately determined without such an assumption of twist angle due to the orthogonal orientation of the $\pi_1{}^*$ and $\pi_3{}^*$ orbitals of the cyano group with respect to the backbone [130]. By solving the following two equations [127], the twist angles can be easily determined:

$$\cos(\alpha_1) = sin(\beta)cos(\gamma) \tag{4.1}$$

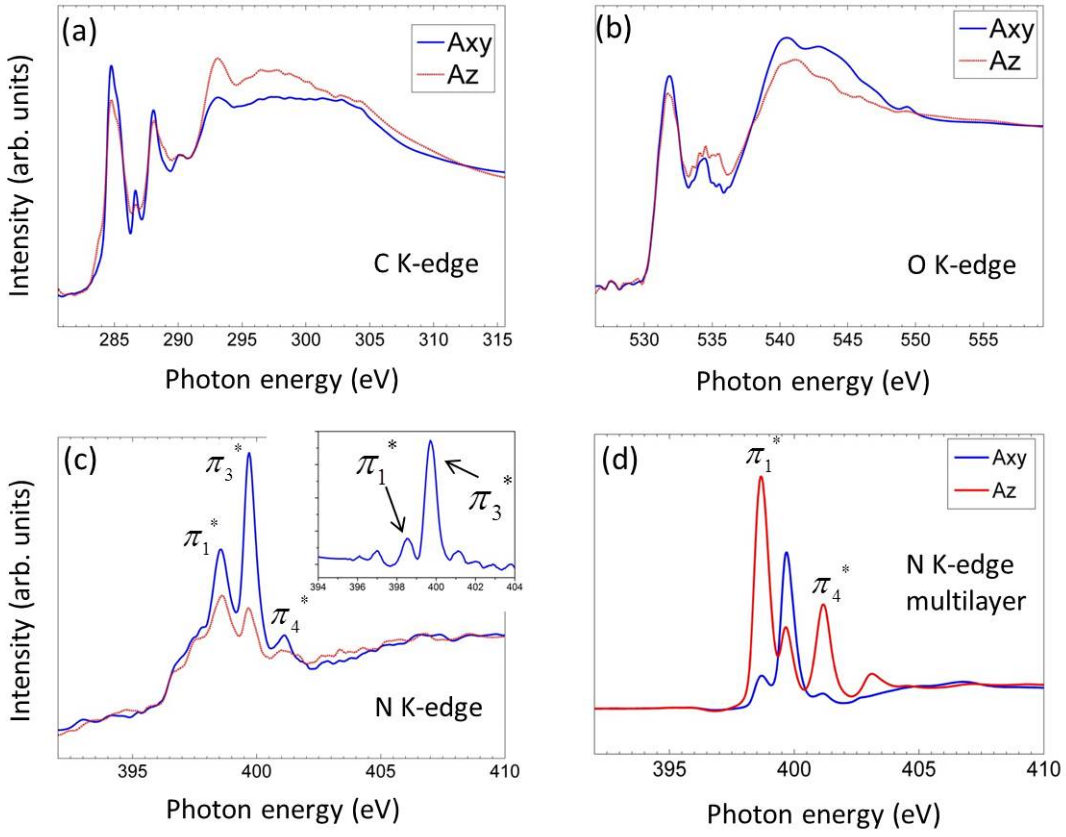

FIGURE 4.19: NEXAFS spectra at the (a) C K-edge, (b) O K-edge and (c) N K-edge of a 4-CBA monolayer for two different polarizations corresponding to the electric field vector of the radiation parallel (A_z) or perpendicular (A_{xy}) to the surface normal. The inset of (c) shows the difference spectrum of A_{xy} and A_z polarizations (A_{xy} - A_z). (d) NEXAFS spectra at the N K-edge of a 4-CBA multilayer.

$$\cos(\alpha_3) = sin(\beta)cos(\pi/2 - \gamma) \tag{4.2}$$

where α_1 and α_3 denote the TDM orientation of the $\pi_1{}^*$ and $\pi_3{}^*$ orbitals and can be determined with equation 2.9. In addition, the obtained twist angle from the N K-edge spectra can be included in the analysis of the π^* resonances of the C and O K-edge. The twist angle was calculated to be 39°, which is close to the typical value of 32° of aromatic bulk systems and the values (around 40°) estimated by *Ballav et al.* in Ref. [127]. The resulting tilt angle determined from N K-edge spectra is calculated to be 40°, while the C and O K-edge spectra yield a tilt angle of 40° and 38°, respectively, by including the estimated twist angle [2].

[2]Here we can only talk of average values, due to the coexistence of differently oriented molecules (see Fig. 4.20 (b)).

The above analysis indicates that the determined twist angle has very little influence on the result. However, it proves the principle that attachment of a cyano tailgroup can serve as a spectroscopic marker and an additional help to determine the molecular orientation, which is more effective than fluorine tailgroup of 4-FBA SAM for this purpose. Change of tailgroup from fluorine to cyano results in an increase of the tilt angle relative to the surface normal from 20° to 40° by comparison of the 4-FBA/Co(0001) and 4-CBA/Co(0001) SAMs. Furthermore, the mixture of bidentate and monodentate bonding of carboxylic headgroup might be associated with the increased tilt angle, as we speculated on the basis of the XPS data. The hypothetical structure of the 4-CBA SAM emerging from the XPS and NEXAFS data is sketched in Fig. 4.20 (b). The presence of the cyano tailgroup has a negative impact on the order of the SAM in this case; however, the NEXAFS analysis, in particular that of N K-edge, indicates that the majority of the molecules must be in a standing-up configuration. In this regard, a specific question is how the monodentate bonding will influence the charge transfer from tailgroup to substrate.

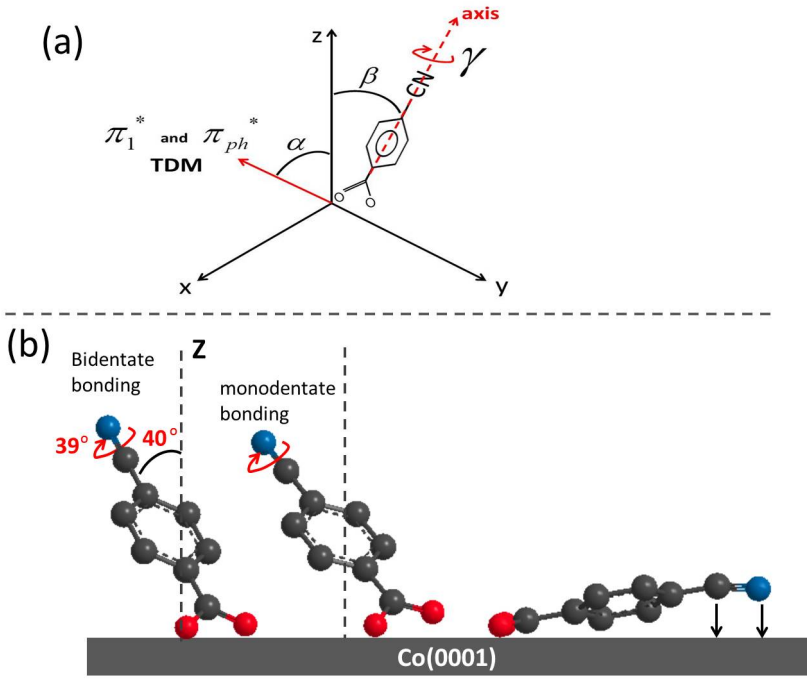

FIGURE 4.20: (a) Schematic drawing showing the angles that describe the exact molecular orientation; the $\pi_1{}^*$ orbitals of the phenyl ring and the nitrile group are collinear and the corresponding TDM is indicated with a red arrow. (b) The hypothetical structure of a 4-CBA SAM based on the XPS and NEXAFS characterization.

TABLE 4.6: Energies of the [N1s]π^* resonances with respect to the Fermi level of cobalt substrate, for a 4-CBA SAM on the Co(0001) surface. With A_{xy} polarization, the minority π^* resonances should be minimized due to the presumably flat-lying geometry.

State of [N1s]π^* orbitals	BE[N1s]	[N1s]π^*	E_{res} = [N1s]π^* - BE[N1s]	
$\pi_1{}^*$ (standing-up CN)	398.7	398.6	-0.1 eV	
$\pi_3{}^*$ (standing-up CN)	398.7	399.7	+1.0 eV	
$\pi_1{}^*$ (rehybridized CN)	397.4	398.6	+1.2 eV	minority
$\pi_3{}^*$ (rehybridized CN)	397.4	399.7	+2.3 eV	minority

4.3.1.2 Charge Transfer Dynamics

Similar to the charge transfer of resonantly excited F 1s electrons to the substrate (discussed in section 4.2.1.3), the charge transfer of resonantly excited N 1s electrons to the substrate can in principle be investigated by analyzing the respective RAES spectra. First of all, the charge transfer to the substrate can only occur when energetically allowed, i.e., the energy of the resonantly excited π^* orbitals ($\pi_1{}^*$ and $\pi_3{}^*$ in our case) of the nitrile group should lie above the Fermi level of the substrate. The requirement can be achieved by comparing the energy of the [N1s]π^* resonance (as determined by NEXAFS) and the binding energy of the N 1s core level (by XPS). We infer that the energy of the [N1s]$\pi_1{}^*$ resonance lies 0.1 eV below the Fermi level of the cobalt film, while that of [N1s]$\pi_3{}^*$ resonance is located 1 eV above the Fermi level. Therefore, electron transfer is energetically allowed for [N1s]$\pi_3{}^*$ resonance, but forbidden for the [N1s]$\pi_1{}^*$ resonance. Note that cyano groups with a N 1s binding energy of 397.4 eV (17% in total) is assigned to the rehybrized states in the previous section, and the corresponding charge transfers are both energetically allowed for this minority species. These estimates are summarized in Table 4.6.

The decay spectra corresponding to [N1s]$\pi_1{}^*$ (upper panel) and [N1s]$\pi_3{}^*$ (bottom panel) resonances are reported in Fig. 4.21 (a). A_{xy} polarization with the electric field of radiation parallel to surface was employed to maximize the decay electron signal (according to the NEXAFS data), and to minimize the signal from the rehybridized CN state. A Shirley-type background as well as the direct photoemission contribution measured about 6 eV below (394 eV in this case) the [N1s]π^* resonance were subtracted from all the decay spectra. The spectrum at the bottom of Fig. 4.21 (a) ("Pure Auger") was acquired at a photon energy of 405.2 eV from the monolayer, representing the pure normal Auger contribution. The spectra at

the top of both panels (pure autoionization channel) were acquired from the multilayer at the [N1s]π_1^* and [N1s]π_3^* resonant energies, providing the lineshapes of the pure autoionization decay channel. The absence of admixture of A1 and A2 features in the "Pure Auto." spectra suggests that no charge transfer occurs in the multilayer. "Mono. decay" denotes the decay spectra of the monolayer measured directly on the maximum of the [N1s]π_1^* and [N1s]π_3^* resonances.

The two broad maxima A1 and A2 of the pure Auger spectrum appear at about 363 eV and 380 eV respectively, and have been assigned to final states with both holes in outer valence orbitals (A1) and holes in outer as well as inner valence orbitals (A2) [124]. Upon resonant [N1s]π_1^* or [N1s]π_3^* excitation, spectator transitions (SP1 and SP2) with 2-hole, 1-electron final states show up in the "mono. decay" spectra. SP1 and SP2 are shifted to higher kinetic energy relative to the A1 and A2 lines due to the so-called "spectator shift" (see section 2.4). Similar to A1 and A2, SP1 and SP2 can be assigned to final states with both holes in outer valence levels (SP1), and one hole in the inner as well as one hole in the outer valence orbitals (SP2). Interestingly, the participator decay lines are largely suppressed in the decay spectrum of [N1s]π_1^* resonance. The fact that same situation occurs for the "Mono. decay" (monolayer) and "Pure Auto." (multilayer) spectra excludes the effect of an orientation since the orientation of the CN group in monolayer and multilayer has been shown to be distinctly different according to the NEXAFS spectra of Fig. 4.19. Previous studies have concluded that the π_1^* orbital is mostly localized on the adjacent phenyl ring, with only a small contribution at the nitrogen site, while the π_3^* orbital resides mostly at the nitrogen site [122, 136]. Based on this fact, Ballav *et al.* ascribed the suppression of the participator lines to the different sites of the three holes involved in the Auger-like transition, namely the initial core vacancy, the vacancy in the π_1^* orbital, and the vacancy left by the other electron taking part in the decay. Conversely, all the three involved vacancies are at one site for the [N1s]π_3^* resonant decay [130].

When comparing the "Mono. decay" spectrum of the [N1s]π_1^* resonance with the "Pure Auger" spectrum, no clear contribution of the normal Auger features can be perceived, suggesting no occurrence of charge transfer within the timescale of the core-hole decay according to the CHC approach. This observation is supported from the energetic point of view, since the [N1s]π_1^* resonance lies below the Fermi level. Note also that the charge transfer in the reverse direction as mentioned in Ref. [8] is excluded in our system. In fact, upon non-resonant excitation (see the

"Pure Auger" spectrum taken at 405.2 eV), transfer of substrate electrons to the π^* orbitals of nitrile would generate final states that are very similar to spectator and participator decay channels. On the other hand, at least the participator lines do not appear in the pure Auger spectrum. As to the [N1s]$\pi_3{}^*$ resonance, the charge transfer is energetically allowed, but the situation is very similar to that of [N1s]$\pi_1{}^*$ resonance in the RAES spectra. There is no contribution of the A2 peak on the low kinetic energy flank of the SP2 peak of the "Mono. decay" spectrum, and the peak profile of A1 is different from the fine structure on the low kinetic energy side of the SP1 peak, which again suggests no occurrence of ultrafast charge transfer. This is illustrated by example of the spectral reconstruction shown in Fig. 4.21 (b), where the reconstructed curves fail to reproduce the important features of the experimental spectra. Therefore, the measured spectrum cannot be satisfactorily reconstructed by linear combination of pure Auger and pure autoionization decay lines.

According to the XPS data, 17% of the cyano tailgroups might hybridize with the substrate and is presumably lying parallel to the surface. For this species, an overwhelming pure Auger decay channel due to ultrafast electron delocalization into the substrate is expected in the RAES spectra (probably with an Auger fraction close to 17%) according to many reported CHC studies [12], and the charge transfer for both $\pi_1{}^*$ and $\pi_3{}^*$ resonances are energetically allowed as shown in Table 4.6. However, this is apparently not the case in the measured RAES spectra, and probably indicates that this specie does not contribute to the RAES spectra since we employed A_{xy} polarization to predominantly excite standing-up cyano groups. On the other hand, as discussed in section 4.2.1.3 with respect to upright 4-FBA/Co(0001) SAMs, the dynamic charge transfer can be associated with a static molecular conductance and be described with an exponential function with attenuation factor β_{ph} ranging from 0.l4 to 0.83 $\mathring{A}^{-1}$. Assuming a similar relationship for the 4-CBA/Co(0001) system as well, the CHC method should be therefore applicable for the standing-up 4-CBA molecules and a contribution of the pure Auger decay channel should be seen in contrast to the experimental evidence.

The lack of normal Auger contribution in RAES spectra was observed in Ref.[130] for biphenylnitrile-based SAMs on Au(111), and it was ascribed to the large attenuation factor introduced by the two phenyl rings, which pushes the charge transfer time beyond the accessible range of the CHC method. A similar situation

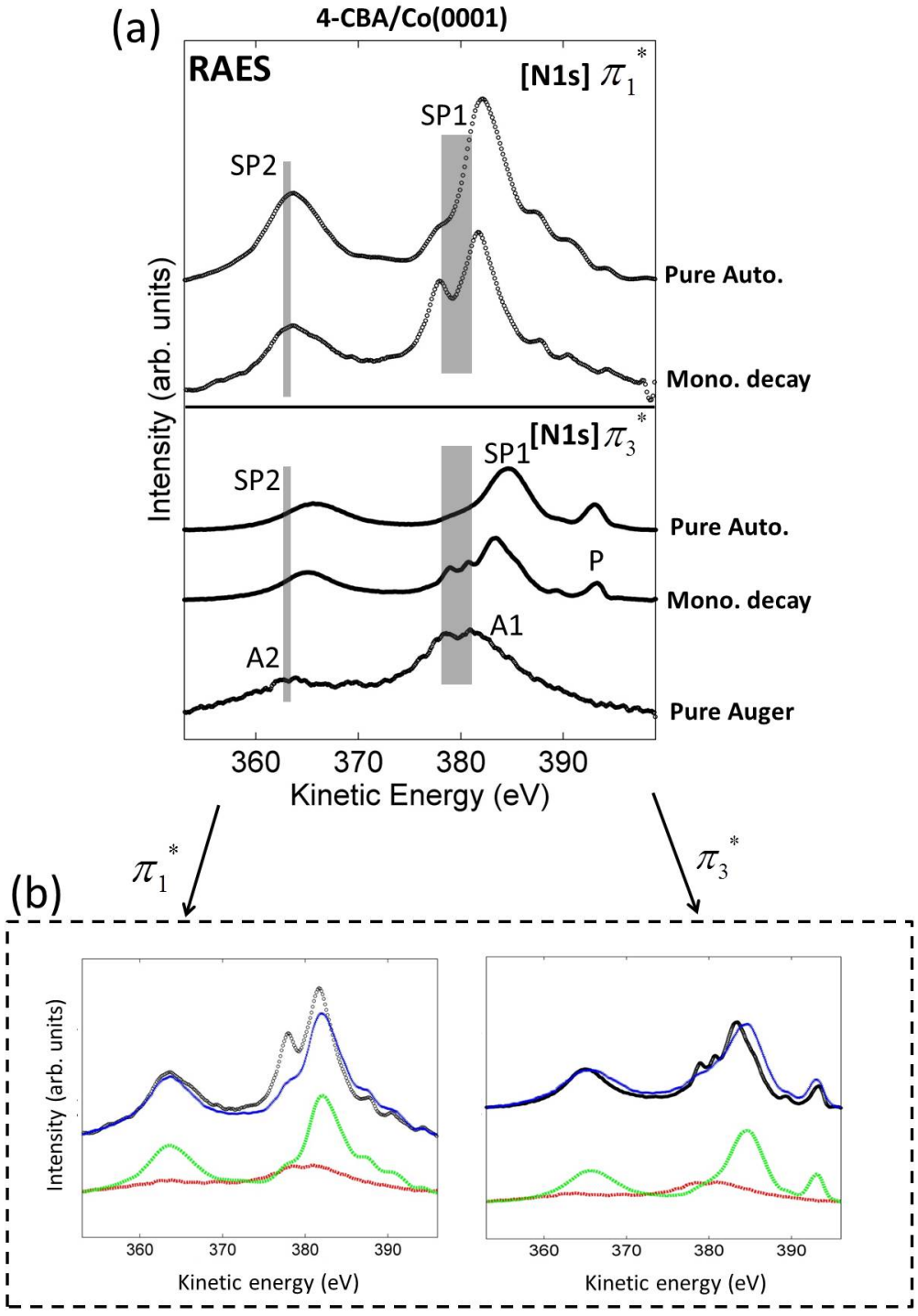

FIGURE 4.21: **(a)** [N1s]π_1^* (top) and [N1s]π_3^* (bottom) RAES spectra of 4-CBA/Co(0001) SAM and multilayer. P, SP1 and SP2 denote the participator and spectator features, while A1 and A2 denotes the features in the pure normal Auger spectrum. "pure Auto." denotes the RAES spectra of a 4-CBA multilayer measured at the respective [N1s]π^* resonance maxima, "Mono.decay" the RAES spectra of monolayer, and "Pure Auger" the normal Auger spectrum measured above the resonance. **(b)** Examples for the failure of the reconstruction (blue lines) for the [N1s]π_1^* (left) and [N1s]π_3^* (right) "Mono. decay" spectra (black circles) by linear combination of "Pure auto." (green dash-dotted lines) and "Pure Auger" (red dash-dotted lines). More details and discussion are included in the text.

was also reported for nitrile terminated SAMs [122, 124]. In Ref. [122], the charge transfer to the Au(111) substrate from π_1^* and π_3^* orbitals of the CN tailgroup of 4-cyanothiolphenol, which has a very similar molecular structure to 4-CBA except for the anchoring group (thiol), was estimated with CHC method. On the other hand, tailgroup-to-substrate charge transfer was observed for 4-FBA in bidentate configuration on Co(0001) (see section 4.2.1.3). This suggests that the absence or presence of charge transfer is critically related to the details of the molecule-to-substrate anchoring. Therefore, for the 4-CBA/Co(0001) SAMs, we may speculate that the coexistence of monodentate and bidentate bonding and the larger degree of disorder in the SAM compared with the 4-FBA/Co(0001) counterpart and with other CN- terminated SAMs on gold hinders the tailgroup-to-substrate charge transfer.

4.3.2 4-CBA/Co(0001): Conclusions

The 4-CBA SAM was prepared under UHV conditions on the Co(0001) surface and characterized by means of XPS, NEXAFS and RAES spectroscopy. A mixture of monodentate and bidentate bonding of the carboxylic headgroup with cobalt as well as a minority CN state stemming from hybridization with cobalt was found in XPS, pointing to larger disorder of the SAM compared with the 4-FBA/Co(0001) analogue. This was attributed to the presence of the CN tailgroup, which has stronger interaction with the substrate than the fluorine tailgroup. However, the nitrile group can be employed as a spectroscopic marker to derive both tilt and twist angles of the molecule by means of NEXAFS due to the presence of orthogonal π_1^* and π_3^* orbitals. According to the NEXAFS data, the molecule in the SAM are predominantly adsorbed in a standing-up configuration, and the majority (82%) of the CN groups are located at the SAM-vacuum interface, albeit with a larger tilt angle (40°) than for 4-FBA (20°) relative to the surface normal.

No tailgroup-to-substrate charge transfer could be evidenced from the RAES spectra for both [N1s]π_1^* and [N1s]π_3^* resonances. Charge transfer following [N1s]π_1^* excitation is energetically forbidden, whereas it is in principle energetically allowed in the case of [N1s]π_3^* excitation. The monodentate bonding of the headgroup with cobalt and the increased SAM disorder compared with the 4-FBA/Co(0001) SAM can probably explain the absence of charge transfer.

Compared with the 4-FBA SAM on the same surface, the change of tailgroup from fluorine to the nitrile has a large impact not only on the SAM structure, but also on the charge transfer dynamics. This significant change remarks the importance of the tailgroup in determining the properties of the SAM. In the following section, the headgroup of the 4-FBA SAM will be changed from carboxylic to the most studied thiol group to shed light on the effect of the headgroup on the surface properties of the SAM.

4.4 4-Fluorothiophenol SAMs on Co(0001)

4.4.1 Introduction

SAMs of organic molecules with well-defined structure are relevant to various important interfacial processes, e.g., corrosion, adhesion, wettability, and charge transfer across interfaces [2, 12]. The formation of thiolate bonded SAMs on metal surfaces has attracted considerable attention during the past two decades owing to the high affinity of the thiol headgroup to metals [1]. In particular, thiolate bonded SAMs on gold surfaces have been regarded as a prototypical systems owing to the robust Au-S anchoring that leads to room temperature stable SAMs [1]. The interface region dominates the electron tunnelling process and a better control of the interfacial structure is expected to improve the charge transport performances, as highlighted in the last two sections concerning 4-FBA and 4-CBA monolayers on Co(0001). The Au-S bonding has been reported to be favourable for ultrafast interfacial electron transfer [9, 135], and this process was found to depend critically on the molecular configuration. For example, in the work of Wang *et al.*, ultrafast charge transfer was observed for molecules lying down on a gold surface and attributed to the delocalization of the molecular orbitals into the gold substrate [11].

Caruso *et al.* suggested that the thiolate bonding to cobalt surfaces is stronger compared to that on gold surfaces [4, 137]. It is therefore important to probe in a detailed fashion the bonding mechanism, structure, stability and interfacial charge transfer of thiolate SAMs on cobalt surfaces, since cobalt has a broad range of applications, e.g., in magnetic recording, information storage and catalysis *etc.* [138, 139]. To date, the number of reports on the formation of SAMs on cobalt

surfaces is very limited due to the strongly oxidizable nature of cobalt metal, which requires either pretreatment of the substrate by electrochemical routes prior to SAM adsorption or a highly controlled UHV environment to achieve an oxide-free surfaces [4, 140, 141]. Moreover, to the best of our knowledge, the charge transfer dynamics at the cobalt/SAM interface remains completely unexplored.

In this section, 4-fluorothiophenol (4-FTP) multilayers, the saturated monolayer, as well as layers in the intermediate coverage regime were prepared on Co(0001) under UHV conditions. The electronic structure and adsorption geometry of the layer is investigated with synchrotron-based spectroscopic techniques, i.e., XPS and NEXAFS. The tailgroup (fluorine) to substrate charge transfer dynamics is studied by analysis of the RAES spectra and the characteristic charge transfer time is derived with the CHC approach. Thiolate-bonded SAMs were reported to exhibit a poor thermal stability on ferromagnetic substrates due to the increased metal-S bond strength, with C-S bond cleavage occurring at low temperature, e.g., 190 K in Ref. [71] and 200 K in Ref. [133]. This results in detectable amounts of atomic sulfur on the surface and thus complicates the analysis [71]. To avoid the unwanted byproduct of atomic sulfur, an alternative procedure was applied in this work, consisting in the SAM preparation at 80 K by incremental dose of 4-FTP up to monolayer completion with multiple steps, as compared with the standard approach based on the annealing at 190 K of a 4-FTP multilayer in a single step. A precise control of the 4-FTP vapor flux is necessary, since during the growth the layer is held at 80 K, where the generation of atomic sulfur can be hindered [71, 133].

4.4.2 Experimental Results and Discussion

Experimental Methods The experiments were performed in the same UHV chamber and the same beamline used for 4-FBA and 4-CBA SAMs on Co(0001), which facilitates direct comparison of the results. The Co(0001) surface was prepared by evaporating cobalt films on a clean W(110) crystal, and the cleanliness as well as the crystalline quality were checked with XPS and LEED, respectively. Prior to dosing, 4-FTP liquid (Sigma-Aldrich, 98% purity) was purified by several freeze-pump-thaw cycles. 4-FTP was deposited directly onto the cobalt surface at 80 K via a stainless steel tube and a leak valve controlled by compressed gas. The exposure of the substrate to 4-FTP can be precisely controlled via an ion-gauge

flux monitor, which facilitated reproducible deposition, and is expressed in Torr*s unit. Two different preparation protocols for the SAM were used, either by incremental deposition of 4-FTP or by annealing of the 4-FTP multilayer (standard approach). In both cases the substrate was held at 80 K when exposed to the 4-FTP vapors. The TPD spectrum of the 4-FTP multilayer recorded at a heating rate of 2K/s shows a pronounced desorption peak at ca. 190 K, as illustrated in Fig. 4.22. Therefore, a 4-FTP SAM can in principle be prepared by annealing the condensed multilayer to 190 K for a few seconds, based on the standard approach. All the XPS and NEXAFS measurements were performed at 80 K. The sample area was scanned with a motor during the measurements, and the photon flux was reduced appropriately to prevent beam damage.

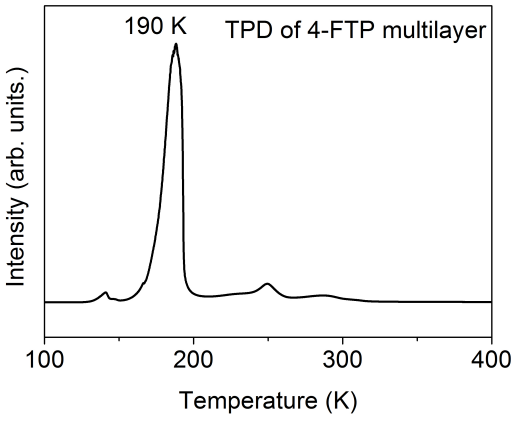

FIGURE 4.22: TPD spectrum from a 4-FTP multilayer corresponding to the mass/charge ratio of the intact 4-FTP molecule upon double ionization and acquired with a heating rate of 2 K/s. The multilayer layer was condensed at 80 K and the desorption peak is centered at 190 K.

4.4.2.1 4-FTP/Co(0001) Multilayer

Thick Multilayer First of all, a multilayer was condensed at 80 K and Fig. 4.23 displays photoemission spectra from the C 1s, F 1s and S 2p core levels. In the C 1s spectrum, the deconvolution shows three peaks with very different intensity. The most pronounced line at about 284.6 eV corresponds to the C-H carbons of the phenyl ring, while the one at 286.6 eV (chemically shifted by ca. 2.0 eV relative to the C-H carbon line) belongs to the fluorinated carbon (C-F). Finally, the weak feature at 285.45 eV can be similarly assigned to the chemically shifted C-S carbon [142, 143]. Note that the C-S carbon only accounts for 3% of

the overall signal, with a strong deviation from the stoichiometric ratio of 4:1:1. This is presumably due to attenuation of the emitted photoelectrons, which was also observed in the photoemission from the S 2p level of thiolate bonded SAMs by Delamarche *et al* [144]. Moreover, the exposure required for preparing the single layer of thiolate with the incremental deposition approach is later estimated to be 0.035 Torr*s, whereas the multilayer herein resulted from an exposure of 0.3 Torr*s. This corresponds to a relatively thick mulitlayer. The thickness of the multilayer is estimated to be 18.5 $\mathring{A}$ based on the attenuation of the $Co\,2p_{3/2}$ core level, according to the relationship $I = I_0 \exp(-d/\lambda)$ [145], where I_0 and I are the intensities of Co 2p line before and after adsorption of a layer of thickness d, and λ is the inelastic mean free path of electrons with kinetic energy of approximately 150 eV (the photon energy used was 950 eV). We can therefore assume that the thick multilayer also contributes to the attenuation with scattering and/or diffraction effects. The F 1s core level shows a single peak at 686.9 eV, as expected for the intact molecule. Instead, the S 2p spectrum exhibits a doublet structure due to the presence of the spin-orbit split $S\,2p_{3/2}$ and $S\,2p_{1/2}$ components. The lineshape was fitted using a 2:1 peak area ratio and ca. 1.2 eV splitting. For simplicity, only the binding energy of the $S2p_{3/2}$ peak will be given in the following analysis. In the S 2p spectrum, two doublets can be discerned, at 163.55 eV and 162.3 eV, respectively. According to previous literature [124, 129, 146], the typical binding energy of $S\,2p_{3/2}$ for unbound thiols lies between ca. 163 and 164 eV, and shifts to a lower binding energy of approximately 162 eV after deprotonation of the S-H group followed by formation of a thiolate bond. Therefore, the two components are representative of unbound thiols (80%) and phenyl thiolate (20%), respectively. No atomic sulfur with binding energy lower than 162 eV and no oxidized sulfur species (such as sulfonates) with binding energy higher than 166 eV can be detected in the multilayer, indicative of oxygen-free environment during both preparation and measurements.

Stability of the Co-S Bond According to the TPD spectrum of a 4-FTP multilayer shown in Fig. 4.22, a 4-FTP monolayer can in principle be prepared by annealing off the thick multilayer at 190 K. Whether C-S bond breaking occurs upon further annealing primarily determines the stability of the thiolate bonding. Fig. 4.24 presents S 2p core-level spectra recorded after sequential annealing of a 4-FTP multilayer to increasing temperatures for ca. 60 s each time. The curve remains largely unchanged by annealing from 80 K to 160 K. At 190 K, where the

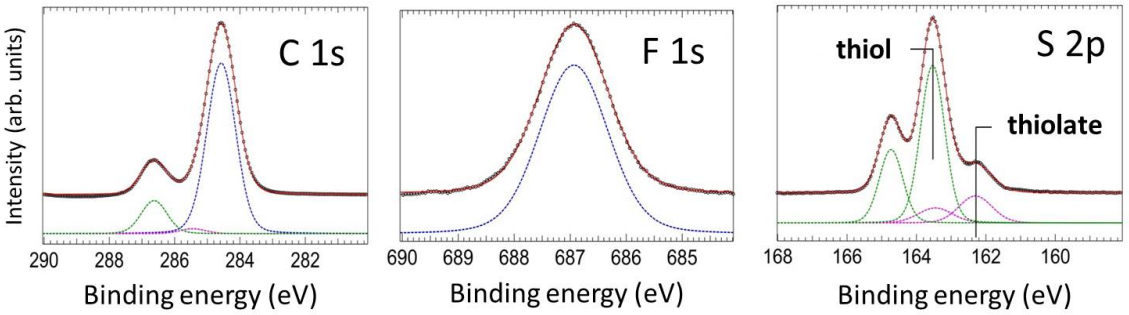

FIGURE 4.23: X-ray photoelectron spectra of the C 1s, F 1s and S 2p core levels from a relatively thick 4-FTP multilayer (0.3 Torr*s) on Co(0001). The fitted curves (red lines) are superimposed on the experimental data (dots), and the decomposition into individual components is shown below the spectra.

curve should correspond to a saturated monolayer based on the standard preparation approach and the TPD data, the thiol component decreases dramatically, and a very small fraction of atomic sulfur also appears. At higher temperatures, the unbound thiol component totally vanishes, while the atomic sulfur and thiolate components both increase. The thiolate and atomic sulfur peaks are relatively broad and asymmetric at and above 190 K, suggesting that there are possibly additional states at slightly different binding energies, since the $S\,2p_{3/2}$ binding energies are known to be different in high- and low-coordination sites [72, 129]. An alternative explanation is that reconstruction of Co(0001) surface takes place and results in multiple adsorption sites on an inhomogeneous surface, as observed for methanethiolate and co-adsorbed atomic sulfur at 250 K on the Ni(111) surface [72]. Therefore, the main conclusion based on Fig. 4.24 is that desorption of the multilayer becomes prominent at 190 K (with a major thiolate component of the first layer that coexists with a small fraction of unbound thiol), but the C-S bond breaking also starts at 190 K. Elevated temperatures can remove the residual unbound thiols, but thiolate and atomic sulfur hence populate different adsorption sites, resulting in asymmetric and broad spectroscopic features.

Thin Multilayer As a reference, a much thinner multilayer corresponding to an exposure of 0.05 Torr*s was prepared at 80 K. Fig. 4.25 (left panel) presents the XP spectra of this system; the binding energies and the relative intensities obtained from the respective fits are summarized in Table 4.7. All the carbon species are shifted to lower binding energies owing to increased screening of the core hole by the metal substrate compared with the thick multilayer. An additional weak

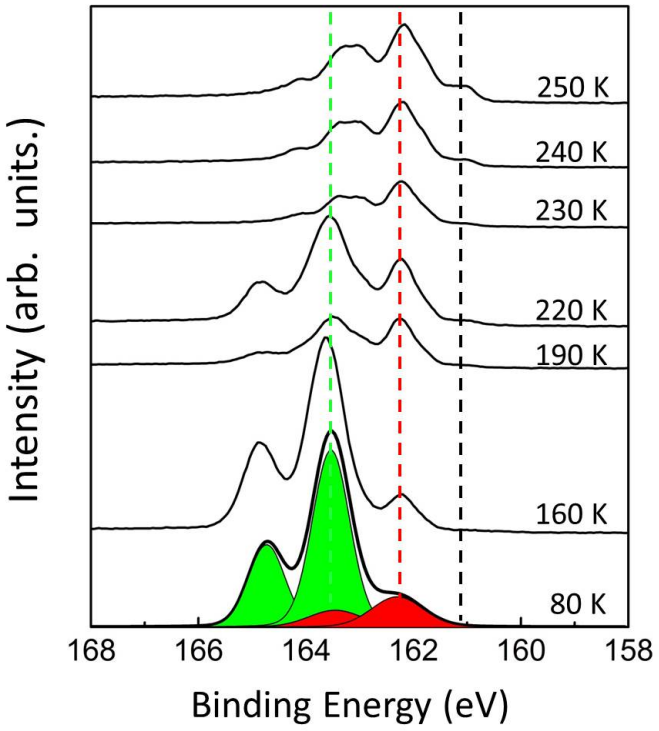

FIGURE 4.24: XP spectra of the S 2p core level from a 4-FTP/Co(0001) thick multilayer upon annealing to increasing temperatures for ca. 60 s. The thiol (green) and thiolate (red) components of the initial multilayer at 80 K are marked by vertical dotted lines, while the black dotted lines indicate the position of atomic sulfur. The photon energy used for recording the spectra was 260 eV.

component at ca. 287.2 eV appears as a weak shoulder, and might stem from shake-up processes or minority species on the surface [143]. Interestingly, the emission from the C-S carbon (18%) increases significantly compared with that of the thick multilayer (3%). Considering the intensity of the C-H (62%) and C-F (16%) carbons, the expected stoichiometry of 4:1:1 is correctly reproduced. Therefore, the attenuation of the C-S carbon in the thick multilayer is most probably related to the layer thickness. In the spectrum of the S 2p core level, approximately 66% of the thiols form thiolate bonds with cobalt while 34% remains weakly bound. This is much less than the amount of unbound thiols (80%) in the thick multilayer. It is therefore inferred that this thin multilayer is close to a saturated monolayer, where most of the molecules are anchored through the thiolate bond at the organic-metal interface. Importantly, no atomic sulfur was observed in both the thick and thin multilayer.

TABLE 4.7: BE positions and area ratios of individual C 1s, F 1s and S 2p components. From left to right: thick multilayer, thin multilayer, the same thin multilayer annealed at 240 K for ca. 30 s, monolayer and submonolayer films. Only the BE of $S\,2p_{3/2}$ is given for simplicity.

	Thick Multi.	Thin Multi.	Thin Multi.(240K)	Mono.	Submono.
C-H	284.55 (84%)	284.3 (62%)	284.3 (79%)	284.3 (68%)	284.2 (72%)
C-S	285.45 (3%)	284.9 (18%)	285.0 (6%)	285.0 (14%)	285.0 (10%)
C-F	286.65 (13%)	286.3 (16%)	286.3 (14%)	286.25 (16%)	286.2 (16%)
Fluorine (F1s)	686.95	687.0	686.85	686.8	686.75
Thiol	163.55 (80%)	163.5 (34%)	163.1 (33%)	163.5 (17%)	163.5 (7%)
Thiolate	162.3 (20%)	162.2 (66%)	162.05 (56%)	162.2 (83%)	162.25 (93%)
Atomic S	-	-	161.05 (11%)	-	-

Fig. 4.25 (right panel) also shows the spectra after annealing of this 4-FTP thin multilayer to 240 K for ca. 30 s. The three main carbon species are only marginally changed in binding energy but the area ratio of C-S carbon emission is decreased to 6% while that of aromatic C-H carbon increases to 79%. The F 1s peak is shifted by -0.l4 eV to 686.85 eV, and this can originate from the different screening of the metal substrate. The most dramatic change occurs in the S 2p spectrum both in terms of the binding energies and relative intensities of the sulfur species. A new S 2p doublet now appears at 161.05 eV, assigned to atomic sulfur following C-S bond breaking and with a relative population of 11%. According to previous literature [142, 143, 147], the doublet at 161.05 eV can be assigned to either atomic sulfur or to a differently bonded sulfur, and the latter assignment was often observed to appear at the early stages of the assembly for low packing densities. Since this doublet is absent in the submonolayer film and only appears upon annealing in our case, the former assignment is by far the most likely one. The binding energies of thiolate and unbound thiol are shifted by -0.13 and -0.42 eV, respectively, and after annealing, the reduction of the thiolate component by 10% is compensated by the generation of atomic sulfur. Compared with the thin multilayer as deposited, the lower binding energy is presumably due to the smaller average spacing between the excited hole and the metal substrate after annealing, which results in increased screening. Note also that the co-adsorbed atomic sulfur can induce restructuring of the metal surface as mentioned above, but this effect generally shifts the binding energy in the other direction. Furthermore, the production of atomic sulfur can explain to some extent the decreased photoemission from the C-S carbon (by approximately 12%) and the stronger relative intensity of aromatic C-H carbon (due to the fragments remaining on the surfaces).

Summarizing the results described above, the physisorbed part of a 4-FTP thick multilayer on Co(0001) surface cannot be effectively desorbed by annealing to

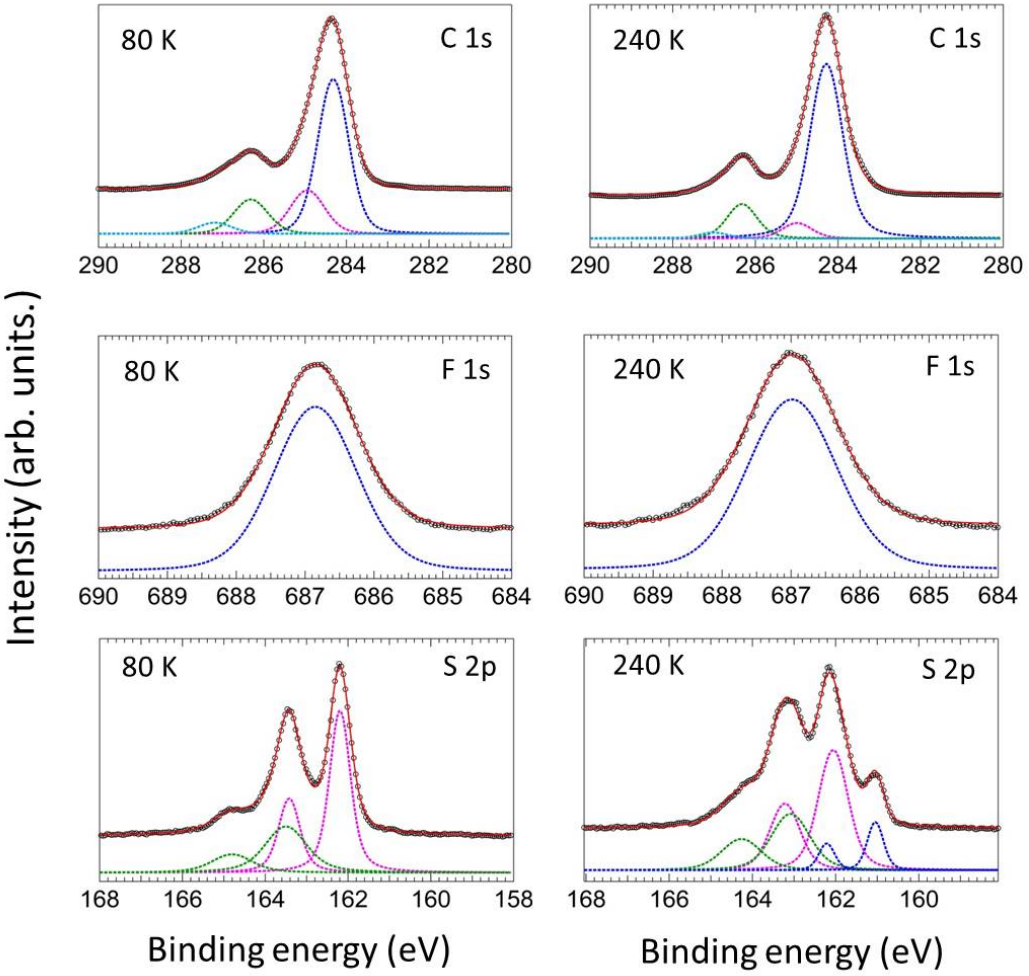

FIGURE 4.25: (Left) XP spectra (circles) and respective curve-fitting (red lines) of a 4-FTP/Co(0001) thin multilayer (0.05 Torr*s) adsorbed at 80 K. The results of curve-fitting decomposition analysis are shown below and the attribution of different components is discussed in the text. (Right) XP spectra of the same thin multilayer annealed at 240 K for ca. 30 s. The core level spectra of C 1s, F 1s and S 2p were recorded at a photon energy of 400 eV, 800 eV and 260 eV, respectively.

create a single monolayer without production of atomic sulfur. Annealing a thinner multilayer to comparable temperatures leaves more atomic sulfur and unbound thiol on the surface. The co-existence of atomic sulfur, unbound thiol, as well as differently bound thiolate largely hinders a reliable comparison of results from separate preparations. In addition, the results also indicate that atomic-sulfur generation can be hindered at low temperature, where the low binding energy component at ca. 161 eV is quenched. Therefore, an alternative approach based on incremental doses of 4-FTP at 80 K up to monolayer completion will be presented in the following subsection.

4.4.2.2 4-FTP/Co(0001) Monolayer and Lower Coverage

Monolayer Following the incremental deposition approach, a monolayer was adsorbed at 80 K with multiple steps until the thiolate S 2p component reaches saturation and the deposition is stopped right before the emergence of the unbound thiol S 2p doublet. This can be controlled by monitoring the $S\,2p_{1/2}$ peak of unbound thiol at ca. 164.7 eV (since it does not overlap with any other S 2p components). We also note that subsequent doses were separated by ca. 5 min intervals to allow for a fast XPS characterization as well as for the adsorbed molecules to reach the thermodynamic equilibrium. The series of XP spectra in the left panel of Fig. 4.26 shows the outcome of the procedure of monolayer preparation with each incremental step corresponding to an exposure of 0.005 Torr*s; the XPS data and curve fitting of the saturated monolayer that corresponds to a total exposure of 0.035 Torr*s are shown in the right panels. In the evolution of the C 1s and S 2p spectra, the binding energies do not shift in the whole process, indicating that the vast majority of the adsorbed molecules form thiolate bond (as noted above, physisorbed molecules result in higher binding energy values). Instead, the F 1s core level is shifted by -0.2 eV at the end of the sequential deposition, and this is most probably due to stronger screening by the substrate stemming from a slight adjustment of the molecular configuration [142]. From the curve-fitting of the XPS data, the three carbon components roughly comply with the carbon stoichiometry of 4:1:1 except that the intensity of C-S carbon peaks is a bit lower probably due to electron attenuation through the film [144]. The binding energy of the F 1s level is on average only 0.15 eV lower than that of the multilayer, indicating that the F atom does not undergo a drastic change of chemical environment and is not directly interacting with the surface. More than 80% of the sulfur is bonded via the thiolate anchor to the cobalt surface, and no atomic sulfur is detected. Note that, even for the densely packed layer assembled from solution, unbound thiol molecules are sometimes observed and hard to wash off [140, 146], and this is also the case here. Nonetheless, the XPS data demonstrates the feasibility of this approach for preparing a well-defined thiolate monolayer free of atomic S on the cobalt surface.

The NEXAFS spectra of the 4-FTP monolayer in the top panel of Fig. 4.27 elucidate the adsorption geometry of the molecules in a direct way. The C K-edge spectra of the 4-FTP monolayer exhibit a strong linear dichroism. The sharp

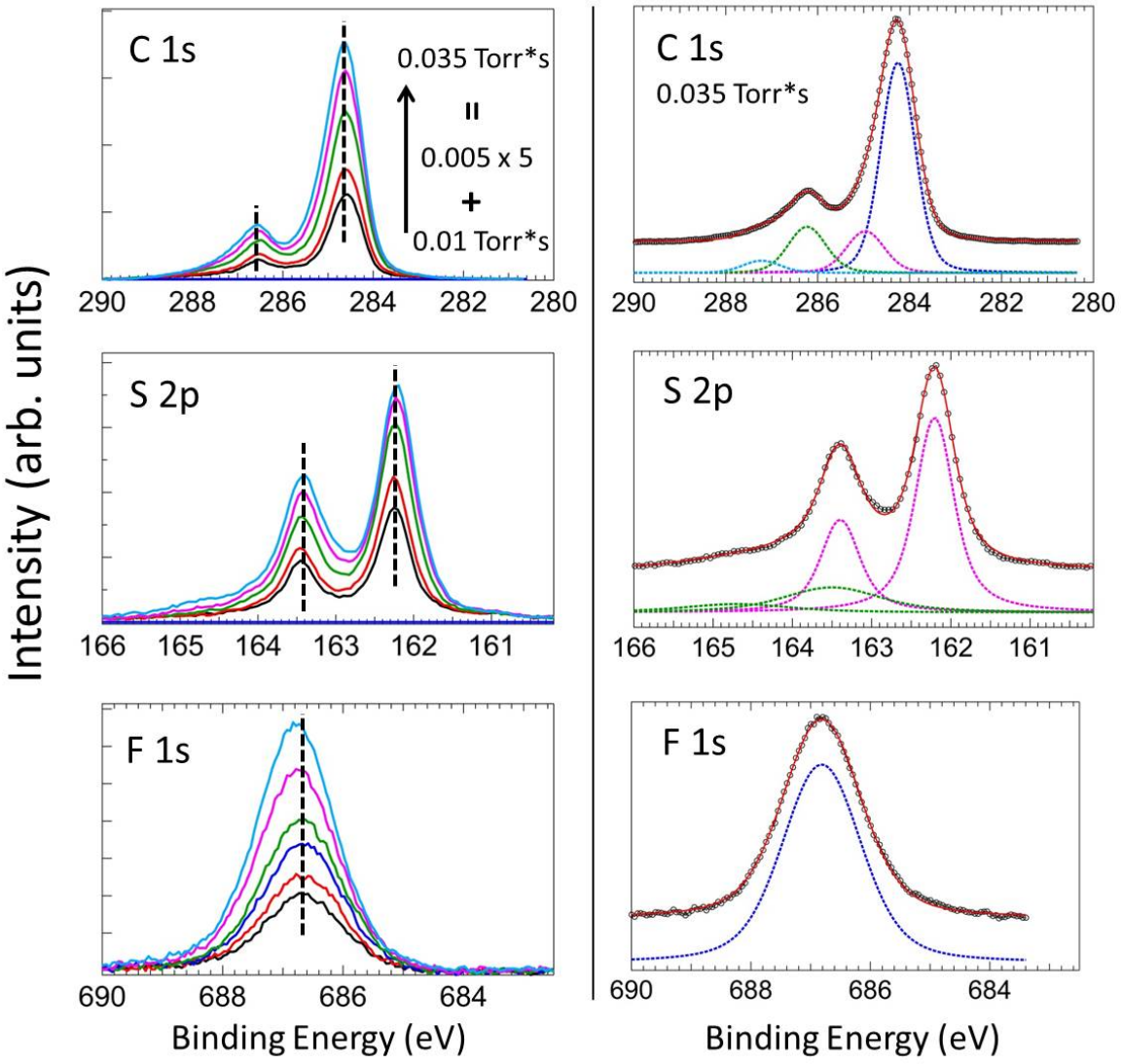

FIGURE 4.26: (Left) Evolution of C 1s, F 1s and S 2p core-level XP spectra with increasing exposure from 0.01 Torr*s to 0.035 Torr*s. (Right) XP spectra (circles) and respective fittings (red lines) of the 4-FTP/Co(0001) saturated monolayer (0.035 Torr*s) corresponding to the last step of the incremental deposition in the left panels.

features below 290 eV are predominantly transitions from C 1s electrons of inequivalent carbon species into the LUMO of π^* character, while those above 290 eV are dominated by the so- called shape resonances with σ^* character, as indicated by the reversed dichroism relative to the π^*-type resonances [11, 106, 107]. The observation that the π^* resonances are strongly quenched for A_{xy} polarization, when the electric field of the radiation is perpendicular to the surface normal, clearly demonstrates a predominantly flat-lying orientation of the molecules in the monolayer. However, the residual π^* intensity at A_z polarization shows that the

molecules are not completely flat, that is a tilt angle of approximately 70° relative to the surface normal can be estimated by quantitative analysis of the NEXAFS spectra. The polarization-dependent linear dichroism in the F K-edge spectra is reversed with respect to that at the C K-edge, and the suppression of resonant features with A_z polarization suggests the dominance of σ^* type resonances and a flat-lying orientation of the C-F bond, in agreement with previous literature [108]. The detailed assignment of F K-edge signatures is, however, hampered due to the significant overlap in energy of π^* and σ^* orbitals, in contrast to the C K-edge where the LUMO features at the lowest energies stem solely from π^* states [108]. Note also that the linear dichroism of C and F K-edge spectra are both reversed with respect to the 4-FBA/Co(0001) system (section 4.2.1), where the molecules in the monolayer adopt an upright configuration.

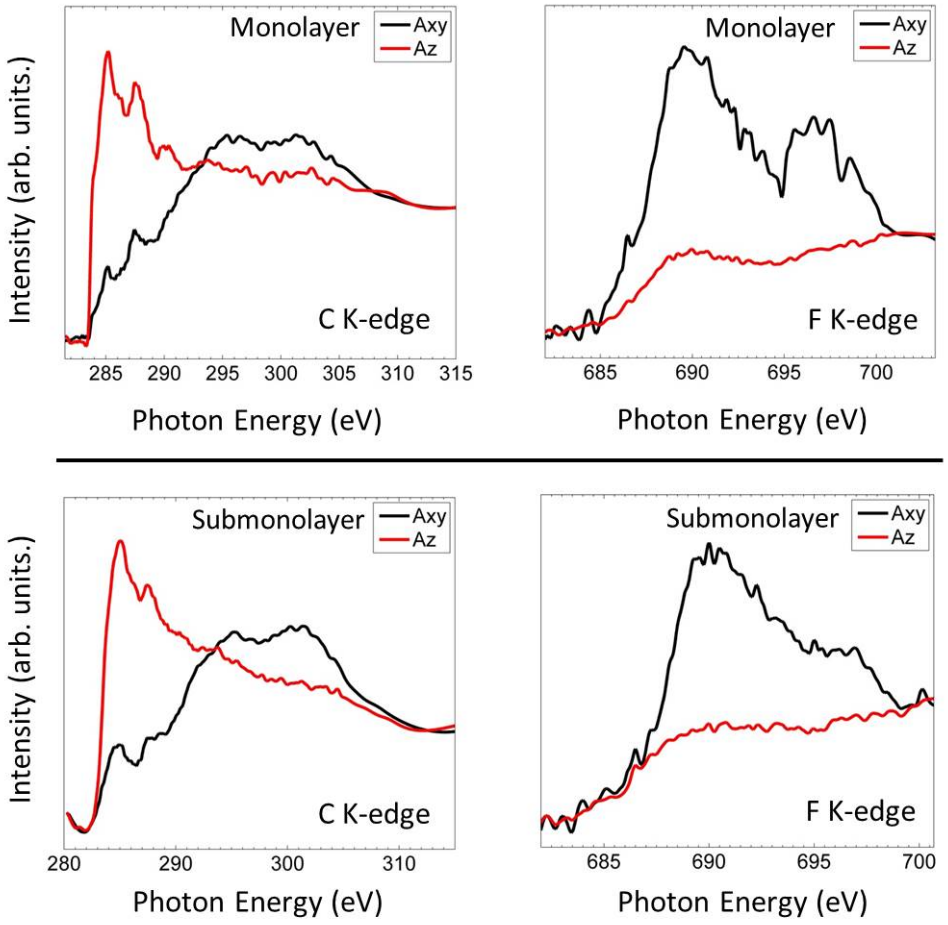

FIGURE 4.27: NEXAFS spectra of the 4-FTP/Co(0001) monolayer (top) and submonolayer film (bottom) at the C and F K-edges for two orthogonal measurement geometries, corresponding to electric field of the radiation almost parallel (A_z) or perpendicular (A_{xy}) to the surface normal.

Previous work by Wang *et al.* [11] on the same molecule on a gold surface found that the 4-FTP monolayer prepared by immersion in solution adopts an upright configuration, while that prepared by vapor-phase deposition in UHV contains molecules with flat-lying orientation. This is in agreement with our work except that the 4-FTP monolayer on gold surface via vapor-phase deposition is stable at room temperature. The lying-down phase (sometimes called striped phase) of thiolate monolayer on gold surfaces was also observed elsewhere either by direct vapor-phase dosing or by thermal annealing of a densely packed SAM prepared from solution [77, 88, 89, 92]. The striped phase with lying-down orientation is generally obtained in the initial stages of the vapor-phase dosing at low packing density and it can convert into the upright full-coverage phase with increasing coverage[92]. Notably, the lying-down phase can be under some circumstances very stable and do not evolve further even with increasing coverage [93]. This has been explained in terms of minimization of van der Waals and covalent bond energy [54, 92]. In our case, a similar behaviour is observed, and only more unbound thiol is generated by further increasing the coverage. As mentioned in section 4.1, the structure (e.g., bonding and orientation) of the intermediate phases that correspond to coverage below the monolayer still remains controversial [57, 91, 92]. In the following part, a submonolayer coverage that can be related to the intermediate phase will be studied, with special focus on the bonding and orientation.

Submonolayer A submonolayer system with relatively diluted adsorbate (corresponding to a total 4-FTP exposure of 0.02 Torr*s, and a coverage of 0.45 ML [3]) was adsorbed at 80 K in a fast single step. The left panel of Fig. 4.28 compares the core-level spectra of such 4-FTP submonolayer film and the respective curves in Fig. 4.26 (left) corresponding to a cumulative exposure of 0.02 Torr*s. The perfect agreement of the spectra from two separate preparations demonstrates the accuracy and the reproducibility of our gas-dosing system. The XPS curve-fitting analysis is shown in the right panel of Fig. 4.28 and the results are summarized in Table 4.7. Compared to the monolayer, the binding energy of the C 1s components of the aromatic C-H carbon and C-F carbon as well as that of F 1s core level are slightly shifted to lower binding energy, indicating sightly stronger interaction with the metal substrate. In the S 2p spectrum, the binding energy remains almost

[3]This is calculated based on the ratio of the integrated peak area of the C 1s signal of this submonolayer to that of the saturated monolayer; the same value was derived from the C 1s and F 1s signal.

identical as in the monolayer and no atomic sulfur appears. Now more than 90% of the molecules adsorb via thiolate bonding, which can be assumed to be due to the larger lateral space available.

The NEXAFS spectra of this submonolayer system presented in the bottom of Fig. 4.27 closely resemble those of the monolayer, again pointing to a flat-lying orientation of the molecules. The tilt angle relative to the surface normal estimated from the NEXAFS spectra (approximately 70°) is virtually indistinguishable from the monolayer case.

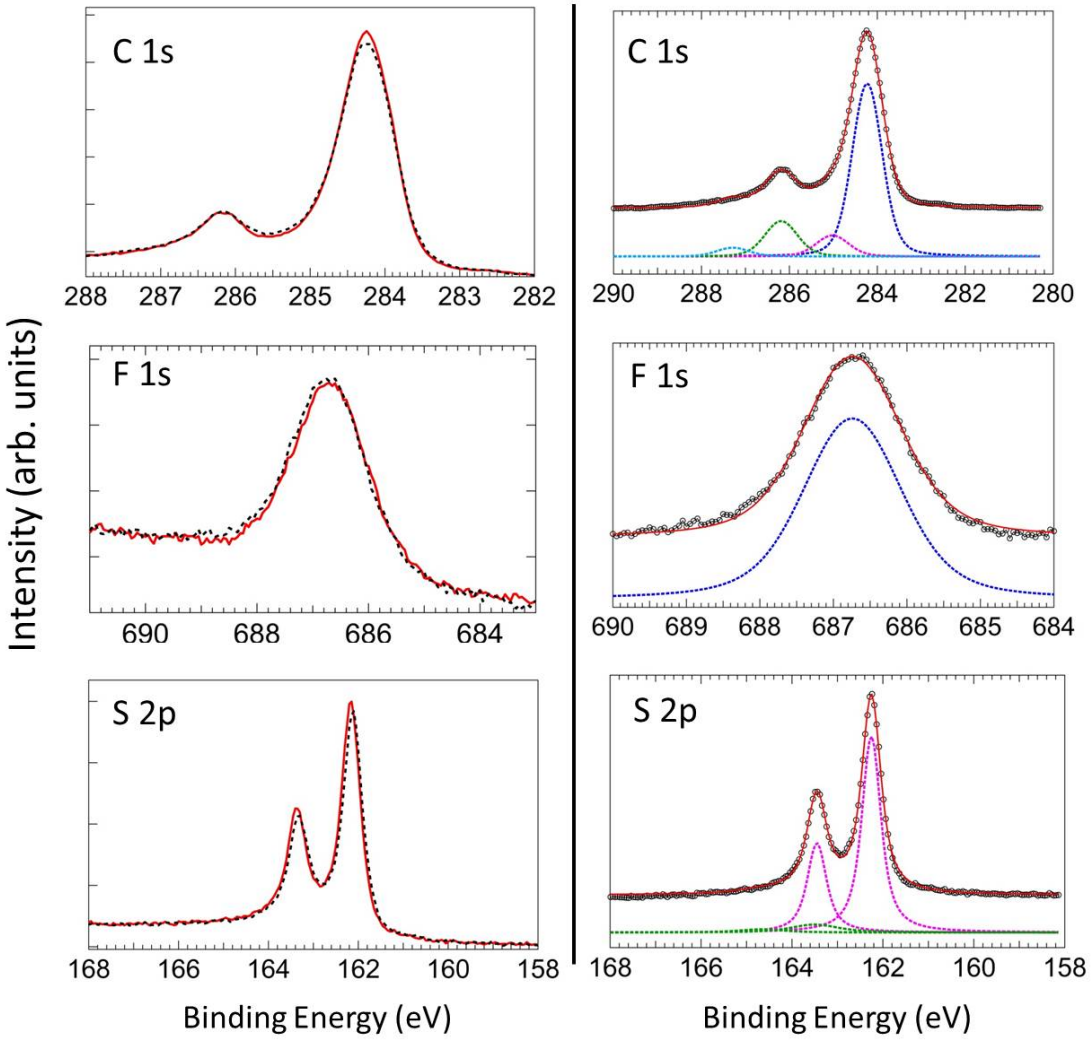

FIGURE 4.28: (Left) Comparison of C 1s, F 1s and S 2p core-level spectra of 4-FTP films at submonolayer coverage prepared according to two different procedures in two separate preparations. The black dotted curves correspond to a submonolayer film adsorbed at 80 K at exposure of 0.02 Torr*s in a single fast step; the red solid curves belong to the submonolayer film prepared by incremental dosing up to 0.02 Torr*s at 80 K in a three-step preparation. (Right) XP spectra and respective fittings of one of the 4-FTP layers of the left panel.

In summary, 4-FTP monolayer and submonolayer films free of atomic sulfur can be prepared by incremental dosing at 80 K, unlike the standard procedure based on annealing at ca. 190 K of the 4-FTP multilayer, which leads to SAMs of lower quality. The NEXAFS data suggest a flat-lying orientation of the molecules in both the mono- and submonolayer films. In contrast, 4-FTP SAMs on the Ni(111) surface prepared with the standard annealing protocol adopt an upright adsorption geometry [133]. We assume that the annealing process in the 4-FTP/Ni(111) case might allow overcoming the threshold, presumably due to the van der Waals interactions between the backbone and the substrate that prevent the molecules from "standing up". However, the orientation of molecules in the SAM is determined by a number of factors, such as the lateral backbone-backbone interaction, the preparation protocol (e.g., incremental vs. single-step dose, as well as annealed vs. non-annealed layer), and the arrangement of the headgroup on the substrate *etc* [57]. To gain further insight, some additional experiments were carried out on the 4-FTP/Ni(111) system, and will be discussed in the appendix A. In the following subsection, the charge transfer from the tailgroup of the 4-FTP/Co(0001) at monolayer and submonolayer coverage to the cobalt substrate will be investigated. Ultrafast charge transfer was already observed and studied qualitatively for 4-FTP molecules lying flat on Au(111) by Wang *et al* [11]. We will derive the characteristic charge transfer time from the RAES spectra with the CHC approach, and the dependence of the charge transfer time on the photon energy and polarization for both mono- and submonolayer films will be discussed.

4.4.2.3 Charge Transfer Dynamics

Analysis of RAES Spectra Fig. 4.29 presents the RAES spectra across the F K-edge absorption region in the form of 2D contour plots for the monolayer (top) and submonolayer systems (bottom) at two different polarizations, A_{xy} and A_z, respectively. The strongest intensity is denoted with red colour, and blue represents the intensity level of the background. The non-resonant background measured at 680 eV and a Shirley-type background are subtracted from all the decay spectra. For the monolayer in the top panels, the intensity of the decay electrons is maximized for A_{xy} polarization and largely quenched for A_z polarization. The decay structure covers a large photon energy range from ca. 687 eV to 695 eV, in good agreement with the NEXAFS spectra. The kinetic energy distribution of decay electrons, stemming from a mixture of resonant spectator and

normal Auger decay channels, is narrower and shows a stronger non-dispersive behaviour compared with that of 4-FBA/Co(0001) shown in Fig. 4.9, indicating a larger weight of the normal Auger decay. The disappearance of participator lines at high kinetic energies reflects a lower influence of the pure autoionization (spectator and participator) decay. Moreover, the Auger decay lines of atomic fluorine originating from C-F bond dissociation are still visible at a kinetic energy of about 663 eV. The observed larger fraction of the normal Auger decay channel suggests the occurrence of a faster interfacial charge transfer compared to the case of 4-FBA/Co(0001) [8, 12], in which the F 1s electrons excited into the unoccupied states delocalize into the Co substrate on the femtosecond time scale. The contour plot of the submonolayer film reported in the bottom panel greatly resembles that of the monolayer, apart from the fact that the intensity of decay electrons is correspondingly lower under the respective polarization. This is not surprising considering the lower packing density in the submonolayer film.

Tailgroup to cobalt charge transfer with CHC The characteristic time for the CT of resonantly excited F 1s electrons to the cobalt substrate was determined with analogous procedures as used for the 4-FBA/Co(0001) system based on the CHC approach. The RAES spectra of a 4-FBA multilayer serve as the pure autoionization contribution in the reconstruction of the 4-FTP decay spectra, since no strong difference is expected for the deexcitation of F 1s core holes in 4-FTP and 4-FBA multilayers. Fig. 4.30 illustrates the photon energy dependence of the Auger fraction and the corresponding CT time for the 4-FTP/Co(0001) monolayer excited with A_{xy} and A_z polarization, respectively. The CT is on average faster for A_z polarization, especially in the region above 691 eV. At 690.7 eV (approximately the resonant absorption maximum), the CT time is 3.1 ± 0.3 fs for both polarizations, in contrast to 12.8 ± 0.2 fs for 4-FBA/Co(0001) system. At increasing photon energy, the CT time for both polarizations decreases but with a relatively larger decline for A_z polarization, e.g., the CT time at 691.6 eV photon energy is 2.9 ± 0.2 fs for A_{xy} and 1.7 ± 0.15 fs for A_z polarization. The CT time is larger under both polarizations when the excitation energy is between 689 eV and 690 eV, which corresponds to the energy of the maximum F^+ yield in both 4-FTP/Ni(111) [20] and 4-FBA/Co(0001) SAMs (we can indeed assume the same situation for 4-FTP on Co(0001)).

The faster tailgroup-to-substrate CT for the 4-FTP/Co(0001) SAM compared to

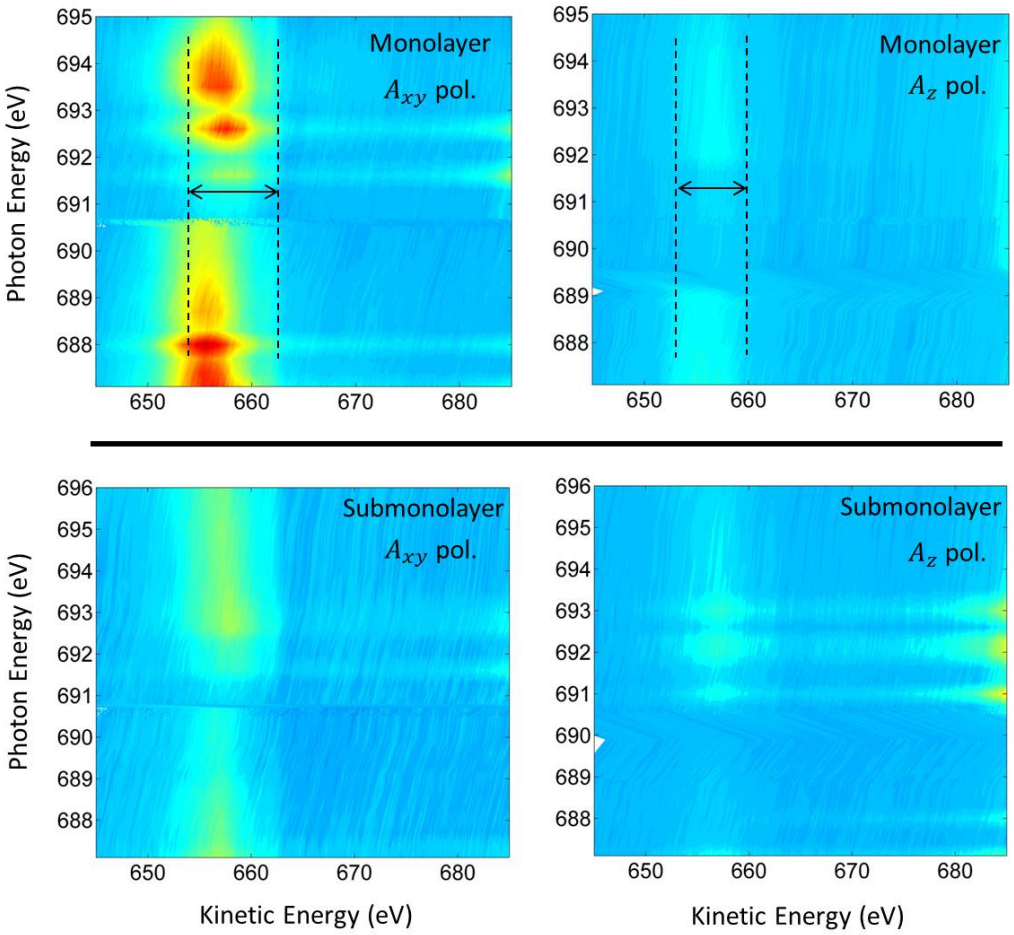

FIGURE 4.29: 2D contour plot representation of RAES spectra across the F K-edge resonance for (top) monolayer and (bottom) submonolayer coverage. The red color scale denotes the strongest intensity and the blue color scale the weakest intensity.

4-FBA/Co(0001) can be rationalized in terms of the different molecular orientation, flat-lying for 4-FTP and upright for 4-FBA. A similar tendency was observed in Ref. [11] for 4-FTP on Au(111), in which case the unoccupied molecular orbitals overlap strongly with the Au substrate for flat-lying orientation while are distributed only around the molecules for upright orientation. Ultrafast CT was therefore observed only for lying-down molecules. In their work, the RAES spectra of carbon were analysed however the site of the excited electrons was ambiguous, in contrast to our work where CT starting from the fluorine headgroup is considered. The fact that in the 4-FTP/Co(0001) SAM the CT is on average faster for A_z polarization than for A_{xy} polarization cannot be simply explained by the energetic position of the resonance or by the DOS of the unoccupied molecular orbitals, because the former is not affected by the polarization, while the latter

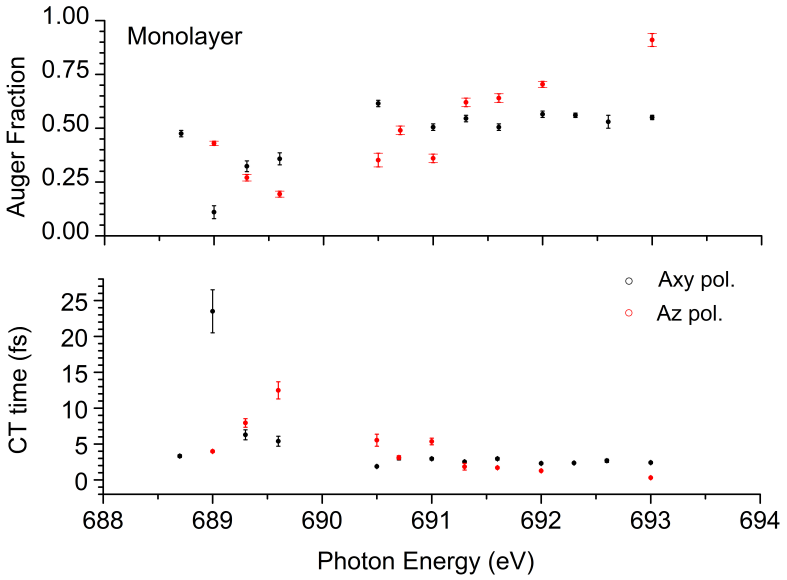

FIGURE 4.30: Variation of the (top) Auger fraction and (bottom) corresponding CT time as a function of the excitation energy for a 4-FTP monolayer on Co(0001) upon resonant F 1s excitation. Black (red) symbols denote the values for excitation with A_{xy} (A_z) polarization.

would instead result in a faster CT for A_{xy} polarization due to the fact that the unoccupied DOS related to fluorine has mainly σ^* character (see NEXAFS) and should be maximized with A_{xy} polarization [108]. A possible explanation is that the π^*-type molecular orbital that is mainly populated with A_z polarization due to the flat-lying orientation is not localized in the tailgroup but extends onto the phenyl ring and the anchoring headgroup [9, 122], and therefore induce a faster CT if a tunnelling mechanism of charge transfer is assumed. However, another factor, the available DOS of cobalt, should be considered since the molecular orbitals could be partly coupled with the substrate as a consequence of the flat-lying molecular orientation. Since the valence band of cobalt has an overwhelming contribution by 3d orbitals [139], assuming that mainly states with d_z character overlap strongly with the π^*-type molecular orbital, a faster CT for A_z polarization could be expected.

Finally, a comparison of the CT time in monolayer and submonolayer films under A_{xy} polarization is reported in Fig. 4.31. A very similar trend is observed - the CT time for both layers decreases with increasing excitation energy except between 689 eV and 690 eV, where the F^+ signal is maximized. A remarkable difference, however, is that an overall larger Auger fraction, implying a faster CT, is observed

for submonolayer coverage. This effect can be tentatively ascribed to a stronger coupling to the substrate in the less densely packed layer.

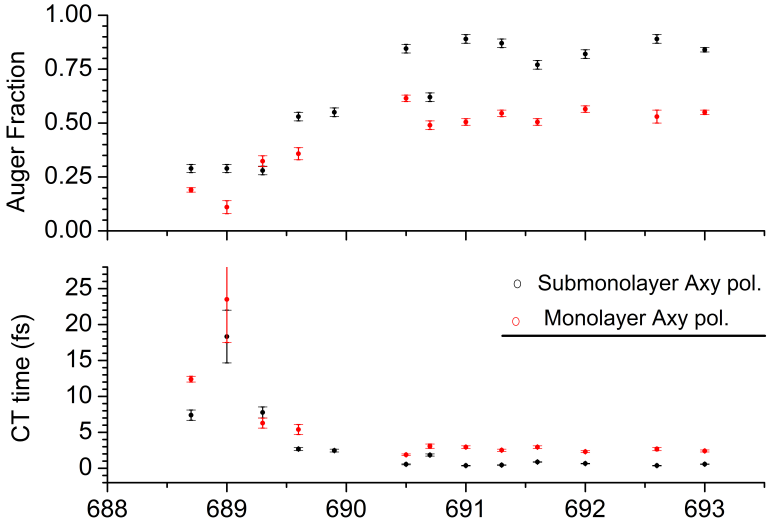

FIGURE 4.31: Comparison of the (top) Auger fraction and (bottom) corresponding CT time as a function of the excitation energy for 4-FTP monolayer (red) and submonolayer (black) films on Co(0001) upon resonant F 1s excitation. A_{xy} radiation polarization was used in the measurement.

4.4.3 Conslusions for the 4-FTP/Co(0001) SAM

Based on the incremental vapor-phase deposition approach rather than on the standard protocol by annealing of the multilayer, well-defined 4-fluorothiophenol monolayer and submonolayer films bonded via the thiolate anchor and containing a negligible amount of atomic sulfur can be prepared on the Co(0001) surface at 80 K. The electronic structure of multilayer, monolayer as well as submonolayer films were comprehensively investigated by means of XPS. The molecules in both the monolayer and submonolayer films are found to adopt a flat-lying orientation (approximately 20° from the surface).

The evaluation of the RAES spectra following resonant F 1s excitation is in agreement with the F K-edge NEXAFS spectra, where the dominant σ^*-type orbitals are maximally populated with A_{xy} radiation polarization due to the flat-lying molecular orientation. According to the CHC approach, the ultrafast tailgroup-to-substrate charge transfer can be determined in the femtosecond range. On

average, a faster charge transfer is found for A_z polarization than for A_{xy} polarization. Moreover, charge transfer in the submonolayer film is faster than in the monolayer probably due to an increased coupling of the molecules to the substrate.

Chapter 5

Interaction with O_2 of Ru Tetraphenyl Porphyrin Monolayers Adsorbed on Ag Surfaces

5.1 Introduction

Porphyrins are one of the most studied classes molecules due to the high chemical stability, and to the vital roles they play in the nature world, e.g., oxygen transport in blood, heme, and photosynthesis *etc.* They consist of a porphine macrocycle, which is made of four pyrrole rings and can host a wide range of metals at its center, thus forming a variety of metalloporphyrins. Moreover, substitutions can be made to the periphery of the porphine ring to modify the interaction of the molecule with its surroundings, rendering porphyrins important building blocks in molecular engineering [148]. Among metalloporphyrin molecules, ruthenium tetraphenyl porphyrins (Ru-TPP) with a common substituent (four phenyl rings) and a Ru atom in the center of the porphine macrocycle have received considerable attention due to the high catalytic activity for the oxidation of a variety of functional groups, e.g., for epoxide reactions through which the high-valent oxo-ruthenium intermediates donate an oxygen atom for epoxidation of alkenes [13]. Additionally, for adsorbed monolayers of metalloporphyrins on surface, the interaction of the metal center with the substrate plays a fundamental role in the electronic and

chemical properties of the system [149], and the substrate surface can therefore sensitively influence and optimise the reactivity of the metal complexes [150].

When Ru-TPP is employed as the catalyst for an epoxide reaction, the formation of oxo- or dioxo-ruthenium species is seen as a necessary intermediate step. For manganese porphyrin catalyst [14], it is also found that oxygen atoms from an O_2 molecule are first bound to an adjacent metal center before their subsequent incorporation into an alkene species to yield an epoxide product. Therefore, the interaction with oxygen is often utilized as a measure of the strength of interaction of a catalyst. In addition, since adsorbed metal complexes are promising candidate for heterogeneous catalyst with well-defined active site, and the substrate (or the support material) can be regarded as a bulky ligand to the metal center and is thought to play a similar role as common ligands such as NO^-, S^{2-} and O^{2-}, the choice of an appropriate substrate is very important for the performance of the metal complexes as catalysts [14, 150].

In this chapter, we first study the formation and the flattening of a monolayer of metal-free 2H-tetraphenylporphyrins (2H-TPP) on Ag(111). Lab-source measurements in our on-campus laboratory, i.e., XPS, UPS and TPD, were employed for the characterization. Afterwards, the interaction of a Ru-TPP monolayer with oxygen was studied on the Ag(111) and Ag(110) surfaces, respectively, to attempt to generate oxo-ruthenium porphyrin product - a necessary intermediate for the catalysis of an epoxide reaction, and to investigate the influence of the substrate on the reactivity of the metal complexes. For this purpose, both lab source and synchrotron radiation were used.

5.2 Experimental Results and Discussion

Experimental The Ag(111) and Ag(110) surfaces were cleaned by cycles of Ar^+ sputtering at 1 keV and annealing at 750 K. The absence of contaminants was checked by means of XPS. All the TPD measurements were performed with a liquid nitrogen cooled QMS in the custom-built UHV chamber as introduced in section 3.1. Prior to acquisition of the TPD spectra, the background H_2 signal has been minimized by use of a titanium sublimation pump mounted inside the QMS.

Purified 2H-TPP molecules were sublimated at 570 K onto the Ag(111) surface kept at 300 K. The 2H-TPP monolayer was obtained by annealing of a 2H-TPP multilayer at 470 K for about 10 min. XP spectroscopic characterization of the 2H-TPP/Ag(111) surface was performed with a commercial hemispherical energy analyzer (Specs Phoibos 100 CCD) and non-monochromatized AlK_α and MgK_α X-ray sources in the E20 laboratory in Garching.

XPS and NEXAFS data of the Ru-TPP/Ag(111) system were collected at the ALOISA beamline of the Elettra Synchrotron in Trieste and the experiments were performed in an UHV chamber with a base pressure of 10^{-10} mbar. NEXAFS spectra were acquired in PEY mode by means of a channeltron. The secondary electrons have been filtered out by a retarding potential (-230 V for the C K-edge, -370 V for the N K-edge and -490 V for the O K-edge). The polarization of the measurement was changed by rotating the sample around the beam axis of the linear-polarized synchrotron radiation, while keeping a constant grazing angle of 6°. The raw data were normalized to the photon flux and corrected for the clean-substrate contribution to the absorption. Prefabricated (CO)-Ru-TPP molecules were sublimated onto Ag(111) at 600 K using an organic molecular beam evaporator while the sample was held at room temperature. The sample was held either at room temperature or at 620 K when exposed to the oxygen molecules. Finally, the study of Ru-TPP on Ag(110) and its interaction with oxygen follows a similar procedure as that for the O-RuTPP/Ag(111) system, but all measurements were performed without synchrotron radiation in Garching.

5.2.1 Preparation and Flattening of 2H-TPP on Ag(111)

TPD measurements It has been reported that 2H-TPP molecules undergo a cyclodehydrogenation or ring closing reaction upon annealing to temperature between 530 K and 620 K on Ag(111) surface, resulting in planar porphyrin derivatives [151, 152]. Therefore, we herein performed TPD measurements monitoring the desorption of 2H-TPP and H_2 molecules, to determine the temperature of the desorption of the physisorbed layer and the dehydrogenation reaction, which are essential for the preparation of a 2H-TPP monolayer and the flattening of the 2H-TPP molecules, respectively. Figure 5.1 (a) shows the TPD spectrum of a 2H-TPP multilayer on Ag(111) for mass/charge ratio of 52 (fragment of the intact molecule) and 2 (H_2), with the heating rate being 0.5 K/s. The pronounced peak

at 470 K for m/e 52 is assigned to the desorption of the multilayer, while the broad feature with an onset at 550 K for m/e 2 is presumably related to the flattening of the molecules because of its large temperature span (more than 80 K) with respect to the desorption peak of the multilayer. In addition, for m/e 52, a broad feature above 500 K extends over the range in which the flattening occurs, and this might be attributed to the desorption of the densely packed molecules to make room for the flattening process, proposed by a STM study in Ref. [30]. Interestingly, the signal of the TPD spectrum for H_2 extends further above 700 K, which might be related to the complete dehydrogenation of the molecules [153] and the occurrence of intermolecular polymerization reactions, leading to the formation of intermolecular C-C bonds [30, 151].

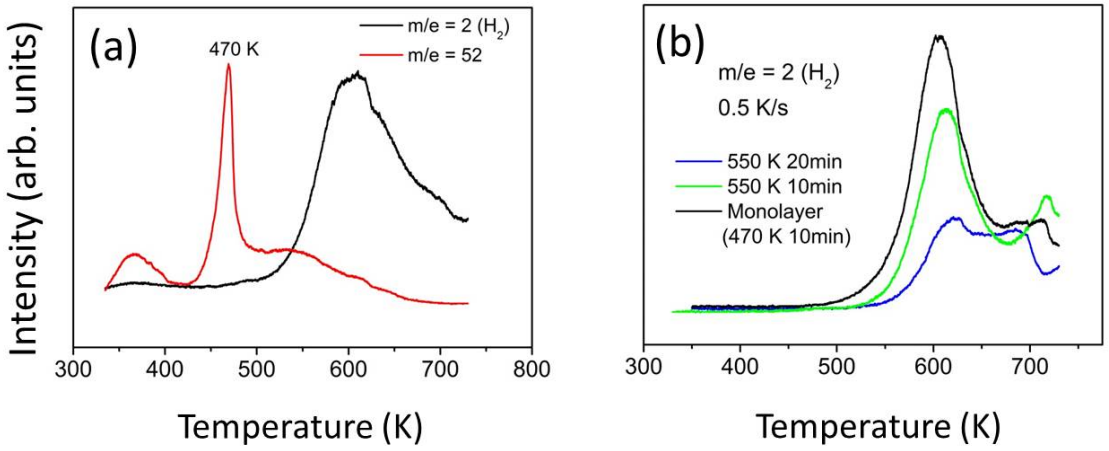

FIGURE 5.1: (a) TPD spectra measured from a multilayer of 2H-TPP on Ag(111) for m/e ratio of 52 (black curve) and 2 (red curve) with a heating rate of 0.5 K/s. (b) TPD spectrum of a 2H-TPP monolayer (black curve) and the monolayer after pre-annealing to 550 K for 10 min (green curve) and 20 min (blue curve), respectively, for m/e 2 with a heating rate of 0.5 K/s.

According to the assignments of Fig. 5.1 (a), a 2H-TPP monolayer is prepared by annealing of a 2H-TPP multilayer at 470 K for 10 min, and the molecules in the monolayer can be then flattened by holding the sample at 550 K for a certain time. To shed further light on the molecular flattening process, TPD measurements (Fig. 5.1 (b)) by collecting the H_2 signal with the same heating rate were performed for the monolayer and for the monolayer after pre-annealing to 550 K for 10 min and 20 min, respectively. The pre-annealing of the monolayer to 550 K for a prolonged period of time should correspond to the presence of an increasing fraction of flattened molecules on the surface, since the molecular

flattening has been demonstrated to be a multi-step process [30]. Therefore, as shown in Fig. 5.1 (b), the procedure results in a decrease of the intensity of H_2 signal and an increase of the temperature of the H_2 desorption peak with increasing pre-annealing time, i.e., from 605 K for the as-prepared monolayer, to ca. 610 K and 620 K for the 10 min and 20 min pre-annealed monolayer, respectively. This implies that the molecules need to be held at 550 K for prolonged time to be totally flattened.

TPD spectra for m/e 2 measured from the 2H-TPP monolayer was also obtained by Di Santo *et al.* with a heating rate of 2 K/s [152]. They saw the most pronounced feature corresponding to the molecular flattening peaking at 640 K, which is higher than our observed temperature around 600 K with 0.5 K/s. Moreover, the onset temperature of the molecular flattening (570 K) they obtained from their TPD measurements does not agree with the temperature (525 K) at which they observed the occurrence of dehydrogenation [152]. This discrepancy was ascribed to the production of H_2 signal being too slow during the flattening process and not detected by their mass spectrometer, and also to the different heating rate they used. To demonstrate that the different heating rate is the main reason for the different location of the desorption peak, we performed TPD measurements with distinct heating rates (Fig. 5.2). In our case, the main H_2 desorption peak is centred at approximately 640 K at the heating rate of 2 K/s, in good agreement with their measurements. In addition, the H_2 desorption peak shifts to higher temperature with increasing heating rate from 0.5 K/s to 2 K/s.

XPS characterization In Fig. 5.3 from top to bottom, the C 1s and N 1s core-level spectra of a multilayer, a monolayer prepared by annealing of the multilayer at 470 K for 10 min, the as-prepared monolayer flattened by annealing at 550 K for 10 min, and the as-flattened monolayer after annealing to 730 K are displayed, respectively. In the multilayer, the N 1s signal shows two distinct peaks with almost equal intensity, located at ca. 400.2 eV (component N1) and 398.2 eV (N2) and corresponding to aminic and iminic N, respectively. After annealing at 470 K (Fig. 5.3 (b)), both N peaks, especially the aminic one, are shifted to lower binding energies (ca. 399.7 eV and 397.9 eV for N1 and N2, respectively), presumably as a consequence of the increased screening of the core hole created upon photoemission due to the closer vicinity to the Ag surface. Upon further annealing to 550 K to flatten the molecules (Fig. 5.3 (c)), the N 1s signal is further shifted toward lower binding energy, possibly due to even smaller distance between the N atoms and

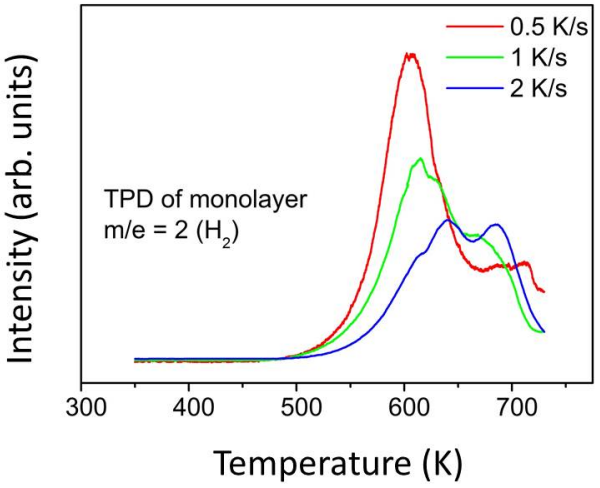

FIGURE 5.2: TPD spectra measured from a monolayer of 2H-TPP on Ag(111) for m/e 2, with the heating rate of 0.5 K/s (red curve), 1 K/s (green curve) and 2 K/s (blue curve), respectively.

the Ag surface upon flattening. A similar trend is also observed for the C 1s signal (right panel). After annealing to 730 K (Fig. 5.3 (d)), a broad new feature peaking at 398.2 eV appears, which might be associated with the thermal decomposition of the porphyrins reported to start between 600 and 700 K [149], and leading to the occurrence of dehydrogenation for part of the aminic N. In the corresponding C 1s signal, we see a similar binding energy evolution with the annealing process. A single component at 284.9 eV was observed in the multilayer, identical with the reported value in Ref. [149]. After annealing at 470 K and 550 K, the C 1s peak shifts toward lower binding energy, in agreement with the N 1s signal. In addition, at and above 550 K, the binding energy shift is accompanied by a broadening of the peak; both the thermal decomposition of the molecules and the intermolecular polymerization may contribute to this observation.

In summary, our TPD measurements prove that the 2H-TPP monolayer can be prepared by annealing of a 2H-TPP multilayer at 470 K and the flattening of the molecules starts at about 550 K. The large temperature separation (more than 80 K) between the multilayer desorption peak and the onset of the molecular flattening allows us to prepare separately 2H-TPP monolayer with molecules non-flattened or flattened, respectively, as evidenced by the distinct binding energy shift of the N 1s and C 1s core levels before and after molecular flattening.

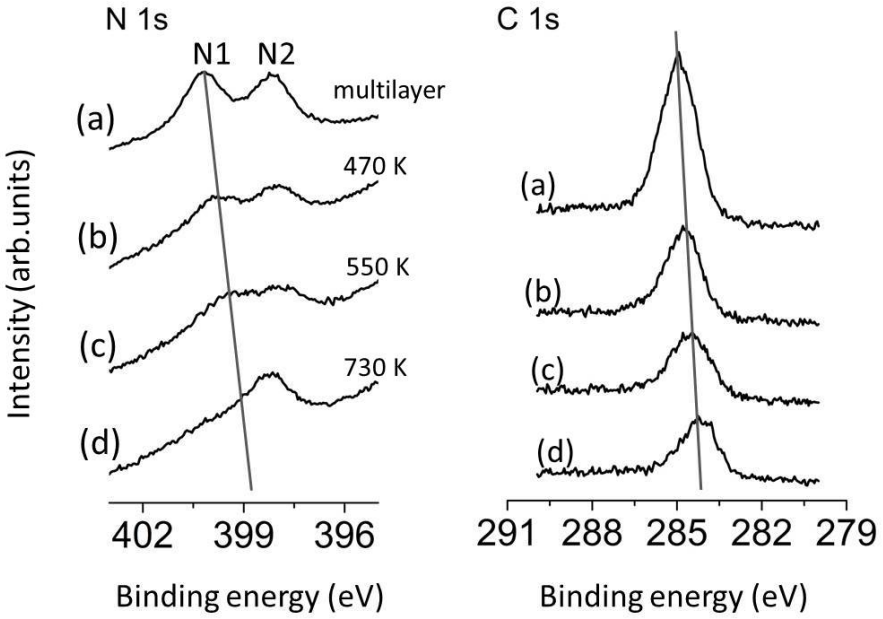

FIGURE 5.3: N 1s and C 1s core-level spectra of 2H-TPP on Ag(111): (a) a 2H-TPP multilayer; (b) a monolayer prepared by annealing of the multilayer to 470 K for 10 min; (c) after annealing the as-prepared monolayer at 550 K for 10 min to flatten the molecules; (d) after further annealing of the as-flattened monolayer to 730 K. The two solid lines highlight the binding energy shift. Non-monochromatized AlK_α radiation was utilized for the acquisition of the spectra.

5.2.2 Preparation and Flattening of Ru-TPP on Ag(111)

It has been demonstrated that a monolayer of flat-adsorbed Ru-TPP molecules can be created on Ag(111) surface by exposure of 2H-TPP molecules to gas-phase ruthenium carbonyl precursors via metal-organic chemical vapour deposition and thermal treatment [15]. In contrast to the metalation approach used in Ref. [15], in this subsection commercially available Ru(CO)-TPP molecules were sublimated onto Ag(111) at 600 K by means of an organic molecular beam evaporator with the sample held at room temperature. The CO ligand was not observed to be present upon adsorption onto the surface, most likely desorbing on heating the molecular powder at 600 K. We then prepared a Ru-TPP monolayer by the method of multilayer desorption and focused on the oxidation of the Ru-TPP molecules by employing O_2 as oxidizing agent.

TPD Fig. 5.4 displays the TPD spectrum of a Ru-TPP multilayer on Ag(111) for m/e 2 (H_2) with a heating rate of 0.5 K/s. The spectrum largely resembles

that of 2H-TPP, except that the onset of the molecular flattening now starts at 620 K, which is 50 K higher than that of 2H-TPP and is presumably associated with the interaction of the coordinated Ru centres with the Ag surface. The main implication is that the Ru-TPP monolayer of flattened molecules can be prepared by annealing of a Ru-TPP multilayer at 620 K. Note that the peak shape is considerably sharper than for the free-base molecules (see Fig. 5.1 (a)).

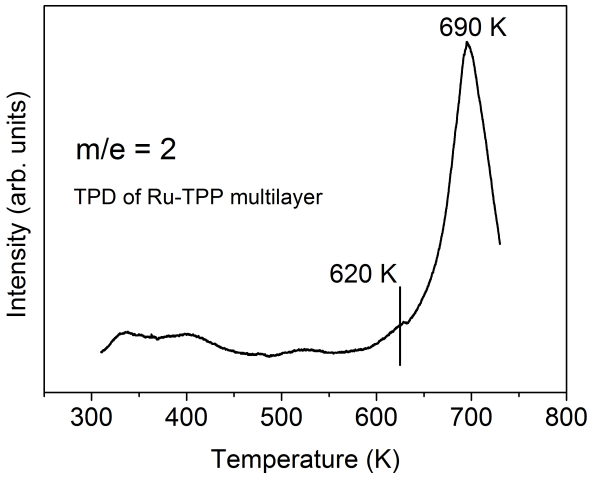

FIGURE 5.4: TPD spectrum measured from a Ru-TPP multilayer on Ag(111) for m/e=2 with a heating rate of 0.5 K/s. The vertical line marks the onset of the molecular flattening (620 K).

NEXAFS According to previous literature [15] and to our TPD data, a Ru-TPP monolayer with tilted phenyl legs can be prepared by annealing of a multilayer at 530 K - 600 K, whereas holding the sample at 620 K for a certain time can flatten the molecules probably through the dehydrogenation reactions between the phenyl rings and the porphyrin macrocycle. Fig. 5.5 (a-d) shows the NEXAFS spectra at the C K-edge after annealing of the Ru-TPP multilayer on Ag (111) with different heating profiles, providing information on the evolution of the molecular configuration with temperature. In the low photon energy region of the spectra, the spectral shape arise from the superposition of the signal of macrocycle and the phenyl substituents. In particular, the first π^* peak (peak 1) at 284.5 eV originates from the macrocycle, whereas the second more intense π^* peak (peak 2) at 285.3 eV is assigned to the four phenyl substituents surrounding the macrocycle [152, 154]. Peak 1 is almost completely quenched for A_{xy} polarization (the polarization vector being parallel to the surface plane for A_{xy}, and perpendicular to the surface plane for A_z) in all four panels, suggesting that the macrocycle is always adsorbed parallel to the Ag surface. However, the configuration of the phenyl legs changes

progressively with the different annealing profile, evolving from a randomly tilted orientation after annealing at 530 K for 5 min (Fig. 5.5 (a), no dichroism) to the completely flat configuration after annealing at 620 K for 10 min (Fig. 5.5 (d)), as determined by the increasing linear dichroism of peak 2. Notably, the surface after annealing at 600 K for 5 min (Fig. 5.5 (b)) corresponds to a monolayer, where the phenyl rings predominantly adopt an almost T-shaped configuration with the macrocycle [152, 154]; holding the system at 620 K for 5 min (Fig. 5.5 (c)) results in a monolayer with the phenyl legs largely oriented towards the substrate. The NEXAFS data demonstrate that the flattening of the Ru-TPP molecules is a multi-step process, analogous to that of 2H-TPP discussed in the last section based on the TPD spectral analysis, and the phenyl legs of the Ru-TPP molecules probably rotate with respect to the porphyrin macrocycle upon annealing.

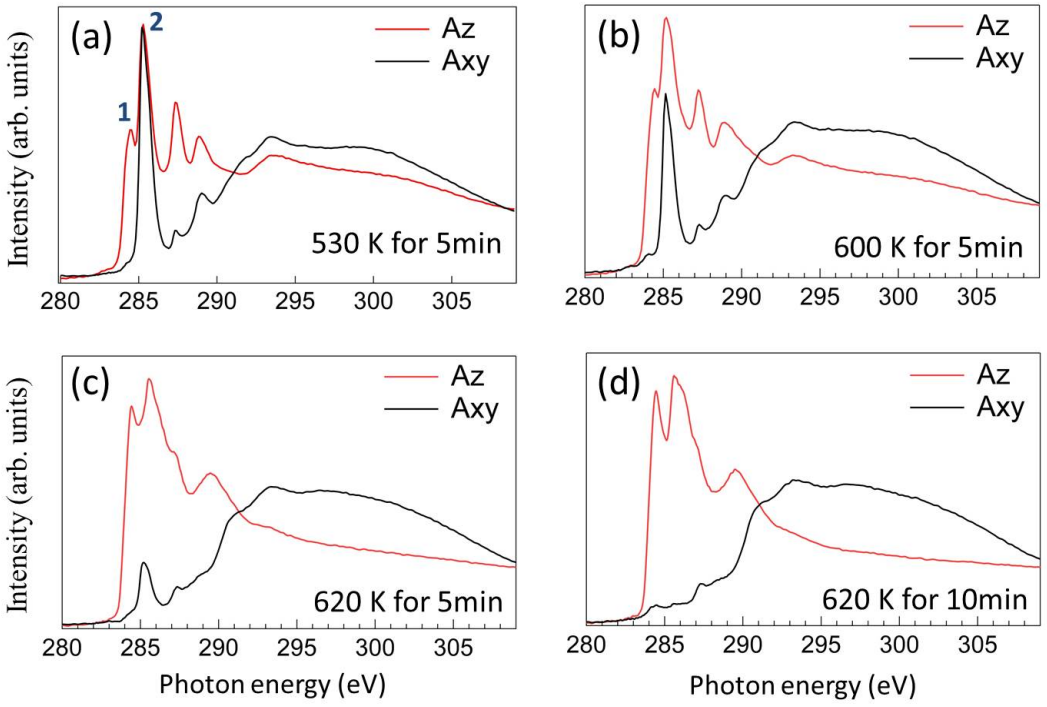

FIGURE 5.5: NEXAFS spectra at the C K-edge after annealing of a Ru-TPP multilayer on Ag(111) with different heating profiles: (a) after annealing at 530 K for 5 min; (b) at 600 K for 5 min; (c) at 620 K for 5 min; and (d) at 620 K for 10 min. The spectra were collected with two almost orthogonal polarizations, namely with the polarization vector parallel (A_{xy}, black) and perpendicular (A_z, red) to the surface plane, respectively. Attribution of the absorption peak 1 and 2 is discussed in the text.

XPS The N 1s and *Ru* $3d_{5/2}$ spectra measured from the flattened monolayer are reported in Fig. 5.6. Note that only the *Ru* $3d_{5/2}$ component of the Ru 3d spin-orbit split doublet is shown for clarity, since the *Ru* $3d_{3/2}$ species at higher binding

energy overlaps with the dominant C 1s peak. In the N 1s signal (Fig. 5.6(a)), only a single component is evident at 398.6 eV because of the incorporation of Ru into the central cavity of the tetrapyrrole ring, in contrast to the two components observed for 2H-TPP; accordingly its binding energy is typical for metalated porphyrins [15, 154]. Moreover, the binding energy of $Ru\,3d_{5/2}$ (279.5 eV, Fig. 5.6(b)) points towards a Ru(0) state rather than the oxidation state of +2 expected for a free-base Ru-TPP molecule. A possible explanation for the discrepancy is the occurrence of charge transfer from the Ag substrate to the molecules and hints to a relatively strong interaction between the metal center and the silver surface [155].

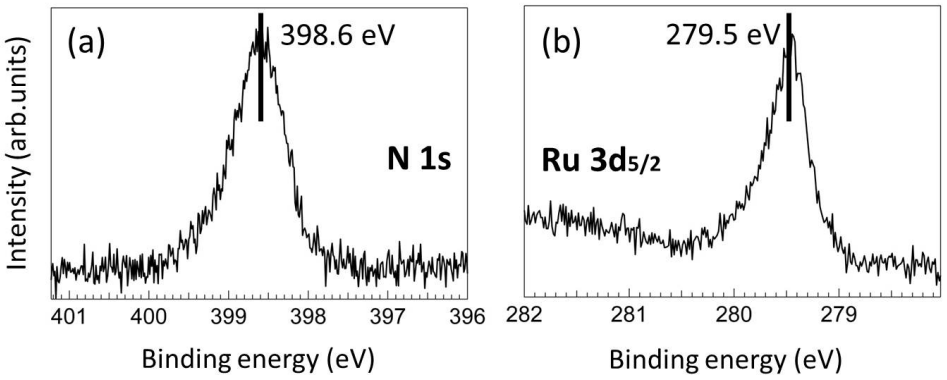

FIGURE 5.6: (a) N 1s and (b) $Ru\,3d_{5/2}$ core-level spectra of the Ru-TPP monolayer prepared by annealing of a Ru-TPP multilayer at 620 K for 5 min. The photon energies used for recording the spectra were 550 eV (N 1s) and 410 eV ($Ru\,3d_{5/2}$), respectively.

UPS Finally, the valence spectra measured after annealing of the Ru-TPP multilayer with different heating profiles (corresponding to (a - d) in Fig. 5.5) are displayed in Fig. 5.7. The most pronounced features occur at the binding energy of 0.5 - 0.8 eV and 1.6 eV, and the former one clearly shifts towards higher binding energy with increasing temperature and prolonged annealing time. According to the previous results on metalloporphyrins, e.g., Co-TPP [156], Fe-TPP [150] and Ce-TPP [157] on Ag(111), the first feature between 0.5 - 0.8 eV results from the electronic interaction of the coordinated metal center (Ru here) with the porphyrin macrocycle and the Ag surface. In particular, this signal was predominantly attributed to the interaction of metal d orbitals with the electronic states of the porphyrin macrocycle and the Ag surface, leading to two new electronic states below the Fermi level of Ag which are populated by electrons from the Ag surface; therefore, 2H-TPP with uncoordinated center [158] or Zn-TPP with completely

occupied $3d$ orbitals and thus negligible interaction with the Ag surface [150] exhibit no signal in the corresponding energy region. The appearance of these two Ru-related states is also in agreement with the Ru(0) state deduced from the XPS results. After annealing at 620 K for 10 min, corresponding to the flattened porphyrins as determined from the NEXAFS data, this feature is located at ca. 0.8 eV, which is close to the value of 0.9 eV reported for the flattened Ru-TPP molecules on Ag(111) in Ref. [15]. Moreover, the shift of this signal towards higher binding energy with the progressive thermal treatment, and accordingly with the reduced Ru-Ag distance and enhanced electronic interaction due to molecular flattening, is consistent with the reported conclusion that Co-TPP exhibits such metal-related feature at higher binding energy than Fe-TPP (0.6 eV for Co-TPP, 0.1 eV for Fe-TPP) due to its stronger interaction with Ag [150]. On the other hand, the position of the second feature (1.6 eV) is not as dependent on the distance between the Ru center and the Ag surface as the first feature. This signal, labelled as HOMO-1 in Ref. [156] (accordingly the first feature is denoted as HOMO), might stem from a considerable interaction of the metal d levels with the electronic system of the porphyrin macrocycle, and is therefore not strongly sensitive to the Ru-Ag distance. Most importantly, such metal-related states are reported to be varied upon coordination of the metal centres to the other ligands (reactant molecules) [150, 156], and can thus provide an additional way to monitor the state of Ru-TPP when exposed to oxidizing agent (O_2 in our case).

5.2.3 Interaction of Ru-TPP with Oxygen on Ag(111)

In this subsection, we focus on the oxidation of Ru-TPP with O_2, to test the potential of the Ru-TPP/Ag(111) system as a catalyst for, e.g., the selective epoxidation of alkenes, for which a major intermediate in the catalytic cycle is considered to be an oxo- or a dioxo-RuTPP. First, some preliminary measurements were carried out on the campus in Garching by preparing a Ru-TPP monolayer with non-flattened porphyrins [15, 29] and exposing the as-prepared monolayer to O_2 with the sample held at room temperature or at 620 K. After exposing the monolayer of Ru-TPP molecules to approximately 20000 L of O_2 at room temperature (Fig. 5.8 (a) and (b)), no oxygen species were observed on the surface and accordingly no shift of the $Ru\,3d_{5/2}$ peak. However, holding the surface at 620 K when exposed to 8000 L of O_2 (Fig. 5.8 (c) and (d)) results in an oxygen species locating at ca. 530 eV, and a slight shift of the $Ru\,3d_{5/2}$ peak by ca. +0.15 eV. The XPS results imply that

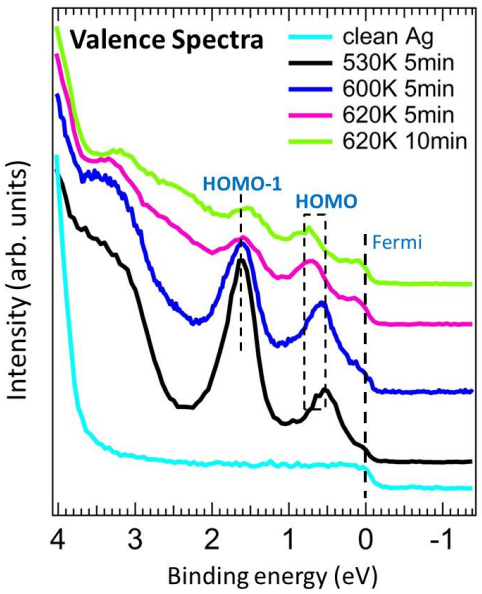

FIGURE 5.7: Valence spectra measured after annealing of the Ru-TPP multilayer with different heating profiles: 530 K for 5 min (black), 600 K for 5 min (blue), 620 K for 5 min (magenta) and 620 K for 10 min (green). The photon energy used for recording the spectra is 130 eV. The spectrum of clean Ag(111) is shown in the bottom for comparison.

the adsorbed Ru-TPP monolayer is inert towards O_2 at room temperature, and that heating the sample during O_2 exposure increases the reactivity, probably due to the enhanced probability for the splitting of O_2 at higher temperatures [159] and to the concomitant dehydrogenation of the molecules during oxygen exposure. Therefore, in the following study with synchrotron radiation in Trieste, we first exposed the flattened Ru-TPP/Ag(111) system to O_2.

In Figure 5.9, exposing the Ru-TPP/Ag(111) surface of flattened molecules held at 620 K to 20000 L of O_2 results in a sharp O 1s peak (Fig. 5.9 (a)) thanks to the high brilliance of the synchrotron radiation. This peak is centred at an almost identical binding energy (529.8 eV) as that described above (see Fig. 5.8 (c) for the spectra excited with lab source). This can be associated to a single oxygen species on the surface and it leads to a very modest shift of the binding energy by -0.1 eV in the $Ru\,3d_{5/2}$ spectrum, as shown in Fig. 5.9 (b). The absence of a distinct shift of the $Ru\,3d_{5/2}$ core level tends to exclude a direct coordination of oxygen to the ruthenium centres. Therefore, the formation of an oxo group pointing perpendicular to the macrocycle plane and the Ag(111) surface can be ruled out. Indeed, in Fig. 5.9 (c), the most pronounced feature in the O K-edge NEXAFS spectra that shows up at 530 eV exhibits the same linear dichroism

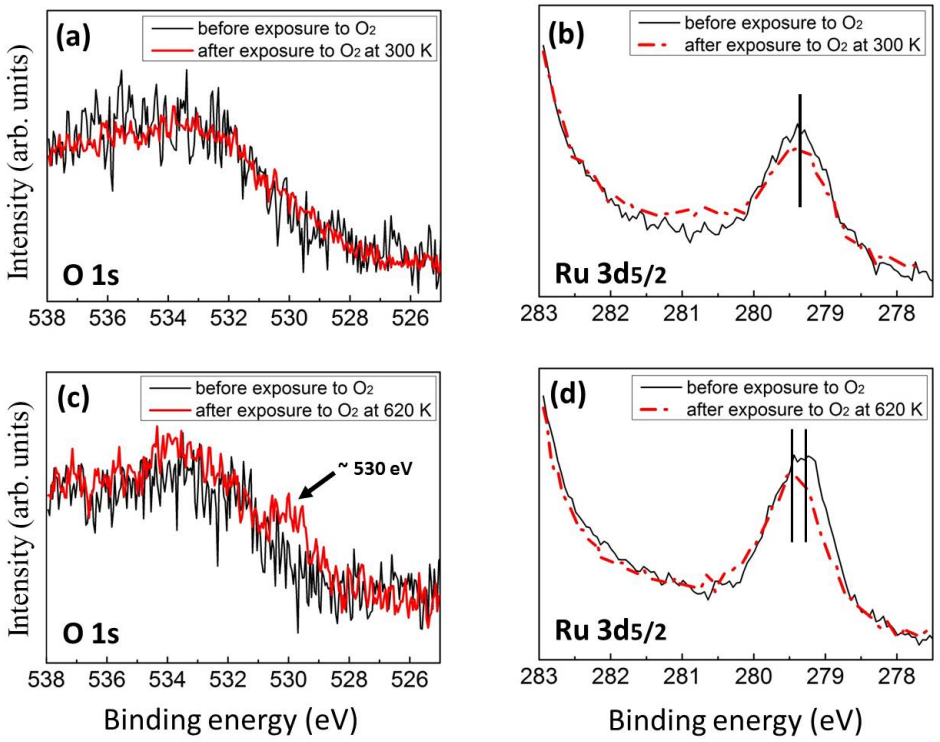

FIGURE 5.8: XP spectra acquired before (black) and after (red) exposure of the Ru-TPP monolayer of non-flattened molecules on Ag(111) to O_2: (a) O 1s and (b) $Ru\,3d_{5/2}$ after 20000 L of O_2 exposure at room temperature, (c) O 1s and (d) $Ru\,3d_{5/2}$ after 8000 L of O_2 exposure at 620 K. Non-monochromatized AlK_α radiation with photon line center at 1486.6 eV was employed for the acquisition of the spectra.

as the π^* peak of the porphyrin macrocycle and the phenyl rings of flattened Ru-TPP molecules(see Fig. 5.5 (d)), implying that the oxygen bonding exhibits a strong π^* character and the orientation of the O bond is largely parallel to the Ag surface. In Ref. [153], M. Roeckert *et al.* reported that the complete dehydrogenation of metalloporphyrins (Cu-TPP in their case) can occur between 600 K to 950 K, leading to the desorption of H_2 from the peripheral phenyl rings. In agreement with their conclusion, we hereby speculate that the O bond with π^* character might stem from the bonding of O with dehydrogenated phenyl ring carbons, possibly yielding C=O units oriented almost parallel to the substrate or C-O-C 'bridges' that lead to orbital hybridization with the aromatic macrocycle. Interestingly, although the resulting O 1s binding energy is almost 2 eV lower than the typical binding energy for carbonyl groups on silver surfaces [160], it is very similar to that reported for the carbonyl oxygens of pentacenetetrone molecules on Ag(111), which were shown to be bent downwards thus lying closer to the silver

surface [161]. Within this picture, the shift of the $Ru\,3d_{5/2}$ peak by -0.1 eV is not related to coordination of oxygen to Ru, but instead it might merely be a relaxation shift due to the closer Ru-Ag distance arising from the flattening and the further dehydrogenation occurring at 620 K.

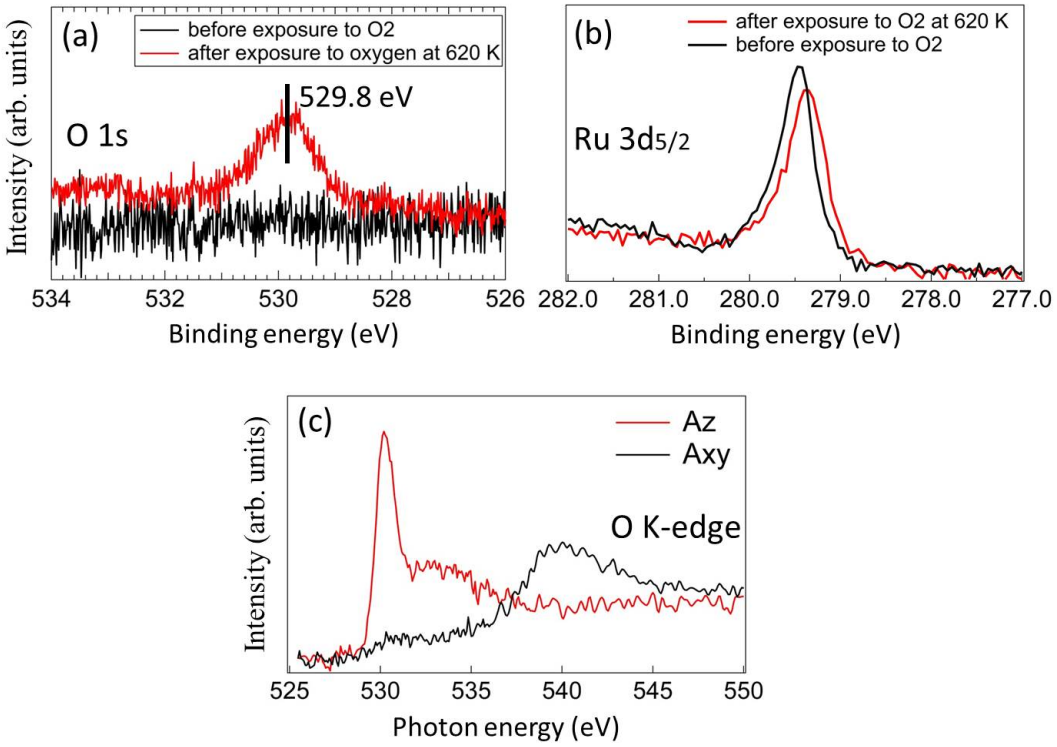

FIGURE 5.9: (a) O 1s and (b) $Ru\,3d_{5/2}$ XP spectra acquired before (black) and after (red) exposure to 20000 L of O_2 of a flattened Ru-TPP/Ag(111) surface held at 620 K. The photon energies used are 680 eV (O 1s) and 410 eV ($Ru\,3d_{5/2}$), respectively. (c) O K-edge NEXAFS spectra acquired after exposure to 20000 L of O_2 at 620 K with polarizations parallel (black, A_{xy}) and perpendicular (red, A_z) to the surface, respectively.

Additionally, the flattened Ru-TPP/Ag(111) surface pre-annealed to 620 K and then held at room temperature was also exposed to 20000 L of O_2. In contrast to the inertness of the monolayer of non-flattened Ru-TPP towards O_2 at room temperature (see Figure 5.8 (a) and (b)), for this surface two species were obtained in the O 1s spectra (Fig. 5.10 (a)). One of the species (530.3 eV, blue dots) has similar binding energy as the single species obtained upon dosing at 620 K (see Fig. 5.9 (a)), while the second species (532.5 eV, magenta dots) is characterized by ca. 2 eV higher binding energy. This indicates that the former oxygen species is probably more strongly adsorbed than the latter one which disappears at 620 K. Moreover, in the O K-edge NEXAFS spectra shown in Figure 5.10 (c), the first

feature (labelled peak 1) also shares a similar energy position and linear dichroism as the spectral feature found for oxygen exposure at 620 K (see Fig. 5.9 (c)), and therefore both of them can be assigned to the O bonded to the dehydrogenated phenyl ring carbons. However, there appears also a second species (peak 2) that shows a significantly different dichroism, corresponding to the second component locating at 532.5 eV in the XP spectrum. Given its polarization dependence, this species has a tilt angle of 40° - 50° relative to the surface, and therefore the O atoms do not lie directly atop the Ru centres. In the $Ru\,3d_{5/2}$ signal (Fig. 5.10 (b)), the peak is now shifted by +0.25 eV towards higher binding energy and distinctly changed in the peak profile, possibly evidencing the coordination of this O species with Ru centres, although both O species (i.e., this species as well as the other species possibly bonded in the periphery of the molecule) deviate from our original objective of an oxo group with O lying directly atop or below the Ru centres. Note that the obtained O-RuTPP species 2 should not be a fully oxidized oxo-RuTPP product, as indicated by the limited shift of the $Ru\,3d_{5/2}$ peak observed in Fig. 5.10 (b).

Finally, upon interaction of the molecule with O, the two new valence states in UPS originating from Ru-related interactions are significantly quenched and slightly shifted in binding energy, as shown in Fig. 5.11 (a) and (b). For the spectrum obtained after exposure to O_2 at 620 K, the decreased intensity of the observed spectral features might be due to the varied electronic structure of the flattened porphyrins and upon bonding of O in the periphery; furthermore, the slight shift of the peak position to lower binding energy may arise from the enhanced screening of the core hole (relaxation effect) after flattening of the molecules. In Fig. 5.11 (b), this modifications are more significant for exposure to O_2 at 300 K, and this is presumably a consequence of the partial coordination of O with the Ru centres. With closer inspection, we found that the energy positions of the two spectral features are shifted in the opposite direction with respect to Fig. 5.11(a), providing another hint to the displacement of electron density from the Ru centres to the coordinated O.

Discussion In summary, the RuTPP/Ag(111) monolayer with tilted phenyl legs is not reactive towards O_2 at room temperature, while its reactivity increases by holding the sample at higher temperatures (620 K in our case) during O_2 exposure. We attribute this to the low dissociative sticking probability of O_2 on Ag(111) ($< 10^{-4}$) at room temperature [162] and the inability of the adsorbed molecules to split

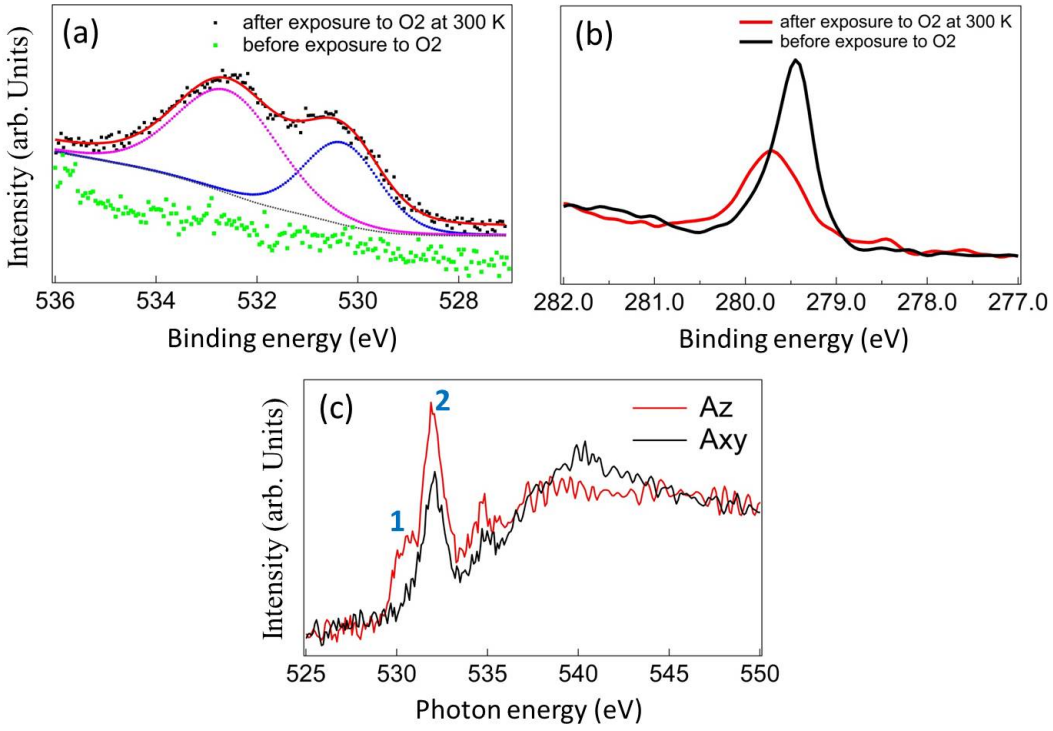

FIGURE 5.10: (a) O 1s core-level spectra acquired before (green dots) and after (black dots) exposure to 20000 L of O_2 of a flattened Ru-TPP/Ag(111) surface held at 300 K. The fitted curve (red line) of the O 1s signal after O_2 exposure is superimposed on the experimental data, with different colours corresponding to different components (see text for discussion). (b) The corresponding signal for the $Ru\,3d_{5/2}$ level. The photon energies used are 680 eV (O 1s) and 410 eV ($Ru\,3d_{5/2}$), respectively. (c) O K-edge NEXAFS spectra acquired after the O_2 exposure with polarization parallel (black, A_{xy}) and perpendicular (red, A_z) to the surface, respectively.

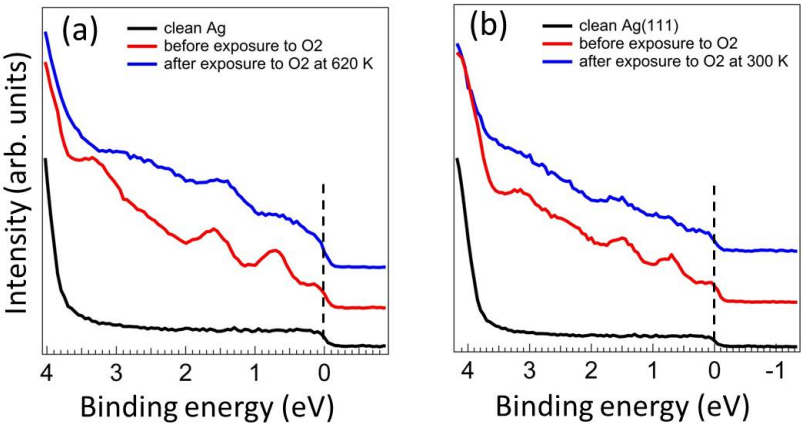

FIGURE 5.11: Valence spectra measured before (red) and after (blue) exposure of a flattened RuTPP/Ag(111) surface held at 620 K (a) and 300 K (b), respectively, to 20000 L of O_2. The photon energy used for recording the spectra is 130 eV. The valence spectra of the clean Ag (black) is shown underneath for comparison.

O_2. On the other hand, the coordination of O with Ru centres of the flattened Ru-TPP/Ag(111) surface held at room temperature is demonstrated by our XPS, UPS and NEXAFS results. However, none of the O species correspond to the expected oxo-RuTPP with O sitting atop or below Ru centres. We may also speculate that the higher reactivity at 620 K or after annealing to 620 K is related to the presence of dehydrogenated Ru-TPP flattened molecules which act as radicals and lead to the coordination of oxygen at the periphery of the molecules and in the molecular plane (rather than perpendicular to it). Moreover, the reactivity of the system towards oxidation is in general very low given that a large exposure of 20000 L of O_2 was used and that only limited binding energy variation of the $Ru\,3d_{5/2}$ peak (shift by less than 0.25 eV) was observed. Since unsupported Ru-TPP has been observed to have a high reactivity towards oxidation for the subsequent donation of oxygen to epoxide reactions [13], we may infer that the inertness of the RuTPP/Ag(111) system presumably originates from a surface-induced quenching of the reactivity. This quenching effect may originate not only from the observed Ag-Ru interaction which leaves the Ru centre in a metallic state, but also from the low dissociative sticking probability of O_2 on the Ag(111) surface (i.e., the Ag(111) surface may passivate the Ru-TPP species). In appendix B, we attempted to further demonstrate the latter assumption by exposing the non-flattened Ru-TPP molecules on Ag(111) to ionized or split oxygen at room temperature, whereby a much higher sticking of O_2 to Ag(111) is achieved and a clear oxidation of Ru centres is observed. On the other hand, the Ag(110) surface has been reported to display a much higher reactivity towards O_2 than Ag(111), with an initial sticking probability of 3×10^{-3} at room temperature [162]. In the following subsection, the interaction of the Ru-TPP/Ag(110) surface with O_2 is investigated through experiments performed in our on-campus laboratory in Garching, which will reveal the effect of the supporting substrate in a direct way.

5.2.4 Interaction of Ru-TPP with Oxygen on Ag(110)

We now turn to explore the reactivity of adsorbed Ru-TPP towards oxygen by changing the supporting substrate from Ag(111) to Ag(110). The TPD spectrum (data not shown) of a Ru-TPP multilayer on Ag(110) largely resembles that on Ag(111), with the onset of molecular flattening starting at 620 K. Therefore, the Ru-TPP/Ag(110) monolayer with non-flattened molecules was prepared by annealing of the multilayer at 550 K.

Fig. 5.13 shows the XP spectra of the O 1s and $Ru\,3d_{5/2}$ levels before and after exposure of the clean Ag(110) surface and Ru-TPP monolayer on Ag(110) to 10000 L of oxygen at room temperature. After exposing of the clean Ag(110) surface to O_2, sharp O 1s peak is observed at a binding energy of 528.3 eV (Fig. 5.13 (a)), in accordance with the reported data for the atomically adsorbed oxygen on Ag(110) [163]. The large atomic-oxygen peak demonstrates the much higher dissociative sticking coefficient of Ag(110) towards O_2 dissociation compared to Ag(111) (according to the literature, this sticking coefficient is almost two orders of magnitude higher on Ag(110) than on Ag(111) [162]). When the same dosage of oxygen is applied to the Ru-TPP monolayer on Ag(110), two additional components locating at 530.0 eV and 532.3 eV (labelled 1 and 2 in Fig. 5.12 (b)), respectively, appears on the high binding energy side of the atomic oxygen peak. Notably, in contrast to the small shift (0.25 eV) of the $Ru\,3d_{5/2}$ peak upon exposing the flattened monolayer on Ru-TPP/Ag(111) to oxygen, the clear oxidation of the Ru centres is evidenced here by a binding energy shift of the $Ru\,3d_{5/2}$ peak by ca. +1.4 eV (red curve, Fig. 5.12 (c)). Therefore, the spectroscopic data support the formation of oxo-RuTPP species in this case. Moreover, according to previous literature, the O 1s binding energy of oxo-MnTPP (Manganese porphyrins) [164] and that of oxo-TiTPP (Titanium porhyrins) [165] are both located at ca. 530 eV. Therefore, we infer that the O species 1 at 530.0 eV pertains to the formation of oxo-RuTPP. The O species 2 has analogous binding energy as the high-binding-energy species (532.5 eV) in Fig. 5.10 (a), which corresponds to the formation of non-fully oxidized O-RuTPP products due to the small binding energy shift of $Ru\,3d_{5/2}$ peak. Therefore, the oxygen species 2 can be related to a different oxidation state of the Ru centres with respect to species 1. Interestingly, we found that the atomic oxygen species on the RuTPP/Ag(110) surface can be completely removed by holding the sample at 370 K for 10 min, while the species 2 remains constant and the species 1 only slightly changes in intensity and position (upper curves of Fig. 5.12 (b)). In the $Ru\,3d_{5/2}$ spectra in Fig. 5.12 (c) (blue curve), the population of oxo-RuTPP decreases and that of Ru-TPP accordingly increases after holding the sample at 370 K, which suggests the cleavage of the O-Ru bond of oxo-RuTPP and as a consequence the intensity of O species 1 should correspondingly decrease. However this is not the case from the O 1s spectrum. A possible explanation is that the adsorbed O at the periphery of the molecules (e.g., C=O or C-O-C units in the dehydrogenated phenyl ring, as shown on Ag(111)) which is also located at ca. 530 eV (see Fig. 5.9 and 5.10) may now contribute to

the spectral feature labelled 1. This third species could be generated by reaction of atomic O adsorbed on bare Ag(110) with the organic molecules upon heating. In addition, the pristine RuTPP/Ag(110) surface was also exposed to increasing dosage of O_2 (1000 - 14000 L) and held at 370 K for 10 min, whereby the oxygen species 2 was always observed to stay constant while the intensity of the peak at ca. 530 eV either remained almost unchanged or increased after annealing. We may speculate that the peripheral O bond is established and compensate the loss of O due to the cleavage of Ru=O bond in the central cavity under certain circumstance. A proof of the given argument clearly requires more detailed STM and spectroscopic studies and is beyond the scope of the present work.

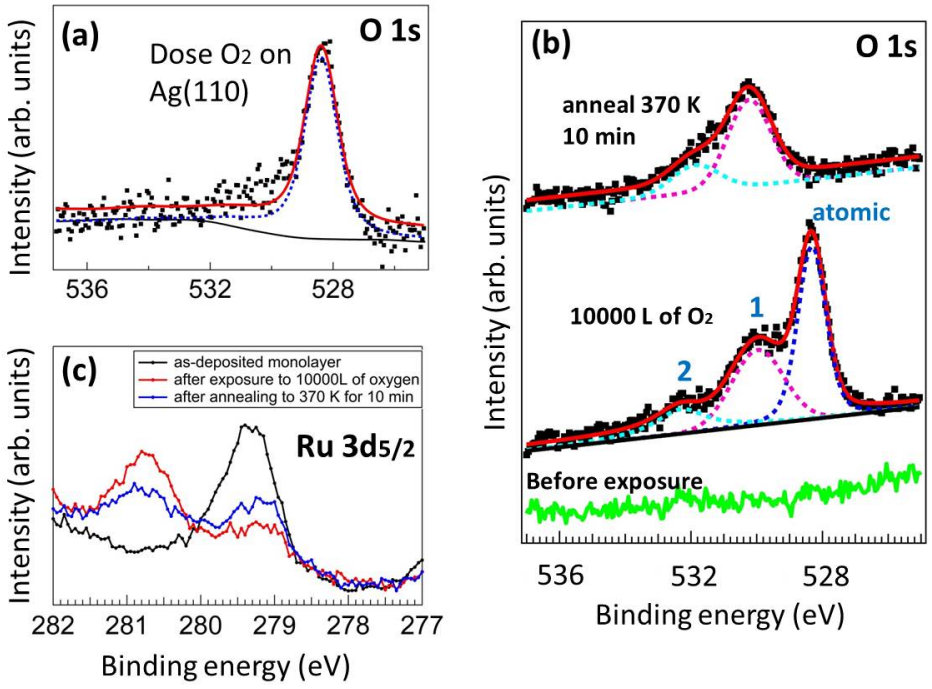

FIGURE 5.12: (a) O 1s spectrum after exposure of the clean Ag(110) surface to 10000 L of O_2 at room temperature. The fitted curves (red line) are superimposed on the experimental data (black dots). (b) O 1s spectra before (green line) and after (middle curve) the same exposure to O_2 of a Ru-TPP monolayer on Ag(110) at room temperature. The upper curve belongs to the O 1s spectrum after annealing the oxygen-exposed surface to 370 K for 10 min. The blue markers (atomic, 1 and 2) label the different components of the O 1s signal displayed underneath the fitted curve and represented with different colors. (c) The corresponding $Ru\,3d_{5/2}$ spectra before (black line) and after (red line) O_2 exposure, and after annealing the oxygen-exposed surface to 370 K for 10 min (blue line). Non-monochromatized MgK_α radiation with photon energy centred at 1253.6 eV was used for the data acquisition.

To gain more insight into the interaction of the Ru-TPP/Ag(110) surface with O_2, the evolution of the O 1s and $Ru\,3d_{5/2}$ spectra with increasing O_2 dosage is

shown in Fig. 5.13. In the $Ru\,3d_{5/2}$ signal (Fig. 5.13 (a)), it can be seen that the oxidation has begun after an exposure of 1000 L, and that the peak intensity corresponding to oxo-RuTPP (vertical red dotted line) gradually increases while that corresponding to Ru-TPP (vertical grey dotted line) accordingly decreases with increasing O_2 dosage. The peak of Ru-TPP is almost extinguished after an exposure of 14000 L. As to the corresponding O 1s signal, the atomic oxygen species on Ag(110) reaches saturation after the first exposure of 1000 L and stays almost constant in the following dosage, which is reasonable since the dissociative sticking probability of O_2 on Ag(110) is reported to be approximately 10^{-3} at room temperature [159, 162]. However, the intensity of the oxygen species 1 is observed to go up gradually with increasing dosage, while that of oxygen species 2 becomes discernible after 8000 L of O_2 exposure; specifically after the exposure of 10000 L the oxidation is probably saturated.

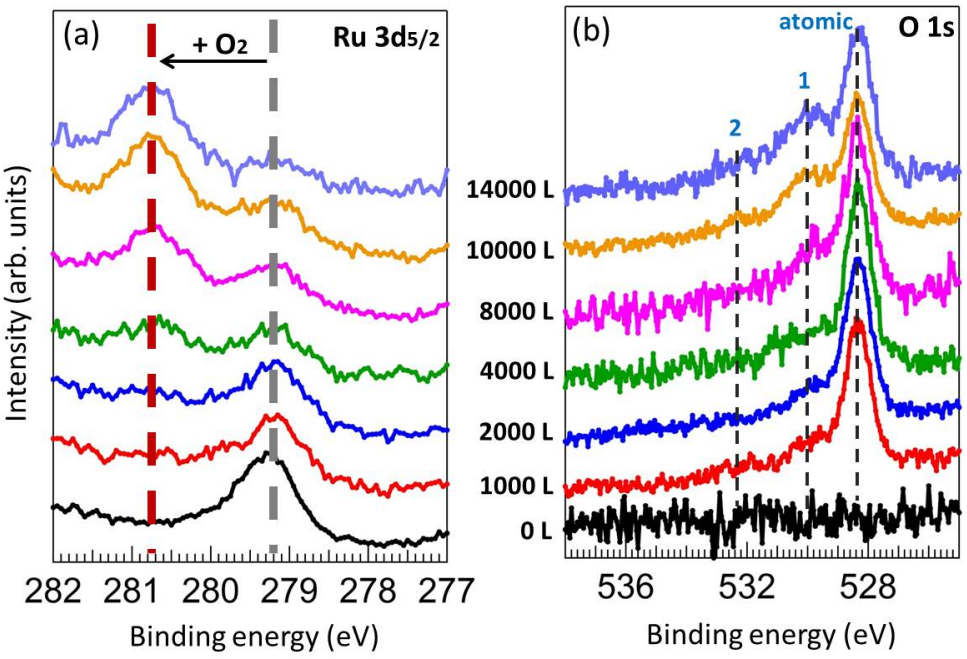

FIGURE 5.13: (a) $Ru\,3d_{5/2}$ and (b) O 1s spectra of a Ru-TPP monolayer on Ag(110) after exposing it to increasing dosage of O_2 at room temperature, from 1000 L to 14000 L as noted in the middle. Non-monochromatized MgK_α radiation was used for the spectral acquisition. A new preparation cycle was performed for each specific oxygen dosage.

It is known that an effective catalyst for an epoxide reactions must form an intermediate species, e.g., dioxo- or oxo-RuTPP in our case, that is weakly bound such that the intermediate species readily donates oxygen to the subsequent epoxide

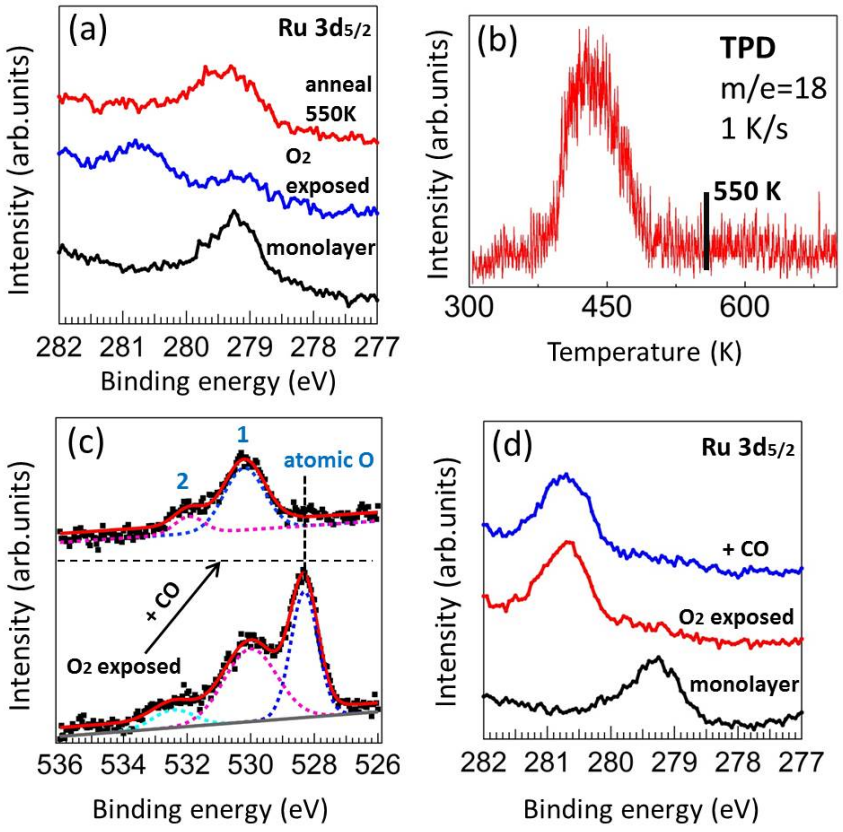

FIGURE 5.14: (a) $Ru\,3d_{5/2}$ spectra of a Ru-TPP monolayer (black) on Ag(110), of the monolayer exposed to 10000 L of O_2 (blue) and of the oxygen-exposed monolayer after annealing to 550 K (red). (b) TPD spectrum for m/e 18 from a Ru-TPP monolayer on Ag(110) exposed to 10000 L of oxygen and subsequently annealed to 370 K for 10 min; the temperature was ramped with a rate of 1 K/s. (c) O 1s spectra of the Ru-TPP monolayer on Ag(110) after exposing it to 10000 L of O_2 (bottom) and then subsequently to 1000 L of CO (upper) at room temperature. (d) $Ru\,3d_{5/2}$ spectra of the as-prepared Ru-TPP monolayer (black) on Ag(110), of the monolayer after exposure to 10000 L of O_2 (red) and of the oxygen-exposed monolayer after exposure to 1000 L of CO (blue) at room temperature. Non-monochromatized MgK_α radiation was employed for the acquisition in (a), and AlK_α radiation was used for the spectra in (c) and (d).

reactions [155]. As indicated above, after exposing RuTPP/Ag(110) surface to O_2 at room temperature and holding at 370 K for 10 min, the atomic oxygen species can be easily cleared up, while the oxygen species 2 at the highest binding energy stays stable below 370 K and the species 1 shows the potential to reversibly interact with O_2 if our assumption can be confirmed. To shed more light on this issue, the TPD measurement for the oxygen-exposed (10000 L) RuTPP/Ag(110) surface after holding it at 370 K for 10 min was performed (Fig. 5.14 (b)). The desorption peak at 450 K for m/e 18 demonstrates that water might be desorbed during annealing, presumably stemming from the recombination of the hydrogen atoms from partial dehydrogenation and the oxygen atoms from either the O bond in the periphery or the O-Ru bond in the central cavity (atomic O has been cleared up below 370 K, see Fig. 5.12 (b)). The TPD spectrum also demonstrates that a high temperature than 370 K is required for the full removal of the coordinated oxygen (i.e., both species 1 and 2). Indeed, in Fig. 5.15 (a), the oxo-RuTPP is almost completely restored to the state before oxygen exposure after annealing to 550 K.

In a different series of experiments, the RuTPP/Ag(110) surface was first exposed to 10000 L of O_2 and then further exposed to 1000 L of CO at room temperature (Fig. 5.14 c-d). Notably, only the atomic oxygen species is observed to be reactive with CO, presumably being removed as CO_2 as reported in Ref. [159]; conversely, the oxygen species 1 and 2 that correspond to oxygen coordinated to Ru or the periphery remain unchanged. Specifically, in the $Ru\,3d_{5/2}$ signal the feature corresponding to the oxo-RuTPP species stays constant upon CO exposure. Thus, the O-RuTPP/Ag(110) system is demonstrated to be stable under a partial CO atmosphere.

5.3 Conclusions

First, based on the lab-source ($Al\,K_\alpha$) XPS and TPD measurements, we demonstrates that 2H-TPP monolayer can be prepared by desorption of the multilayer at 470 K and the molecular flattening starts at 550 K. Due to the large temperature separation between the multilayer desorption and the molecular flattening, well-defined monolayers with non-flattened or flattened molecules can be separately prepared.

The Ru-TPP monolayer on Ag(111) with tilted phenyl legs can be prepared with a similar protocol as that used for 2H-TPP on Ag(111), but higher temperature is required for both the multilayer desorption and the molecular flattening. The flattening of Ru-TPP molecules was found to be a multi-step process according to the NEXAFS results, and the XPS and UPS data both indicate an interaction of the Ru metal centre with the Ag surface. Upon exposure to O_2, the non-flattened Ru-TPP molecules on Ag(111) were shown to be completely inert towards oxygen coordination at room temperature. Conversely, two coordinated oxygen species were observed when the flattened Ru-TPP molecules (and presumably further dehydrogenated in the peripheral aromatic rings after annealing to 620 K) on the Ag(111) surface were exposed to the same dosage of oxygen at room temperature. In addition, when the surface is held at 620 K during the oxygen exposure, a single oxygen species is retained, which does not appear to come from the formation of oxo-RuTPP but rather from oxygen coordinated to the periphery of the molecules. On the whole, the energy shift of the $Ru\,3d_{5/2}$ peak which can be regarded as a direct monitor of the oxidation state of the Ru centres is very limited probably due to the Ru-Ag interaction that leaves the Ru centre in a quasi metallic state and to the low dissociative sticking probability of O_2 on Ag(111). In conclusion, the reactivity of the Ru-TPP molecules is quenched by the underlying Ag(111) surface.

For further understanding, the Ag(110) surface with a much higher reactivity towards O_2 than Ag(111) was employed as a support for the Ru-TPP molecules. From the XPS results, the Ru centre is in a similar metallic state as on Ag(111), but the oxidation of the non-flattened Ru-TPP molecules upon O_2 exposure at room temperature is now observed. Moreover, a clear component of atomic oxygen locating at ca. 528.3 eV is observed on both the bare Ag(110) and RuTPP/Ag(110) surfaces, indicating the high dissociative sticking coefficient of O_2 on Ag(110). This atomic oxygen species can be removed by light annealing to 370 K or by exposure to CO, while the two oxygen species coordinated to the molecules are still retained. In particular, after annealing to 370 K, we speculate that the coordinated oxygen species at lower binding energy (530.0 eV) that we attribute to the formation of oxo-RuTPP owns the potential to reversibly interact with oxygen, which is crucial for catalysis of epoxide reactions. Furthermore, both of the coordinated oxygen species can be removed after annealing to 550 K and the Ru centres restored to the state before oxygen exposure. These results demonstrate that the Ru-TPP/Ag(110) may represent a better system than Ru-TPP/Ag(111) in terms

of its reactivity towards oxygen and of its potential catalytic activity in epoxide reactions. The comparison of the Ru-TPP/Ag(111) and Ru-TPP/Ag(110) system also suggests that the substrate can optimise the reactivity of heterogeneous systems.

Chapter 6

Summary, Conclusions and Outlook

In this thesis, by combination of synchrotron-based and conventional (lab-based) spectroscopic techniques, the electronic and geometric structure, the thermal stability, and the charge transfer dynamics of aromatic SAMs on a ferromagnetic Co(0001) surface, as well as the interaction with oxygen of self-assembled ruthenium tetraphenyl porphyrin molecules on Ag surfaces (either Ag(111) or Ag(110)) have been explored.

In a first set of experiments, a well-defined monolayer of 4-fluorobenzoic acid (4-FBA) molecules has been prepared and characterized in depth. A bidentate bonding of the molecules with cobalt is formed through the carboxylate headgroup, while the fluorine tailgroup is located at the SAM-vacuum interface and has no direct contact to the substrate. Accordingly, the NEXAFS results indicate an almost upright geometry for the adsorbed molecules. The monolayer is found to be stable up to 390 K, as highlighted by fast-XPS measurements. The characteristic electron transfer time from the carboxylate headgroup and the fluorine tailgroup, respectively, to the cobalt substrate has been determined with the Core Hole Clock (CHC) approach. The charge transfer of the core-excited tailgroup to the Co(0001) surface takes place on the femtosecond time scale, being in the range between approximately 1 and 22 fs when the photon energy is detuned across the resonance, and with a decreasing trend at increasing photon energy. Moreover, the dynamic charge transfer time determined with the CHC method is found to be in good agreement with the theory of static molecular conductance, thus evidencing

the tunnelling mechanism of the tailgroup-to-substrate electron transfer. As to the headgroup-to-substrate charge transfer, the overwhelming contribution of the normal Auger decay channels gives evidence of the ultrafast charge transfer time in the attosecond regime (the upper limit for the CT time being 0.6 fs), and again a general decrease of the transfer time of the core-excited O 1s electron to the substrate is observed as the photon energy is scanned across the O 1s-$2\pi^*$ resonance.

Subsequently, a SAM of 4-cyanobenzoic acid (4-CBA) molecules with a cyano tailgroup and the same headgroup as 4-FBA was prepared on the Co(0001) surface. A mixture of monodentate and bidentate bonding of the carboxylic headgroup with cobalt as well as a minority lying down phase (18%) involving the hybridization of CN with cobalt were found, pointing toward a much larger structural disorder of the 4-CBA SAM compared with its 4-FBA counterpart on cobalt. Nonetheless, the NEXAFS data indicate that the cyano tailgroup can be employed as a better spectroscopic marker than the fluorine tailgroup due to the existence of two orthogonal π^* orbitals in the former case. In the majority phase, the molecules of the 4-CBA SAM adsorb with a larger tilting angle (relative to surface normal) than in the 4-FBA SAM. In contrast to the ultrafast tailgroup-to-substrate charge transfer at the 4-FBA/Co interface, no such charge transfer is evidenced for 4-CBA on cobalt, probably due to the coexisting monodentate bonding of the headgroup to cobalt and to the larger disorder in the SAM. These findings demonstrate that on reactive metals the change of molecular tailgroup (here: from F to CN) has a large impact not only on the structure of the SAMs and on the molecule-substrate interactions, but also on the charge transfer dynamics, thus highlighting the importance of the control of the interfacial structure to tailor charge transfer performances in electronic applications.

Furthermore, to study the effect of the headgroup on the interfacial properties of SAMs, a monolayer of thiolate-bonded 4-fluorothiolphenol (4-FTP) molecules, which can be regarded as a replacement of the headgroup of 4-FBA from carboxylate to thiolate, was prepared on the Co(0001) surface. As a result, the C-S bond was found to start breaking at or below 190 K, indicative of much lower thermal stability of the 4-FTP SAM compared with that of the 4-FBA SAM. Therefore, we applied an incremental vapour-phase deposition approach at 80 K instead of the commonly used method of multilayer desorption to minimize the

occurrence of C-S bond breaking. On the other hand, the price of this incremental low temperature deposition approach is that the molecules in both the mono- and submonolayer films lie flat on the cobalt surface, in contrast to the other approach where the 4-FTP molecules tend to stand up after the standard annealing protocol (e.g., on Ni(111)). On the other hand, thanks to the flat-lying orientation of the molecules, the tailgroup-to-substrate charge transfer for the 4-FTP/Co(0001) SAM is distinctly faster than that for the 4-FBA/Co(0001) SAM, where the 4-FBA molecules adopt a standing-up adsorption configuration. Moreover, with further polarization-dependent CHC investigations, we found that the charge transfer time for A_z polarization is on average faster than for A_{xy} polarization. This phenomenon is tentatively explained by the more efficient excitation of the π^*-type molecular orbital, which extends over the entire molecule and presumably overlaps with Co 3d orbitals, upon use of linear polarization directed almost perpendicular to the plane of the lying-down aromatic molecules. Finally, we observed a faster charge transfer in the submonolayer film than in the monolayer film, probably as a consequence of the stronger coupling to the substrate of the less densely-packed molecules.

Based on the comprehensive comparative investigation of the electronic and geometric structure, the thermal stability and the charge transfer dynamics of these three aromatic SAMs on cobalt, the 4-FBA/Co SAM appears to be superior in terms of both thermal stability and conductivity and therefore represents a promising candidate for fundamental studies and applications in the field of molecular electronics and spintronics. In particular, we envisage the carboxylate bonding to be a promising alternative to the thiolate-mediated anchoring of SAMs, thanks to the higher thermodynamic stability, thus providing suitable model systems for the study of the spin-dependent transport at the SAM/ferromegnetic metals interfaces.

In an additional set of experiments, 2H-TPP and Ru-TPP porphyrin molecules on Ag substrates were investigated through our experimental multi-technique approach. A 2H-TPP monolayer on Ag(111) was prepared by desorption of the multilayer at 470 K, and the molecular flattening due to cyclo-dehydrogenation of the molecules was shown to start at 550 K by monitoring the signal of mass 2 (H_2) in TPD measurements. The Ru-TPP monolayer on Ag(111) was prepared with an analogous protocol. However, the onset of the flattening of the Ru-TPP molecules appears to be shifted to 620 K, most likely due to the stronger interaction of

the molecules with the underlying Ag substrate via the centrally coordinated Ru atoms. Afterwards, the interaction of the RuTPP/Ag(111) system with molecular oxygen under UHV conditions was utilized as a measure of its catalytic activity. The spectroscopic results demonstrate that the reactivity of the Ru-TPP/Ag(111) system toward splitting and coordination of oxygen is quenched by the Ag(111) surface, probably due to the Ru-Ag interaction that leaves the Ru centres in a metallic state and to the low dissociative sticking probability of O_2 on Ag(111). Conversely, for Ru-TPP molecules adsorbed on the Ag(110) surface, a higher dissociative sticking probability and the clear oxidation of the Ru centres upon O_2 exposure at room temperature are observed. Moreover, the oxygen species coordinated to the Ru centres are stable under a partial CO atmosphere and can only be removed by annealing to 550 K in UHV, thus restoring the Ru oxidation state of the molecules. The different behaviour of the Ru-TPP monolayers on the Ag(111) and Ag(110) surfaces demonstrates that the Ru-TPP/Ag(110) system may represent a better candidate in site-selective heterogeneous catalysis thanks to its potential catalytic activity. Forthcoming studies will be devoted to gain further insight into the role of the substrate on the reactivity of the organic layers, e.g., by using a semiconducting layer (such as graphene or boron nitride) to electronically decouple the metal complexes from the underlying metal surface.

Appendix A

Determination of the Molecular Orientation in 4-FTP SAMs

Effect of the Deposition Procedure In a 4-FTP/Co(0001) SAM prepared via incremental deposition at 80 K, the molecules adopt a flat-lying molecular orientation, while 4-FTP SAMs on Ni(111) prepared with the standard approach by annealing of a 4-FTP multilayer at 200 K exhibit upright molecular orientation. Apart from the different substrates in the two above situations, the incremental deposition without annealing step used to prepare the 4-FTP/Co(0001) SAM compared to the single-step deposition followed by an annealing step for 4-FTP/Ni(111) SAM might also be at the origin of the different orientation. To identify the cause, some off-line XPS and UPS measurements were carried out with non-monochromatized MgK_α and $AlK\alpha$ radiation, and helium lamp equipped with a linear polarizer (see section 3.2). These proof-of-principle experiments were done focusing on the 4-FTP/Ni(111) system. Based on the fact that the 4-FBA/Co(0001) (section 4.2) and 4-FBA/Ni(111) SAM [20, 133] prepared with the same procedure present very similar electronic structure, adsorption geometry and charge transfer dynamics, and that both cobalt and nickel belong to the iron group, we may assume the conclusions for the 4-FTP/Ni(111) system are also applicable to 4-FTP/Co(0001).

4-FTP molecules were adsorbed onto Ni(111) with the same procedure as for 4-FTP/Co(0001). The Ni(111) single-crystal surface was cleaned by cycles of Ne^+ or Ar^+ ion sputtering and annealing to 1100 K, until no contamination was detected with XPS and LEED shows a sharp (1 x 1) hexagonal pattern. Details of the

experimental methods and the photon source can be found in section 2 and section 3.2, respectively.

First of all, a comparison of the C 1s, F 1s and S 2p core-level spectra of the 4-FTP/Ni(111) monolayer prepared according to two different procedures is displayed in Fig. A.1. The standard preparation followed the same procedure as in Ref. [20, 133], and the stepwise protocol corresponds to the incremental deposition of 4-FTP up to monolayer completion (0.04 Torr*s) at 80 K, followed by an annealing step to 200 K. According to the XPS data, these two protocols yield identical results. However, XPS data are not capable of providing information of the molecular orientation.

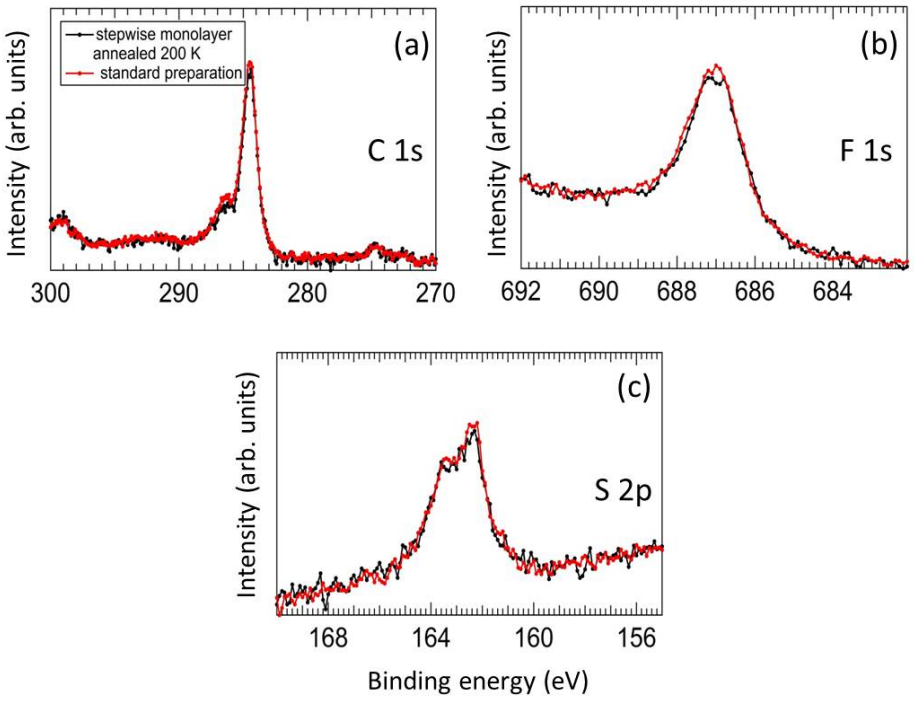

FIGURE A.1: Comparison of the (a) C 1s, (b) F 1s and (c) S 2p core-level spectra of 4-FTP monolayers prepared with the standard and the stepwise approach (both followed by an annealing step to 200 K), respectively. The photon source used to excite the XP spectra is the non-monochromatized Al K_α radiation with photon line centered at 1486.6 eV.

Polarization-dependent UPS measurements were performed to assess the molecular orientation in the monolayers. Two polarizations were employed, with the *s*-polarized radiation and *p*-polarized radiation being parallel and perpendicular to the surface plane, respectively. The incidence angle of the photons (grazing incidence) and the detection geometry (normal emission) of photoelectrons are

identical in all the measurements. The resulting dichroism (i.e., the difference spectrum between *s*-polarized and *p*-polarized spectra after normalization at the Fermi edge) is a fingerprint of the molecular orientation, in much the same way as provided by NEXAFS. Fig. A.2 displays the UP spectra representative of the standard 4-FTP SAM, excited with *s*- and *p*-polarized He I radiation, respectively. The comparison of its dichroism to the analogous signal from the "stepwise" 4-FTP monolayer is displayed in the inset. In both UP spectra, three pronounced features can be observed at ca. 6 eV, 8 eV and 10.4 eV, respectively. According to the previous work [166], the feature at ca. 6 eV comprises major sulfur contributions being affected by the thiolate-metal bond; the feature at ca. 8 eV was related to the aromatic ring, e.g., benzene-related states of π symmetry, and the one at ca. 10.4 eV can be related to the fluorinated and benzene-related states. The valence spectra of the standard 4-FTP SAM shows a strong linear dichroism (inset: magenta dotted line), indicating a strong preferential ordering in the SAM and a good agreement with the NEXAFS measurement [20, 133]. Since the molecular orientation in the standard 4-FTP SAM is close-to-upright, the stronger intensities of these spectral features with *s*-polarized radiation suggest a prevailing contribution of states with π symmetry. On the other hand, the similarity of the two dichroic signals (inset) demonstrates a very similar molecular configuration in both SAMs. Based on the XPS and UPS data, we therefore conclude that, for the 4-FTP/Ni(111) SAM, the stepwise deposition does not cause a different molecular orientation as long as a final annealing step to 200 K is applied.

Furthermore, a comparison of the valence spectra of the stepwise monolayer at 80 K to those of the stepwise monolayer after flash to 200 K is presented in Fig. A.3, aiming to investigate the role of the annealing step in establishing the molecular orientation. In the spectra of the monolayer at 80 K (Fig. A.3 (a)), the three spectral features mentioned above are apparently suppressed compared with their counterparts for the annealed monolayer (Fig. A.3 (b)). The dichroic signal of the monolayer at 80 K (magenta line, Fig. A.3 (c)) again indicates a preferential ordering of molecules in the film. However, the clear difference from the dichroic signal of the annealed monolayer (blue dotted line) suggest a difference in molecular configuration, i.e., a more flat-lying orientation of the molecules in the monolayer at 80 K as suggested by the features at 8.9 eV (Fig. A.3 (c)), which are almost in anti-phase. At a closer inspection, we found that the spectral features of the monolayer at 80 K are located at higher binding energies than those of the annealed monolayer (indicated with green and black vertical lines).

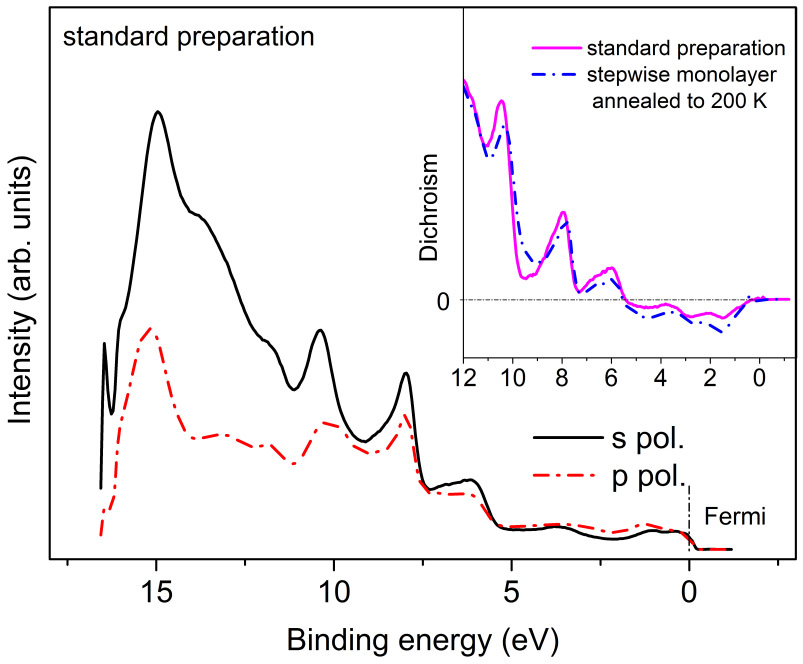

FIGURE A.2: UP spectra of the standard (see text) 4-FTP/Ni(111) SAM excited with (black line) *s*- and (red dotted line) *p*-polarized He I radiation. The inset shows the dichroic signal of 4-FTP/Ni(111) SAMs prepared stepwise (blue dotted line) and in the standard way (magenta line), respectively. The spectra have been normalized to the step at the Fermi edge for comparison.

It has been reported that the molecular π^* levels are shifted to higher binding energy as a consequence of the interaction with the metal substrate when the molecules are flat-lying on the surface [167]. Therefore, in our case, the shifted binding energies and the distinct dichroism both point towards a more flat-lying molecular orientation in the monolayer at 80 K. We infer that the backbone-substrate interaction is relatively strong in the flat configuration, and reorientation into the upright geometry is thermally activated, requiring an annealing step to 200 K. Notably, this demonstrates that the annealing step plays a dominant role in the reorientation of molecules in the 4-FTP/Ni(111) monolayer.

Effect of Lateral Interactions Finally, a submonolayer with a lower packing density was deposited in a single step at 80 K. Figure A.4 (a) shows a comparison of the core-level spectra of the standard monolayer and this submonolayer film. The clear contrast of intensity demonstrates the lower packing density in the low-coverage film. The spectral features are almost identical, except for the presence

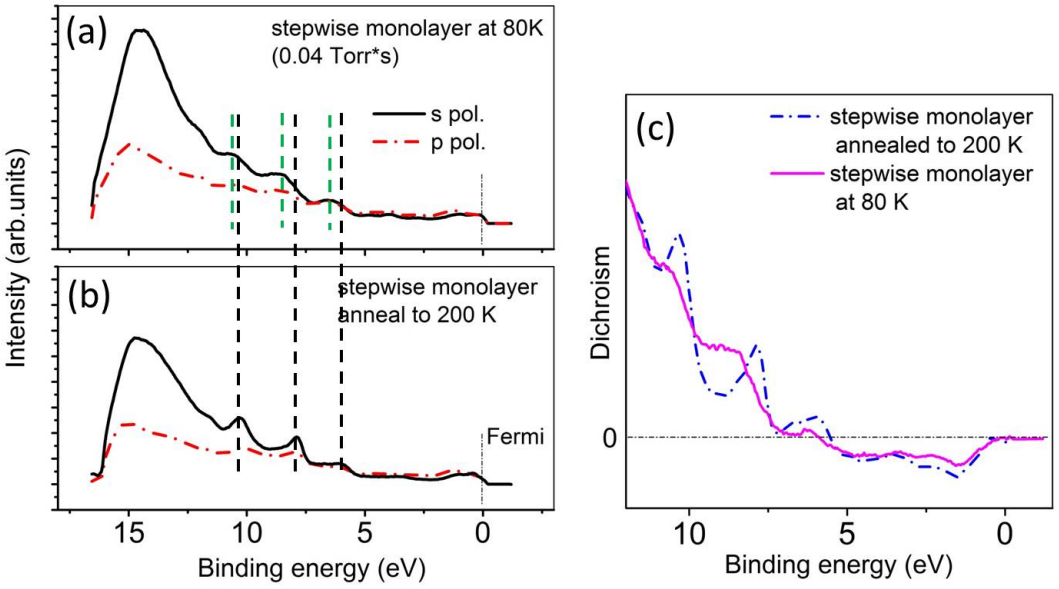

FIGURE A.3: UP spectra of a 4-FTP/Ni(111) monolayer (a) prepared stepwise by incremental deposition up to monolayer completion at 80 K, and (b) of the same monolayer after an annealing step to 200 K. The right panel shows the dichroic signal of the as-deposited (magenta line) and annealed (blue dotted line) monolayers.

of a minor component at ca. 161 eV in the $S\,2p_{3/2}$ level of the standard monolayer characteristic of atomic sulfur (This is in agreement with our conclusion for the 4-FBA/Co(0001) system that the generation of atomic sulfur is temperature dependent).

The submonolayer film was then annealed to 200 K for a few seconds. A comparison of the valence spectra of this system before and after annealing is displayed in Fig A.4 (b). Under both polarizations, the near-overlap of the curves indicates that the molecular orientation at submonolayer coverage does not change upon annealing. In addition, the quenching of the main spectral features, similar to the spectra of the stepwise monolayer at 80 K as shown in Fig. A.3 (a), indicates a more flat-lying orientation of molecules relative to the standard monolayer. It can be noted that this conclusion is also confirmed by preliminary NEXAFS data (not shown) taken at 80 K on low-coverage films of 4-FTP on Ni(111). The flat-lying

orientation is often observed in the initial stage of gas-phase dosing [57, 89, 91–93], and can be ascribed to the lack of sufficient intermolecular interaction and the maximization of the interaction of the molecules with the substrate.

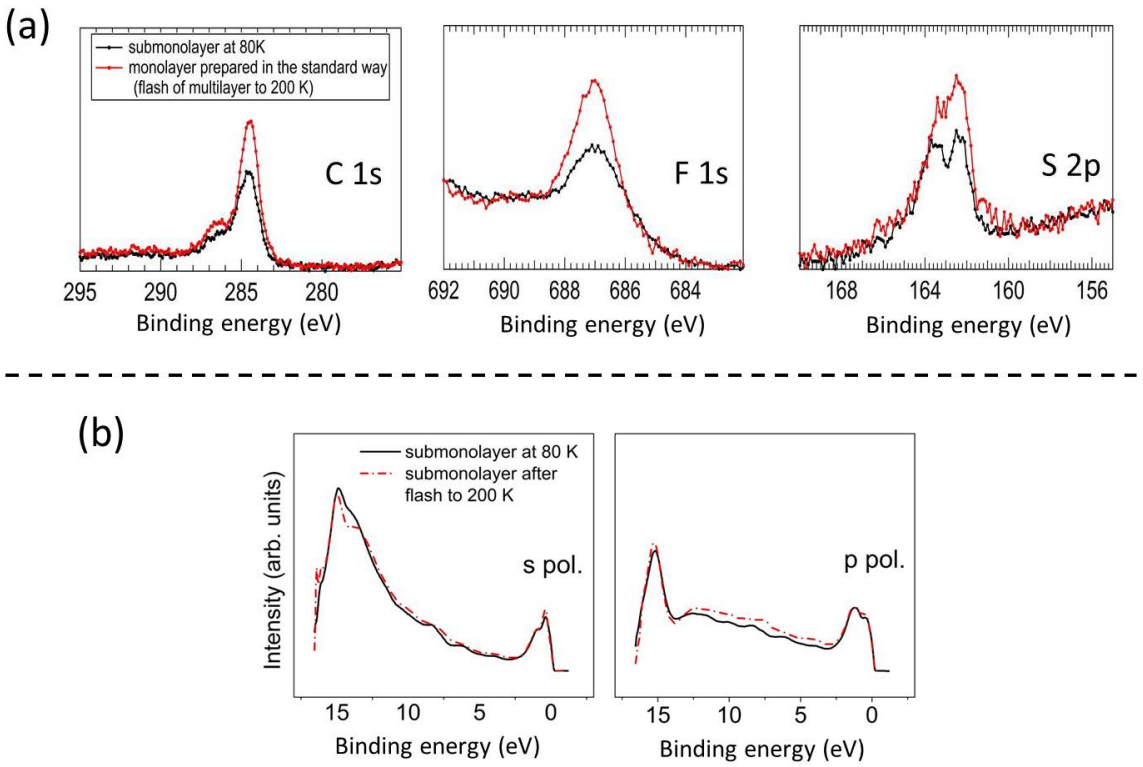

FIGURE A.4: (a) Comparison of the core-level spectra of the 4-FTP/Ni(111) submonolayer film (black lines) deposited in a single step at 80 K to those of the 4-FTP/Ni(111) monolayer (red lines) prepared with the standard protocol. (b) Valence spectra of the 4-FTP/Ni(111) submonolayer film before (black lines) and after (red dash lines) annealing to 200 K. The spectra were taken in a grazing incidence and normal emission geometry, and curves excited with *s* and *p* polarization are shown.

We therefore tentatively conclude that the annealing step (200 K in the case of 4-FTP/Ni(111)) rather than the deposition procedure (i.e., stepwise or single-step deposition) plays a dominant role in the molecular orientation in the 4-FTP/Ni(111) monolayer. The molecules first adopt a flat-lying orientation upon incremental deposition up to monolayer completion at 80 K, but they reorient themselves into the upright configuration upon annealing to 200 K. However, the molecular orientation in a submonolayer with a much lower packing density than in the monolayer does not change with the annealing step, indicating the importance of intermolecular interaction on the molecular orientation. An analogous

mechanism is probably applicable to interpret the flat-lying orientation of 4-FTP SAM on Co(0001) discussed in section 4.4.

Appendix B

Dosing O_2 Through Sputter Gun onto Ru-TPP/Ag(111) Surface at 300 K

To confirm our assumption that the low sticking probability of the Ag(111) surface toward O_2 dissociation may passivate the reactivity of the RuTPP/Ag(111) system, a series of experiments were carried out by exposing the non-flattened Ru-TPP molecules on Ag(111) to only 600 L of ionized oxygen (O_2^- or O_2^{2-} or split oxygen) at room temperature. The oxygen was ionized by passing through a conventional sputter gun facing the Ag(111) surface, and the accelerative high-voltage of the sputter gun was switched off (i.e., the energy of ions set to 0) to prevent the Ru-TPP/Ag(111) surface from being sputtered. As a consequence, a much higher sticking coefficient of oxygen on the Ag(111) surface is achieved, which is directly reflected by the appearance of the atomic oxygen peak in Fig. B.1 (c). Fig. B.1 (a - b) shows the O 1s and $Ru\,3d_{5/2}$ spectra before and after exposing the RuTPP/Ag(111) surface held at room temperature to the ionized oxygen. In the O 1s signal, two oxygen species are located at 530.3 (majority species) and 533.0 eV (minority species), respectively; in the $Ru\,3d_{5/2}$ spectrum, a binding energy shift of the peak by more than +1 eV supports the formation of oxo-RuTPP. Therefore, the former oxygen species at 530.3 eV that is typical of oxygen coordinated to the centre of metalloporphyrins (e.g., oxo-MnTPP in Ref. [164] and oxo-TiTPP in Ref. [165]) can be related to oxo-RuTPP. In analogy to the assignment made in Fig. 5.12 (b), the oxygen species at higher binding energy can be tentatively assigned to a different oxidation state of the Ru centres.

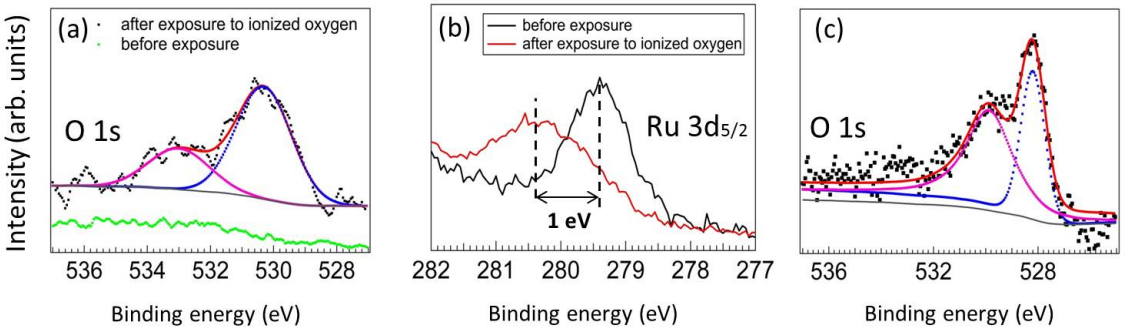

FIGURE B.1: (a) O 1s and (b) $Ru\,3d_{5/2}$ spectra measured before and after exposure of the Ru-TPP/Ag(111) surface held at room temperature to oxygen ions. (c) O 1s spectrum measured after the adsorption of oxygen ions on clean Ag(111) surface. The fitted curves (red lines) are superimposed on the experimental data (black dots), with different colours corresponding to different components. Assignments are included in the text. Non-monochromatized AlK_α radiation was used for the spectral acquisition.

In summary, since non-flattened Ru-TPP molecules on the Ag(111) surface kept at room temperature have been demonstrated to be completely inert towards molecular oxygen (see Fig. 5.8 (a-b)), the results presented above suggest that the reactivity of the RuTPP/Ag(111) system toward oxygen at room temperature can be significantly enhanced when the dissociative sticking probability of O_2 on the substrate is improved (either by using ionized O_2 or by changing the substrate to Ag(110)).

Bibliography

[1] J. C. Love, L. A. Estroff, J. K. Kriebel, R. G. Nuzzo, and G. M. Whitesides. Self-assembled monolayers of thiolates on metals as a form of nanotechnology. *Chemical Reviews*, 105:1103–1170, 2005.

[2] A. Ulman. Formation and structure of self-assembled monolayers. *Chemical Reviews*, 96:1533–1554, 1996.

[3] Z. Mekhalif, J. Riga, J.-J. Pireaux, and J. Delhalle. Self-assembled monolayers of n-dodecanethiol on electrochemically modified polycrystalline nickel surfaces. *Langmuir*, 13:2285–2290, 1997.

[4] A. N. Caruso, L. G. Wang, S. S. Jaswal, E. Y. Tsymbal, and P. A. Dowben. The interface electronic structure of thiol terminated molecules on cobalt and gold surfaces. *Journal of Materials Science*, 41:6198–6206, 2006.

[5] F. Blobner, R. Han, and P. Feulner et al. Spin-dependent electron transfer dynamics probed by resonant photoemission spectroscopy. *Phys. Rev. Lett.*, 112:086801, 2014.

[6] H. B Akkerman and B. de Boer. Electrical conduction through single molecules and self-assembled monolayers. *Journal of Physics: Condensed Matter*, 20:013001, 2008.

[7] S. M. Lindsay and M. A. Ratner. Molecular transport junctions: Clearing mists. *Advanced Materials*, 19:23, 2007.

[8] P. A. Brühwiler, O. Karis, and N. Martensson. Charge-transfer dynamics studied using resonant core spectroscopies. *Rev. Mod. Phys.*, 74:703–740, 2002.

[9] F. Blobner, P. B. Coto, F. Allegretti, M. Bockstedte, and P. Feulner et al. Orbital-symmetry-dependent electron transfer through molecules assembled

on metal substrates. *The Journal of Physical Chemistry Letters*, 3:436–440, 2012.

[10] W. Wurth and D. Menzel. Ultrafast electron dynamics at surfaces probed by resonant auger spectroscopy. *Chemical Physics*, 251:141 – 149, 2000.

[11] L. Wang, L. Liu, W. Chen, Y. Feng, and A. T. S. Wee. Configuration-dependent interface charge transfer at a molecule-metal junction. *Journal of the American Chemical Society*, 128:8003–8007, 2006.

[12] L. Wang, W. Chen, and A. T. S. Wee. Charge transfer across the molecule/metal interface using the core hole clock technique. *Surface Science Reports*, 63:465 – 486, 2008.

[13] J. T. Groves and J. S. Roman. Nitrous oxide activation by a ruthenium porphyrin. *Journal of the American Chemical Society*, 117:5594–5595, 1995.

[14] B. Hulsken, R. V. Hameren, and J. W. Gerritsen et al. Real-time single-molecule imaging of oxidation catalysis at a liquidsolid interface. *Nature Nanotechnology*, 2:285–289, 2007.

[15] A. C. Papageorgiou, S. Fischer, and J. V. Barth et al. Self-terminating protocol for an interfacial complexation reaction in vacuo by metal organic chemical vapor deposition. *ACS Nano*, 7:4520–4526, 2013.

[16] M. F. Ebel and H. Ebel. About the charging effect in X-ray photoelectron spectrometry. *Journal of Electron Spectroscopy and Related Phenomena*, 3: 169 – 180, 1974.

[17] S. Hüfner. *Photoelectron Spectroscopy: principles and applications*. Springer, 2003.

[18] C. S. Fadley and D. A. Shirley. Multiplet splitting of metal-atom electron binding energies. *Phys. Rev. A*, 2:1109–1120, 1970.

[19] J. L. Gervasoni, N. R. Arista, and R. O. Barrachina. Surface and residual-hole effects in electron emission from solids. *Nuclear Instruments and Methods in Physics Research Section B: Beam Interactions with Materials and Atoms*, 67:659 – 663, 1992.

[20] F. Blobner. *Adsorbate on noble and ferromagnetic mmetal: from structural and electronic properties to ultrafast spin-dependent electron trasnport.* Phd thesis, Technische Universitaet Muenchen, 2012.

[21] B. D. Ratner and D. G. Castner. *Electron Spectroscopy for Chemical Analysis (Chapter 4), in: Surface Analysis: the Principal Techniques.* J. Wiley & Sons Ltd., 1997.

[22] C. L. A. Lamont and J. Wilkes. Attenuation length of electrons in self-assembled monolayers of n-alkanethiols on gold. *Langmuir*, 15:2037–2042, 1999.

[23] Y. Park, V. Choong, Y. Gao, B. R. Hsieh, and C. W. Tang. Work function of indium tin oxide transparent conductor measured by photoelectron spectroscopy. *Applied Physics Letters*, 68:2699–2701, 1996.

[24] V. G. Horton, E. T. Arakawa, R. N. Hamm, and M. W. Williams. A triple reflection polarizer for use in the vacuum ultraviolet. *Applied Optics*, 8: 667–670, 1969.

[25] J. Stöhr. *NEXAFS Spectroscopy.* Springer, Berlin 1991.

[26] J. Stöhr and D. A. Outka. Determination of molecular orientations on surfaces from the angular dependence of Near-Edge X-ray-Absorption-Fine-Structure spectra. *Phys. Rev. B*, 36:7891–7905, 1987.

[27] Philip E. Miller and M. Bonner Denton. The quadrupole mass filter: Basic operating concepts. *Journal of Chemical Education*, 63:617, 1986.

[28] J. A. W. Elliott and C. A. Ward. Temperature programmed desorption: A statistical rate theory approach. *The Journal of Chemical Physics*, 106: 5677–5684, 1997.

[29] G. Di Santo, S. Blankenburg, and C. Cudia. Supramolecular engineering through temperature-induced chemical modification of 2H-tetraphenylporphyrin on Ag(111): Flat phenyl conformation and possible dehydrogenation reactions. *Chemistry - A European Journal*, 17:14354–14359, 2011.

[30] A. Wiengarten, Julian A. Lioyd, A. C. Papageorgiou, K. Seufert, and J. V. Barth et al. Surface-assisted cyclodehydrogenation: break the symmetry, enhance the selectivity. *Chemistry - A European Journal*, 21:12285–12290, 2015.

[31] K. Oura, M. Katayama, A.V. Zotov, V.G. Lifshits, and A.A. Saranin. Surface analysis i. diffraction methods. In *Surface Science*, Advanced Texts in Physics, pages 47–75. Springer Berlin Heidelberg, 2003.

[32] C. W. Tang and S. A. VanSlyke. Organic electroluminescent diodes. *Applied Physics Letters*, 51:913–915, 1987.

[33] Peter Peumans, Aharon Yakimov, and Stephen R. Forrest. Small molecular weight organic thin-film photodetectors and solar cells. *Journal of Applied Physics*, 93(7):3693–3723, 2003.

[34] M. Gratzel. Photoelectrochemical cells. *Nature*, 414:338–344, 2001.

[35] A. Nitzan and M. A. Ratner. Electron transport in molecular wire junctions. *Science*, 300:1384–1389, 2003.

[36] T. Hannappel, B. Burfeindt, W. Storck, and F. Willig. Measurement of ultrafast photoinduced electron transfer from chemically anchored ru-dye molecules into empty electronic states in a colloidal anatase TiO2 film. *The Journal of Physical Chemistry B*, 101:6799–6802, 1997.

[37] A. Fohlisch, P. Feulner, F. Hennies, A. Fink, D. Menzel, D. Sanchez-Portal, P. M. Echenique, and W. Wurth. Direct observation of electron dynamics in the attosecond domain. *Nature*, 436:373–376, 2005.

[38] C. Keller, M. Stichler, G. Comelli, F. Esch, S. Lizzit, D. Menzel, and W. Wurth. Femtosecond dynamics of adsorbate charge-transfer processes as probed by high-resolution core-level spectroscopy. *Phys. Rev. B*, 57:11951–11954, 1998.

[39] W. Chen, L. Wang, and A. T. S. Wee et al. Effect of functional group (fluorine) of aromatic thiols on electron transfer at the molecule-metal interface. *Journal of the American Chemical Society*, 128:935–939, 2006.

[40] J.L. Campbell and T. Rapp. *Atomic Data and Nuclear Data Tables*, 77: 1–56, 2001.

[41] F. Blobner, S. Neppl, and P. Feulner. A versatile partial electron yield detector with large acceptance angle and well-defined threshold energy and gain. *Journal of Electron Spectroscopy and Related Phenomena*, 184:483 – 486, 2011.

[42] J. Bauer. Spin and angle effect in the measurement of ultrafast charge transfer times using the core hole clock method. Master's thesis, Technische Universitaet Muenchen, 2012.

[43] T. Coffey, S.G Urquhart, and H. Ade. Characterization of the effects of soft X-ray irradiation on polymers. *Journal of Electron Spectroscopy and Related Phenomena*, 122:65 – 78, 2002.

[44] SPECS. *PHOIBOS Hemispherical Energy Analyzer User Manual V1.2.*

[45] I. W. Drummond. *XPS: Instrumentation and Performance (Chapter 5), in: Surface Analysis by Auger and X-ray Photoelectron Spectroscopy.* IM Publications and SurfaceSpectra Limited, 2003.

[46] N. Koji and O. Toshiaki. Improvement of the detection system in the soft X-ray absorption spectroscopy. *Surface and Interface Analysis*, 44:784–788, 2012.

[47] X. Gao, S. Chen, T. Liu, W. Chen, and A. T. S. Wee. Si clusters on reconstructed SiC (0001) revealed by surface extended X-ray absorption fine structure. *Applied Physics Letters*, 95:144102, 2009.

[48] E. Umbach and Z. Hussain. Angle-dependent changes of auger line shapes from adsorbed molecules. *Phys. Rev. Lett.*, 52:457–460, 1984.

[49] Philip Willmott. *An Introduction to Synchrotron Radiation: Techniques and Applications.* John Wiley & Sons, 2011.

[50] HZB. http://www.helmholtz-berlin.de/.

[51] Elettra Sincrotrone Trieste. http://www.elettra.trieste.it/.

[52] PSP Vacuum Technology. http://home.btconnect.com/pspvacuum99/.

[53] Omicron NanoTechnology. *Instruction Manual: VUV Source HIS 13.*

[54] F. Schreiber. Structure and growth of self-assembling monolayers. *Progress in Surface Science*, 65:151 – 257, 2000.

[55] W.C. Bigelow, D.L. Pickett, and W.A. Zisman. Oleophobic monolayers: I. films adsorbed from solution in non-polar liquids. *Journal of Colloid Science*, 1:513 – 538, 1946.

[56] Ralph G. Nuzzo and David L. Allara. Adsorption of bifunctional organic disulfides on gold surfaces. *Journal of the American Chemical Society*, 105: 4481–4483, 1983.

[57] F. Schreiber, A. Eberhardt, T. Y. B. Leung, P. Schwartz, S. M. Wetterer, D. J. Lavrich, L. Berman, P. Fenter, P. Eisenberger, and G. Scoles. Adsorption mechanisms, structures, and growth regimes of an archetypal self-assembling system: Decanethiol on Au(111). *Phys. Rev. B*, 57:12476–12481, 1998.

[58] L. H. Dubois and R. G. Nuzzo. Synthesis, structure, and properties of model organic surfaces. *Annual Review of Physical Chemistry*, 43:437–463, 1992.

[59] P. E. Laibinis, G. M. Whitesides, D. L. Allara, Y. T. Tao, A. N. Parikh, and R. G. Nuzzo. Comparison of the structures and wetting properties of self-assembled monolayers of n-alkanethiols on the coinage metal surfaces, copper, silver, and gold. *Journal of the American Chemical Society*, 113: 7152–7167, 1991.

[60] M. D. Porter, T. B. Bright, D. L. Allara, and C. E. D. Chidsey. Spontaneously organized molecular assemblies. 4. structural characterization of n-alkyl thiol monolayers on gold by optical ellipsometry, infrared spectroscopy, and electrochemistry. *Journal of the American Chemical Society*, 109:3559–3568, 1987.

[61] M. A. Bryant and J. E. Pemberton. Surface raman scattering of self-assembled monolayers formed from 1-alkanethiols: behavior of films at gold and comparison to films at silver. *Journal of the American Chemical Society*, 113:8284–8293, 1991.

[62] A. Carvalho, M. Geissler, H. Schmid, B. Michel, and E. Delamarche. Self-assembled monolayers of eicosanethiol on palladium and their use in microcontact printing. *Langmuir*, 18:2406–2412, 2002.

[63] A. D. Vogt, T. Han, and T. P. Beebe. Adsorption of 11-mercaptoundecanoic acid on Ni(111) and its interaction with probe molecules. *Langmuir*, 13: 3397–3403, 1997.

[64] Z. Mekhalif, J. Delhalle, J-J. Pireaux, S. Noeel, F. Houze, and L. Boyer. Surface modifications of nickel substrates with self-assembled monolayers of alkanethiols for electrical contact applications. *Surface and Coatings Technology*, 100:463 – 468, 1998.

[65] Z. Mekhalif, F. Laffineur, N. Couturier, and J. Delhalle. Elaboration of self-assembled monolayers of n-alkanethiols on nickel polycrystalline substrates: Time, concentration, and solvent effects. *Langmuir*, 19:637–645, 2003.

[66] S. Bengi, M. Fonticelli, and R. C. Salvarezza et al. Electrochemical self-assembly of alkanethiolate molecules on Ni(111) and polycrystalline Ni surfaces. *The Journal of Physical Chemistry B*, 109:23450–23460, 2005.

[67] L. Tortech, Z. Mekhalif, J. Delhalle, F. Guittard, and S. Geribaldi. Self-assembled monolayers of semifluorinated thiols on electrochemically modified polycrystalline nickel surfaces. *Thin Solid Films*, 491:253 – 259, 2005.

[68] P. G. Hoertz, J. R. Niskala, P. Dai, H. T. Black, and W. You. Comprehensive investigation of self-assembled monolayer formation on ferromagnetic thin film surfaces. *Journal of the American Chemical Society*, 130:9763–9772, 2008.

[69] Y. Takata, T. Yokoyama, S. Yagi, N. Happo, H. Sato, K. Seki, T. Ohta, Y. Kitajima, and H. Kuroda. Thiophenol adsorption on Ni(100) studied by S K-edge SEXAFS and XANES. *Surface Science*, 259:266 – 274, 1991.

[70] D. R. Huntley. The mechanism of the desulfurization of benzenethiol by nickel (110). *The Journal of Physical Chemistry*, 96:4550–4558, 1992.

[71] T. S. Rufael, D. R. Huntley, D. R. Mullins, and J. L. Gland. Adsorption and reactions of benzenethiol on the Ni(111) surface. *The Journal of Physical Chemistry*, 98:13022–13027, 1994.

[72] T. S. Rufael, D. R. Huntley, D. R. Mullins, and J. L Gland. Adsorption and reaction of dimethyl disulfide on the Ni(111) surface. *The Journal of Physical Chemistry B*, 102:3431–3440, 1998.

[73] R. G. Musket, W. McLean, C. A. Colmenares, D. M. Makowiecki, and W. J. Siekhaus. Preparation of atomically clean surfaces of selected elements: A review. *Applications of Surface Science*, 10:143 – 207, 1982.

[74] R. G. Nuzzo, B. R. Zegarski, and L. H. Dubois. Fundamental studies of the chemisorption of organosulfur compounds on gold(111). implications for molecular self-assembly on gold surfaces. *Journal of the American Chemical Society*, 109:733–740, 1987.

[75] M. Neuber, M. Zharnikov, J. Walz, and M. Grunze. The adsorption geometry of benzoic acid on Ni(110). *Surface Review and Letters*, 06:53–75, 1999.

[76] F. Tarazona-Vasquez and P. B. Balbuena. Complexation of the lowest generation poly(amidoamine)-NH2 dendrimers with metal ions, metal atoms, and Cu(ii) hydrates: An ab initio study. *The Journal of Physical Chemistry B*, 108:15992–16001, 2004.

[77] N. Camillone, T. Y. B. Leung, P. Schwartz, P. Eisenberger, and G. Scoles. Chain length dependence of the striped phases of alkanethiol monolayers self-assembled on Au(111): An atomic beam diffraction study. *Langmuir*, 12:2737–2746, 1996.

[78] D. J. Lavrich, S. M. Wetterer, S. L. Bernasek, and G. Scoles. Physisorption and chemisorption of alkanethiols and alkyl sulfides on Au(111). *The Journal of Physical Chemistry B*, 102:3456–3465, 1998.

[79] M. D. Porter, T. B. Bright, D. L. Allara, and C. E. D. Chidsey. Spontaneously organized molecular assemblies. 4. structural characterization of n-alkyl thiol monolayers on gold by optical ellipsometry, infrared spectroscopy, and electrochemistry. *Journal of the American Chemical Society*, 109:3559–3568, 1987.

[80] S. E. Creager and C. M. Steiger. Conformational rigidity in a self-assembled monolayer of 4-mercaptobenzoic acid on gold. *Langmuir*, 11:1852–1854, 1995.

[81] A. Dhirani, R. W. Zehner, R. P. Hsung, P. Guyot-Sionnest, and L. R. Sita. Self-assembly of conjugated molecular rods: A high-resolution stm study. *Journal of the American Chemical Society*, 118:3319–3320, 1996.

[82] H. J. Himmel, K. Weiss, and Ch. Woell et al. Ultrahigh vacuum study on the reactivity of organic surfaces terminated by OH and COOH groups prepared by self-assembly of functionalized alkanethiols on au substrates. *Langmuir*, 13:4943–4947, 1997.

[83] O. Dannenberger, K. Weiss, H. J. Himmel, and C. Woell. An orientation analysis of differently endgroup-functionalised alkanethiols adsorbed on au substrates. *Thin Solid Films*, 307:183 – 191, 1997.

[84] J. M. Tour, L. Jones, D. L. Pearson, J. J. S. Lamba, T. P. Burgin, G. M. Whitesides, D. L. Allara, A. N. Parikh, and S. Atre. Self-assembled monolayers and multilayers of conjugated thiols, α, ω-dithiols, and thioacetyl-containing adsorbates. understanding attachments between potential molecular wires and gold surfaces. *Journal of the American Chemical Society*, 117: 9529–9534, 1995.

[85] D. M. Alloway, M. Hofmann, D. L. Smith, and N. R. Armstrong et al. Interface dipoles arising from self-assembled monolayers on gold: UV-photoemission studies of alkanethiols and partially fluorinated alkanethiols. *The Journal of Physical Chemistry B*, 107:11690–11699, 2003.

[86] C. E. D. Chidsey and D. N. Loiacono. Chemical functionality in self-assembled monolayers: structural and electrochemical properties. *Langmuir*, 6:682–691, 1990.

[87] L. Strong and G. M. Whitesides. Structures of self-assembled monolayer films of organosulfur compounds adsorbed on gold single crystals: electron diffraction studies. *Langmuir*, 4:546–558, 1988.

[88] R. Staub, M. Toerker, T. Fritz, T. Schmitz-Huebsch, F. Sellam, and K. Leo. Flat lying pin-stripe phase of decanethiol self-assembled monolayers on Au(111). *Langmuir*, 14:6693–6698, 1998.

[89] N. Camillone, P. Eisenberger, T. Y. B. Leung, P. Schwartz, G. Scoles, G. E. Poirier, and M. J. Tarlov. New monolayer phases of n-allkane thiols self-ssembled on Au(111): Preparation, surface characterization, and imaging. *The Journal of Chemical Physics*, 101:11031–11036, 1994.

[90] H. Kondoh, C. Kodama, H. Sumida, and H. Nozoye. Molecular processes of adsorption and desorption of alkanethiol monolayers on Au(111). *The Journal of Chemical Physics*, 111:1175–1184, 1999.

[91] P. Schwartz, F. Schreiber, P. Eisenberger, and G. Scoles. Growth kinetics of decanethiol monolayers self-assembled on Au(111) by molecular beam deposition: An atomic beam diffraction study. *Surface Science*, 423:208 – 224, 1999.

[92] G. E. Poirier. Coverage-dependent phases and phase stability of decanethiol on Au(111). *Langmuir*, 15:1167–1175, 1999.

[93] R. Gerlach, G. Polanski, and H. G. Rubahn. Growth of ultrathin organic films on Au(111) surfaces. *Thin Solid Films*, 318:270 – 272, 1998.

[94] A. Aviram and M. A. Ratner. Molecular rectifiers. *Chem. Phys. Lett.*, 29: 277–283, 1974.

[95] P. Jiang and G. M. Morales. Synthesis of diode molecules and their sequential assembly to control electron transport. *Angewandte Chemie International Edition*, 43:4471, 2004.

[96] G. S. Tulevski, M. B. Myers, M. S. Hybertsen, M. L. Steigerwald, and C. Nuckolls. Formation of catalytic metal-molecule contacts. *Science*, 309: 591–594, 2005.

[97] M. Konopka, R. Rousseau, I. Stich, and D. Marx. Detaching thiolates from copper and gold clusters: Which bonds to break? *Journal of the American Chemical Society*, 126:12103–12111, 2004.

[98] Y. Takata, T. Yokoyama, S. Yagi, N. Happo, H. Sato, K. Seki, T. Ohta, Y. Kitajima, and H. Kuroda. Thiophenol adsorption on Ni(100) studied by S K-edge SEXAFS and XANES. *Surface Science*, 259:266 – 274, 1991.

[99] T. S. Rufael, D. R. Huntley, D. R. Mullins, and J. L. Gland. Adsorption and reactions of benzenethiol on the Ni(111) surface. *The Journal of Physical Chemistry*, 98:13022–13027, 1994.

[100] J. Stöhr, D. A. Outka, R. J. Madix, and U. Döbler. Evidence for a novel chemisorption bond: Formate HCO2 on Cu(100). *Phys. Rev. Lett.*, 54:1256–1259, 1985.

[101] M.D. Crapper, C.E. Riley, D.P. Woodruff, A. Puschmann, and J. Haase. Determination of the adsorption structure for formate on Cu(110) using sexafs and nexafs. *Surface Science*, 171:1–12, 1986.

[102] B. G. Frederick, M. R. Ashton, N. V. Richardson, and T. S. Jones. Orientation and bonding of benzoic acid, phthalic anhydride and pyromellitic dianhydride on Cu(110). *Surface Science*, 292:33 – 46, 1993.

[103] K. G. Purcell, J. Jupille, and D. A. King. Coordination number and surface core-level shift spectroscopy: Stepped tungsten surfaces. *Surface Science*, 208:245 – 266, 1989.

[104] B. H. McQuaide and M. S. Banna. The core binding energies of some gaseous aromatic carboxylic acids and their relationship to profon affinities and gas phase acidities. *Canadian Journal of Chemistry*, 66:1919–1922, 1988.

[105] A. E. Baber, K. Mudiyanselage, and D. J. Stacchiola et al. Assisted deprotonation of formic acid on Cu(111) and self-assembly of 1d chains. *Phys. Chem. Chem. Phys.*, 15:12291–12298, 2013.

[106] T. Bitzer, N.V. Richardson, and S. Reiss. Sodium-induced ordering of the benzoate species on Si(100)-2x1: a combined hreels, xps and nexafs study. *Surface Science*, 458:173 – 184, 2000.

[107] B.G. Frederick, Q. Chen, F.M. Leibsle, M.B. Lee, K.J. Kitching, and N.V. Richardson. Long-range periodicity in c(8x2) benzoate/Cu(110): a combined stm, leed and hreels study. *Surface Science*, 394:1 – 25, 1997.

[108] D. G. de Oteyza, A. Sakko, A. El-Sayed, E. Goiri, L. Floreano, A. Cossaro, J. M. Garcia-Lastra, A. Rubio, and J. E. Ortega. Inversed linear dichroism in F K-edge NEXAFS spectra of fluorinated planar aromatic molecules. *Phys. Rev. B*, 86:075469, 2012.

[109] U. Hergenhahn, A. Ruedel, K. Maier, A. M. Bradshaw, R. F. Fink, and A. T. Wen. The resonant auger spectra of formic acid, acetaldehyde, acetic acid and methyl formate. *Chemical Physics*, 289:57 – 67, 2003.

[110] M.D. Crapper, C.E. Riley, D.P. Woodruff, A. Puschmann, and J. Haase. Determination of the adsorption structure for formate on Cu(110) using sexafs and nexafs. *Surface Science*, 171:1–12, 1986.

[111] C. L. A. Lamont and J. Wilkes. Attenuation length of electrons in self-assembled monolayers of n-alkanethiols on gold. *Langmuir*, 15:2037–2042, 1999.

[112] K. C. Prince, R. Richter, M. De Simone, and M. Coreno. X-ray absorption spectra of some small polyatomic molecules. *Surface Review and Letters*, 09: 159–164, 2002.

[113] A. P. Hitchcock, P. Fischer, Aharon. Gedanken, and M. B. Robin. Antibonding $\sigma*$ valence MOs in the inner-shell and outer-shell spectra of the fluorobenzenes. *The Journal of Physical Chemistry*, 91:531–540, 1987.

[114] O. Plashkevych, L. Yang, O. Vahtras, H. Agren, and L. G.M. Petterson. Substituted benzenes as building blocks in near-edge X-ray absorption spectra. *Chemical Physics*, 222:125 – 137, 1997.

[115] C. J. Barnes, M. Valden, and M. Pessa. The unusal adsorption baheviour of benzene on Co(1010). *Surface Review and Letters*, 07(01n02):67–74, 2000.

[116] P. Salek, V. Carravetta, F. Kh. Gelmukhanov, H. Agren, B. Schimmelpfennig, M.-N. Piancastelli, and L. Sorensen et al. Dynamical suppression of atomic peaks in resonant dissociative photoemission. *Chemical Physics Letters*, 343:332 – 338, 2001.

[117] K. Wiesner, A. Naves de Brito, S.L. Sorensen, F. Burmeister, M. Gisselbrecht, S. Svensson, and O. Bjoerneholm. The dynamic auger-doppler effect in HF and DF: control of fragment velocities in femtosecond dissociation through photon energy detuning. *Chemical Physics Letters*, 354:382 – 388, 2002.

[118] P. Morin and I. Nenner. Atomic autoionization following very fast dissociation of core-excited HBr. *Phys. Rev. Lett.*, 56:1913–1916, 1986.

[119] A. Foehlisch, D. Menzel, P. Feulner, M. Ecker, R. Weimar, K.L. Kostov, G. Tyuliev, S. Lizzit, R. Larciprete, F. Hennies, and W. Wurth. Energy dependence of resonant charge transfer from adsorbates to metal substrates. *Chemical Physics*, 289:107 – 115, 2003.

[120] W. Wurth. Femtosecond dynamics of adsorbate charge transfer processes. *Applied Physics A*, 65:597–601, 1997.

[121] C. Keller, M. Stichler, G. Comelli, F. Esch, S. Lizzit, D. Menzel, and W. Wurth. Resonant auger processes in adsorbates. *Journal of Electron Spectroscopy and Related Phenomena*, 93:135–141, 1998.

[122] H. Hamoudi, S. Neppl, P. Kao, B. Schuepbach, P. Feulner, A. Terfort, D. Allara, and M. Zharnikov. Orbital-dependent charge transfer dynamics in conjugated self-assembled monolayers. *Phys. Rev. Lett.*, 107:027801, 2011.

[123] C. Keller, M. Stichler, G. Comelli, F. Esch, S. Lizzit, W. Wurth, and D. Menzel. Ultrafast charge transfer times of chemisorbed species from auger resonant raman studies. *Phys. Rev. Lett.*, 80:1774–1777, 1998.

[124] P. Kao, S. Neppl, P. Feulner, D. L. Allara, and M. Zharnikov. Charge transfer time in alkanethiolate self-assembled monolayers via resonant auger electron spectroscopy. *The Journal of Physical Chemistry C*, 114:13766–13773, 2010.

[125] V. B. Engelkes, J. M. Beebe, and C. D. Frisbie. Length-dependent transport in molecular junctions based on sams of alkanethiols and alkanedithiols: Effect of metal work function and applied bias on tunneling efficiency and contact resistance. *Journal of the American Chemical Society*, 126:14287–14296, 2004.

[126] D. J. Wold, R. Haag, M. A. Rampi, and C. D. Frisbie. Distance dependence of electron tunneling through self-assembled monolayers measured by conducting probe atomic force microscopy: Unsaturated versus saturated molecular junctions. *The Journal of Physical Chemistry B*, 106:2813–2816, 2002.

[127] N. Ballav, B. Schuepbach, O. Dethloff, P. Feulner, A. Terfort, and M. Zharnikov. Direct probing molecular twist and tilt in aromatic self-assembled monolayers. *Journal of the American Chemical Society*, 129: 15416–15417, 2007.

[128] Ph. Parent, C. Laffon, and F. Bournel. Core-induced photofragmentation of acetonitrile adsorbed on Au(111) and Pt(111). *The Journal of Chemical Physics*, 112:986–991, 2000.

[129] L. Hallmann, A. Bashir, T. Strunskus, and F. Tuczek et al. Self-assembled monolayers of benzylmercaptan and p-cyanobenzylmercaptan on Au(111) surfaces: Structural and spectroscopic characterization. *Langmuir*, 24:5726–5733, 2008.

[130] N. Ballav, B. Schuepbach, S. Neppl, P. Feulner, A. Terfort, and M. Zharnikov. Biphenylnitrile-based self-assembled monolayers on Au(111): Spectroscopic characterization and resonant excitation of the nitrile tail group. *The Journal of Physical Chemistry C*, 114:12719–12727, 2010.

[131] C. N. R. Rao and G. R. Rao. Nature of nitrogen adsorbed on transition metal surfaces as revealed by electron spectroscopy and cognate techniques. *Surface Science Reports*, 13:223 – 263, 1991.

[132] T. Nakayama, K. Inamura, Y. Inoue, S. Ikeda, and K. Kishi. Adsorption of benzonitrile and alkyl cyanides on evaporated nickel and palladium films studied by XPS. *Surface Science*, 179:47 – 58, 1987.

[133] F. Blobner, P. N. Abufager, R. Han, J. Bauer, D. A. Duncan, R. J. Maurer, K. Reuter, P. Feulner, and F. Allegretti. Thiolate-bonded self-assembled monolayers on Ni(111): Bonding strength, structure and stability. *J. Phys. Chem. C*, 119:15455–15468, 2015.

[134] L. H. Dubois, B. R. Zegarski, and R. G. Nuzzo. Spontaneous organization of carboxylic acid monolayer films in ultrahigh vacuum. kinetic constraints to assembly via gas-phase adsorption. *Langmuir*, 2:412–417, 1986.

[135] S. Neppl, U. Bauer, D. Menzel, P. Feulner, A. Shaporenko, M. Zharnikov, P. Kao, and D.L. Allara. Charge transfer dynamics in self-assembled monomolecular films. *Chemical Physics Letters*, 447:227 – 231, 2007.

[136] S. Rangan, J.-J. Gallet, F. Bournel, S. Kubsky, K. Le Guen, G. Dufour, F. Rochet, F. Sirotti, S. Carniato, and V. Ilakovac. Adsorption of benzonitrile on Si(001)-2x1 at 300 k. *Phys. Rev. B*, 71:165318, 2005.

[137] A. N. Caruso, R. Rajesh, G. Gallup, J. Redepenning, and P. A. Dowben. Orientation and bonding of biphenyldimethyldithiol. *Journal of Physics: Condensed Matter*, 16:845, 2004.

[138] D. K. Zhong and D. R. Gamelin. Photoelectrochemical water oxidation by cobalt catalyst (CoPi)-a-Fe2O3 composite photoanodes: Oxygen evolution and resolution of a kinetic bottleneck. *Journal of the American Chemical Society*, 132:4202–4207, 2010.

[139] S. Arabzadeh and M. R. Benam. Study the band structure and density of state of Co using density functional theory. *International Journal of Engineering Research and Applications*, 3:1604, 2013.

[140] S. Devillers, A. Hennart, J. Delhalle, and Z. Mekhalif. 1-dodecanethiol self-assembled monolayers on cobalt. *Langmuir*, 27:14849–14860, 2011.

[141] M. Getzlaff, J. Bansmann, and G. Schoenhense. The electronic structure of benzene adsorbed on thin Fe(110) and Co(0001) films. *Surface Science*, 323: 118 – 128, 1995.

[142] T. Weidner, A. Kramer, C. Bruhn, M. Zharnikov, A. Shaporenko, U. Siemeling, and F. Trager. Novel tripod ligands for prickly self-assembled monolayers. *Dalton Trans.*, pages 2767–2777, 2006.

[143] A. Shaporenko, A. Terfort, M. Grunze, and M. Zharnikov. A detailed analysis of the photoemission spectra of basic thioaromatic monolayers on noble metal substrates. *Journal of Electron Spectroscopy and Related Phenomena*, 151:45 – 51, 2006.

[144] E. Delamarche, B. Michel, H. Kang, and C. Gerber. Thermal stability of self-assembled monolayers. *Langmuir*, 10:4103–4108, 1994.

[145] T. Kondo, M. Yanagida, K. Shimazu, and K. Uosaki. Determination of thickness of a self-assembled monolayer of dodecanethiol on Au(111) by angle-resolved X-ray photoelectron spectroscopy. *Langmuir*, 14:5656–5658, 1998.

[146] D. G. Castner, K. Hinds, and D. W. Grainger. X-ray photoelectron spectroscopy sulfur 2p study of organic thiol and disulfide binding interactions with gold surfaces. *Langmuir*, 12:5083–5086, 1996.

[147] A. Shaporenko, K. Heister, A. Ulman, M. Grunze, and M. Zharnikov. The effect of halogen substitution in self-assembled monolayers of 4-mercaptobiphenyls on noble metal substrates. *The Journal of Physical Chemistry B*, 109:4096–4103, 2005.

[148] W. Auwärter, D. Ecija, F. Klappenberger, and J. V. Barth. Porphyrins at interfaces. *Nature Chemistry*, 7:105–120, 2015.

[149] T. Lukasczyk, K. Flechtner, L. R. Merte, N. Jux, F. Maier, J. M. Gottfried, and H. Steinrueck. Interaction of cobalt(ii) tetraarylporphyrins with a Ag(111) surface studied with photoelectron spectroscopy. *The Journal of Physical Chemistry C*, 111:3090–3098, 2007.

[150] W. Hieringer, K. Flechtner, A. Kretschmann, K. Seufert, W. Auwaerter, J. V. Barth, and J. M. Gottfried et al. The surface trans effect: Influence of axial ligands on the surface chemical bonds of adsorbed metalloporphyrins. *Journal of the American Chemical Society*, 133:6206–6222, 2011.

[151] A. Wiengarten, K. Seufert, W. Auwärter, D. Ecija, and J. V. Barth et al. Surface-assisted dehydrogenative homocoupling of porphine molecules. *Journal of the American Chemical Society*, 136:9346–9354, 2014.

[152] G. D. Santo, S. Blankenburg, C. Castellarin-Cudia, and A. Goldoni. Supramolecular engineering through temperature-induced chemical modification of 2h-tetraphenylporphyrin on Ag(111): Flat phenyl conformation and possible dehydrogenation reactions. *Chemistry - A European Journal*, 17:1435414359, 2011.

[153] M. Röckert, M. Franke, Q. Tariq, and O. Lytken et al. Insights in reaction mechanistics: Isotopic exchange during the metalation of deuterated tetraphenyl-21, 23D-porphyrin on Cu(111). *The Journal of Physical Chemistry C*, 118:26729–26736, 2014.

[154] K. Diller, F. Klappenberger, F. Allegretti, and J. V. Barth et al. Investigating the molecule-substrate interaction of prototypic tetrapyrrole compounds: Adsorption and self-metalation of porphine on Cu(111). *The Journal of Chemical Physics*, 138:154710, 2013.

[155] D. A. Duncan, P. S. Deimel, F. Allegretti, and J. V. Barth et al. Immobilised molecular catalysts and the role of the supporting metal substrate. *Chem. Commun.*, 51:9483–9486, 2015.

[156] W. Auwärter, K. Seufert, and J. V. Barth et al. Site-specific electronic and geometric interface structure of Co-tetraphenyl-porphyrin layers on Ag(111). *Phys. Rev. B*, 81:245403, 2010.

[157] A. Weber-Bargioni, J. Reichert, and J. V. Barth et al. Interaction of cerium atoms with surface-anchored porphyrin molecules. *The Journal of Physical Chemistry C*, 112:3453–3455, 2008.

[158] S. C. Khandelwal and J. L. Roebber. The photoelectron spectra of tetraphenylporphine and some metallotetraphenylporphyrins. *Chemical Physics Letters*, 34:355 – 359, 1975.

[159] C. T. Campbell. Atomic and molecular oxygen adsorption on Ag(111). *Surface Science*, 157:43 – 60, 1985.

[160] A. C. Papageorgiou, S. Fischer, J. Reichert, and J. V. Barth et al. Chemical transformations drive complex self-assembly of uracil on close-packed coinage metal surfaces. *ACS Nano*, 6:2477–2486, 2012.

[161] G. Heimel, S. Duhm, I. Salzmann, and N. Koch et al. Charged and metallic molecular monolayers through surface-induced aromatic stabilization. *Nature Chemistry*, 5:187–194, 2013.

[162] H. A. Engelhardt and D. Menzel. Adsorption of oxygen on silver single crystal surfaces. *Surface Science*, 57:591 – 618, 1976.

[163] F. Sedona, M. Di Marino, D. Forrer, and M. Sambi et al. Tuning the catalytic activity of Ag(110)-supported fe phthalocyanine in the oxygen reduction reaction. *Nature Materials*, 11:970–977, 2012.

[164] B. E. Murphy, S. A. Krasnikov, N. N. Sergeeva, and I. V. Shvets et al. Homolytic cleavage of molecular oxygen by manganese porphyrins supported on Ag(111). *ACS Nano*, 8:5190–5198, 2014.

[165] P. Deimel. Ligation of adducts to tetrapyrrolic metal-organic complexes adsorbed on Ag(111). Master's thesis, Technische Universität München, 2014.

[166] C. Schmidt, A. Witt, and G. Witte. Tailoring the Cu(100) work function by substituted benzenethiolate self-assembled monolayers. *The Journal of Physical Chemistry A*, 115:7234–7241, 2011.

[167] V. D. Castro., F. Bussolotti, and C. Mariani. The evolution of benzenethiol self-assembled monolayer on the Cu(100) surface. *Surface Science*, 598:218 – 225, 2005.

List of Figures

2.1 Schematic depiction of the X-ray Photoemission and subsequent Auger de-excitation process. . . . 6
2.2 UPS spectra of the 4-FTP SAMs measured with two perpendicular polarizations. . . . 11
2.3 Schematic depiction of the X-ray absorption process and the measurement geometry for a vector-type orbital. . . . 12
2.4 Schematic depiction of the TPD measurement. . . . 17
2.5 Schematic overview of the working principle of core hole clock spectroscopy. . . . 21
2.6 Schematic illustration of the Auger Resonant Raman Effect and Spectator Shift. . . . 24

3.1 Schematic drawing of the UHV chamber. . . . 27
3.2 Schematic diagram of a hemispherical electron energy analyzer. . . . 30
3.3 Schematic of the PEY detector. . . . 32
3.4 Optical layout of the beamline U49-2 PGM1. . . . 35
3.5 Optical layout of beamline Aloisa in Elettra. . . . 35

4.1 Schematic of SAM. . . . 40
4.2 Scheme of SAM growth approach. . . . 46
4.3 4FBA molecule Co LEED W4f. . . . 50
4.4 XPS spectra of 4-FBA multilayer and monolayer. . . . 52
4.5 NEXAFS spectra of 4-FBA multilayer. . . . 54
4.6 TPD spectrum obtained for the 4-FBA multilayer on Co(0001). . . . 55
4.7 NEXAFS spectra of 4-FBA monolayer. . . . 58
4.8 Fast-XPS of 4-FBA monolayer. . . . 60
4.9 2D contour plot of multilayer and monolayer decay spectra after resonant F 1s excitation. . . . 64
4.10 Electron decay spectra at several different excitation energies and NEXAFS spectrum of 4-FBA monolayer. . . . 65
4.11 Reconstruction of the monolayer decay spectra. . . . 68
4.12 Auger fraction and charge transfer time following resonant absorption at the F K-edge as a function of the excitation energy. . . . 69
4.13 Contour plot of Oxygen resonant Auger spectra at the O 1s to $2\pi^*$ resonance as a function of excitation energy. . . . 70
4.14 Reconstruction of the oxygen monolayer decay spectra. . . . 72

4.15 Variation of the normal Auger ratio as a function of the excitation energy. . . . 73
4.16 Comparison of the CT time of F 1s electrons acquired with theory of static conductance and that obtained with CHC approach. . . . 74
4.17 TPD spectrum obtained for the 4-CBA multilayer. . . . 77
4.18 XPS spectra of 4-CBA monolayer. . . . 80
4.19 NEXAFS spectra of 4-CBA multilayer and monolayer. . . . 82
4.20 Schematic drawing of the orientation of 4-CBA molecules. . . . 83
4.21 N1s-π_1^* and N1s-π_3^* RAES spectra of 4-CBA/Co(0001) SAM and multilayer, as well as the respective failure examples of reconstruction. 87
4.22 TPD spectrum from a 4-FTP multilayer measured with a QMS. . . 91
4.23 X-ray photoelectron spectra of the C 1s, F 1s and S 2p core levels from the thick 4-FTP multilayer on Co(0001). . . . 93
4.24 XPS of S 2p core level from 4-FTP/Co(0001) thick multilayer acquired after annealing to increasing temperatures. . . . 94
4.25 XP spectra of 4-FTP/Co(0001) thin multilayer adsorbed at 80 K and that after annealing at 240 K for ca. 30 s. . . . 96
4.26 Evolution of C 1s, F 1s and S 2p core-level XP spectra with increasing coverage for exposures from 0.01 Torr*s to 0.035 Torr*s, and XP spectra as well as curve-fitting analysis of the saturated monolayer that corresponds to 0.035 Torr*s. . . . 98
4.27 NEXAFS spectra of the 4-FTP/Co(0001) monolayer and submonolayer at the C and F K-edges for two orthogonal measurement geometries. . . . 99
4.28 Comparison of C 1s, F 1s and S 2p core level spectra of 4-FTP submonolayer that corresponds to a gas flux of 0.02 Torr*s prepared according to different procedures in two separate preparations, and the curve-fitting analysis of the XPS data of the submonolayer. . . . 101
4.29 2D contour plot representation of RAES spectra across the F K-edge resonance region for monolayer and submonolayer. . . . 104
4.30 Variation of the Auger fraction and corresponding CT time as a function of the excitation energy for a 4-FTP monolayer on Co(0001) for resonant F 1s excitation. . . . 105
4.31 Comparison of the Auger fraction and corresponding CT time as a function of excitation energy obtained for 4-FTP monolayer (0.035 Torr*s) and submonolayer (0.02 Torr*s) on Co(0001) for resonant F 1s excitation. . . . 106

5.1 TPD spectra of a multilayer of 2H-TPP on Ag(111) for m/e ratio of 52 and 2, respectively; TPD spectrum of a 2H-TPP monolayer and the monolayer after pre-annealing to 550 K for different times. . 111
5.2 TPD spectra measured from a monolayer of 2H-TPP on Ag(111) for m/e 2, with varied heating rate. . . . 113
5.3 Sequential N 1s and C 1s core-level spectra of 2H-TPP on Ag(111). 114
5.4 TPD spectrum measured from a Ru-TPP multilayer on Ag(111) for m/e 2 with a heating rate of 0.5 K/s. . . . 115

5.5 NEXAFS spectra at the C K-edge after annealing of a Ru-TPP multilayer on Ag(111) with different heating profiles. 116
5.6 N 1s and $Ru\,3d_{3/2}$ core-level spectra of the Ru-TPP monolayer. . . 117
5.7 Valence spectra measured after annealing of the Ru-TPP multilayer with different heating profiles. 119
5.8 XP spectra of O 1s and $Ru3d_{5/2}$ levels acquired before and after exposure of non-flattened Ru-TPP molecules on Ag(111) to 20000 L and 8000 L of O_2 at 300 K and 610 K, respectively. 120
5.9 XP spectra of O 1s and $Ru3d_{5/2}$ levels, and O K-edge NEXAFS of a flattened Ru-TPP/Ag(111) surface after exposure to 20000 L of O_2 at 620 K. 121
5.10 XP spectra of O 1s and $Ru\,3d_{5/2}$ levels, and O K-edge NEXAFS spectra of a flattened Ru-TPP/Ag(111) surface after exposure to 20000 L of O_2 at 300 K. 123
5.11 Valence spectra measured before and after exposure of a flattened RuTPP/Ag(111) surface held at 620 K and 300 K, respectively, to 20000 L of O_2. 123
5.12 O 1s and $Ru\,3d_{5/2}$ spectra before and after exposure of clean Ag(110) and Ru-TPP/Ag(110) monolayer to 10000 L of O_2 at RT. The spectra after holding the oxygen-exposed surface at 370 K for 10 min are also shown. 126
5.13 $Ru\,3d_{5/2}$ and O 1s spectra of Ru-TPP monolayer on Ag(110) after the exposure to increasing dosage of O_2 at RT 127
5.14 O 1s and $Ru\,3d_{5/2}$ spectra of the oxygen-exposed (10000 L) RuTPP monolayer on Ag(110) after further annealing to 550 K or exposing to 1000 L of CO at RT; TPD spectrum of the oxygen-exposed monolayer pre-annealed to 370 K for m/e 18. 128

A.1 Comparison of C 1s, F 1s and S 2p core-level spectra of 4-FTP monolayers prepared with standard approach and stepwise approaches, respectively. 137
A.2 UP spectra of 4-FTP/Ni(111) SAM prepared in the standard way excited with s- and p-polarized He I radiation. Inset shows the dichroic signal from 4-FTP/Ni(111) SAM prepared stepwise and in the standard way. 139
A.3 UP spectra of 4-FTP/Ni(111) SAM prepared stepwise by incremental doses up to monolayer completion at 80 K, and of the same SAM followed by an annealing step to 200 K. The right panel shows the dichroic signal of the unannealed (80 K) and annealed (200 K) SAMs. 140
A.4 Comparison of the core-level spectra of the 4-FTP/Ni(111) submonolayer film deposited at 80 K and the standard 4-FTP/Ni(111) monolayer; valence spectra of the 4-FTP/Ni(111) submonolayer prepared at 80 K and the same submonolayer followed by an annealing step to 200 K. 141

B.1 O 1s and $Ru3d_{5/2}$ spectra measured before and after exposure of the Ru-TPP/Ag(111) surface held at room temperature to ionized oxygen. 144

List of Acronyms

XPS	X-Ray Photoelectron Spectroscopy
UPS	Ultraviolet Photoelectron Spectroscopy
AES	Auger Electron Spectroscopy
NEXAFS	Near Edge X-ray Absorption Fine Structure
CHC	Core Hole Clock
DOS	Density Of States
HOMO	Highest Occupied Molecular Orbital
LUMO	Lowest Unoccupied Molecular Orbital
TPD	Thermal Programmed Desorption
QMS	Quadrupole Mass Spectrometer
UHV	Ultra-High Vacuum
LEED	Low Energy Electron Diffraction
eV	electron Volts
fs	femtosecond
as	attosecond
RAES	Resonant Auger Electron Spectroscopy
4-FTP	4-Fluorothiophenol
4-FBA	4-Fluorobenzoic Acid
4-CBA	4-Cyanobenzoic Acid
4-CTP	4-Cyanothiophenol

Acknowledgements

First of all, I want to thank Prof. Johannes Barth for accepting me as a PhD student in E20 in 2011 and offering me the opportunity to come from China to Germany, and for providing me such a relaxed environment in the past four years of study. I thank Prof. Peter Feulner for guiding my experimental work since the first day I entered the PSD lab, for each beamtime in Bessy, and for helping me not only in experiments with his expertise and patience but also when I have problems outside of work. I will never forget the long talk with him when I got lost during my PhD. I thank Dr. Francesco Allegretti for providing me many interesting subjects and ideas as alternatives of the main CHC investigation; I would not be able to finish the experiments and acquire so many data relating to porphyrins without his help and guidance, and I thank him for correcting my thesis and teaching me a lot about scientific writing.

I thank Dr. Florian Blobner for instructing the operations of the PSD chamber and for the beamtime together in Bessy. I thank Dr. David A. Duncan and Johannes Bauer for the time together in the beamline as well as in the PSD lab. I also want to thank the secretary of E20, Viktoria Blaschek, for helping me whenever I got confused by the German documents and procedures. Reinhold Schneider, Karl Koelbl, and Karl Eberle provided technical support during my PhD study. Kamila Wilson helped me to find my first accommodation in Munich about four years ago. My officemates Kaposi Tobias and Nacho Urgel established a relaxed working atmosphere for me. My friends in the group, Hai, Yuxiang, Yuanqin and Juan spend a lot of pleasant time of afternoon tea with me. I thank all of you!

I must mention that my wife, Yaru, is always under the same mood as me during the last year of my PhD study. In the past year, it is not boring at all because of her carefulness and consideration. My parents provided me financial and psychological support all the time. I am very grateful for their companionship in all aspects of my life.